Subcritical Behaviour in Rotating Convection and Convectively-Driven Dynamos

Robert George Cooper

Supervised by
Céline Guervilly
Paul J. Bushby

Thesis submitted for the degree of
Doctor of Philosophy



School of Mathematics, Statistics & Physics
Newcastle University
Newcastle upon Tyne
United Kingdom

June 2022

Acknowledgements

Firstly I would like to thank my supervisors Céline Guervilly and Paul Bushby for their guidance and supervision throughout my PhD. I truly appreciate their time invested in answering my queries and attempting to understand my codes. Thank you also to the IT staff in the department: John Nicholson, Michael Beaty, and especially George Stagg who frequently solved my weird and wonderful computer issues.

I thank all of those in the department who have helped me in the past 8 years, ranging from Carlo Barenghi who first inspired me to pursue research in fluid dynamics, to my fellow PhD students and researchers both in Newcastle and afar, especially: Clarissa Barrett, Em Rickinson, Hayley Stagg, Stephen Mason, Rathish Ratnasingam, Alex Hindle, Matina Trachana, Sultan Alyobi, Rob Long, Craig Duguid and many more.

Throughout my PhD I have benefitted from the love, support and prayers of my various church families (in Cramlington Parish, Parish of North Wearside and very recently, Oxclose Church). I'd especially like to thank Aidan Brierley, the Hutchins, the Noppen/Harbottle-Noppens and the Walsh family (Frankie, Tom, Lilith and Evelyn).

To my mum, Chris, Charlie and Grandma Smith: Thank you for sticking by me, being available to listen, visiting us up North, and supporting me throughout my PhD. And thank you to my dad for always driving me to be better. Similarly I thank Paul and Dilys for their support and availability to nip round the corner to help out. I thank my puppy, Bailey, for helping me to de-stress and always bringing energy and joy. And more than anything, I thank my beautiful, loving and patient wife, Becca, who had to listen to me endlessly rambling on about mathematics or debating whether I should quit throughout my PhD. I truly could not have managed this without your love and care, I'm so proud of everything we've been through and look forward to our future together.

Finally, I want to thank God, for being a part of my life throughout this time. I give thanks for Your guidance by the Holy Spirit, Your answers to my prayers, and Your faithfulness in ensuring I am always held by You. I pray for every single person who has been a part of my journey to where I am now and pray that You will be with each and every one of them, always. Amen

> *For I know the plans I have for you, plans to prosper you and not to harm you, plans to give you hope and a future.* - Jeremiah 29:11

Abstract

In planets and stars, convection is thought to be key for generating and maintaining large-scale magnetic fields. Many planets possess a hydromagnetic dynamo driven by convective motions, such as the geodynamo. However, a number of smaller planetary bodies, such as Mars, show evidence of once possessing a dynamo that suddenly ceased to exist. One suggested cause for the sudden cessation of the Martian dynamo is that it was operating in a subcritical parameter regime, that is, the dynamo continued to exist when its controlling parameter decreased below the critical value for linear onset, before eventually collapsing towards the non-magnetic trivial state. This thesis aims to explore subcritical behaviour in dynamo action and convection in order to better understand the dynamic processes that affect planetary dynamos.

In the first part of this thesis, we focus upon the simpler problem of rotating convection in the absence of a magnetic field. In two-dimensional rotating convection, localised states, known as 'convectons', have previously been observed for moderate rotation rates. Convectons are associated with systematic shear flows which locally reduce the inhibiting nature of rotation on convection, potentially promoting subcritical behaviour. We study convectons in 2D Boussinesq convection in a rotating plane layer and perform parametric surveys in both a fully-truncated model with restricted symmetries, and a model where the full horizontal structure is allowed. We successfully obtain rotating convectons for rapid rotation and explore their bifurcation structure, stability and key features. In particular, we show that convectons are typically associated with a full local reduction in the effective rotation.

In the second part of this thesis, we study dynamo action using 3D numerical simulations of planar Boussinesq convection at rapid rotation, focussing again on subcritical behaviour. We first generate a large-scale magnetic field in the supercritical regime that significantly influences convective motions. Subcritical solutions are then found by tracking this solution branch into the subcritical regime. Here the dynamo is sustained for convective driving below the critical value for the linear onset of non-magnetic convection. We show that increasing rotation leads to an extension of the subcritical range to an optimal value. At more rapid rotation, subcriticality is then hampered by the emergence of a large-scale convective mode. The inability of the large-scale mode to sustain dynamo action leads to an intermittent behaviour that appears to inhibit subcriticality. Finally, we study the key parameter regimes at which subcritical dynamos exist, such as an optimal magnetic Reynolds number.

Contents

1 Introduction **1**

1.1 Overview . . . 1

1.2 Planetary Magnetic Fields . . . 2

1.2.1 Convection and the Geodynamo . . . 2

1.2.2 The Martian Dynamo . . . 5

1.2.3 Other Planetary Magnetic Fields . . . 8

1.3 Outline . . . 9

2 Theoretical Background **11**

2.1 Governing Equations of Plane Layer Convection . . . 11

2.2 The Boussinesq Approximation . . . 13

2.3 Rotating Convection . . . 14

2.3.1 The Taylor-Proudman Effect . . . 15

2.4 Convective Onset . . . 15

2.4.1 Onset of Stationary Convection . . . 19

2.4.2 Onset of Overstable Convection . . . 20

2.5 Magnetohydrodynamics (MHD) . . . 22

2.5.1 Maxwell Equations and the Induction Equation . . . 22

2.5.2 MHD/Dynamo Equations . . . 24

2.6 Dynamo Theory . . . 25

2.6.1 Kinematic Dynamos . . . 26

2.6.2 The Alpha and Omega Effects . . . 26

2.6.3 Mean Field Electrodynamics . . . 27

2.6.4 The Childress-Soward Dynamo . . . 29

2.6.5 Force Balances . . . 30

3 Localised States in Rapidly Rotating Plane Layer Convection **33**

3.1 Introduction . . . 33

3.2 Governing Equations and Numerical Schemes . . . 36

3.2.1 Full Truncation (AUTO model) . . . 39
3.2.2 Full Horizontal Structure (MATLAB model) . . . 42
3.2.3 Output Parameters . . . 43
3.2.4 Solution Branch Naming Convention . . . 44
3.3 Model Testing . . . 45
3.4 Results . . . 48
3.4.1 Initial Investigation in AUTO . . . 48
3.4.2 Branch Tracking in MATLAB . . . 51
3.5 Conclusions . . . 64

4 Subcritical Dynamos in Rapidly Rotating Plane Layer Convection 68
4.1 Introduction . . . 68
4.2 Model . . . 71
4.2.1 Governing Equations and Boundary Conditions . . . 71
4.2.2 Definition of the Output Quantities . . . 72
4.3 Results . . . 74
4.3.1 Supercritical Dynamos at Moderate Ekman Numbers . . . 77
4.3.2 Subcritical Dynamos at Moderate Ekman Numbers . . . 84
4.4 Conclusions . . . 92

5 Intermittent Dynamo Action at Low Ekman Numbers 94
5.1 Introduction . . . 94
5.2 Results . . . 95
5.3 Conclusions . . . 110

6 Conclusions 113
6.1 Rapidly Rotating Convection . . . 113
6.2 Subcritical Dynamos . . . 116
6.3 Intermittent Dynamos at Rapid Rotation . . . 118
6.4 Final Remarks . . . 119

A Derivations in Fully Truncated Model 121
A.1 Nonlinear Terms in AUTO-07p . . . 121
A.1.1 Cosine-Cosine Nonlinearities . . . 122
A.1.2 Sine-Sine Nonlinearities . . . 122
A.1.3 Sine-Cosine Nonlinearities . . . 123
A.2 AUTO-07p Output Quantities . . . 123

Chapter 1

Introduction

1.1 Overview

Convection is an important mechanism in fluid dynamics affecting many geophysical and astrophysical systems throughout the universe. In planets and stars, convection is thought to be key for generating and maintaining large-scale magnetic fields (Elsasser, 1939). In most astrophysical bodies, magnetic fields are thought to be generated by a self-sustaining hydromagnetic dynamo, originally proposed by Larmor (1919) as an explanation for the Sun's magnetic field. In a hydromagnetic dynamo, kinetic energy from fluid motions is converted into magnetic energy, leading to the amplification of the magnetic field. Once the magnetic field has become sufficiently strong, this reacts back on the fluid motions causing a modification of the flow. Furthering our understanding of convection is therefore paramount to better understanding the generation and maintenance of dynamo action in the universe around us.

The laws that govern dynamo action involve fusing the governing equations of fluid motion, the famous Navier-Stokes equation, with the foundations of electromagnetism summarised in Maxwell's equations. When applied to astrophysical bodies, a number of other factors enter the fray, such as the effects of rotation and other body forces such as gravity, leading to complex behaviour which can rarely be solved analytically. We must therefore turn to the ever-advancing study of numerical solutions to the dynamo equations, making use of the computational resources available. In this thesis we will be interested in numerical solutions of both the Navier-Stokes (with rotation but without a magnetic field) and the full dynamo equations, both driven by thermal convection in a rotating plane layer. Clearly many bodies such as planets and stars are approximately spherical, however the study of plane layer convection allows us to explore more extreme parameter regimes whilst still capturing much of the important observed dynamics. The governing equations are presented in Section 2.

Primarily, the work in this thesis will involve theoretically exploring convectively driven dynamos, leading to results relevant for a wide range of rotating convective bodies and dynamos. This work is especially motivated by exploring how rotation and magnetic fields influence fluid flow, and hence dynamo action, with applications to the cessation of the Martian dynamo and the dynamics of the present geodynamo. This will be discussed in more detail in the following sections.

1.2 Planetary Magnetic Fields

1.2.1 Convection and the Geodynamo

We begin by introducing the structure of the Earth's magnetic field and the relevance of convection to the geodynamo.

The ancient Chinese were the first known to have investigated the Earth's magnetic field at the end of the first millennia, i.e. $\sim$ 1000CE, with the first mention of a compass in 1088 (Needham, 1976). However, the Western world began to investigate the Earth's interior structure in the Middle Ages. In 1269, potential explanations were offered for magnetic attraction and repulsion; how a compass functions; what some of the properties of magnetic materials are; and the concept of magnetic poles (Arnold, 1904). Magnetic field reversals were also vaguely described at the time. Gilbert (1600) later showed that the direction of a compass is controlled by the Earth's global magnetic field.

Over time, navigators had witnessed slow changes in the Earth's magnetic field, now referred to as 'secular variation' and Halley (1683, 1692) later proposed that the geomagnetic field originates from a fluid shell within the Earth's interior. Eventually this led to the model of the Earth's structure we recognise today, quantitatively modelled for the first time by Wiechert (1897) and shown in Figure 1.1(a). At the time, the model included a metallic core at the centre of the Earth, surrounded by a rocky mantle, with chemical and physical deviations between the two regions. The discontinuity between these layers later became known as the 'core-mantle-boundary' (CMB) at radius $r_o \approx 3480$km, located initially by Gutenberg (1912). This is approximately 55% of the Earth's radius, $r_\oplus \approx 6378$km.

Meanwhile, Oldham (1906) had identified seismic P-waves and S-waves travelling through the Earth's interior, with P-waves exhibiting slower behaviour in the core and S-waves unable to travel through the core at all (often referred to as the 'P-wave shadow'). Jeffreys (1926) showed that such behaviour could be satisfied by the existence of a fluid outer core. The boundary between this fluid outer core and the solid inner core is called the 'inner-core-boundary' (ICB) and lies at $r_i \approx 1220$km.

The presence of a liquid outer core is thought to be key to the secular variation in the geomagnetic field, with Zollner (1871) forming the first model which included elec-

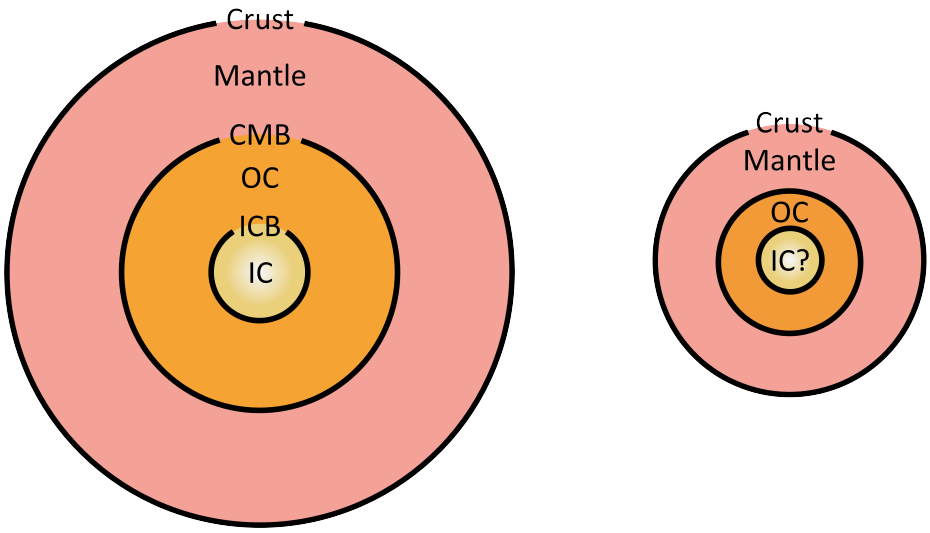
trical currents induced within the liquid core. Zollner also recognised the importance of considering the interaction between the core and the mantle at the CMB. The dominant geomagnetic field originating in the core is currently estimated to be at least 3.4Ga years old (3.4 billion years) according to rock samples (Tarduno *et al.*, 2010), and could have existed since the formation of the core itself. In 1848, Gauss introduce a method of studying the geometries of planetary magnetic fields by fitting spherical harmonics to the observed magnetic field, before investigating which of the coefficients, referred to as *Gauss coefficients*, are dominant (Campbell, 2003). The geomagnetic field is observed to be dipolar, especially when averaged over long timescales. Studies of non-dipolar parts of the magnetic field exhibit variations over timescales of centuries, thus the dipole is dominant on a scale of millenia. Overall, the Earth's magnetic field does exhibit fluctuations on a wide range of timescales, such as magnetic field reversals (e.g. Jackson & Finlay, 2015). There is little evidence for overall decay in the dipole moment on geological timescales, which, grouped with the long-lasting existence of such a global field and the inadequacy of permanent magnetisation as a viable solution, require a mechanism which can regenerate the magnetic field. Based on estimates of the electrical conductivity in the core, the dipole part of the geomagnetic field has an e-fold decay time of 30-50kyr (Olson, 2015), but the strong magnetic field requires regeneration on a timescale much shorter than this. Furthermore, the Earth has possessed its magnetic field for at least 3.4×10^9 years (Kono & Tanaka, 1995). Something must still be maintaining the geomagnetic field. The solution is a hydromagnetic dynamo driven by convection.

A more detailed discussion of dynamo theory is included in Chapter 2.6. Larmor (1919) was the first to suggest the existence of a self-sustaining fluid dynamo, motivated by the Sun, however the idea is similarly applicable to the Earth. Larmor proposed that since circulation of a conducting fluid in the presence of a pre-existing magnetic field could induce an electric field, under the right conditions this electric field could create and maintain a stronger overall magnetic field. Evidence from seismology indicates that the Earth's outer core is predominantly iron, but also possesses other lighter elements (Birch, 1952, 1964). Fluids made up of such iron compounds possess low viscosity (de Wijs *et al.*, 1998). At sufficiently low viscosity, and as the Earth's core gradually cools, convective fluid motion is able to occur due to temperature gradients across the core, as well as wave behaviour, turbulence and other fluid motions. Today, typical velocities of fluid motion within the core are estimated at ~ 20km/yr (Olson, 2015). Whilst this appears slow, it is still sufficient to drive a dynamo. Such fluid motion is able to convert kinetic energy into electromagnetic energy, creating the geodynamo. This mechanism is also influenced by the Earth's global rotation, via the Coriolis force. Based on estimates of typical velocity and length scales within the outer core, the Rossby number (which quantifies the ratio of inertial forces to the Coriolis force) is of order 10^{-6}, indicating that rotation completely

dominates inertial forces in the outer core and must be influential to core convection (Jones, 2015). The generated magnetic field then exerts forces back on the fluid in the outer core via the Lorentz force, altering the flow and obtaining an equilibrium which leads to the saturation of the dynamo. Fluid motion in the outer core is most likely thought to be driven by a mixture of thermal and compositional convection (Jones, 2011). Thermal convection is generated by inner core growth and heat loss through the CMB, whilst compositional convection is driven by lighter elements being expelled at the ICB as the inner core crystallises. Precession and tidal interactions have also been suggested to have an effect on the geodynamo (Malkus, 1994; Tilgner, 2007).

A century of theoretical and numerical work in magnetohydrodynamics have since followed, aiming to produce self-sustaining fluid dynamos which reproduce the observed behaviour in the Earth. In the last few decades some success has been made in numerical work, beginning with Glatzmaier & Roberts (1995), who were the first to produce fully nonlinear 3D dynamo simulations, shown in Figure 1.2. Their work was remarkably able to produce some of the slow secular variation observed in the geodynamo, as well as capturing a magnetic field reversal. The challenge of numerical simulations since, has been reaching the extreme parameter regimes relevant to planetary conditions. Advances in high-performance computing constantly allow us to reach more realistic conditions, but we still remain some way from true planetary core conditions. For example, the dimensionless Ekman number represents the ratio of viscous forces to the Coriolis force. In the Earth this is estimated to be of order 10^{-15} (Olson, 2015) yet numerical simulations in spherical geometries have only recently reached Ekman numbers of order 10^{-7} (e.g. Schaeffer *et al.*, 2017). Notably, numerical dynamo simulations study systems which overestimate the importance of viscous effects relative to rotation, are not turbulent enough and have a higher kinematic viscosity relative to thermal diffusivity than in realistic planetary conditions. Despite this, by exploring regimes which exhibit force balances similar to those expected in planetary cores, we can perhaps further understand the dynamic processes which result in a convectively-driven fluid dynamo (e.g. Schwaiger *et al.*, 2021).

At rapid rotation, Childress & Soward (Childress & Soward, 1972; Soward, 1974) were the first to demonstrate that convective motions were capable of sustaining a dynamo, identifying several possible force balances depending on the strength of the magnetic field. Importantly, they observe the presence of a mean magnetic field that is able to influence the convective flow, changing the flow structures that originally amplified the seed magnetic field. A more thorough discussion of dynamo theory is presented in Chapter 2. Two of the key questions in dynamo theory today that we explore in this thesis are: how does the mean magnetic field interact with the fluid motion that led to its amplification? And how are the convective flows able to continue to sustain dynamo action after being modified by the mean field?



(a) (b)

Figure 1.1: A simple diagram of (a) the Earth's structure showing the inner core (IC), inner-core-boundary (ICB) at $\sim$ 1220km, outer core (OC) and core-mantle-boundary (CMB) at $\sim$ 3480km, as well as (b) Mars' structure featuring the outer core (OC) and possible inner core (IC). (To scale according to recent estimates).

1.2.2 The Martian Dynamo

As one of our nearest neighbours, it is only natural that we look to Mars to further understand the universe around us. A number of similarities occur between Earth and Mars, with Mars expected to have a similar overall structure, shown in Figure 1.1(b). Like Earth, Mars possesses an outer crust with a mantle underneath and metallic core at the centre. We are confident that Mars possesses at least a liquid outer core (Yoder *et al.*, 2003), however it is unclear as to whether Mars has a solid inner core and its size.

The first mission equipped to record Mars' magnetic field observed no evidence of a self-generated field. However, in 1997 the Mars Global Surveyor produced astonishing findings. During aerobraking phases, the Mars Global Surveyor approached $\sim$ 100km above the Martian surface and detected magnetic field sources of multiple scales, strengths and geometries emanating from the surface (Acuña *et al.*, 1999). The history of a planet's magnetic field can be determined by studying remanent magnetisation in rocks, since igneous rocks contain ferromagnetic minerals. This occurs when rocks cool below the temperature at which a mineral becomes magnetic in the presence of a surrounding magnetic field, called the Curie temperature. The magnetic field strength and direction of the field can then be determined at the time of rock formation.

Early measurements had previously concluded that Mars does not currently possess an active global magnetic field. However, the fact that the northern lowlands showed little

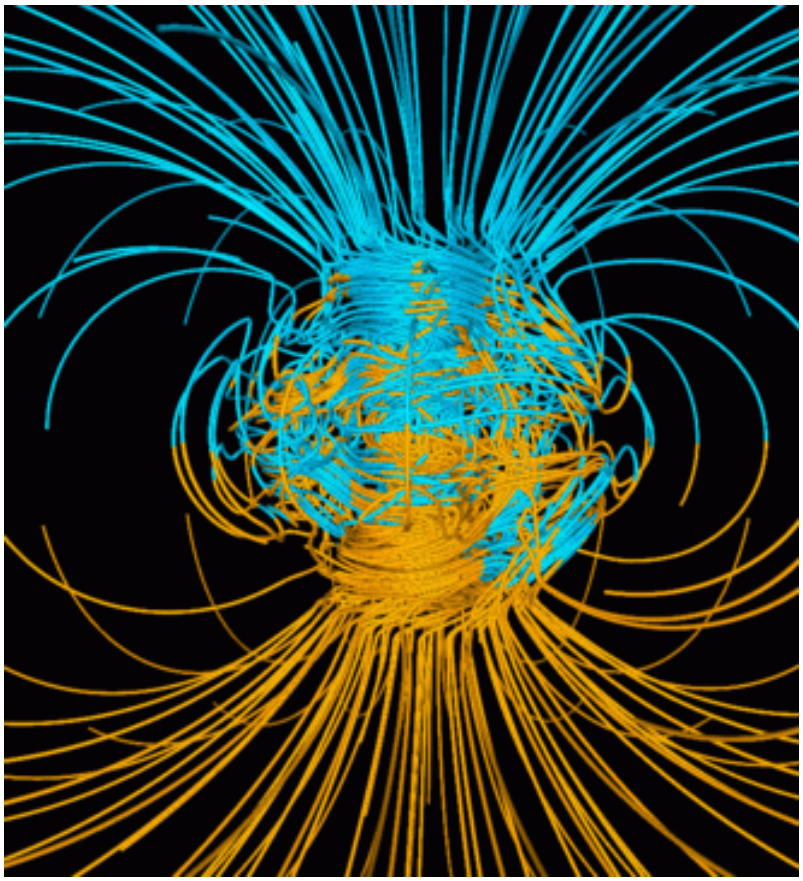


Figure 1.2: Glatzmaier & Roberts (1995) were among the first to successfully simulate many of the features of the geodynamo, including capturing a successful field reversal. This figure shows magnetic field lines displaying dipolar behaviour away from the core with yellow lines indicating that the radial magnetic field is directed outwards and blue lines directed inwards.

or weak magnetisation, in comparison to the strong, small scale magnetisation localised to the southern highlands can only be explained by an active dynamo which has now become extinct. Fig 1.3 shows the radial component of the magnetic field at the crust, superimposed over a map of cratered regions on the Martian surface. The absence of crustal magnetisation in large impact basins such as Argyre and Hellas implies that the dynamo was not active at the time of impact. The ages of the Argyre and Hellas basins indicate that the Martian dynamo ceased to be active at least ~ 4.1 billion years ago (Strom *et al.*, 1992). Lillis *et al.* (2008) further add that the cessation occurred rapidly, over $1 - 20$ million years.

The physical discrepancy in magnetic field strength between the weak northern lowlands and strong southern highlands could imply that Mars had a hemispherical dynamo. In a hemispherical dynamo, the resultant magnetic field produced by dynamo action is confined to one hemisphere of a rotating spherical shell (Grote & Busse, 2000). Numerical dynamo simulations suggest that a hemispherical dynamo could be produced by

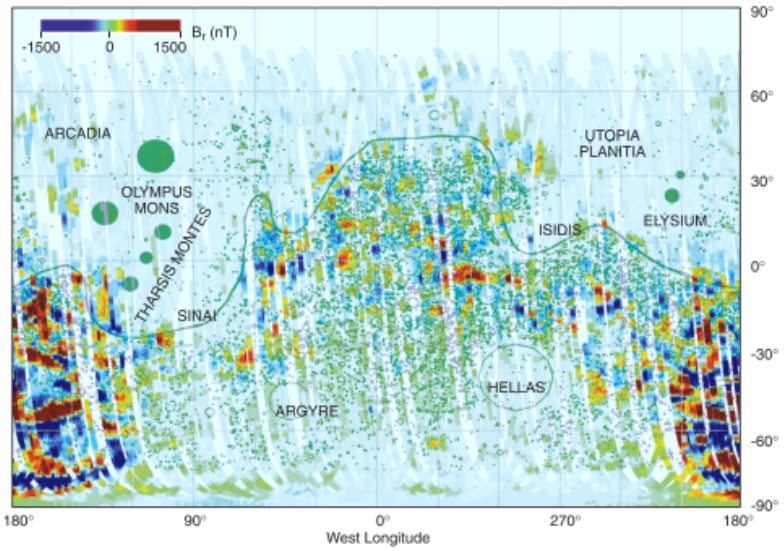


Figure 1.3: The radial component of the magnetic field at the crust, B_r, superimposed over a map of cratered regions on the Martian surface. From Acuña *et al.* (1999).

variations in mantle convection and heat flow through the core-mantle-boundary between hemispheres (e.g. Stanley *et al.*, 2008). However, using dynamo simulations with heterogeneous boundary conditions, Dietrich & Wicht (2013) observe frequent field reversals over relatively short timescales, and insufficiently strong and uniformly oriented fields to produce the local magnetisation observed in the southern highlands. Furthermore, Landeau & Aubert (2011) suggest that from estimates of the parameters within the Martian core, the symmetry-breaking of the flow would not be large enough to generate a hemispherical dynamo. An alternative explanation is that giant impacts and alterations after the cessation of Mars' dynamo have removed the pre-existing crustal magnetism in some areas.

Kuang *et al.* (2008) were the first to propose that the rapid cessation of the Martian dynamo could have been caused by a subcritical dynamo. That is, at the time of cessation, Mars possessed sufficient energy to sustain its large-scale magnetic field against Ohmic dissipation, but not enough to have initially amplified a weak seed field. In order to amplify a weak seed magnetic field by dynamo action, vigorous fluid motion is required, typically driven by thermal convection. Whilst, compositional convection likely has some effect on fluid motions, estimates of the thermal and compositional diffusion coefficients in planetary cores suggest that thermal diffusion occurs at a much higher rate. For example, in the Earth the thermal diffusivity is estimated to be $\sim \mathcal{O}(10^{-6})$, whilst the compositional diffusion coefficient is estimated to be $\sim \mathcal{O}(10^{-9})$ (Olson, 2015). The amplification of the magnetic field leads to a field that is then able to influence the convective flow. Once the dynamo has been created, gradual cooling in the liquid core could lead to convective

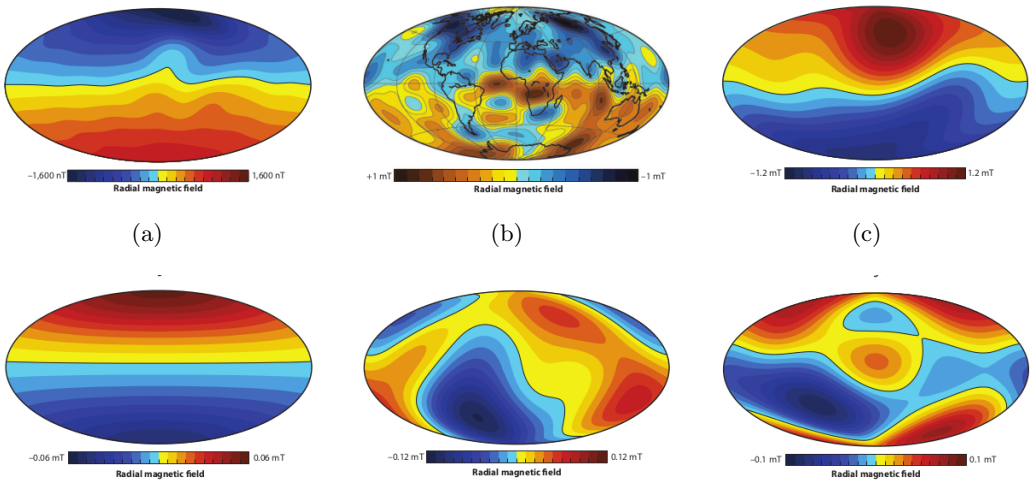
motions becoming weaker. Since the influence of the field on the flow can allow the energy required to sustain a dynamo to be less than required to create it, the energy produced by convection could still have sustained the Martian dynamo despite this cooling. Kuang *et al.* further show that less than a 1% reduction in the imposed heat flow in this subcritical regime could then lead to a rapid collapse of the dynamo. Since the fluid motions now produce less energy than when the dynamo was generated, Mars would then not be able to restart its dynamo, with an increased heat flow of 25% then required to reactivate it according to Kuang *et al.*.

To date, the influence of subcritical behaviour on dynamo action has rarely been explored. Individual examples of subcritical dynamo action have been studied through numerical simulations (e.g. St. Pierre, 1993; Stellmach & Hansen, 2004), however, it is unknown how the subcritical behaviour changes with the variation of key parameters such as the rotation rate. It is also unclear what the optimal parameter regime is and what the important features are for such dynamos to exist. We explore these questions in Section 4, which has been published in Cooper *et al.* (2020).

1.2.3 Other Planetary Magnetic Fields

Like Earth and Mars, other planets and astrophysical bodies also generate magnetic fields. Most planets within our solar system (with the exception of Venus and Mars) currently possess an internally generated global magnetic field. Their strengths and geometries vary but most commonly appear to be dipolar. Thorough discussions of magnetic fields in other planetary bodies can be found in Jones (2011) or Christensen (2019), for example, with some of the general overall features highlighted in this section. A visual summary of the radial components of the magnetic field for some of the planets discussed is shown in Figure 1.4. It should be noted that we have far better data for Earth than for other planets in our solar system.

Mercury's magnetic field is predominantly dipolar but is much weaker than the Earth's (Anderson *et al.*, 2010). Interestingly, its field is highly symmetric about its rotation axis. In contrast, Venus shows no evidence of having possessed a magnetic field (Russell, 1980). However, the lack of remanent magnetisation at the surface is not unexpected as its surface temperature is close to the Curie point. Our own moon also shows signs of previously possessing its own magnetic field, with evidence from the Apollo missions discovering remanent magnetisation in samples. It is thought that our moon once generated a small-scale magnetic field, i.e. a magnetic field dominated by larger Gauss coefficients, with surface magnetisation potentially as strong as the present magnetic field of the Earth (Cisowski *et al.*, 1983). Jupiter's magnetic field is much stronger than Earth's but appears similarly dipolar at large scales (Acuña & Ness, 1976). However, Jupiter appears to show differences in the magnetic field at smaller scales and appears to have a different structural dynamo



(a) (b) (c)

(d) (e) (f)

Figure 1.4: Contours of the radial component of the magnetic field at (a) Mercury's core-mantle-boundary, (b) Earth's core-mantle-boundary, (c) Jupiter's surface, (d) Saturn's surface, (e) Uranus' surface and (f) Neptune's surface. Figures taken from Jones (2011).

region. Additionally, it is unknown how exactly Jupiter's strong zonal winds interact with its dynamo (e.g. Wicht *et al.*, 2019). In 2011, NASA launched its 'Juno' space probe which entered Jupiter's orbit in 2016, aiming to further understand Jupiter's magnetic field origin and structure. Saturn's magnetic field appears to be strongly dipolar, with little variation from the dipole (Ness *et al.*, 1981). Cowling produced a set of anti-dynamo theorems, one of which states that a perfectly axisymmetric magnetic field cannot be maintained by a dynamo (Cowling, 1934). Apparently, "Saturn's magnetic field exists solely to annoy Cowling" (Tobias, 2021). However, in order to overcome Cowling's Theorem and produce a dynamo we expect a more complicated field geometry within Saturn's interior than we are presently able to observe. Uranus and Neptune appear to be multipolar magnetic fields, meaning that they have more than two dominant magnetic poles according to their Gauss coefficients, with their dipole axes heavily tilted (Connerney *et al.*, 1987, 1991). Furthermore, Ganymede is the only satellite in our solar system known to currently have its own dynamo, appearing to be approximately dipolar (Kivelson *et al.*, 1996).

1.3 Outline

In the next chapter we present the fundamental governing equations of Boussinesq convection in a rotating frame of reference. Since we will be interested in dynamical behaviour close to and below the onset of convection, we derive the critical values at which convection is able to onset from the trivial state under the influence of rotation. Following this, we

introduce a magnetic field through Maxwell's equations, deriving the equations which govern convectively-driven dynamo action in magnetohydrodynamics. Finally, towards the end of Chapter 2 we discuss many of the fundamental ideas relevant to dynamo theory.

In Chapter 3 we explore localisation in two-dimensional rotating convection. Building on previous work, we present localised states known as 'convectons' which locally reduce the effects of rotation leading to isolated convective cells. Firstly we implement a 'restricted symmetries', fully-truncated model which we explore numerically using the bifurcation and continuation software, AUTO-07p, written in fortran. Then we implement a model which allows the full horizontal structure. We examine the parametric dependencies of our rotating convectons and explore their bifurcation structures, stability and key features.

Chapter 4 numerically explores convectively-driven dynamo action in a three-dimensional rotating plane layer, focussing on subcritical behaviour. We first study large-scale magnetic field generation in the supercritical regime where a mean horizontal magnetic field is able to significantly influence the flow. We then track such solutions to convective driving below the critical value for the linear onset of non-magnetic rotating convection. We explore the parameter regions at which subcritical behaviour exists, determining the key force balances and parameters in order to sustain a subcritical dynamo, such as optimum values of the Elsasser number and magnetic Reynolds number (both defined in Chapter 2).

We then extend the work of the previous chapter in Chapter 5, applying the same methods and performing additional analysis on cases at more rapid rotation. We observe that subcriticality is hampered by the emergence of a large-scale convective mode. The inability of this large-scale mode to sustain a dynamo leads to complicated intermittent behaviour which appears to inhibit subcriticality.

Chapter 2

Theoretical Background

In this thesis we will be studying both rapidly rotating convection and convective dynamo action. In the rapidly rotating convection case we are interested in the quantitative effects of rotation on the form and efficiency of convection, as well as the convective onset. We begin by introducing the Navier-Stokes equation before adding rotation and deriving the governing equations of incompressible rotating convection in a Cartesian domain. Since we are interested in subcritical behaviour, motivated by the cessation of the Martian dynamo, we derive the critical values for the onset of convection within the system in Section 2.4. Finally, in Section 2.5 we introduce a magnetic field to our governing equations ahead of exploring convection-driven dynamos.

2.1 Governing Equations of Plane Layer Convection

The key equations which govern the behaviour of a fluid involve the conservation of momentum, more famously known as the Navier-Stokes equation, and the conservation of mass, commonly known as the continuity equation. In the inertial frame of reference the i-th component of the Navier-Stokes can be written as

$$\rho\frac{\partial u_i}{\partial t} + \rho u_j \frac{\partial u_i}{\partial x_j} = F_i + \frac{\partial P_{ij}}{\partial x_j}, \tag{2.1}$$

where t is time, x_i is the i-th component of the position vector and u_i is the i-th component of the fluid velocity, $\boldsymbol{u}$. Repeated indices indicate a summation, and the fluid has density ρ, F_i represents the effects of external body forces such as gravity and magnetic fields, and P_{ij} is the stress tensor. The continuity equation is then

$$\frac{\partial \rho}{\partial t} + \frac{\partial}{\partial x_j}\left(\rho u_j\right) = 0. \tag{2.2}$$

The stress tensor represents internal forces within the fluid, notably pressure and viscosity. The stress within a fluid must be related to its rate of strain and it is typically assumed that these are linearly related. Since the relation must be invariant under transformations to other coordinate systems, the stress tensor can be written

$$P_{ij} = -\mathcal{P}\delta_{ij} + \mu\left(\frac{\partial u_i}{\partial x_j} + \frac{\partial u_j}{\partial x_i}\right) - \frac{2}{3}\mu\frac{\partial u_k}{\partial x_k}\delta_{ij}, \tag{2.3}$$

where $\mathcal{P}$ is the isotropic pressure under no strain, δ_{ij} is the Kronecker delta and μ is the viscosity of the fluid. The derivation of Equation 2.3 is shown in Chandrasekhar (1961) for example. Substituting this form of the stress tensor back into the Navier-Stokes equation gives

$$\rho\frac{\partial u_i}{\partial t} + \rho u_j\frac{\partial u_i}{\partial x_j} = F_i - \frac{\partial \mathcal{P}}{\partial x_i} + \frac{\partial}{\partial x_j}\left[\mu\left(\frac{\partial u_i}{\partial x_j} + \frac{\partial u_j}{\partial x_i}\right) - \frac{2}{3}\mu\frac{\partial u_k}{\partial x_k}\delta_{ij}\right]. \tag{2.4}$$

In many astrophysical bodies, thermal effects, gravity and the influences of rotation and magnetic fields are also important. We will begin by introducing gravity, which in our Cartesian geometry will always take the form

$$F_i = -\rho g\hat{z}_i, \tag{2.5}$$

where g is the constant acceleration due to gravity and $\hat{\mathbf{z}}$ is the unit vector in the vertical direction. In this thesis we will always consider the case where rotation and gravity are both aligned with the vertical, and thus $i = 3$ in Equation 2.5. This setup is most applicable to polar regions of the Earth's core. The temperature is governed by the heat equation, the derivation of which can also be found in Chandrasekhar (1961) based on the conservation of energy,

$$\rho\frac{\partial}{\partial t}(cT) + \rho u_j\frac{\partial}{\partial x_j}(cT) = \frac{\partial}{\partial x_j}\left(k\frac{\partial T}{\partial x_j}\right) - \mathcal{P}\frac{\partial u_j}{\partial x_j} + \Phi, \tag{2.6}$$

where c is the specific heat at constant volume, k is the thermal conductivity and

$$\Phi = \frac{1}{2}\mu\left(\frac{\partial u_i}{\partial x_j} + \frac{\partial u_j}{\partial x_i}\right)^2 - \frac{2}{3}\mu\left(\frac{\partial u_j}{\partial x_j}\right)^2, \tag{2.7}$$

which represents viscous heating.

Finally, we relate the density and temperature through the equation of state,

$$\rho = \rho_0\left(1 - \alpha\Delta T\right), \tag{2.8}$$

where α is the coefficient of thermal expansion, ρ_0 is the density corresponding to a mean

temperature of T_0 and ΔT is the deviation in temperature from T_0 with

$$\Delta T = T - T_0. \tag{2.9}$$

If we suppose a constant mean temperature gradient in the vertical direction, $-\beta$ (for $\beta > 0$), then,

$$T = T_0 - \beta x_j \hat{z}_j + \theta, \quad \Delta T = -\beta x_j \hat{z}_j + \theta. \tag{2.10}$$

where θ is the deviation in temperature from the mean, $T_0 - \beta x_j \hat{z}_j$.

2.2 The Boussinesq Approximation

Our governing equations can be simplified further under the Boussinesq approximation (Spiegel & Veronis, 1960). We assume that the density and other coefficients only vary by small amounts and that the coefficient of thermal expansion is small. Under the Boussinesq approximation we can thus treat the density, ρ, as a constant. However there is an important exception, the density cannot be treated as a constant within the external force term, F_i, since accelerations related to density fluctuations can be comparable to other terms in the governing equations. Assuming that ρ is a constant also leads us to the assumption that ν, c, α and k are also constants.

Letting $\rho = \rho_0$ be constant, except for within the external force term, we apply the Boussinesq approximation to our governing equations (Equations 2.2, 2.4 and 2.6). The continuity equation becomes

$$\frac{\partial u_j}{\partial x_j} = 0, \tag{2.11}$$

and thus the fluid velocity is solenoidal. The Navier-Stokes equation, with gravity as the only external force, becomes

$$\frac{\partial u_i}{\partial t} + u_j \frac{\partial u_i}{\partial x_j} = -\frac{1}{\rho_0}\frac{\partial \mathcal{P}}{\partial x_i} - \frac{\rho}{\rho_0} g \hat{z}_i + \nu \frac{\partial^2 u_i}{\partial x_j \partial x_j}, \tag{2.12}$$

where $\nu = \mu/\rho_0$ is the kinematic viscosity. Finally, the heat equation becomes

$$\frac{\partial T}{\partial t} + u_j \frac{\partial T}{\partial x_j} = \kappa \frac{\partial^2 T}{\partial x_j \partial x_j}, \tag{2.13}$$

where $\kappa = k/(\rho_0 c)$ is the thermal diffusivity. Viscous heating is neglected since it becomes small in typical liquids, of order 10^{-7} or 10^{-8}.

2.3 Rotating Convection

Since we will be interested in the effects of rotation on plane layer convection, we must introduce two further rotational terms to the Navier-Stokes equation due to the acceleration involved in the rotating frame. We define $\boldsymbol{\Omega} = \Omega\hat{\boldsymbol{\Omega}}$, where the fluid rotates about some axis, $\hat{\boldsymbol{\Omega}}$, at constant angular velocity, Ω, and introduce the Coriolis force, $2\rho_0 (\boldsymbol{\Omega} \times \boldsymbol{u})$, and the centrifugal force, $\frac{1}{2}\rho_0 \nabla \left(|\boldsymbol{\Omega} \times \boldsymbol{x}|^2 \right)$ to the Navier-Stokes equation (Chandrasekhar, 1961). Here we have assumed that the Boussinesq approximation also applies to both rotational forces. Equation 2.12, retaining subscript notation, then becomes

$$\frac{\partial u_i}{\partial t} + u_j \frac{\partial u_i}{\partial x_j} = -\frac{1}{\rho_0}\frac{\partial \mathcal{P}}{\partial x_i} - \rho g \hat{z}_i + \nu \frac{\partial^2 u_i}{\partial x_j \partial x_j} - 2\Omega \epsilon_{ijk} \hat{\Omega}_j u_k + \frac{1}{2}\frac{\partial}{\partial x_i}\left(|\Omega \epsilon_{jkl} x_k \hat{\Omega}_l|^2 \right), \quad (2.14)$$

where $\boldsymbol{\Omega} = \Omega\hat{\boldsymbol{\Omega}}$ for constant rotation, Ω, and ϵ_{ijk} is the Levi-Civita symbol. This is more commonly written in vector form as

$$\frac{\partial \boldsymbol{u}}{\partial t} + (\boldsymbol{u} \cdot \nabla)\boldsymbol{u} = -\frac{1}{\rho_0}\nabla \mathcal{P} - \rho g \hat{\mathbf{z}} + \nu \nabla^2 \boldsymbol{u} - 2(\boldsymbol{\Omega} \times \boldsymbol{u}) + \frac{1}{2}\nabla \left(|\boldsymbol{\Omega} \times \boldsymbol{x}|^2 \right). \quad (2.15)$$

The additional terms in the Navier-Stokes due to the rotating frame of reference allow rotation to significantly affect the dynamics of fluid motion, especially through the Coriolis force. The importance of rotation on the dynamics is typically quantified by a dimensionless number known as the Rossby number, which is the ratio of inertial forces to the Coriolis force. For typical flow lengthscales and velocities, $\mathcal{L}$ and $\mathcal{U}$ respectively, and rotation rate, Ω, the Rossby number is defined as

$$\mathrm{Ro} \sim \frac{|(\boldsymbol{u} \cdot \nabla)\boldsymbol{u}|}{|2(\boldsymbol{\Omega} \times \boldsymbol{u})|} \sim \frac{\mathcal{U}}{2\Omega\mathcal{L}}. \quad (2.16)$$

If the Rossby number is small then rotational effects are important and strongly influence the flow. For example, in Earth's fluid outer core the Rossby number is expected to be $\mathrm{Ro} \sim 10^{-6}$ (Jones, 2015) and thus $|2(\boldsymbol{\Omega} \times \boldsymbol{u})| \gg |(\boldsymbol{u} \cdot \nabla)\boldsymbol{u}|$ at the scale of the core radius.

Similarly, the ratio of viscous forces to the Coriolis force is quantified via a dimensionless number known as the Ekman number, where

$$\mathrm{Ek} = \frac{|\nu \nabla^2 \boldsymbol{u}|}{|2(\boldsymbol{\Omega} \times \boldsymbol{u})|} = \frac{\nu}{2\Omega\mathcal{L}^2}. \quad (2.17)$$

In Earth's fluid outer core, the Ekman number is estimated to be $\mathrm{Ek} \sim 10^{-15}$ (Olson, 2015) and thus viscous forces are dominated by the Coriolis force in this region at large scales. At smaller scales, other forces become more important, which will be discussed later in § 2.6.5.

2.3.1 The Taylor-Proudman Effect

We now consider an inviscid, homogeneous fluid (i.e. $\nu = 0$ and the buoyancy term vanishes) with motions that are steady and slow moving (hence $\partial/\partial t = 0$ and we can neglect products of $\boldsymbol{u}$). When the Rossby number is zero (and hence $(\boldsymbol{u} \cdot \nabla)\,\boldsymbol{u}$ is neglected), the Navier-Stokes equation in a rotating frame (Equation 2.14) reduces to

$$2\Omega\epsilon_{ijk}u_j\hat{\Omega}_k = \frac{1}{\rho_0}\frac{\partial P}{\partial x_i}, \tag{2.18}$$

where $P = \mathcal{P} + \rho_0|\Omega\epsilon_{jkl}x_k\hat{\Omega}_l|^2/2$ is a new 'effective' pressure. In vector form this can be written

$$2\,(\boldsymbol{u} \times \boldsymbol{\Omega}) = \frac{1}{\rho_0}\nabla P. \tag{2.19}$$

Here we observe a balance between the Coriolis force and pressure gradients, often referred to as 'geostrophy'. In the Earth's fluid outer core, Coriolis forces dominate both viscous and inertial forces at large scales and thus at leading order the outer core is geostrophic.

If we take the curl of the geostrophic balance for constant rotation, many of the terms are eliminated since $\nabla \times \nabla P = 0$, $\nabla \cdot \boldsymbol{u} = 0$ due to incompressibility, and $\nabla \cdot \boldsymbol{\Omega} = 0$ for constant rotation, leaving

$$2\,(\boldsymbol{\Omega} \cdot \nabla)\,\boldsymbol{u} = \boldsymbol{0}. \tag{2.20}$$

This equation only possesses solutions where $\boldsymbol{u}$ does not vary parallel to the rotation axis, $\boldsymbol{\Omega}$. This is the Taylor-Proudman theorem, that is, the slow, steady motion of a rotating inviscid, inhomogeneous fluid does not vary parallel to the rotation axis (Taylor, 1916; Proudman, 1916).

2.4 Convective Onset

In this thesis, we are interested in subcritical behaviour in rotating convection and convectively-driven dynamos. At sufficiently high thermal driving, convection is able to overcome the diffusive forces that oppose convection and onsets from the conducting state. Critical values for the linear onset of convection in the presence of rotation are derived in Chandrasekhar (1961). Once convection has onset, the level of thermal driving can be reduced below that which was required to initially generate the convection, leading to subcritical behaviour. In this section we follow the derivations of Chandrasekhar and present such critical values.

Consider an incompressible Boussinesq fluid confined within a layer of depth, d with boundaries at $z = 0$, $z = d$. Suppose gravity acts in the vertical direction, $\boldsymbol{g} = -g\hat{\boldsymbol{z}}$ and that the fluid layer is rotating at constant rate with $\boldsymbol{\Omega} = \Omega\hat{\boldsymbol{\Omega}}$. Firstly we begin with the

momentum equation, simplified from Equation 2.14,

$$\rho_0 \left(\frac{\partial u_i}{\partial t} + u_j \frac{\partial u_i}{\partial x_j} \right) = -\frac{\partial P}{\partial x_i} + \rho_0 \nu \nabla^2 u_i - g\rho \hat{z}_i + 2\rho_0 \Omega \epsilon_{ijk} u_j \hat{\Omega}_k, \tag{2.21}$$

where $\nabla^2 = \partial^2/\partial x_j \partial x_j$ and $\partial u_j/\partial x_j = 0$ in an incompressible fluid. Here ρ is the fluid density. The heat equation is then

$$\frac{\partial T}{\partial t} + u_j \frac{\partial T}{\partial x_j} = \kappa \nabla^2 T, \tag{2.22}$$

where $\boldsymbol{u}$ is the velocity, ρ is the density, P is the pressure, T is the temperature, ν is the kinematic viscosity and κ is the thermometric conductivity.

Substituting Equations 2.8 and 2.10 into Equations 2.21 and 2.22 then gives,

$$\frac{\partial u_i}{\partial t} + \frac{\partial}{\partial x_j} u_i u_j = -\frac{\partial \varpi}{\partial x_i} + \gamma \theta \hat{z}_i + \nu \nabla^2 u_i + 2\Omega \epsilon_{ijk} u_j \hat{\Omega}_k, \tag{2.23}$$

$$\frac{\partial \theta}{\partial t} - \beta x_j \hat{z}_j + u_j \frac{\partial \theta}{\partial x_j} = \kappa \nabla^2 \theta, \tag{2.24}$$

where $\gamma = \alpha g$ and $\varpi = P/\rho_0 - g x_j \hat{z}_j - (\beta\gamma/2) x_j x_k \hat{z}_j \hat{z}_k$ (Chandrasekhar, 1961).

Since we are interested in the linear onset of convection, we linearise in u_i and θ obtaining,

$$\frac{\partial u_i}{\partial t} = -\frac{\partial \varpi}{\partial x_i} + \gamma \theta \hat{z}_i + \nu \nabla^2 u_i + 2\Omega \epsilon_{ijk} u_j \hat{\Omega}_k, \tag{2.25}$$

$$\frac{\partial \theta}{\partial t} = \beta w + \kappa \nabla^2 \theta, \tag{2.26}$$

where $w = u_j \hat{z}_j$ is the vertical component of the velocity.

Now take the curl of Equation 2.25 in order to eliminate ϖ, obtaining the vorticity equation,

$$\frac{\partial \omega_i}{\partial t} = \gamma \epsilon_{ijk} \frac{\partial \theta}{\partial x_j} \hat{z}_k + \nu \nabla^2 \omega_i + 2\Omega \frac{\partial u_i}{\partial x_j} \hat{\Omega}_j, \tag{2.27}$$

where $\omega_i = \epsilon_{ijk}(\partial u_k/\partial x_j)$ is the i-th component of the vorticity. Multiplying the above equation by $\hat{z}_i$ and summing over i gives,

$$\frac{\partial \zeta}{\partial t} = \nu \nabla^2 \zeta + 2\Omega \frac{\partial w}{\partial x_j} \hat{\Omega}_j, \tag{2.28}$$

where $\zeta = \omega_i \hat{z}_i$ is the z-component of the vorticity.

Next we take the curl of equation (2.27), noting that due to incompressibility,

$$\nabla \times \boldsymbol{\omega} = -\nabla^2 \boldsymbol{u}, \tag{2.29}$$

giving,

$$-\frac{\partial}{\partial t}\nabla^2 u_i = \gamma\left(\frac{\partial^2\theta}{\partial x_i \partial x_j}\hat{z}_j - \nabla^2\theta\hat{z}_i\right) - \nu\nabla^4 u_i + 2\Omega\frac{\partial\omega_i}{\partial x_j}\hat{\Omega}_j. \tag{2.30}$$

In the $\hat{z}_i$ direction, this is

$$-\frac{\partial}{\partial t}\nabla^2 w = \gamma\left(\frac{\partial^2\theta}{\partial x_i \partial x_j}\hat{z}_i\hat{z}_j - \nabla^2\theta\right) - \nu\nabla^4 w + 2\Omega\frac{\partial\zeta}{\partial x_j}\hat{\Omega}_j. \tag{2.31}$$

The basic equations we will analyse then consist of Equations 2.26, 2.28 and 2.31.

Our fluid is confined within two parallel planes at $z = 0$ and $z = d$. Our boundaries are impermeable and thus fluid cannot pass through the boundaries and thus $\boldsymbol{u} \cdot \hat{\mathbf{n}} = 0$, where $\hat{\mathbf{n}}$ is the unit normal vector to the boundary. Additionally, we uniformly heat the fluid and thus the temperature at the boundaries remains constant. Hence our first set of boundary conditions for the temperature perturbation, θ, and velocity, $\boldsymbol{u} = (u, v, w)$, consist of

$$\theta = 0, \quad w = 0 \quad \text{for} \quad z = 0, \quad z = d. \tag{2.32}$$

We consider our boundaries to be free surfaces to avoid viscous boundary layers. Realistically, rigid boundaries are likely the most appropriate for the Earth's core (Wicht & Sanchez, 2019), however since the Earth is rapidly rotating, the boundary layers become too influential on the flow. Many works therefore assume stress-free boundary conditions to negate this (e.g. Grote & Busse, 2000; Aubert, 2013). On a free surface boundary, no stresses act tangentially to the boundary. This means that the P_{xz} and P_{yz} components of the stress-tensor are zero. In the stress-tensor (Equation 2.3), any terms involving δ_{xz} or δ_{yz} are now also zero by definition. Thus,

$$\mu\left(\frac{\partial u}{\partial z} + \frac{\partial w}{\partial x}\right) = 0, \quad \mu\left(\frac{\partial v}{\partial z} + \frac{\partial w}{\partial y}\right) = 0 \quad \text{for} \quad z = 0, \quad z = d, \tag{2.33}$$

and since we already have $w = 0$ at the boundary from our previous set of boundary conditions,

$$\frac{\partial u}{\partial z} = 0, \quad \frac{\partial v}{\partial z} = 0 \quad \text{for} \quad z = 0, \quad z = d. \tag{2.34}$$

Differentiating the continuity equation with respect to z gives

$$\frac{\partial^2 w}{\partial z^2} = 0 \quad \text{for} \quad z = 0, \quad z = d. \tag{2.35}$$

For the z-component of the vorticity, ζ, we can then deduce our final boundary condition,

$$\frac{\partial\zeta}{\partial z} = 0 \quad \text{for} \quad z = 0, \quad z = d. \tag{2.36}$$

We begin from Equations 2.26, 2.28 and 2.31 and consider the case where the axis of

rotation, $\hat{\boldsymbol{\Omega}}$, is aligned with the vertical, $\hat{\mathbf{z}}$, giving

$$\frac{\partial \theta}{\partial t} = \beta w + \kappa \nabla^2 \theta, \tag{2.37}$$

$$\frac{\partial \zeta}{\partial t} = \nu \nabla^2 \zeta + 2\Omega \frac{\partial w}{\partial z}, \tag{2.38}$$

$$-\frac{\partial}{\partial t}\nabla^2 w = -\gamma \left(\frac{\partial^2}{\partial x^2} + \frac{\partial^2}{\partial y^2} \right) \theta - \nu \nabla^4 w + 2\Omega \frac{\partial \zeta}{\partial z}. \tag{2.39}$$

The corresponding boundary conditions remain those in Equations 2.32, 2.35, and 2.36.

Convection is expected to onset in the form of horizontally symmetric convection cells with wavenumber, $k = \sqrt{k_x^2 + k_y^2}$, where $\boldsymbol{k} = (k_x, k_y)$ is the wavevector. We therefore separate the variables letting $w = W(z) \exp\{i\boldsymbol{k} \cdot \boldsymbol{x} + pt\}$, $\theta = \Theta(z) \exp\{i\boldsymbol{k} \cdot \boldsymbol{x} + pt\}$ and $\zeta = Z(z) \exp\{i\boldsymbol{k} \cdot \boldsymbol{x} + pt\}$ where p may be complex. Derivatives are then simplified to

$$\frac{\partial}{\partial t} = p, \quad \frac{\partial^2}{\partial x^2} + \frac{\partial^2}{\partial y^2} = -k^2, \quad \nabla^2 = \frac{\partial}{\partial z^2} - k^2. \tag{2.40}$$

Note that technically the partial derivatives in z are full derivatives, however they will be kept to avoid confusion with the vertical height of the box, d. The governing equations become

$$p\Theta = \beta W + \kappa \left(\frac{\partial^2}{\partial z^2} - k^2 \right) \Theta, \tag{2.41}$$

$$pZ = 2\Omega \frac{\partial W}{\partial z} + \nu \left(\frac{\partial^2}{\partial z^2} - k^2 \right) Z, \tag{2.42}$$

$$p \left(\frac{\partial^2}{\partial z^2} - k^2 \right) W = -\gamma k^2 \Theta + \nu \left(\frac{\partial^2}{\partial z^2} - k^2 \right)^2 W - 2\Omega \frac{\partial Z}{\partial z}. \tag{2.43}$$

We now make the above equations dimensionless with $k = a/d$ and by letting $\sigma = pd^2/\nu$, which is the time derivative on the viscous timescale. This also introduces a dimensionless parameter, known as the Prandtl number,

$$\text{Prandtl:} \qquad \mathrm{Pr} = \frac{\nu}{\kappa}. \tag{2.44}$$

The Prandtl number is the ratio of viscous to thermal diffusivities. In dimensionless form, we now consider

$$\left(D^2 - a^2 - \sigma \mathrm{Pr}\right) \Theta = -\frac{\beta d}{\kappa} W, \tag{2.45}$$

$$\left(D^2 - a^2 - \sigma\right) Z = -\frac{2\Omega d}{\nu} DW, \tag{2.46}$$

$$\left(D^2 - a^2\right) \left(D^2 - a^2 - \sigma\right) W - \frac{2\Omega d^3}{\nu} DZ = \frac{\gamma d^2}{\nu} a^2 \Theta, \tag{2.47}$$

where $D = d(\partial/\partial z)$ is the dimensionless z-derivative. Now apply the operator $(D^2 - a^2 - \sigma)(D^2 - a^2 - \sigma\mathrm{Pr})$ to Equation 2.47 and eliminate terms in Θ or Z using Equations 2.45-2.46 giving

$$\left(D^2 - a^2 - \sigma\mathrm{Pr}\right)\left\{\left(D^2 - a^2 - \sigma\right)^2\left(D^2 - a^2\right) + \mathrm{Ta}D^2\right\}W = -a^2\mathrm{Ra}\left(D^2 - a^2 - \sigma\right)W. \tag{2.48}$$

We have now introduced two further dimensionless parameters, known as the Taylor and Rayleigh numbers, and defined as

$$\text{Taylor:} \qquad \mathrm{Ta} = \frac{1}{\mathrm{Ek}^2} = \frac{4\Omega^2 d^4}{\nu^2}, \tag{2.49}$$

$$\text{Rayleigh:} \qquad \mathrm{Ra} = \frac{g\alpha\left(\Delta T\right)d^3}{\kappa\nu}. \tag{2.50}$$

The Taylor number represents the ratio of Coriolis forces to viscous forces, whilst the Rayleigh number determines how successfully buoyancy forces overcome the diffusive forces that oppose convection.

From Chandrasekhar (1961), Equation 2.48 has solutions of the form

$$W = W_n \sin(n\pi z), \tag{2.51}$$

for integer values of n provided the Rayleigh number satisfies,

$$\mathrm{Ra} = \frac{\left(n^2\pi^2 + a^2 + \sigma\mathrm{Pr}\right)\left\{\left(n^2\pi^2 + a^2 + \sigma\right)^2\left(n^2\pi^2 + a^2\right) + n^2\pi^2\mathrm{Ta}\right\}}{a^2\left(n^2\pi^2 + a^2 + \sigma\right)}. \tag{2.52}$$

Instability will first onset in the lowest mode, hence $n = 1$, giving

$$\mathrm{Ra} = \frac{\left(\pi^2 + a^2 + \sigma\mathrm{Pr}\right)\left\{\left(\pi^2 + a^2 + \sigma\right)^2\left(\pi^2 + a^2\right) + \pi^2\mathrm{Ta}\right\}}{a^2\left(\pi^2 + a^2 + \sigma\right)}. \tag{2.53}$$

2.4.1 Onset of Stationary Convection

We shall first consider the case in which stationary convection onsets, and thus the marginal stability is governed by the aforementioned system of equations with time independence (hence $\partial/\partial t = 0$, $p = 0$, and thus $\sigma = 0$ in Equation 2.53). The critical Rayleigh number for the onset of stationary convection for a wave mode with amplitude a, in the presence of rotation, is then

$$\mathrm{Ra}_c(a) = \frac{\pi^6}{a^2}\left\{\left(1 + \frac{a^2}{\pi^2}\right)^3 + \frac{\mathrm{Ta}}{\pi^4}\right\} \tag{2.54}$$

We simplify this further by letting $x = a^2/\pi^2$, giving

$$\mathrm{Ra}_c(x) = \frac{\pi^4}{x}\left\{(1+x)^3 + \frac{\mathrm{Ta}}{\pi^4}\right\}. \tag{2.55}$$

The overall critical Rayleigh number for the onset of stationary convection, Ra_c is then the minimum across all possible values for x. This occurs when x satisfies

$$2x^3 + 3x^2 = 1 + \frac{\mathrm{Ta}}{\pi^4}. \tag{2.56}$$

When Ta/π^4 becomes sufficiently large, the root of the previous equation tends to $\left[\mathrm{Ta}/\left(2\pi^4\right)\right]^{1/3}$ as $\mathrm{Ta} \to \infty$. Then $a_{min} \to \left(\pi^2\mathrm{Ta}/2\right)^{1/6} \simeq 1.3048\mathrm{Ta}^{1/6}$ and the critical Rayleigh number approaches

$$\mathrm{Ra}_c \to 3\pi^4\left(\frac{\mathrm{Ta}}{2\pi^4}\right)^{2/3} \simeq 8.6956\mathrm{Ta}^{2/3} \quad \text{as} \quad \mathrm{Ta} \to \infty. \tag{2.57}$$

As the Taylor number becomes very large, the critical wavenumber scales with $\mathrm{Ta}^{1/6}$ whilst the critical Rayleigh number for the onset of stationary convection scales like $\mathrm{Ta}^{2/3}$. At rapid rotation this therefore implies an inhibiting effect on convective onset due to the Coriolis force. The inhibition of convection by rotation is therefore increased for increasing rate of rotation, Ω, or decreasing kinematic viscosity, ν. Fluid motions tend to drag associated vortex lines along with them, with an increased level of attachment at larger angular momentum and lower viscosity. This leads to behaviour which becomes more in-line with the Taylor-Proudman theorem since it then becomes difficult for fluid motions to act perpendicularly to the axis of rotation. Similarly, the wavenumber which eventually onsets increases at large Ta and thus as $\mathrm{Ta} \to \infty$ the convective cells become thinner and the horizontal scale becomes much smaller than the vertical scale which is aligned with the rotation axis.

2.4.2 Onset of Overstable Convection

In Chandrasekhar (1961), the previous case is generalised to show that time-dependent solutions can also onset from the trivial conducting state. These take the form of overstable solutions, where oscillatory motions onset just above the critical Rayleigh number. For instability to onset in the form of overstability, σ must have a non-zero imaginary part, whilst in the marginal modes, the real part of the growth rate is zero. So let $\sigma = si$ for real s, where s is the frequency. We also require the Rayleigh number to be real. Then

$$\mathrm{Ra} = \frac{\left(\pi^2 + a^2 + si\mathrm{Pr}\right)\left\{\left(\pi^2 + a^2 + si\right)^2\left(\pi^2 + a^2\right) + \pi^2\mathrm{Ta}^2\right\}}{a^2\left(\pi^2 + a^2 + si\right)}. \tag{2.58}$$

Now let $a^2 = \pi^2 x$ and substitute in giving

$$\mathrm{Ra} = \frac{1}{x}\left(1 + x + \frac{si\mathrm{Pr}}{\pi^2}\right)\left\{\pi^4 (1+x)\left(1 + x + \frac{si}{\pi^2}\right) + \frac{\mathrm{Ta}}{1 + x + \frac{si}{\pi^2}}\right\}. \tag{2.59}$$

Recalling that the Rayleigh number must be real we now equate real and imaginary parts. The real part gives

$$\mathrm{Ra} = \frac{1+x}{x}\left\{\pi^4 (1+x)^2 - s^2\mathrm{Pr} + \frac{\mathrm{Ta}}{1+x}\left[\frac{(1+x)^2 + \mathrm{Pr}\,\frac{s^2}{\pi^4}}{(1+x)^2 + \frac{s^2}{\pi^4}}\right]\right\}, \tag{2.60}$$

and the imaginary part gives

$$(1+x)(1+\mathrm{Pr}) = \frac{\mathrm{Ta}}{\pi^4}\left\{\frac{1-\mathrm{Pr}}{(1+x)^2 + \frac{s^2}{\pi^4}}\right\}. \tag{2.61}$$

It can be shown using Equation 2.61 that

$$\frac{\mathrm{Ta}}{1+x}\left[\frac{(1+x)^2 + \mathrm{Pr}\,\frac{s^2}{\pi^4}}{(1+x)^2 + \frac{s^2}{\pi^4}}\right] = \frac{\mathrm{Ta}}{1+x} - (1+\mathrm{Pr})\,s^2, \tag{2.62}$$

and hence the Rayleigh number becomes

$$\mathrm{Ra} = \frac{1}{x}\left\{\pi^4 (1+x)^3 + \mathrm{Ta} + (1+x)(1+2\,\mathrm{Pr})\,s^2\right\}. \tag{2.63}$$

If we solve Equation 2.61 for s^2 we obtain

$$s^2 = \frac{\mathrm{Ta}\,(1-\mathrm{Pr})}{(1+x)(1+\mathrm{Pr})} - \pi^4 (1+x)^2. \tag{2.64}$$

Importantly, for s to remain real we require $s^2 > 0$ and hence

$$\mathrm{Ta} > \pi^4 \frac{1+\mathrm{Pr}}{1-\mathrm{Pr}}(1+x)^3. \tag{2.65}$$

We use Equation 2.64 to simplify Equation 2.63, giving the critical Rayleigh number for the onset of overstable convection in the presence of rotation,

$$\mathrm{Ra}_0(x) = \frac{2\,(1+\mathrm{Pr})}{x}\left\{\pi^4 (1+x)^3 + \frac{\mathrm{Pr}^2}{(1+\mathrm{Pr})^2}\mathrm{Ta}\right\}, \tag{2.66}$$

which is minimal for

$$2x^3 + 3x^2 = 1 + \frac{\mathrm{Pr}^2}{(1+Pr)^2}\frac{\mathrm{Ta}}{\pi^4}. \tag{2.67}$$

When Ta/π^4 becomes sufficiently large, the critical Rayleigh number for overstable convection approaches

$$\mathrm{Ra}_0 \to 2\pi^4 (1+\mathrm{Pr}) \left\{ 3 \left[\frac{\mathrm{Pr}^2}{(1+\mathrm{Pr})^2} \frac{\mathrm{Ta}}{2\pi^4} \right]^{2/3} \right\} \quad \text{as} \quad \mathrm{Ta} \to \infty. \tag{2.68}$$

For large Ta, we must determine whether it is stationary convection or overstable convection which onsets first for varying Ra. The distinguishing case is where Ra_c and Ra_0 are equal. Equating the two different critical Rayleigh numbers for large Ta and rearranging gives

$$2\frac{\mathrm{Pr}^{4/3}}{(1+\mathrm{Pr})^{1/3}} = 1, \tag{2.69}$$

which has a root at $\mathrm{Pr}_* \cong 0.67659$. Therefore, for overstable convection to onset we require

$$\mathrm{Pr} \lesssim 0.67659. \tag{2.70}$$

Thus, for $\mathrm{Pr} \lesssim 0.67659$ numbers overstable convection will onset before stationary convection. Conversely, for $\mathrm{Pr} \gtrsim 0.67659$ stationary convection will be first to onset.

2.5 Magnetohydrodynamics (MHD)

2.5.1 Maxwell Equations and the Induction Equation

In planetary systems, magnetic fields are also able to influence fluid motion and evolve temporally. We must therefore make further additions to Equation 2.14, factoring in Maxwell's equations of electromagnetism (see, for example, Weiss & Proctor (2014)). These are

$$\text{Gauss' Law:} \qquad \nabla \cdot \boldsymbol{E} = \frac{\rho_c}{\epsilon_0}, \tag{2.71}$$

$$\text{Gauss' Law for Magnetism:} \qquad \nabla \cdot \boldsymbol{B} = 0, \tag{2.72}$$

$$\text{Faraday's Law:} \qquad \nabla \times \boldsymbol{E} = -\frac{\partial \boldsymbol{B}}{\partial t}, \tag{2.73}$$

$$\text{Ampère's Law:} \qquad \nabla \times \boldsymbol{B} = \mu_0 \boldsymbol{J} + \frac{1}{c^2}\frac{\partial \boldsymbol{E}}{\partial t}, \tag{2.74}$$

where $\boldsymbol{E}$ and $\boldsymbol{B}$ are electrical and magnetic fields respectively, $\boldsymbol{J}$ is the current density, ρ_c is the charge density, ϵ_0 is the permittivity of free space, μ_0 is the magnetic permeability and $c = (\epsilon_0 \mu_0)^{-1/2}$ is the speed of light.

Under certain conditions it is possible to further simplify Maxwell's equations. If l_0 is a typical lengthscale and t_0 a typical timescale then we can define a typical velocity scale,

$u_0 = l_0/t_0$. Equating both sides of Equation 2.73 gives

$$\frac{E}{l_0} \sim \frac{B}{t_0}, \tag{2.75}$$

where B and E are typical scales for the magnetic field and electrical field respectively. In non-relativistic fluids $u_0 \ll c$, taking the ratio of two of the terms in Equation 2.74 then gives

$$\left|\frac{1}{\nabla \times \boldsymbol{B}}\right| \left|\frac{1}{c^2}\frac{\partial \boldsymbol{E}}{\partial t}\right| \sim \frac{l_0 E}{c^2 t_0 B} \sim \frac{l_0^2}{c^2 t_0^2} \sim \frac{u_0^2}{c^2} \ll 1, \tag{2.76}$$

and hence Equation 2.74 can be approximated by

$$\nabla \times \boldsymbol{B} = \mu_0 \boldsymbol{J}. \tag{2.77}$$

To derive an equation governing the temporal evolution of $\boldsymbol{B}$ we make use of Ohm's law for a moving conductor, which is

$$\boldsymbol{J} = \sigma \left(\boldsymbol{E} + \boldsymbol{u} \times \boldsymbol{B}\right), \tag{2.78}$$

where σ is the electrical conductivity and $\boldsymbol{u}$ is the velocity of the conductor. Substituting this into Equation 2.77 for $\boldsymbol{J}$ gives

$$\nabla \times \boldsymbol{B} = \mu_0 \sigma \left(\boldsymbol{E} + \boldsymbol{u} \times \boldsymbol{B}\right). \tag{2.79}$$

Taking the curl of this equation and making use of Faraday's law (Equation 2.73) then gives the induction equation,

$$\frac{\partial \boldsymbol{B}}{\partial t} = \nabla \times (\boldsymbol{u} \times \boldsymbol{B}) - \nabla \times (\eta \nabla \times \boldsymbol{B}), \tag{2.80}$$

where $\eta = 1/(\mu_0 \sigma)$ is the magnetic diffusivity. If the magnetic diffusivity is constant, we can use the fact that the field is solenoidal ($\nabla \cdot \boldsymbol{B} = 0$) to rewrite the induction equation as

$$\frac{\partial \boldsymbol{B}}{\partial t} = \nabla \times (\boldsymbol{u} \times \boldsymbol{B}) + \eta \nabla^2 \boldsymbol{B}. \tag{2.81}$$

The evolution of the magnetic field as a result of fluid motion then relies on the competing effects of magnetic induction ($\nabla \times (\boldsymbol{u} \times \boldsymbol{B})$) and Ohmic diffusion ($\eta \nabla^2 \boldsymbol{B}$). In the absence of fluid motion, the magnetic field simply decays, whereas in order to amplify the magnetic field, advection must exceed diffusion. The ratio of magnetic induction to Ohmic diffusion is commonly defined by the magnetic Reynolds number,

$$\mathrm{Rm} = \frac{|\nabla \times (\boldsymbol{u} \times \boldsymbol{B})|}{|\eta \nabla^2 \boldsymbol{B}|} = \frac{\mathcal{U}\mathcal{L}}{\eta}, \tag{2.82}$$

where $\mathcal{L}$ and $\mathcal{U}$ are typical flow lengthscales and velocities respectively. The magnetic Reynolds number can also be re-written as the ratio of the electromagnetic diffusion time to the fluid advection time, $\mathrm{Rm} = \mathcal{T}_\eta/\mathcal{T}_u$, where $\mathcal{T}_\eta = \mathcal{L}^2/\eta$ and $\mathcal{T}_u = \mathcal{L}/\mathcal{U}$.

In a perfect conductor there is zero dissipation (i.e. $\eta = 0$ and hence $\mathrm{Rm} \to \infty$), Alfvén's theorem then states that magnetic flux tubes move as though they are 'frozen' to the fluid (Alfvén, 1942). In the Earth's fluid outer core, expected flow lengthscales and velocities are $\mathcal{L} = 2\times10^6\mathrm{m}$ (approximately the size of the outer core) and $\mathcal{U} = 2\times10^{-4}\mathrm{ms}^{-1}$ respectively, whilst the magnetic diffusivity is estimated at $\eta = 2\mathrm{m}^2\mathrm{s}^{-1}$, giving $\mathrm{Rm} = 200$ (Roberts, 2015). However uncertainties in the exact values of the respective parameters can lead to estimates as high as $\mathrm{Rm} = 2000$ (Olson, 2015).

2.5.2 MHD/Dynamo Equations

As a result of the addition of a magnetic field, an electromagnetic force is exerted on the electrically conducting fluid by the Lorentz force. The Lorentz force per unit volume is calculated by

$$\boldsymbol{F}_L = \boldsymbol{J} \times \boldsymbol{B}. \tag{2.83}$$

Introducing this additional force to the Navier-Stokes equation which governs the motion of a rotating fluid gives

$$\frac{\partial \boldsymbol{u}}{\partial t} + (\boldsymbol{u}\cdot\nabla)\,\boldsymbol{u} + 2\boldsymbol{\Omega}\times\boldsymbol{u} = -\frac{1}{\rho_0}\nabla P - \frac{\rho}{\rho_0}g\hat{\boldsymbol{z}} + \frac{1}{\rho_0}\left(\boldsymbol{J}\times\boldsymbol{B}\right) + \nu\nabla^2\boldsymbol{u}. \tag{2.84}$$

This equation, alongside the induction equation (Equation 2.81), Gauss' law ($\nabla\cdot\boldsymbol{B} = 0$), our equation for incompressibility ($\nabla\cdot\boldsymbol{u} = 0$) and equation of heat conservation (Equation 2.22) form the governing equations for an electrically conducting, incompressible fluid in the presence of a magnetic field and rotation. As a reminder, the temperature perturbation and velocity are related by the equation of state.

As in previous sections, we introduce dimensionless variables. As a reminder, in this thesis we will always be considering a planar geometry, with a computational domain that has depth d in the vertical direction and has width λd in each horizontal direction. The gravitational acceleration will always be perfectly aligned with the vertical direction, $\boldsymbol{g} = -g\hat{\boldsymbol{z}}$, and the system will rotate about the vertical axis at constant rotation rate, Ω. The plane will then be uniformly heated from below with vertical temperature difference ΔT across the layer. The fluid has constant kinematic viscosity ν, thermal diffusivity κ, magnetic diffusivity η, fluid density ρ, thermal expansion coefficient α and magnetic permeability μ_0. To make the system dimensionless we scale lengths by d, time with respect to the thermal diffusion time d^2/κ, temperature with ΔT and the magnetic field

is scaled with respect to $(\mu_0\rho_0)^{1/2}\,\kappa/d$. The system of governing equations then becomes

$$\frac{\partial \boldsymbol{u}}{\partial t} + \boldsymbol{u}\cdot\nabla\boldsymbol{u} + \frac{\mathrm{Pr}}{\mathrm{Ek}}\hat{\boldsymbol{z}}\times\boldsymbol{u} = -\nabla P + \mathrm{Pr}\nabla^2\boldsymbol{u} + \mathrm{PrRa}\theta\hat{\boldsymbol{z}} + \boldsymbol{J}\times\boldsymbol{B}, \tag{2.85}$$

$$\nabla\cdot\boldsymbol{u} = 0, \tag{2.86}$$

$$\frac{\partial \theta}{\partial t} + \boldsymbol{u}\cdot\nabla\theta = w + \nabla^2\theta, \tag{2.87}$$

$$\frac{\partial \boldsymbol{B}}{\partial t} + \boldsymbol{u}\cdot\nabla\boldsymbol{B} - \boldsymbol{B}\cdot\nabla\boldsymbol{u} = \frac{\mathrm{Pr}}{\mathrm{Pm}}\nabla^2\boldsymbol{B}, \tag{2.88}$$

$$\nabla\cdot\boldsymbol{B} = 0, \tag{2.89}$$

where $\boldsymbol{u} = (u, v, w)$ is the fluid velocity, P is the pressure, $\boldsymbol{B}$ is the magnetic field, θ is the temperature fluctuation from the linear background profile, and $\boldsymbol{J} = \nabla\times\boldsymbol{B}$ is the dimensionless current density. It should be noted that we have rewritten the induction equation using $\nabla\times(\boldsymbol{u}\times\boldsymbol{B}) = (\boldsymbol{B}\cdot\nabla)\,\boldsymbol{u} - (\boldsymbol{u}\cdot\nabla)\,\boldsymbol{B}$, since the fluid is incompressible and the field is solenoidal. Additionally, we can write $\eta/\kappa = \mathrm{Pr}/\mathrm{Pm}$.

The dimensionless parameters that appear in the governing equations are again the Prandtl number Pr, Ekman number Ek, and Rayleigh number Ra previously defined. However we have now introduced an additional dimensionless parameter, the magnetic Prandtl number, defined as

$$\text{Magnetic Prandtl:} \qquad \mathrm{Pm} = \frac{\nu}{\eta}. \tag{2.90}$$

The magnetic Prandtl number quantifies the ratio between fluid viscosity and magnetic diffusivity.

2.6 Dynamo Theory

In the introductory chapter we discussed how a self-excited dynamo could generate and maintain the Earth's magnetic field, driven by convective fluid motion. In this section we will delve deeper into the fundamentals of dynamo theory, aiming to solve the system of equations in the previous subsection.

In 1867, Siemens became the first to formulate and build a self-excited dynamo which he publicly demonstrated (Siemens, 1867). His idea was to make use of the fact that electrical currents were always accompanied by the presence of a magnetic field. Half a century later, (Larmor, 1919) suggested that such self-excited dynamos could produce the observed magnetic fields of the Sun. The quest then began to investigate how we could develop fluid motions that sufficiently self-generate a magnetic field, known as the 'kinematic dynamo problem'.

2.6.1 Kinematic Dynamos

In kinematic dynamo theory, a velocity field is prescribed which can vary temporally but is not influenced by the magnetic field, achieved by removing the Lorentz force contribution to the Navier-Stokes equation. The evolution of the magnetic field is then evolved given this fluid flow structure to determine whether the prescribed flow is able to produce a desired magnetic field. Mathematically, this is explored using the magnetic induction equation (Equation 2.81). Since the magnetic field, $\boldsymbol{B}$, is divergence free (by Gauss' law for magnetism), it is commonplace to decompose the magnetic field into toroidal and poloidal parts,

$$\boldsymbol{B} = \boldsymbol{B}_T + \boldsymbol{B}_P, \tag{2.91}$$

where $\boldsymbol{B}_T = \nabla \times T\boldsymbol{e}_r$ is the toroidal field and $\boldsymbol{B}_P = \nabla \times \nabla \times S\boldsymbol{e}_r$ is the poloidal field in spherical polar coordinates. Whilst this is commonly done in spherical geometries, a similar process can be applied to Cartesian geometries. Here both fields act in the unit radial direction, $\boldsymbol{e}_r$, and $T(t, \boldsymbol{x})$, $S(t, \boldsymbol{x})$ are scalar functions. For an axisymmetric magnetic field, T and S are independent of the azimuthal angle, ϕ and the toroidal magnetic field acts purely in the $\boldsymbol{e}_\phi$-direction whilst the poloidal part acts in $\boldsymbol{e}_\theta$ and $\boldsymbol{e}_r$ only.

Whilst prescribing the velocity field simplifies the induction equation and allows us to only solve for the magnetic field, some magnetic field configurations and flow structures become inaccessible, i.e. are not possible solutions of the kinematic dynamo problem. Notably, there exist a number of anti-dynamo theorems, the most famous of which is Cowling's theorem (Cowling, 1934). Cowling's theorem states that a hydromagnetic dynamo is completely incapable of maintaining a steady, purely axisymmetric magnetic field. This was also demonstrated in Braginsky (1964). Other anti-dynamo theorems include that a two-dimensional magnetic field cannot be maintained by a dynamo or that a purely toroidal field cannot be maintained by a dynamo. Further explanations, including other anti-dynamo theorems can be found in Roberts (2015).

2.6.2 The Alpha and Omega Effects

Early kinematic dynamos focussed on exploring the Sun's magnetic field. It was known already that different parts of the solar convection zone rotate at different angular velocities, leading to differential rotation which can play an important role in the solar dynamo (Bullard & Gellman, 1954). Differential rotation is able to stretch poloidal magnetic field lines in the direction of the fluid flow, this generates toroidal magnetic field which is 'frozen' to the plasma. This is commonly known as the 'ω-effect'. If a reverse process which could generate poloidal field from toroidal could be found, then the loop would be closed and a dynamo could sustainably operate.

Parker (1955) solved this problem with what is commonly known as the 'α-effect'. Parker's idea was based on the stretching of toroidal field lines by vertical convective motions as they interact with the Coriolis force. Vertical motion in the fluid causes toroidal magnetic field to 'bulge' leading to the associated field lines twisting to form an Ω shape, conserving angular momentum. The twisting motion forms a closed loop in the meridional plane and drives a current in the toroidal direction. When averaged over many convective cyclones this results in a net generation of poloidal mean magnetic field. Mathematically, this was represented by adding a source term, including α, to the poloidal field equation which allowed Parker to find solutions to the kinematic dynamo problem. This also provides a way around Cowling's theorem.

The twisting motion of magnetic field lines via the α-effect is associated with the concept of helicity (Soward, 1972). Helicity arises naturally in rotating convective systems, resulting from the correlation between the fluid velocity, $\boldsymbol{u}$, and its vorticity, $\boldsymbol{\omega} = \nabla \times \boldsymbol{u}$, calculated by

$$\mathcal{H} = \boldsymbol{u} \cdot \boldsymbol{\omega}. \tag{2.92}$$

A cyclone can be visualised as a corkscrew motion of fluid around its direction of motion, generating kinetic helicity. Helicity is a scalar quantity which changes sign when reflecting in spatial coordinates and so is related to the topology of the twisting motion of the α-effect. When the α coefficient in the mathematical source term is negative ($\alpha < 0$), the twisting is right-handed and the helicity is positive. Conversely, $\alpha > 0$ results in negative helicity. Thus helicity appears important in the promotion of dynamo action since Coriolis forces influence the generation of cyclonic motions relevant for the α-effect. However, Cattaneo & Hughes (2006) show that when the rotation is important, a kinetic helicity distribution that is antisymmetric about the midplane forms which has no effect on large-scale dynamo action.

2.6.3 Mean Field Electrodynamics

The net generation of a mean magnetic field by the cyclonic motions involved in the α-effect led to the concept of mean field electrodynamics (e.g. Moffatt, 1978), primarily aiming to explore the production of large-scale magnetic fields. That is, where the magnetic energy is primarily at lengthscales much larger than the fluid lengthscale. In turbulent fluids, quantities can often be decomposed into a mean part (taken over spatial or temporal averages) and a fluctuating part as long as there is a scale separation between the two. One caveat is that many mean field theories assume that small-scale magnetic fluctuations result from the breakdown of the large-scale mean magnetic field by turbulent motions. Whilst this is entirely possible, the removal of the mean magnetic field also then results in the removal of small-scale fields. However small-scale dynamos also occur, often producing

fields which fluctuate close to and even below the turbulent fluid lengthscale, which are distinct from the small-scale fields produced by large-scale dynamo action (Schekochihin *et al.*, 2004). In this thesis, we shall solely be interested in large-scale dynamos. Assuming an adequate scale separation, the prescribed velocity field, $\boldsymbol{u}$, and the resultant magnetic field, $\boldsymbol{B}$, can be decomposed as

$$\boldsymbol{u} = \langle \boldsymbol{u} \rangle + \boldsymbol{u}' = \boldsymbol{U}_0 + \boldsymbol{u}', \tag{2.93}$$

$$\boldsymbol{B} = \langle \boldsymbol{B} \rangle + \boldsymbol{b}' = \boldsymbol{B}_0 + \boldsymbol{b}', \tag{2.94}$$

where $\langle ... \rangle$ represents an average over intermediate lengthscales. $\boldsymbol{U}_0$ and $\boldsymbol{B}_0$ are the mean fluid velocity and magnetic field respectively, whilst $\boldsymbol{u}'$ and $\boldsymbol{b}'$ are the corresponding fluctuating parts which satisfy

$$\langle \boldsymbol{u}' \rangle = \langle \boldsymbol{b}' \rangle = 0. \tag{2.95}$$

Substituting this decomposition into the induction equation (Equation 2.81) and separately considering terms which contribute towards the mean and fluctuating quantities gives governing equations for the mean and fluctuating fields,

$$\frac{\partial \boldsymbol{B}_0}{\partial t} = \nabla \times \boldsymbol{\mathcal{E}} + \nabla \times (\boldsymbol{U}_0 \times \boldsymbol{B}_0) + \eta \nabla^2 \boldsymbol{B}_0, \tag{2.96}$$

$$\frac{\partial \boldsymbol{b}'}{\partial t} = \nabla \times \left(\boldsymbol{U}_0 \times \boldsymbol{b}'\right) + \nabla \times \left(\boldsymbol{u}' \times \boldsymbol{B}_0\right) + \nabla \times \left(\boldsymbol{u}' \times \boldsymbol{b}' - \boldsymbol{\mathcal{E}}\right) + \eta \nabla^2 \boldsymbol{b}', \tag{2.97}$$

where $\boldsymbol{\mathcal{E}} = \langle \boldsymbol{u}' \times \boldsymbol{b}' \rangle$ is the mean electromotive force (e.m.f.). Since $\boldsymbol{u}$ is prescribed in kinematic theory, $\boldsymbol{B}_0$ and $\boldsymbol{b}'$ can be linearly related (assuming there is no small-scale dynamo action) and thus, so can $\boldsymbol{\mathcal{E}}$ and $\boldsymbol{B}_0$. This also assumes that the mean field is not influenced by the mean flow (hence setting $\boldsymbol{U}_0 = 0$ in the mean field equation), and that solutions decay in time. The $\nabla \times (\boldsymbol{u} \times \boldsymbol{B}_0)$ term then acts as a source term for the fluctuating field and the relation between $\boldsymbol{\mathcal{E}}$ and $\boldsymbol{B}_0$ takes the form

$$\boldsymbol{\mathcal{E}}_i = \alpha_{ij} \boldsymbol{B}_{0j} + \beta_{ijk} \frac{\partial \boldsymbol{B}_{0j}}{\partial x_k} + ..., \tag{2.98}$$

where α_{ij} and β_{ijk} are tensor coefficients and higher order derivatives are hidden within '...' but could be included. The properties of these coefficients are discussed in Moffatt (1978) but if turbulence is assumed to be isotropic and α, β are constant, the mean e.m.f. can be written as a function of α and β. Substituting into the mean field equation produces the mean field dynamo equation,

$$\frac{\partial \boldsymbol{B}_0}{\partial t} = \nabla \times \left[\alpha \boldsymbol{B}_0 - \beta \left(\nabla \times \boldsymbol{B}_0\right)\right] + \nabla \times (\boldsymbol{U}_0 \times \boldsymbol{B}_0) + \eta \nabla^2 \boldsymbol{B}_0. \tag{2.99}$$

The α-term represents an average current that is parallel to the mean magnetic field,

whilst the β-term can be interpreted as an eddy diffusivity i.e. the method by which turbulent eddies enhance the dissipation of the magnetic field. Further assuming that Rm is small, that there is zero mean flow, and that the magnetic field is uniform, it can then be shown that α is related to the kinetic helicity and β can be related to the turbulent (small-scale) kinetic energy of the fluid (e.g. Moffatt, 1978).

When the magnetic field is stronger, the Lorentz force becomes important and α and β depend on the magnetic field. Motion of the bulk of the fluid transports magnetic field lines at small scales, however strong magnetic fields will eventually oppose this by a process called α-quenching. Similarly, β is also quenched by the back reaction of the Lorentz force on fluid motion. These mechanisms are what allow mean field dynamos to saturate. By choosing the value of α, Cowling's theorem can be defied, sustaining the mean field and allowing the study of nonlinear features such as the saturation of the dynamo where the Lorentz force reaches equilibrium.

Finally, it is important to note that mean field electrodynamics relies on a number of questionable assumptions briefly discussed throughout this section. For a more in-depth discussion of mean field electrodynamics and the validity of the assumptions made, see Hughes (2018), for example.

2.6.4 The Childress-Soward Dynamo

Childress & Soward (Childress & Soward, 1972; Soward, 1974) applied some of the ideas of mean field theory to study dynamo action in a Cartesian domain. Childress & Soward considered Rayleigh-Bènard convection in a Boussinesq fluid confined between rapidly rotating plane layers and performed an asympotic expansion in two spatial scales to explore dynamo action. At large Ta, the critical Rayleigh number for stationary convection varies as $\mathrm{Ra}_c \sim \mathrm{Ta}^{2/3}$ with the most unstable horizontal wavelengths proportional to $\mathrm{Ta}^{-1/6}$ as shown in Section 2.4.1. Childress & Soward asymptotically expand in $\mathrm{Ta}^{-1/6}$, solving the induction equation at different scales, showing for the first time that convective motions near the onset of convection are capable of sustaining a dynamo, now commonly referred to as the Childress-Soward dynamo. One of the key features of the Childress-Soward dynamo is the presence of a horizontal mean magnetic field which is able to influence the convective flow. Furthermore, they identified several possible force balances in the governing equations that depended on the strength of the generated magnetic field. If the induced magnetic field is weak (Soward, 1974), called the 'weak-field' regime, it plays a negligible dynamical role and the dominant force balance at leading order is 'geostrophic'. In the 'intermediate' and 'strong-field' limits (e.g. Fautrelle & Childress, 1982), the Lorentz force plays an increasingly important role in the dynamics of the dynamo, significantly perturbing the driving flow. The presence of these different force balances suggest the existence of multiple dynamo branches.

Different aspects of the Childress-Soward dynamo have been explored by many authors (e.g. St. Pierre, 1993; Jones & Roberts, 2000; Rotvig & Jones, 2002; Stellmach & Hansen, 2004; Favier & Proctor, 2013; Calkins *et al.*, 2015) and in this thesis, we study dynamos of this type in Sections 4-5.

2.6.5 Force Balances

In the dimensionless Navier-Stokes equation, governing the dynamics of a rotating fluid in the presence of a magnetic field (Equation 2.85), we observe six key forces,

$$\underbrace{\frac{\partial \boldsymbol{u}}{\partial t} + \boldsymbol{u}\cdot\nabla\boldsymbol{u}}_{\text{inertia}} + \underbrace{\frac{\mathrm{Pr}}{\mathrm{Ek}}\hat{\mathbf{z}}\times\boldsymbol{u}}_{\text{Coriolis}} = -\underbrace{\nabla p}_{\text{pressure}} + \underbrace{\mathrm{Pr}\nabla^2\boldsymbol{u}}_{\text{viscosity}} + \underbrace{\mathrm{PrRa}\theta\hat{\boldsymbol{z}}}_{\text{buoyancy}} + \underbrace{\boldsymbol{J}\times\boldsymbol{B}}_{\text{Lorentz}}. \tag{2.100}$$

The use of various dimensionless numbers and estimates of relevant flow and field scales in planetary cores enable us to estimate the relative importance of each of these forces to core convection and dynamo action. Many of these dimensionless numbers have previously been defined and discussed in this chapter e.g. Ro, Ek, Ra, Pr, Rm and Pm in Equations 2.16, 2.49, 2.50, 2.44, 2.82 and 2.90 respectively.

However, we have not yet related the Coriolis and Lorentz forces to determine the relevance of rotation and magnetic field to the system. The concepts of 'weak' and 'strong' field branches were introduced by Roberts (1978) and Roberts & Soward (1992) depending on the level of influence of the magnetic field. Traditionally, the ratio of Lorentz to Coriolis force is determined by the Elsasser number,

$$\Lambda = \frac{B^2}{\rho\mu_0\eta\Omega}, \tag{2.101}$$

where $B = |\boldsymbol{B}|$ is the magnetic field strength, ρ is the fluid density, μ_0 is the magnetic permeability, η is the magnetic diffusivity and Ω is the constant rate of rotation. Thus when the Elsasser number is large, the magnetic field is more influential than the effects of rotation. In studies of the onset of magnetoconvection (i.e. studying how a convective system responds to an imposed magnetic field), Soward (1979) showed that the critical Rayleigh number increases with Λ until $\Lambda \sim \mathcal{O}(\mathrm{Ek}^{1/3})$, now associated with the weak field regime. Similarly, Fearn (1979*b*,*a*) then showed that this eventually decreases to a minimum at $\Lambda \sim \mathcal{O}(1)$, associated with the strong field regime. Estimates of the Earth's fluid outer core predict $\Lambda \sim 10$ (Schwaiger *et al.*, 2021). However, recent studies (e.g. Soderlund *et al.*, 2012; Dormy, 2016) argue that in a turbulent dynamo some of the assumptions made in calculating the Elsasser number are not satisfied. For example, parameters such as the Ekman number are not asymptotically small in numerical simulations, leading to overestimates of the influence of the Lorentz force. Instead, they propose a dynamic Elsasser

number based on estimates of the typical velocity and length scales, $\mathcal{U}$ and $\mathcal{L}$ respectively, of the form

$$\Lambda' = \frac{B^2}{\rho\mu_0\Omega\mathcal{U}\mathcal{L}}. \tag{2.102}$$

In contrast to the traditional Elsasser number, the dynamic Elsasser number is estimated to be of order 10^{-2} (Schwaiger *et al.*, 2021) indicating that the convective flow is more rotationally dominated than field dominated. This dynamic Elsasser number therefore implies that the dominant force balance is between pressure gradients and the Coriolis force, making the system geostrophic at leading order (e.g. Busse, 1970). In this scenario, the Taylor-Proudman theorem would result in columnar convective structures aligned with the rotation axis. However, if the traditional Elsasser number is accurate then the Lorentz force dominates over the Coriolis force and the dominant force balance is then between pressure gradients and the Lorentz force, called 'magnetostrophy' (e.g. Roberts, 1978). The Lorentz force could then relax the rotational constraint, breaking the Taylor-Proudman theorem and allowing a larger scale flow. Realistically, these force balances will vary depending on the lengthscales chosen in their calculation, producing different dominant force balances at different scales (Aurnou & King, 2017).

Observations currently imply that the Earth's fluid outer core is dominantly geostrophic at large scales (e.g. Pais & Jault, 2008; Gillet *et al.*, 2011; Aubert, 2020). If this is the case we can take the curl of the Navier-Stokes equation, giving the vorticity equation. This then removes the pressure terms and the geostrophic part of the Coriolis force that competes with it. We can then estimate the force balances at the next highest order, which depend on the convective lengthscale chosen. Typically, a thermal wind balance is observed i.e. the balance involves the buoyancy force and ageostrophic part of the Coriolis force. The third relevant force in the balance is expected to be the force that relaxes the Taylor-Proudman constraint from the remaining (ageostrophic) part of the Coriolis force. This remaining force can either be viscous, inertial, or the Lorentz force. Depending on the convective lengthscale involved in calculating the force balance these are often referred to as 'VAC balance' (involving the **V**iscous, **A**rchimedean/buoyancy and ageostrophic **C**oriolis terms), 'CIA balance' (involving the ageostrophic **C**oriolis, **I**nertial and **A**rchimedean terms) or 'MAC balance' (which includes the **M**agnetic force exerted by the field, **A**rchimedean force and ageostrophic **C**oriolis force). Due to the Ekman number and Rossby number being small in the Earth's outer core, we expect that the dominant force balance at this order will be MAC balance (e.g. Yadav *et al.*, 2016; Aubert *et al.*, 2017; Calkins, 2018). With geostrophic balance at leading order and MAC balance at the next highest order, this is often referred to as QG-MAC balance (where QG stands for **Q**uasi-**G**eostrophic). In multipolar dynamos close to the onset of dynamo action, states can be found where inertia or viscosity are able to replace the Lorentz force in the previ-

ous force balance, leading to QG-CIA or QG-VAC balances respectively (Schwaiger *et al.*, 2019). Furthermore, in weak dipolar dynamos, viscous effects can be present in the leading order force balance (Dormy *et al.*, 2018).

It is hoped that by exploring dynamo action through numerical simulations operating at the relevant lengthscales and force balances, we can further understand the Earth's core dynamics.

Chapter 3

Localised States in Rapidly Rotating Plane Layer Convection

In this section we aim to explore the existence of spatially localised states in rotating planar convection, where solutions can be separated into isolated regions of amplified or suppressed convection. At low Prandtl numbers, relevant to the liquid metals found in planetary cores, inertial forces are strong and zonal flows exhibit large amplitudes leading to localisation, such as in convective nests. We solve the two-dimensional Boussinesq equations considering two different truncated models. We first truncate the governing equations in both dimensions and apply a bifurcation and continuation programme called AUTO-07p, aiming to locate the regions in parameter space at which localised states exist. We then substitute the solutions discovered into a higher resolution pseudospectral code, truncated to a minimal number of Fourier modes in the vertical direction but allowing the full horizontal structure. We then carry out a more detailed survey of the parameter space, following a branch tracking procedure and exploring the various solution branches discovered.

3.1 Introduction

In many astrophysical bodies, a number of additional forces influence the ability of convection to generate a magnetic field. In particular, rotation plays a significant role since many planets and stars are rapidly rotating.

Localised and modulated states are widely encountered phenomena in physical systems, where solutions can be isolated into spatial regions of amplified/suppressed amplitudes. Examples range from d-wave superconductors (Lee, 1993) to quasi-free-standing monolayer graphene (Cavallucci *et al.*, 2018) and in the observation of cellular buckling when bending beams (Wadee & Gardner, 2012). It has also been shown that the Swift-

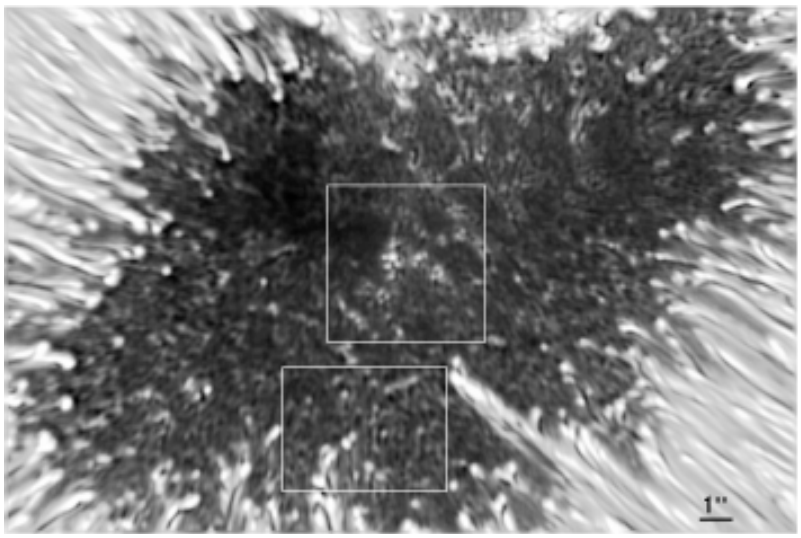


Figure 3.1: An image of sunspot group NOAA 10634 from the 1m Swedish Solar Telescope. The upper rectangle includes a number of bright localised umbral dots. Image taken from Sobotka & Puschmann (2009).

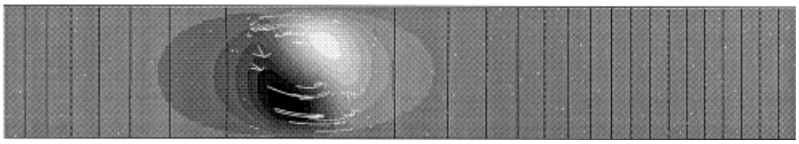


Figure 3.2: Numerical studies of magnetoconvection are able to produce localised states called 'convectons' such as this one from Blanchflower (1999). This image shows a contour plot of the temperature perturbation from the imposed linear profile. The vertical lines show corresponding magnetic field lines. Convection is suppressed in the regions outside of the convecton by almost uniform vertical magnetic field, leading to localisation.

Hohenberg equation can produce an abundance of stable localised states (e.g. Burke & Knobloch, 2006; Sakaguchi & Brand, 1997). Ginzburg-Landau type equations also exhibit localised behaviour which includes the onset of finite-amplitude convection (e.g. Bernoff, 1994; Deissler & Brand, 1994). Spatially localised states have also been simulated in fluids with temperature-dependent viscosity (Solomatov, 2012) and in binary-fluid convection (Niemela *et al.*, 1990).

In magnetoconvection, the study of localised states was originally motivated by observations of sunspots. Strong vertical magnetic fields cause darkened regions inside sunspots known as umbrae, as shown in Figure 3.1. Inside umbrae, bright localised features known as umbral dots are observed (Sobotka *et al.*, 1997). Results in the study of localised states in magnetoconvection began with the numerical discovery of steady localised states in two-dimensional Boussinesq magnetoconvection by Blanchflower (1999), referred to as 'convectons'. An example is shown in Figure 3.2. Convection is known to expel magnetic flux (Weiss, 1966). Blanchflower observed a single convective roll that was able to expel

almost all of the magnetic flux from its neighbourhood. Since the magnetic flux is a conserved quantity in the configuration adopted by Blanchflower, it builds up in the remainder of the computational domain, creating regions of strong, almost uniform magnetic field that suppress convection entirely. Matthews & Cox (2000) show that the presence of a conserved quantity strongly affects the bifurcation structure. Due to the conserved quantity, neutral large-scale modes destabilise supercritical convection close to onset. This, coupled with the ability of such states to locally reduce the forces which oppose convection, makes localised states particularly relevant to subcritical behaviour in rotating convection and dynamo action.

Blanchflower & Weiss (2002) also successfully reproduced convectons in 3D Boussinesq magnetoconvection. Furthermore, oscillatory localised states were more recently discovered in two dimensions which expel magnetic flux less efficiently than their steady counterparts (Buckley & Bushby, 2013).

In rapidly rotating stars, vigorous convection and rotation couple to provide shear through differential rotation and meridional circulation (Brown *et al.*, 2007). Such flows influence the generation and subsequent evolution of magnetic fields in stars and so are of vast importance. Localised convection is observed numerically in the most rapidly rotating cases, with convective nests of locally enhanced convection near the equatorial region. Convection acts to maintain differential rotation, with active convective nests potentially existing due to competition between shearing from differential rotation and Reynolds stresses maintaining strong zonal flows (Grote & Busse, 2001; Brown *et al.*, 2008).

The effects of rotation on localised convection have been less studied than convectons in magnetoconvection. Beaume *et al.* (2013) performed the most significant numerical analysis to date on localised states in two-dimensional rotating plane layer convection. At various fluid Prandtl numbers and Taylor numbers they observe convectons which exist within a self-generated shear layer. In Figure 3.3(a) we see a range of localised states in the streamfunction, $\psi(x, z)$, defined by $\boldsymbol{u} = (-\partial\psi/\partial z, v, \partial\psi/\partial x)$ where $\boldsymbol{u}$ is the velocity. Localised states occur at $\mathrm{Pr} = 0.1$, $\mathrm{Ta} = 400$, $0.68\mathrm{Ra}_c \lesssim \mathrm{Ra} \lesssim 1.02\mathrm{Ra}_c$, with a box width of $10\lambda_c$, where λ_c is the critical wavenumber at onset. The depth-averaged zonal velocity, V, is defined as

$$V(x) = \int_0^1 v(x, z)dz, \tag{3.1}$$

where $v(x, z)$ is the zonal velocity (i.e the perpendicular velocity to the surface of the plane layer). A 'saw-tooth' profile is observed in V spanning the convecton. Similarly to magnetohydrodynamic convectons which expel magnetic flux, these rotational convectons locally reduce angular momentum by up to 70%, expelling it to the remainder of the computational domain. Again this is influenced by the presence of a conserved quantity:

the integral of the zonal velocity as a result of horizontal stress-free boundaries (Cox & Matthews, 2001). An interesting feature known as 'slanted snaking' is observed in the bifurcation structure of the localised states as shown in Figure 3.3(b). This comprises of pairs of solution branches with even and odd parity which intertwine with each other, linked by 'rungs' of asymmetric states. As the energy increases (heading up the snake with increasing Rayleigh number), the convectons grow by nucleating additional cells at either side (see Figure 3.3(a)) before reaching the profile at onset consisting of 10 cells in the streamfunction since the computational domain size is $10\lambda_c$.

Beaume *et al.* (2013) analyse the important features and parameters for the presence of such localised states, showing that a sufficiently wide computational domain is required to allow space for such states to form, and locating an optimum region in the Taylor number. In Figure 3.4 we see that as Ta is increased, the region in Ra where localised states exist widens, until at sufficiently large Ta the rotation becomes too strong and reduces the amplitude of convection, leaving it unable to sufficiently reduce the angular momentum. At $\mathrm{Pr} = 0.6$, the widest region where localised states occur is only at moderate Taylor number, $\mathrm{Ta} \sim \mathcal{O}(10^3)$. However, a key caveat of Beaume *et al.*'s study is that they do not address the stability of the localised states observed.

Localised and modulated convective states have also been investigated in 3D Boussinesq simulations in rotating spherical fluid shells in the absence of magnetic fields. At moderate Rayleigh numbers, localised states appear due to an equilibrium between differential rotation from Reynolds stresses and the destruction of convective eddies by the shear.

In this section, we consider two truncated models, applying a bifurcation and continuation programme, and a higher resolution pseudospectral code to the two-dimensional Boussinesq equations. We aim to expand on the work of Beaume *et al.* (2013), further exploring the parameters and conditions at which localised states occur in rotating plane layer convection. Importantly, we also seek to confidently determine the stability properties of convectons and explore their subcriticality.

3.2 Governing Equations and Numerical Schemes

The equations governing the motion of a Boussinesq fluid within a rotating plane layer were derived in Section 2.3 and linearised in Section 2.4.

We consider a horizontally periodic rotating plane layer bounded at $z = \{0, d\}$, with horizontal width Γd. The gravitational acceleration is $\boldsymbol{g} = -g\hat{\mathbf{z}}$, where $\hat{\mathbf{z}}$ is the unit vector in the z-direction. The layer rotates about the vertical axis at constant rotation rate, Ω. A vertical temperature difference, ΔT, is imposed across the layer such that the fluid is uniformly heated from below. The fluid has constant kinematic viscosity

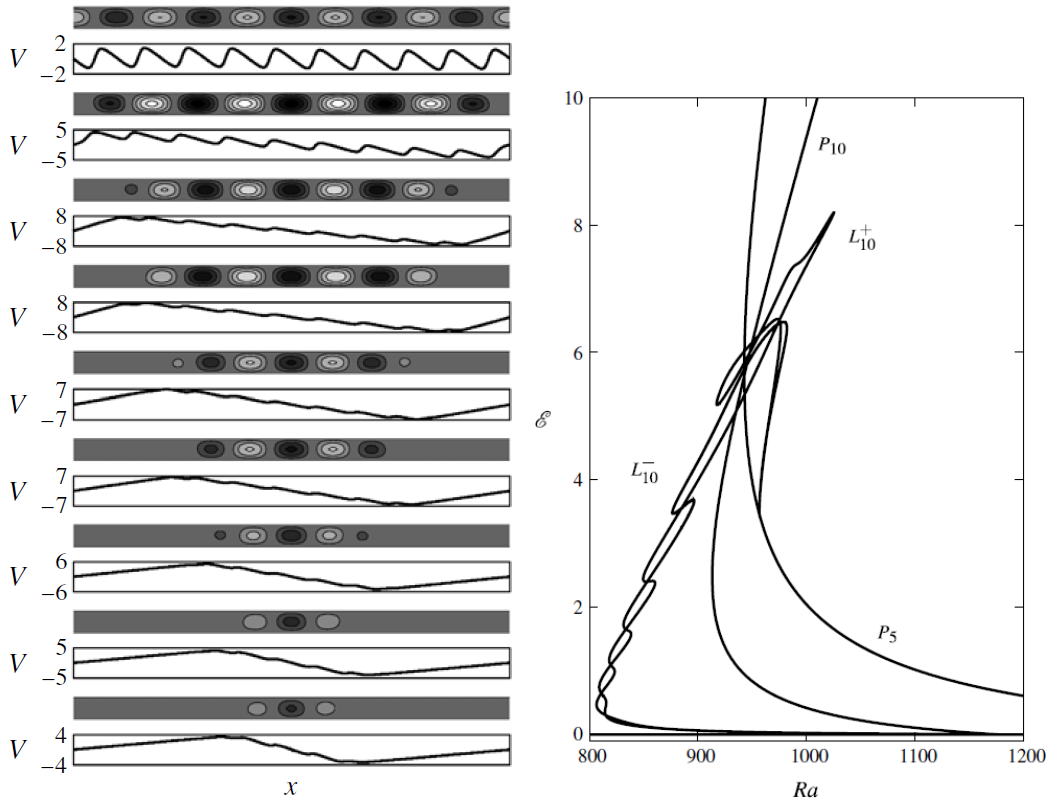


Figure 3.3: Results from Beaume *et al.* (2013) at Pr = 0.1, Ta = 400, $0.68\mathrm{Ra}_c \lesssim \mathrm{Ra} \lesssim 1.02\mathrm{Ra}_c$ presenting (a) solution profiles of convection from different solution branches showing (top) the streamfunction, $\psi(x, z)$, and (bottom) the depth-integrated zonal velocity, $V(x)$, defined in Equation 3.1. (b) The average poloidal kinetic energy, $\mathcal{E}$ as a function of Ra along each solution branch. Slanted snaking in the bifurcation structure is observed where localised states occur and as we head up the 'snake' from the bottom-left in (b), solutions become less localised as shown in (a) until we eventually reach the solution profile corresponding to convective onset.

ν, thermal diffusivity κ, density ρ and thermal expansion coefficient, α. The system is solved in dimensionless form, scaling lengths with d, time with respect to the thermal diffusion time d^2/κ and temperature with ΔT. We then study two-dimensional convection, where variables are three-dimensional but spatial variations only occur in the (x, z)-plane, e.g. for the velocity, $\boldsymbol{u}(t, x, z) = (u(t, x, z), v(t, x, z), w(t, x, z))$. We further introduce the streamfunction, $\psi(t, x, z)$, which corresponds to $\boldsymbol{u} = (u, v, w) = (\partial\psi/\partial z, v, -\partial\psi/\partial x)$, and then define the y-component of the vorticity, $\eta = [\nabla \times \boldsymbol{u}]_y = \nabla^2\psi$. The governing equations for the streamfunction, $\psi(t, x, z)$, the temperature perturbation from the linear temperature profile, $T(t, x, z)$, and the zonal velocity, $v(t, x, z)$, are found by following

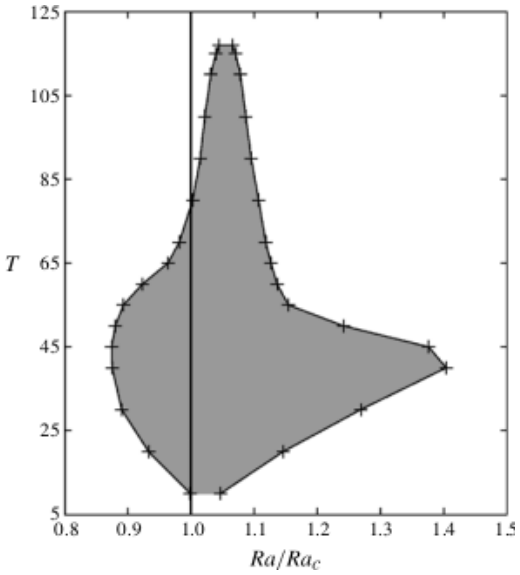


Figure 3.4: Results from Beaume *et al.* (2013) at Pr = 0.6 showing the region in Ta and $\mathrm{Ra}/\mathrm{Ra}_c$ at which localised states are observed (indicated by a grey shaded area). It should be noted that they define $T = \sqrt{\mathrm{Ta}}$.

Veronis (1966), giving

$$\frac{1}{\mathrm{Pr}}\left(\frac{\partial \eta}{\partial t} - \mathcal{J}(\psi, \eta)\right) = \sqrt{\mathrm{Ta}}\frac{\partial v}{\partial z} - \mathrm{Ra}\frac{\partial T}{\partial x} + \nabla^2 \eta, \tag{3.2}$$

$$\frac{\partial T}{\partial t} - \mathcal{J}(\psi, T) = -\frac{\partial \psi}{\partial x} + \nabla^2 T, \tag{3.3}$$

$$\frac{1}{\mathrm{Pr}}\left(\frac{\partial v}{\partial t} - \mathcal{J}(\psi, v)\right) = -\sqrt{\mathrm{Ta}}\frac{\partial \psi}{\partial z} + \nabla^2 v, \tag{3.4}$$

where $\mathcal{J}(f, g) = (\partial f/\partial x)(\partial g/\partial z) - (\partial f/\partial z)(\partial g/\partial x)$ is the Jacobian. Additionally, the three non-dimensional parameters are

$$\text{Prandtl:} \qquad \mathrm{Pr} = \frac{\nu}{\kappa}, \tag{3.5}$$

$$\text{Taylor/Ekman:} \qquad \mathrm{Ta} = \frac{1}{\mathrm{Ek}^2} = \frac{4\Omega^2 d^4}{\nu^2}, \tag{3.6}$$

$$\text{Rayleigh:} \qquad \mathrm{Ra} = \frac{g\alpha\,(\Delta T)\,d^3}{\kappa\nu}. \tag{3.7}$$

where Pr, is the ratio of viscous to thermal diffusivities; Ta is the ratio of Coriolis forces to viscous forces; and Ra determines how successfully buoyancy forces overcome the diffusive forces that oppose convection.

In dimensionless form, our boundaries now lie at $z = \{0, 1\}$ where we impose boundaries which are flat, stress-free and impermeable, maintained at constant temperature.

This results in the boundary conditions,

$$\psi = 0, \quad \frac{\partial^2 \psi}{\partial z^2} = 0, \quad T = 0, \quad \frac{\partial v}{\partial z} = 0 \quad \text{at} \quad z = \{0, 1\}, \tag{3.8}$$

with periodic boundaries at $x = \{0, \Gamma\}$.

Since we will be interested in subcritical behaviour, the critical Rayleigh number for the linear onset of stationary convection can be found in Equation 2.55. Additionally, at low Prandtl numbers ($\mathrm{Pr} \lesssim 0.67$) overstable convection also occurs, with the critical Rayleigh number for the onset of such states given in Equation 2.66. However, these are both calculated in an infinite computational domain. In a restricted domain and truncated model, the finite box-size and discretisation may alter the critical Rayleigh numbers slightly if the box is not large enough or discretisation does not allow the critical wavenumber to onset.

3.2.1 Full Truncation (AUTO model)

To study localised states we must first determine their location in parameter space. Once a solution of interest is found we can then track the solution branch. However, achieving a desired state potentially requires a wide parameter sweep and an initial investigation in our MATLAB model (described in the following section) proved unable to locate convectons by simply time-stepping the governing equations due to the sensitive nature of localised solution branches making them difficult to obtain. We therefore make use of a software package called AUTO-07p (Doedel *et al.*, 2007) which should enable us to determine the origin of localised states in 2D rotating convection and better understand the parameter regions at which they can be located. Throughout this chapter we shall refer to AUTO-07p as simply AUTO from now on.

AUTO is a bifurcation and continuation software package developed in Fortran to solve systems of ordinary differential equations of the form

$$u'(t) = f(u(t), pars) \quad \text{with} \quad f, u \in \mathcal{R}^n, \tag{3.9}$$

where $pars$ is one or more relevant parameters to the system, t is time, and $f, u \in \mathcal{R}^n$ means that they are real functions in n dimensions. AUTO is able to locate a range of bifurcation points such as branch points, Hopf bifurcations and saddle nodes, as well as determine the stability of solutions by calculating the sign of a solution's eigenvalues. It is then able to track the solution branches which branch off from unstable solutions, however it can only do this for cases with real eigenvalues. This prevents AUTO from branch tracking overstable solutions, as in §2.4.2 we required complex values for the onset of such states. This means that AUTO can successfully tell us where overstable solutions

may exist (onsetting from Hopf bifurcations) but we cannot track those solution branches. The branch tracking procedure first looks for all the branch points on the trivial state (call this 'Branch 0') up until a maximum parameter (defined by the user). Let's assume it finds two branch points, 'Point 0A' and 'Point 0B'. It next tracks the solution branch starting from Point 0A (call this 'Branch 1') and finds the branch points along it (which are points '1A, 1B, ...'). At the end of this branch, it does the same for the branch starting at Point 0B, tracking 'Branch 2' and finding points '2A, 2B, ...'. It continues to move through every solution branch beginning from every branch point located in order until stopped.

In order to apply AUTO to rotating Boussinesq convection, we implement a 'restricted symmetries' Fourier expansion of the form

$$\psi = \left\{ \sum_{k=1}^{N} A_k(t) \sin\left(\frac{2\pi k}{\Gamma} x\right) \right\} \sin(\pi z), \tag{3.10}$$

$$T = \left\{ \sum_{k=0}^{N} B_k(t) \cos\left(\frac{2\pi k}{\Gamma} x\right) \right\} \sin(\pi z) + \left\{ \sum_{k=0}^{N} C_k(t) \cos\left(\frac{2\pi k}{\Gamma} x\right) \right\} \sin(2\pi z), \tag{3.11}$$

$$v = \sum_{k=1}^{N} D_k(t) \sin\left(\frac{2\pi k}{\Gamma} x\right) + \left\{ \sum_{k=1}^{N} E_k(t) \sin\left(\frac{2\pi k}{\Gamma} x\right) \right\} \cos(\pi z), \tag{3.12}$$

where N is the number of modes in the expansion, k is the wavenumber which we sum over, and $A_k, ..., E_k$ are the corresponding coefficients at wavenumber k. For each variable we could have implemented a full horizontal Fourier expansion. However, implementing such an expansion results in a large number of equations to be solved which becomes computationally expensive. Additionally, this restricted symmetries approach breaks the translational symmetry of the problem required for solving the system in AUTO. The caveat here, is that AUTO will now fail to produce all solutions that do not satisfy the symmetry,

$$(x, z) \to (-x, z), \quad (A, B, C, D, E) \to (A, -B, -C, D, E). \tag{3.13}$$

Amongst others, this symmetry excludes the state featuring a single roll in the streamfunction as well as other solutions with an odd number of convective rolls. Our restricted symmetries approach will therefore provide a subset of the possible solutions.

The governing equations for $\{A_k(t), ..., E_k(t)\}$ are obtained by substituting Equations 3.10-3.12 into Equations 3.2-3.4, followed by collecting coefficients of $\sin(n\pi z)$ and

$\cos(n\pi z)$, and terms that contribute at the k-th wavenumber. This gives

$$\partial_t A_k = -\mathrm{Pr}\left(\left(\frac{2\pi k}{\Gamma}\right)^2 + \pi^2\right) A_k - \mathrm{PrRa}\left(\frac{2\pi k}{\Gamma}\right)\left(\left(\frac{2\pi k}{\Gamma}\right)^2 + \pi^2\right)^{-1} B_k + \pi\mathrm{Pr}\sqrt{\mathrm{Ta}}\left(\left(\frac{2\pi k}{\Gamma}\right)^2 + \pi^2\right)^{-1} E_k, \quad (3.14)$$

$$\partial_t B_k = \begin{cases} -\pi^2 B_0 - \pi\left[A'C\right]_0 - \frac{\pi}{2}\left[AC'\right]_0 & k = 0 \\ -\left(\frac{2\pi k}{\Gamma}\right) A_k - \left(\left(\frac{2\pi k}{\Gamma}\right)^2 + \pi^2\right) B_k - \pi\left[A'C\right]_k - \frac{\pi}{2}\left[AC'\right]_k & k > 0 \end{cases} \quad (3.15)$$

$$\partial_t C_k = \begin{cases} -4\pi^2 C_0 + \frac{\pi}{2}\left[A'B\right]_0 - \frac{\pi}{2}\left[AB'\right]_0 & k = 0 \\ -\left(\left(\frac{2\pi k}{\Gamma}\right)^2 + 4\pi^2\right) C_k + \frac{\pi}{2}\left[A'B\right]_k - \frac{\pi}{2}\left[AB'\right]_k & k > 0 \end{cases} \quad (3.16)$$

$$\partial_t D_k = -\mathrm{Pr}\left(\frac{2\pi k}{\Gamma}\right)^2 D_k - \frac{\pi}{2}\left[A'E\right]_k - \frac{\pi}{2}\left[AE'\right]_k, \quad (3.17)$$

$$\partial_t E_k = -\mathrm{Pr}\left(\left(\frac{2\pi k}{\Gamma}\right)^2 + \pi^2\right) E_k - \pi\mathrm{Pr}\sqrt{\mathrm{Ta}} A_k - \pi\left[AD'\right]_k. \quad (3.18)$$

where $[g]_k$ indicates the contribution from the nonlinear term, g, to the k-th wavenumber. Evaluating the nonlinear terms requires a summation over pairs of wavenumbers, extracting values at which they contribute to the k-th mode. A full derivation for each nonlinear term can be found in Appendix A.1. This leaves $5N + 2$ equations to be solved within AUTO.

Furthermore, in larger computational domains and at more extreme parameters (e.g. high Ta, low Pr), a higher number of modes are required to remain well-resolved. AUTO tracks the stability of a solution by checking the stability of its eigenvalues, inverting a matrix of mode amplitudes which occasionally become too large to cope with. For this reason, we introduce a scaling of our variables adjusted from that of Knobloch *et al.* (1981), rescaling time with respect to $p = (2\pi/\Gamma)^2 + \pi^2$. The exact scalings were determined by substituting those from Knobloch *et al.* in and evaluating, before making minor alterations to the scalings to ensure terms simplify. The coefficients in Equations 3.10-3.12 are then

replaced with

$$A_k \to (2p)^{1/2} \frac{\Gamma}{\pi} \widetilde{A}_k, \tag{3.19}$$

$$B_k \to 2\,(2/p)^{1/2}\, \widetilde{B}_k, \tag{3.20}$$

$$C_k \to (2\pi)^{-1}\, \widetilde{C}_k, \tag{3.21}$$

$$D_k \to \left(\frac{\Gamma}{2\pi}\right) \widetilde{D}_k, \tag{3.22}$$

$$E_k \to 2\,(2/p)^{1/2}\, \Gamma \widetilde{E}_k. \tag{3.23}$$

The aim is that once we have located localised states of interest using AUTO (either the original or scaled version), we can use the solution as an initial condition to further explore the state in our higher-resolved model.

3.2.2 Full Horizontal Structure (MATLAB model)

In comparison to the horizontal structure, the vertical structure of convection is relatively simple close to the onset of convection. In this model, we therefore retain the full horizontal structure for ψ, T and v whilst projecting onto a minimal number of vertical Fourier modes which maintain nonlinearity. These take the form,

$$\psi(t,x,z) = A(t,x)\sin(\pi z), \tag{3.24}$$

$$T(t,x,z) = B(t,x)\sin(\pi z) + C(t,x)\sin(2\pi z), \tag{3.25}$$

$$v(t,x,z) = D(t,x) + E(t,x)\cos(\pi z), \tag{3.26}$$

where the selection of sines and cosines is chosen to satisfy the boundary conditions at $z = 0, 1$ in Equation 3.8. Calculating $\eta = \nabla^2\psi$ gives

$$\eta = \alpha \sin(\pi z), \tag{3.27}$$

where $\alpha = A'' - \pi^2 A$, with primes denoting a derivative with respect to x. Substituting into Equations 3.2, 3.3 and 3.4 gives

$$\partial_t \alpha = \mathrm{Pr}\left(\alpha'' - \pi^2\alpha\right) - \mathrm{PrRa}B' - \pi\mathrm{Pr}\sqrt{\mathrm{Ta}}E. \tag{3.28}$$

$$\partial_t B = \left(B'' - \pi^2 B\right) - \pi A'C - \frac{\pi}{2}AC' - A', \tag{3.29}$$

$$\partial_t C = \left(C'' - 4\pi^2 C\right) + \frac{\pi}{2}A'B - \frac{\pi}{2}AB'. \tag{3.30}$$

$$\partial_t D = \mathrm{Pr}D'' - \frac{\pi}{2}A'E - \frac{\pi}{2}AE', \tag{3.31}$$

$$\partial_t E = \mathrm{Pr}\left(E'' - \pi^2 E\right) - \pi A D' - \pi \mathrm{Pr}\sqrt{\mathrm{Ta}}A. \tag{3.32}$$

These five equations form the system which will be solved numerically in MATLAB, exploring subcriticality and the existence of localised states.

We solve the system pseudospectrally, making use of Fast Fourier Transforms from MATLAB's library to solve all horizontal derivatives, then implementing an Adams-Bashforth (2nd order) time-stepping regime. The code is initialised using a superposition of small-amplitude Fourier modes, similar to the expansion in § 3.2.1, and features optional dealiasing using the standard 2/3 rule.

3.2.3 Output Parameters

AUTO automatically measures the amplitude of its solutions by outputting a measure known as the $L2$-Norm or L^2-Norm, calculated by

$$L^2\text{-Norm} = \sqrt{\int_0^1 \sum_{k=1}^{\mathrm{NDIM}} U_k(x)^2 dx}, \tag{3.33}$$

where NDIM is the number of dimensions in the system, for us NDIM$= 5N + 2$, and U_k is the k-th mode amplitude. In our scaled variables this will be denoted $\widetilde{L}^2$-Norm. In our system, L^2-Norm$= 0$ corresponds to the trivial conducting state. More commonly, the efficiency of convection is determined by the Nusselt number, which is the ratio of convective heat flow to conductive heat transfer in the absence of motions. This can be computed in MATLAB or AUTO respectively by

$$Nu = 1 + \langle |\nabla T|^2 \rangle_V = 1 - \pi \left(\langle B \rangle_x + 2\langle C \rangle_x \right) = 1 - \pi \left(B_0 + 2C_0 \right), \tag{3.34}$$

where $\langle ... \rangle_V$ denotes the volume average; $\langle ... \rangle_x$ denotes the average in the horizontal direction; B and C are our MATLAB model variables; and B_0 and C_0 are the unscaled $k = 0$ mode amplitudes from our AUTO model. The trivial state is then represented by $Nu = 1$ where all heat flux is dissipated by conduction. Possessing a $Nu > 1$ thus indicates that convective motions are present in the system, corresponding to L^2-Norm> 0.

In Beaume *et al.* (2013), slanted snaking is best observed in the average poloidal kinetic energy. This is calculated in AUTO as

$$\mathcal{E} = \frac{1}{2\Gamma} \int_V |\nabla \psi|^2 dx dz = \frac{1}{8} \sum_{k=1}^{N} \left\{ \left(\frac{2\pi k}{\Gamma} \right)^2 + \pi^2 \right\} A_k^2, \tag{3.35}$$

in our unscaled variables, where $\langle ... \rangle_V$ denotes the volume-average. A derivation is shown in Appendix A.2.

Beaume *et al.* also display the depth-integrated zonal velocity, V. In our system, this simply corresponds to

$$V = \langle v \rangle_z = \sum_{k=1}^{N} D_k \sin\left(\frac{2\pi k}{\Gamma} x\right), \tag{3.36}$$

where $\langle ... \rangle_z$ denotes the depth-average and D_k are the relevant AUTO coefficients.

We also wish to quantify the reduction in angular momentum associated with rotational convectons. We define a local Rossby number, Ro, normalised with respect to the Prandtl and Taylor numbers as

$$Ro = \frac{1}{\mathrm{Pr}\sqrt{\mathrm{Ta}}} \frac{\partial D}{\partial x}, \tag{3.37}$$

where our MATLAB truncation defines $D = \langle v \rangle_z$ as the depth-averaged zonal velocity and $Ro = -1$ corresponds to locally non-rotating.

In order to explore the characteristic lengthscale of convectons, we find the horizontal distance between the maximum and minimum depth-averaged zonal velocity and normalise with respect to the box-width and number of convective rolls. Following Beaume *et al.*, this can be calculated by

$$L_{conv} = \frac{1}{N_{conv}\Gamma} |x(D_{max}) - x(D_{min})|, \tag{3.38}$$

where $x(D_{max})$ and $x(D_{min})$ denote the horizontal locations of the maximum and minimum depth-averaged zonal velocities respectively and N_{conv} is the number of convective rolls in the streamfunction. It should be noted that this measure is somewhat subjective and that $x(D_{max})$ and $x(D_{min})$ are not necessarily unique. This therefore does frequently require visual inspection to verify.

3.2.4 Solution Branch Naming Convention

In our results we will consider branches consisting of a number of convective rolls, some of which are localised and which can either be steady or time-dependent. In order to refer to solution branches easily, the following naming convention will be used:

1. The number of convective rolls in the streamfunction,
2. The temporal behaviour of the state, indicated by the Nusselt number (e.g. 's' for steady; 'o' for oscillatory),
3. Whether the solution is localised ('l' for localised, or nothing otherwise).

For example, '4sl' refers to the solution branch which has 4 convective rolls in the streamfunction, is steady ('s') and is localised ('l'), whilst '12o' has 12 convective rolls, is oscillatory ('o') in the Nusselt number, and is not localised (no 'l'). In our results there are cases

where we see more than one convecton in the computational domain. If this is the case the solution branch will be named '2x 1sl' for example, indicating that we have two single roll convectons simultaneously existing which are steady and localised. It should be noted that the labelling of oscillatory is determined by the temporal evolution of the Nusselt number. What is referred to as an oscillatory convecton here does not necessarily mean that the convecton oscillates in sign over time, in contrast to the oscillatory convectons found in magnetoconvection (Buckley & Bushby, 2013).

3.3 Model Testing

To begin, testing both codes successfully reproduces the critical Rayleigh numbers for the onset of stationary and overstable convection (Equations 2.55 and 2.66 respectively), confirming that the linear terms are correct.

Furthermore, we are able to use the solutions produced by AUTO as initial conditions for MATLAB runs, where the full horizontal structure is allowed. Since both codes are solving the same fundamental equations, when we do this our stable AUTO solutions 'sit' without variation as we time-step in MATLAB, indicating that both codes agree on the existence of such states and their stability. As a sanity check, using an unstable solution from AUTO also results in the solution destabilising and settling onto a different solution branch in MATLAB.

To test AUTO more intensively we aim to make a quantitative comparison with the results of Beaume *et al.* (2013), followed by substituting the solutions into our MATLAB code. We do not however expect a perfect comparison due to our truncations of the variables and restricted symmetries approach. The convectons initially presented by Beaume *et al.* are at low Prandtl number ($\mathrm{Pr} = 0.1$) and moderate rotation ($\mathrm{Ta} = 400$). Similarly, we set $\mathrm{Pr} = 0.1$, $\mathrm{Ta} = 400$, and explore a slightly wider range of Rayleigh numbers, $0 \leq \mathrm{Ra} \leq 2000$. At this Pr and Ta, Beaume *et al.* use a horizontal box width of $\Gamma = 10\lambda_c \approx 20$, where λ_c is the critical wavelength for the onset of convection. After a number of tests, aiming to compromise upon the size of the horizontal domain and the horizontal resolution required, we are able to produce similar results at $\Gamma = 14$. In AUTO we use $N = 42$ points (totalling 212 points across all variables) which corresponds to a horizontal resolution of 128 in our MATLAB model (with dealiasing).

Figure 3.5 shows the bifurcation structure of the kinetic energy, $\mathcal{E}$, and the L^2-Norm across all of our scaled variables, as we vary the Rayleigh number. In the Figure, solid blue curves indicate that the solution is stable, whereas red dotted curves are unstable. We observe a range of solutions with varying numbers of convective rolls, including steady localised states (labelled '4sl', '6sl' and '8sl'). Firstly, we are able to conclusively state that convectons are stable in rotating plane layer convection. The streamfunctions and depth-

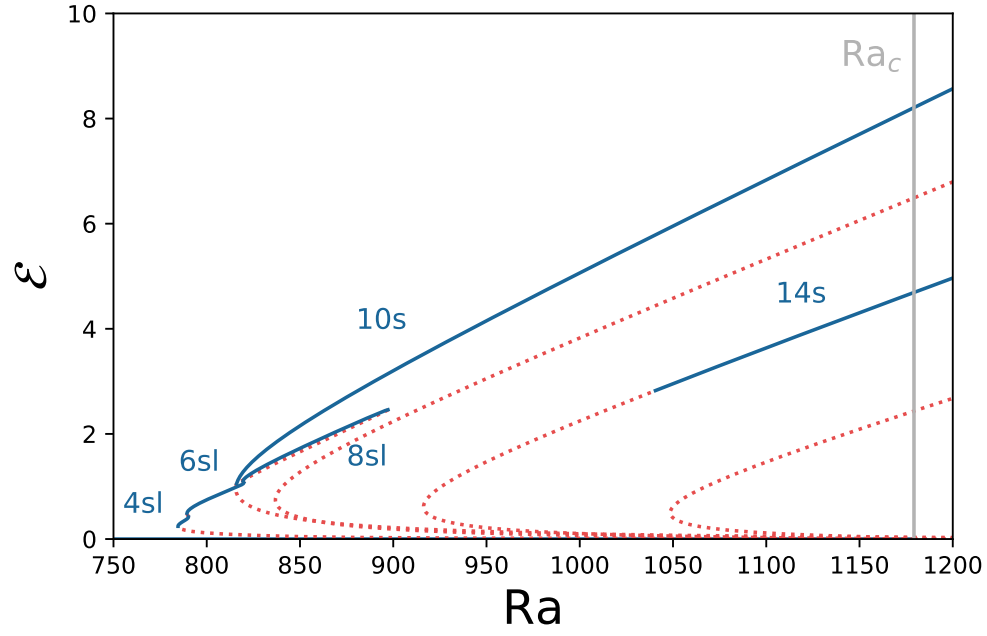
averaged zonal velocities of all stable solutions are presented in Figure 3.6. In this case, localisation is observed at Rayleigh numbers below the critical Rayleigh numbers for the linear onset of convection ($\mathrm{Ra}_c = 1179.2$, $\mathrm{Ra}_0 = 1461.0$) and display hints of the slanted snaking behaviour in the kinetic energy previously observed. The most localised case gains stability at $\mathrm{Ra} = 784.6$ and gains energy as the Rayleigh number increases. Eventually this solution becomes unstable and the kinetic energy snakes backwards (towards decreasing Ra), nucleating an additional convective cell on either side before regaining stability and again increasing in energy with Ra. If we track the bifurcation of the scaled L^2-Norm in Figure 3.5(b) we see that it is a secondary bifurcation (at a branch point) from the branch representing convective onset which eventually leads to localisation. After convection has onset (leading to the non-localised pattern state labelled '14s'), a new branch quickly bifurcates which decreases in Ra before displaying a 'looping' structure in L^2-Norm. On this loop, we observe stable convectons bifurcating from saddle nodes, which eventually end by attaching to the 10-roll steady branch ('10s') as it becomes stable. This is the point at which our convectons have nucleated sufficiently many cells either side to fill the computational domain and is therefore no longer localised.

It should be noted that our 'restricted symmetries' approach and smaller computational domain leads to AUTO only producing a subset of the solutions presented in Beaume *et al.*. Notably, we are unable to produce a single convective roll in the streamfunction, and in this case we have also not picked up the 2-roll steady solution. This is likely due to our compromised resolution in such a large computational domain.

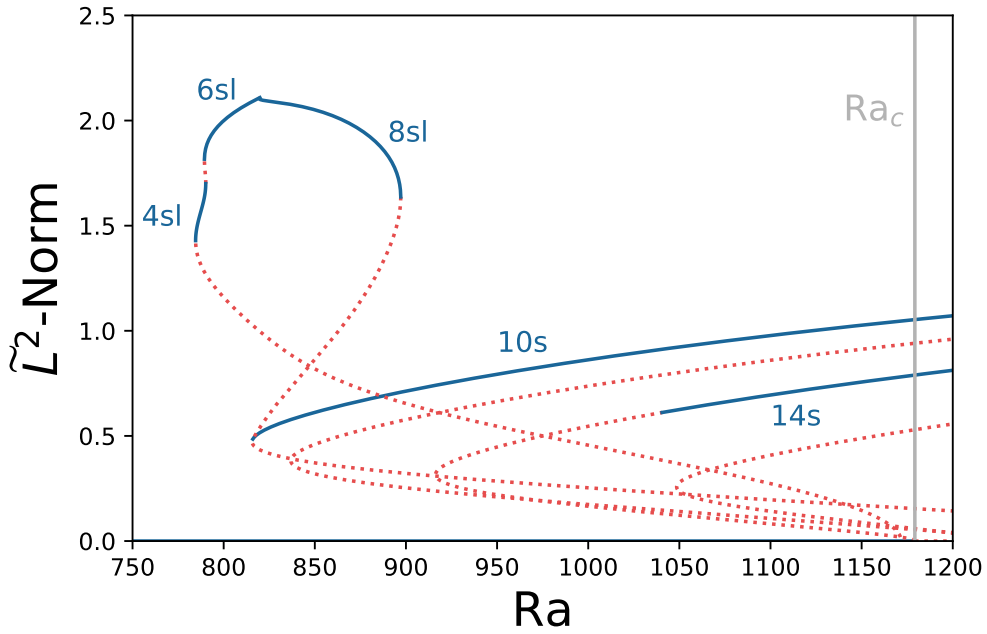
Within our localised states we observe a linearly decreasing profile in the depth-averaged zonal velocity, exhibiting a saw-tooth structure as in Beaume *et al.* (2013) due to shearing either side of each convective roll which becomes more pronounced as we increase in energy. Since the integral of the zonal velocity is a conserved quantity this must be accounted for in the remainder of the computational domain where convection is suppressed. Additionally, the lengthscale of each convective cell appears to slightly increase as we gain energy up the snake.

As a final test, we take a range of our AUTO solutions and use them as initial conditions in MATLAB, where the full horizontal structure is allowed. This successfully results in the expected behaviour: stable AUTO solutions remain stable in MATLAB and are steady, unvarying as the time is evolved. Similarly unstable AUTO solutions decay when evolved in MATLAB, resulting in the location of an alternative solution branch or simply decaying to the trivial conducting state. Furthermore, if we use solutions on the edges of stable branches as initial conditions and marginally decrease/increase Ra, the solution either remains on the solution branch (if moving towards the centre of the branch) or becomes unstable and decays (if moving past the end point of a branch).

We can now be confident that both our AUTO and MATLAB models produce correct



(a)



(b)

Figure 3.5: Bifurcation structure of (a) the kinetic energy, $\mathcal{E}$, and (b) scaled version of L^2-Norm (labelled $\widetilde{L}^2$-Norm) verses Rayleigh number, Ra, aiming to reproduce the results of Beaume *et al.* (2013) in AUTO-07p at Pr = 0.1, Ta = 400, $\Gamma = 14$. Ra_c is the critical Rayleigh number for the onset of steady convection in an infinite domain. $\mathrm{Ra}_0 < \mathrm{Ra}_c$, however AUTO is unable to track time-dependent solutions. Stable solutions are shown by a solid blue curve, whereas unstable solutions are dotted in red. Our branch naming convention is explained in §3.2.4.

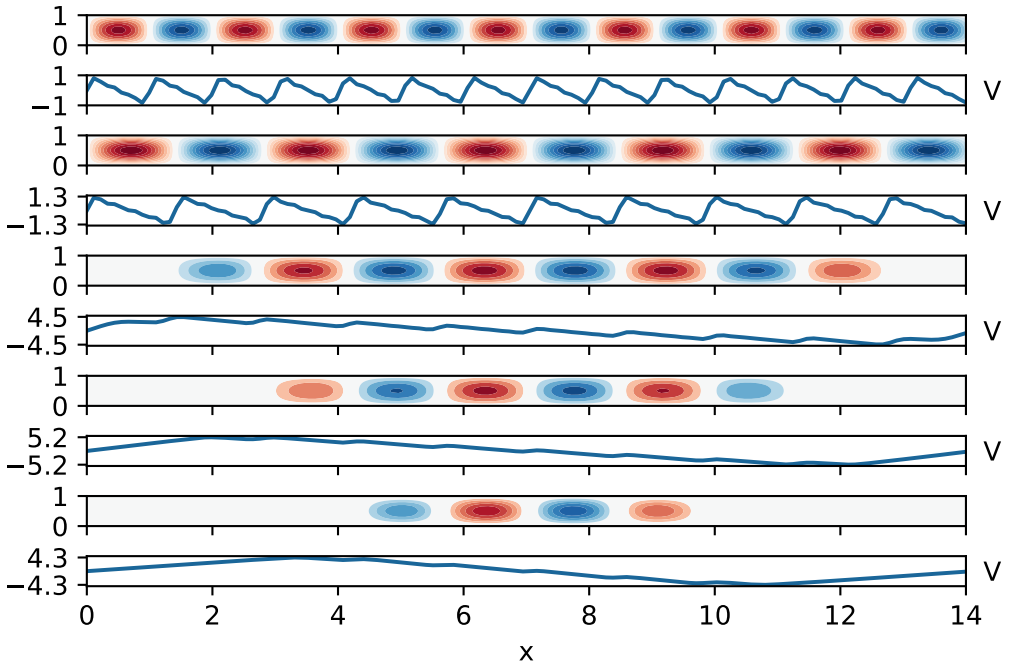


Figure 3.6: Localised states from each of the solution branches produced by AUTO-07p aiming to reproduce Beaume *et al.* (2013) at Pr = 0.1, Ta = 400, $\Gamma = 14$ showing the streamfunction (top) and depth-averaged zonal velocity (bottom). States are presented increasing upwards with kinetic energy and are from the solution branches labelled 4sl, 6sl, 8sl, 10s, and 14s heading upwards.

results and are in agreement over the existence of stable localised states in 2D rotating planar convection.

3.4 Results

In this section, we aim to further explore the parameter regimes at which localised states occur in 2D rotating convection. In particular, we hope to locate convectons at higher Taylor numbers and lower Prandtl numbers, more relevant to planetary cores than previous work. Furthermore, we aim to determine the key features which allow the occurrence of such localised states, and how these enable subcritical behaviour to occur.

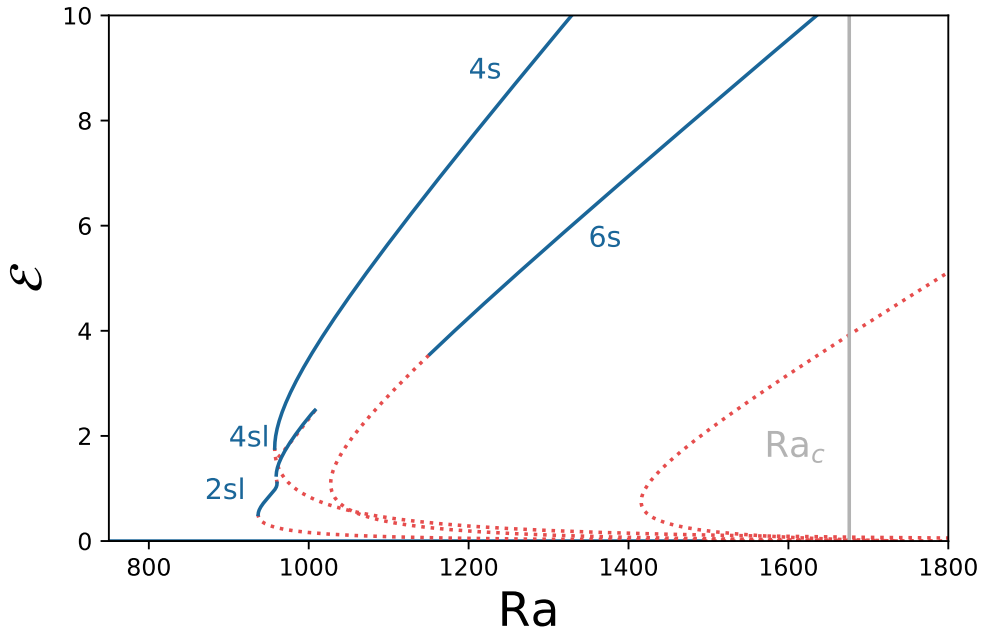
3.4.1 Initial Investigation in AUTO

We further increase Ta from the parameter regime explored in (Beaume *et al.*, 2013), hoping to locate further convectons at more rapid rotation. In order to maintain a manageable resolution in our AUTO code, we further reduce the size of the computational domain to $\Gamma = 6$, as localised states have been observed in magnetoconvection in similar

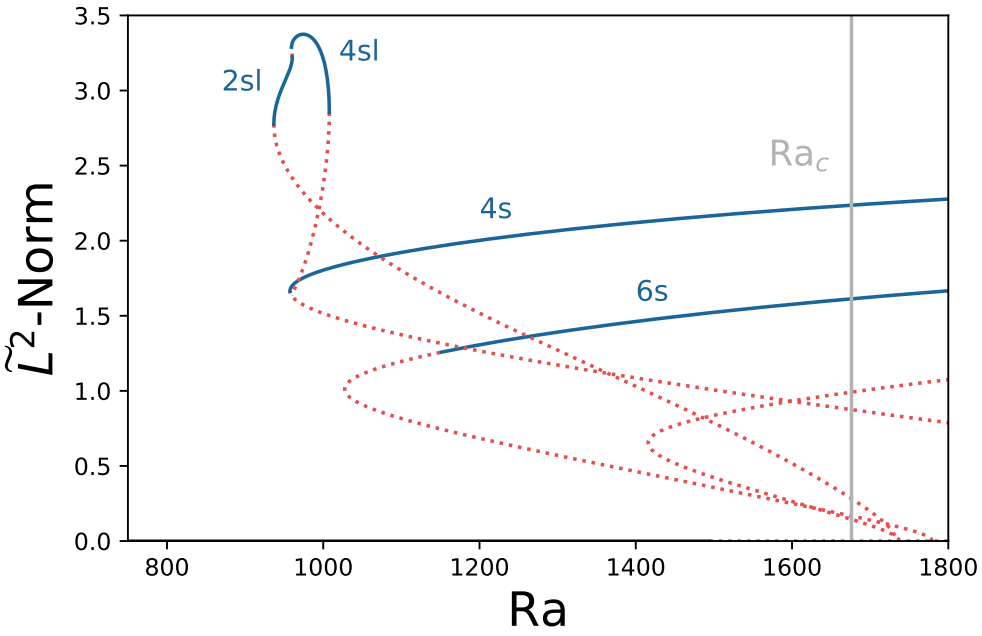
sized domains (e.g. Buckley & Bushby, 2013). It should be noted that the box-size may limit the range of localised solutions which we are able to achieve. With a decrease in horizontal domain size, we are also able to decrease the spatial resolution in AUTO to $N = 32$ points (giving 162 individual equations to be solved overall), which corresponds to a horizontal resolution of 96 in our MATLAB model (with dealiasing). At $\mathrm{Pr} = 0.1$, $\mathrm{Ta} = 1000$ and $\Gamma = 6$, the critical Rayleigh numbers are $\mathrm{Ra}_c = 1676.1$ and $\mathrm{Ra}_0 = 1482.2$, however we present Ra_c on any AUTO-related Figures since AUTO is unable to track overstable solution branches. At these parameters we are still able to locate subcritical localised states, which exhibit slanted snaking behaviour in the kinetic energy and looping behaviour in the L^2-Norm as shown in Figure 3.7. In this case, the first branch to onset from the trivial state does not come at Ra_c (calculated for an infinite box), due to the computational box size allowing a different convective mode to onset. For $\Gamma = 6$ and $N = 42$ points, the minimum Rayleigh number for the onset of steady convection is at $\mathrm{Ra}_c = 1736.9$ which is where our first branch onsets in AUTO. AUTO then continues to search for possible solutions by increasing/decreasing Ra along the branch until the branch leading to localised states begins with a secondary bifurcation from the first mode to onset. After our convectons have nucleated additional convective cells on either side, the looping structure in the L^2-Norm ends just after a non-localised branch has become stable (the '4s' branch).

The streamfunctions and depth-averaged zonal velocities of stable solutions are shown in Figure 3.8. At these parameters, we are able to discover the most localised state permitted in our restricted symmetries approach, consisting of a single pair of counter-rotating convective rolls in the streamfunction (labelled '2sl'). As in previous convectons presented, this state exhibits a saw-tooth structure in the depth-averaged zonal velocity. Similarly, as the energy is increased, the convecton loses stability before regaining it once an extra convective roll on each side is generated, leading to the '4sl' localised state. Interestingly, this '4sl' state fills a fairly large region of the computational domain, leaving the system unable to fit in a 6-roll, localised state. This solution branch thus terminates on a 4-roll non-localised state which looks like an expanded version of its previous localised state. It should be noted that in a larger box, it is entirely possible that larger localised states (with a higher number of convective rolls) exist and thus solutions are somewhat dependent on the available box-size.

In Figure 3.9 we investigate the convective heat transport via the Nusselt number, Nu, which has previously been unexplored in relation to the efficiency of rotational convectons. In this parameter regime, we observe slanted snaking behaviour in the Nusselt number along localised solution branches, just as in the kinetic energy. At lower Ra numbers and with much of the convection suppressed by strong angular momentum, it is unsurprising that steady convectons are far less effective at transferring heat in comparison to



(a)



(b)

Figure 3.7: Bifurcation structure of (a) the kinetic energy, $\mathcal{E}$, and (b) the scaled version of L^2-Norm (labelled $\widetilde{L}^2$-Norm) versus Rayleigh number, Ra in AUTO-07p at Pr = 0.1, Ta = 1000, $\Gamma = 6$. Stable solutions are shown by a solid blue curve, whereas unstable solutions are dotted in red. Ra_c is the critical Rayleigh number for the onset of steady convection in an infinite domain. At these parameters, $Ra_0 = 1482.2 < Ra_c$, however AUTO is unable to track overstable solution branches. Our branch naming convention is explained in §3.2.4.

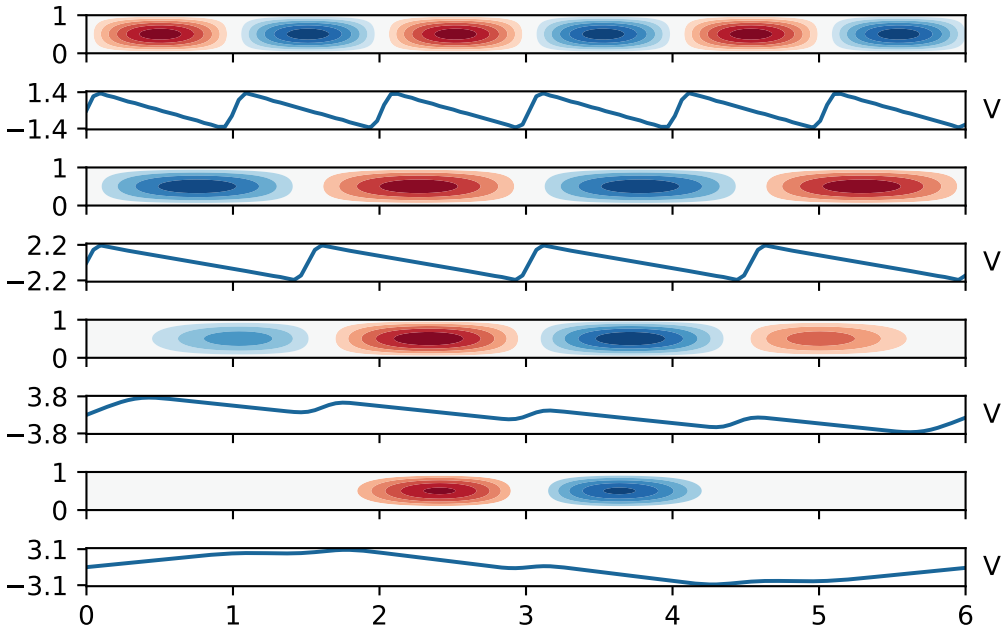


Figure 3.8: Localised states produced by AUTO-07p at Pr = 0.1, Ta = 1000, $\Gamma = 6$ showing the streamfunction (top) and depth-averaged zonal velocity (bottom). States are presented increasing upwards with kinetic energy from the '2sl', '4sl', '4s' and '6s' branches respectively.

non-localised steady states. Similarly, it is unsurprising that as the convecton nucleates additional cells, its Nusselt number increases, indicating more efficient convective heat transfer. Similar behaviour is observed in magnetohydrodynamic convectons (Buckley & Bushby, 2013).

3.4.2 Branch Tracking in MATLAB

Now that we have located localised states in rotating plane layer convection using AUTO, and have confirmed their stability, we can use such states as initial conditions for further branch tracking in MATLAB, where we retain their full horizontal structure. One of the benefits of tracking solutions in MATLAB is that we no longer have a restricted symmetries approach, allowing the single-roll convecton and other symmetry breaking localised states. Additionally, in MATLAB we are now able to study the time-dependence of convectons. So far, AUTO has provided us with steady solutions only, confirmed by time-stepping the AUTO solutions in MATLAB. At low Prandtl numbers, overstable motions occur which are time-dependent. In magnetoconvection, oscillatory localised states were located by Buckley & Bushby (2013) which were less efficient at expelling magnetic flux than steady convectons. Similarly, we hope to locate oscillatory convectons in our system to observe

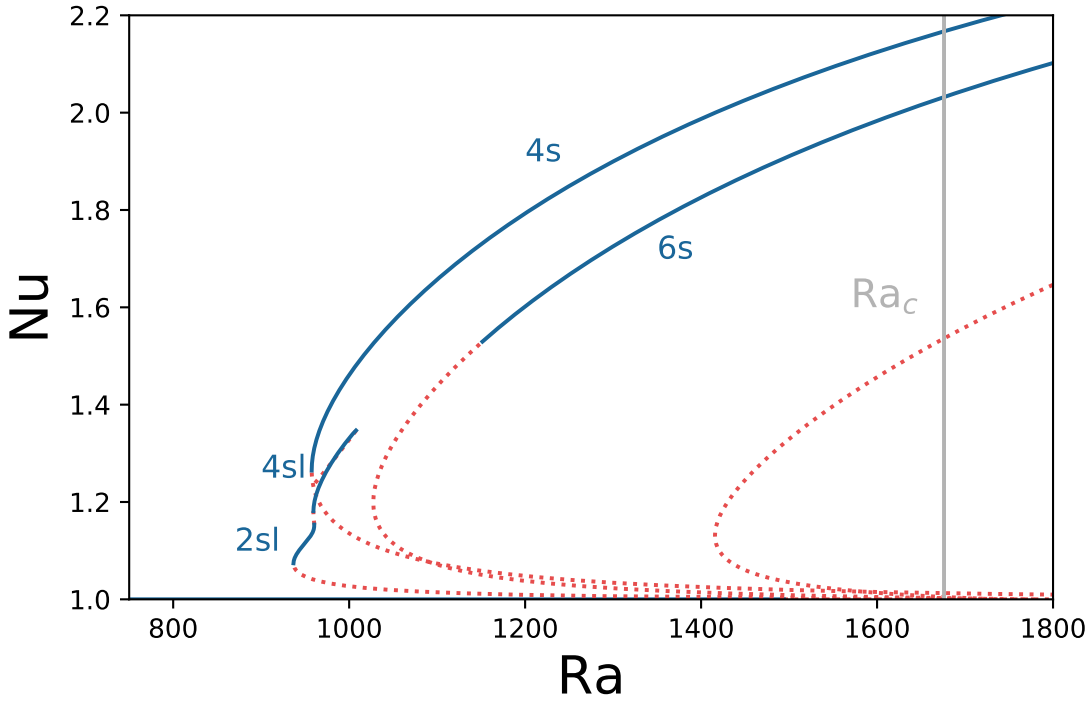


Figure 3.9: Bifurcation structure of the Nusselt number, Nu versus Rayleigh number, Ra in AUTO-07p at Pr = 0.1, Ta = 1000, $\Gamma = 6$. Stable solutions are shown by a solid blue curve, whereas unstable solutions are dotted in red. Ra_c is the critical Rayleigh number for the onset of steady convection in an infinite domain. At these parameters, $\mathrm{Ra}_0 = 1482.2 < \mathrm{Ra}_c$, however AUTO is unable to track overstable solution branches. Our branch naming convention is explained in §3.2.4.

whether similar effects occur in rotating convection.

We begin by taking the most localised solution produced so far in AUTO: the stable '2sl' convecton located at Pr = 0.1, Ta = 1000, Ra $\approx$ 960 in a computational domain of size $\Gamma = 6$. Equivalently to our AUTO model, we begin using a horizontal resolution of 96 points. This state consists of 2 convective rolls in the streamfunction and is at the highest stable Ra on its solution branch. Summaries of the parametric dependence of all solutions located are shown in Figure 3.10. We begin by lowering the Ra, which confirms the width of the solution branch according to AUTO, dropping off the branch onto the trivial conducting state at Ra $\lesssim$ 936. We had hoped to locate the convecton consisting of a single convective roll at lower Ra but were unsuccessful. Next we try increasing Ra, where the solution rapidly breaks symmetry and locates a new convecton. At Ra $>$ 960, still below the linear onset of convection (for both steady and oscillatory motions) we locate the '3sl' convecton, shown in Figure 3.11(a). We then continue tracking the solution branch to higher Ra and Ta before locating the '1sl' solution at Ra = 2000, Ta = 22000, which is just 3% below the critical Rayleigh number for the onset of overstable convection at

$\mathrm{Ra}_0 = 2062.1$, shown in Figure 3.11(c). We were unable to sustain this solution branch further subcritically by lowering Ra. Further branch tracking is able to follow the '1sl' branch to higher Ra and Ta, but is unable to retain subcritical localised states at such values. This would suggest that subcritical convectons only exist at moderate Taylor numbers ($\mathrm{Ta} \sim \mathcal{O}(10^2)$). When we have reached the lowest Ra or highest Ta at which our single roll state exists, the solution decays to the conducting state, before the oscillatory pattern state onsets since $\mathrm{Ra} > \mathrm{Ra}_0$.

Following on from our localised states at $\mathrm{Pr} = 0.1$ we perform parametric surveys across various values of Pr, Ra and Ta, shown in Figure 3.10. Overall, we explore $\mathrm{Pr} \in \{0.025, 0.05, 0.1, 0.25, 0.5\}$, Rayleigh numbers ranging from $0 < \mathrm{Ra} < 2 \times 10^4$ and Taylor numbers from $\mathcal{O}(10^3) \lesssim \mathrm{Ta} \lesssim \mathcal{O}(10^7)$, locating a wide range of rotational convectons. The ends of each solution branch have been checked by continuing to vary the parameters explored towards subcriticality, however solutions were lost either to the trivial conducting state (if subcritical) or to a periodic non-localised state (if supercritical). The parametric dependence of such states is discussed in the following subsections. At lower Prandtl numbers, larger Taylor numbers and larger Rayleigh numbers, we often require an increase in spatial resolution from the 96 points used in our initial investigation. The majority of cases use 512 points in the horizontal direction, all for a horizontal domain of size $\Gamma = 6$. The resolution is checked by re-running solutions at increased resolution, confirming that the solution remains identical, and by considering the smoothness of $\partial v/\partial x$ across the horizontal domain. All simulations have a run time of at least $t_r \geq 50 t_\kappa$, where t_κ is the thermal diffusion timescale.

Key Features of Rotational Convectons

The convectons located at $\mathrm{Pr} = 0.1$ are presented in Figure 3.11, where we observe localised states consisting of 1-3 convective rolls in the streamfunction. Below the streamfunction, instead of presenting the depth-integrated zonal velocity, as in Beaume *et al.* (2013), we show the local Rossby number across the horizontal spatial domain. This is calculated using the horizontal derivative of the depth-averaged zonal velocity, normalised with respect to the Prandtl and Taylor numbers (as defined in Equation 3.37). In Beaume *et al.*, rotational convectons were shown to locally reduce angular momentum by up to 70%. In our convectons, localised convective regions reduce the local Rossby number to $Ro = -1$, indicating that the 'effective' rotation in the region is zero and thus the convective region is effectively uninfluenced by rotation. For example, an effective Taylor number can be calculated using $\widetilde{\mathrm{Ta}} = \mathrm{Ta}(1+Ro)^2$, giving $\widetilde{\mathrm{Ta}} = 0$ in the region where localised states exist. Since the angular momentum is a conserved quantity in this system, the local reduction in angular momentum by a convecton is accompanied by an increase in the effective rotation outside of the convecton (indicated by $Ro > 0$ and thus $\widetilde{\mathrm{Ta}} > \mathrm{Ta}$), which further promotes

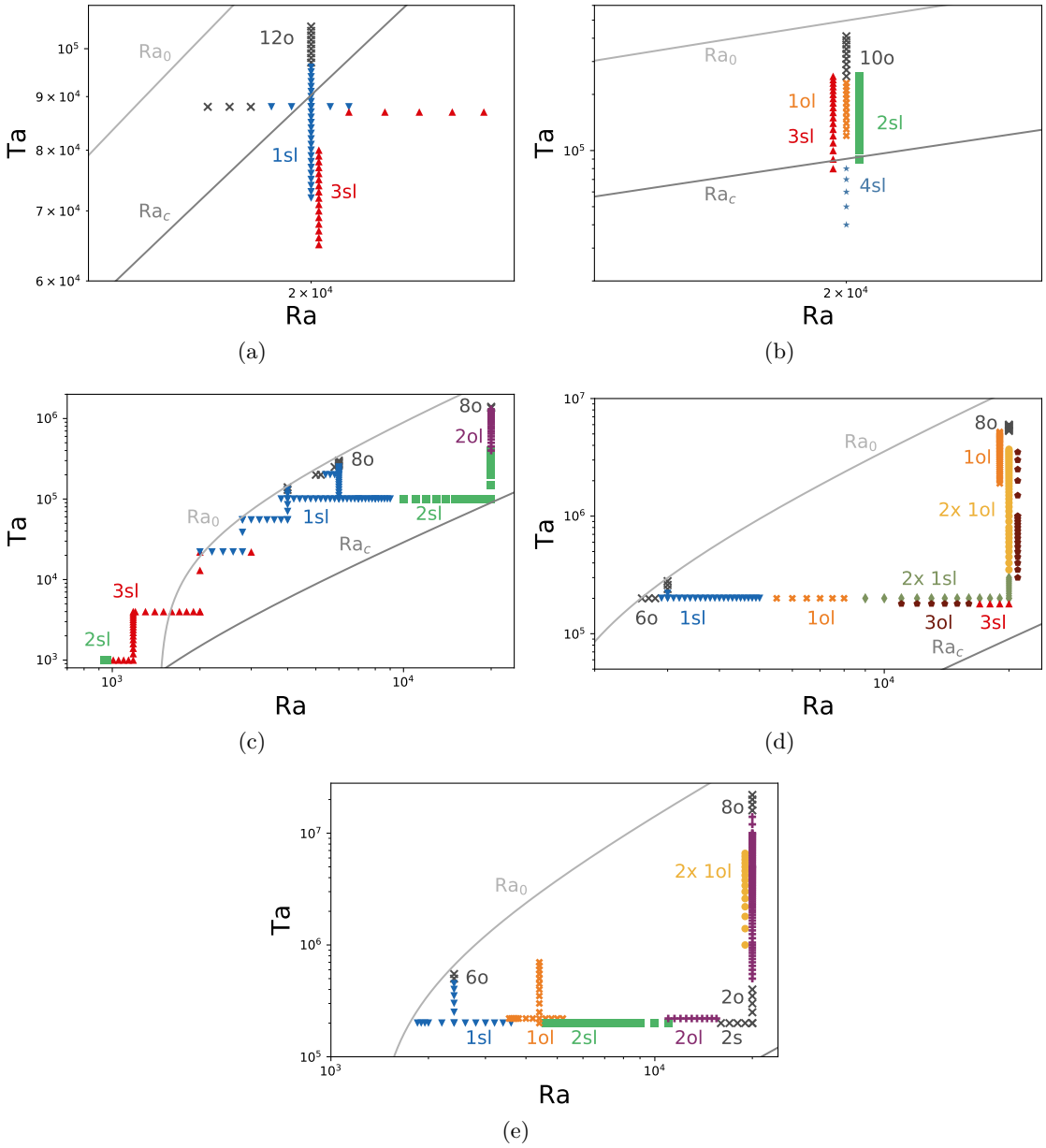


Figure 3.10: Branch tracking of localised states in Ra vs Ta in our MATLAB model at (a) Pr = 0.5, (b) Pr = 0.25, (c) Pr = 0.1, (d) Pr = 0.05 and (e) Pr = 0.025. Colouring and markers are consistent across figures and non-localised solutions are shown in dark grey crosses. The labelling of solution branches is explained in § 3.2.4 and all branches have been fully tracked until either their maximum Ta or minimum Ra. It should be noted that some solution branches have been shifted slightly where they overlap with another for visual purposes.

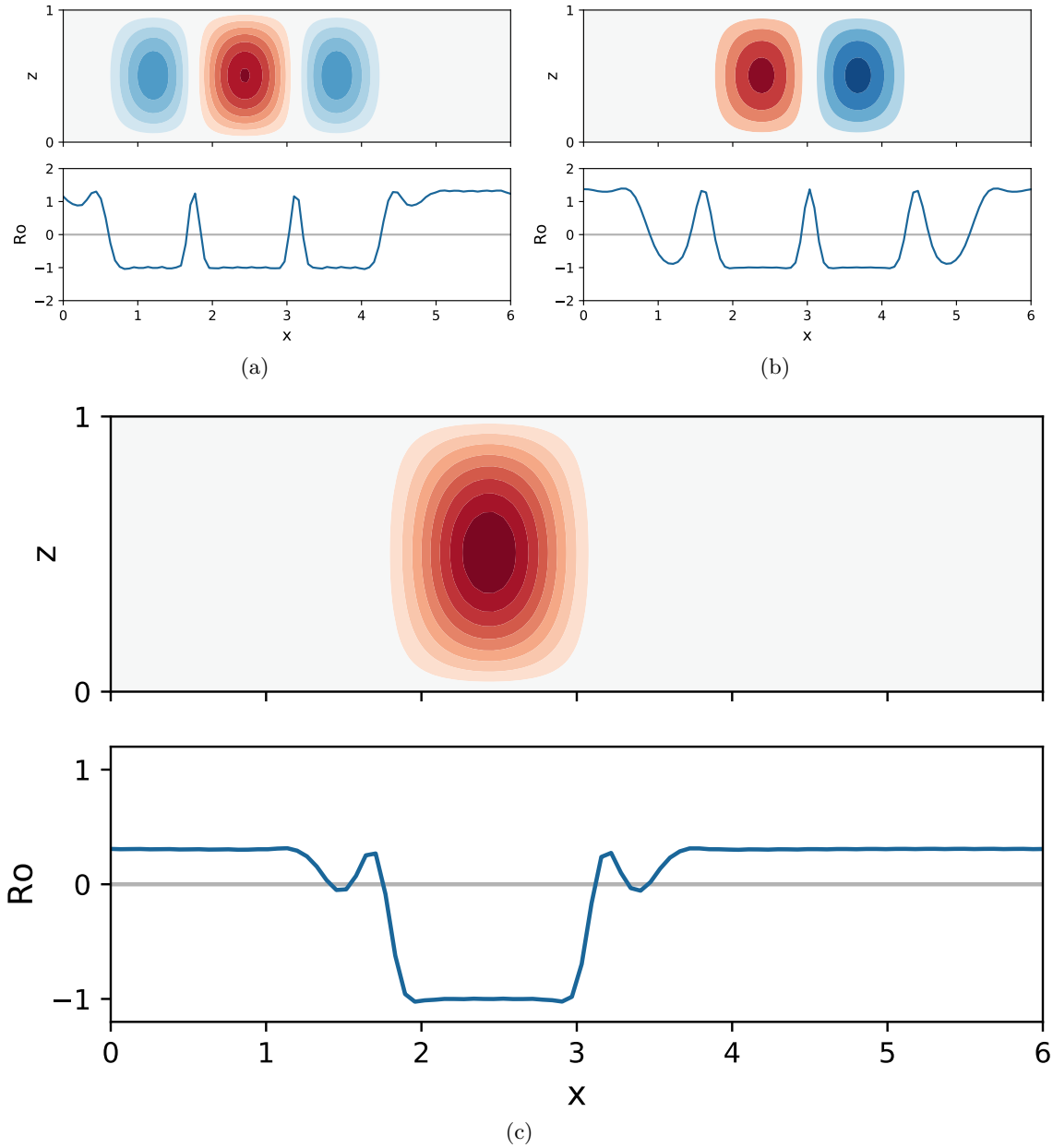


Figure 3.11: Contours of the streamfunction (top) and Rossby number (bottom) at Pr = 0.1 for solutions on (a) the '3sl' branch at Ra = 1200, Ta = 4000, (b) the '2sl' branch at Ra = 960, Ta = 1000, and (c) the '1sl' branch at Ra = 2000, Ta = 22000. It should be noted that convection is not entirely suppressed in all areas outside of the convectons as indicated by the slight decreases in Ro just outside the visible convective cells. However these have much lower amplitudes in the streamfunction and are thus not visible due to the colour scale.

the suppression of convection by rotation in this region. Finally, we have tried artificially removing the Coriolis term from our governing equations in MATLAB, which causes our convectons to collapse.

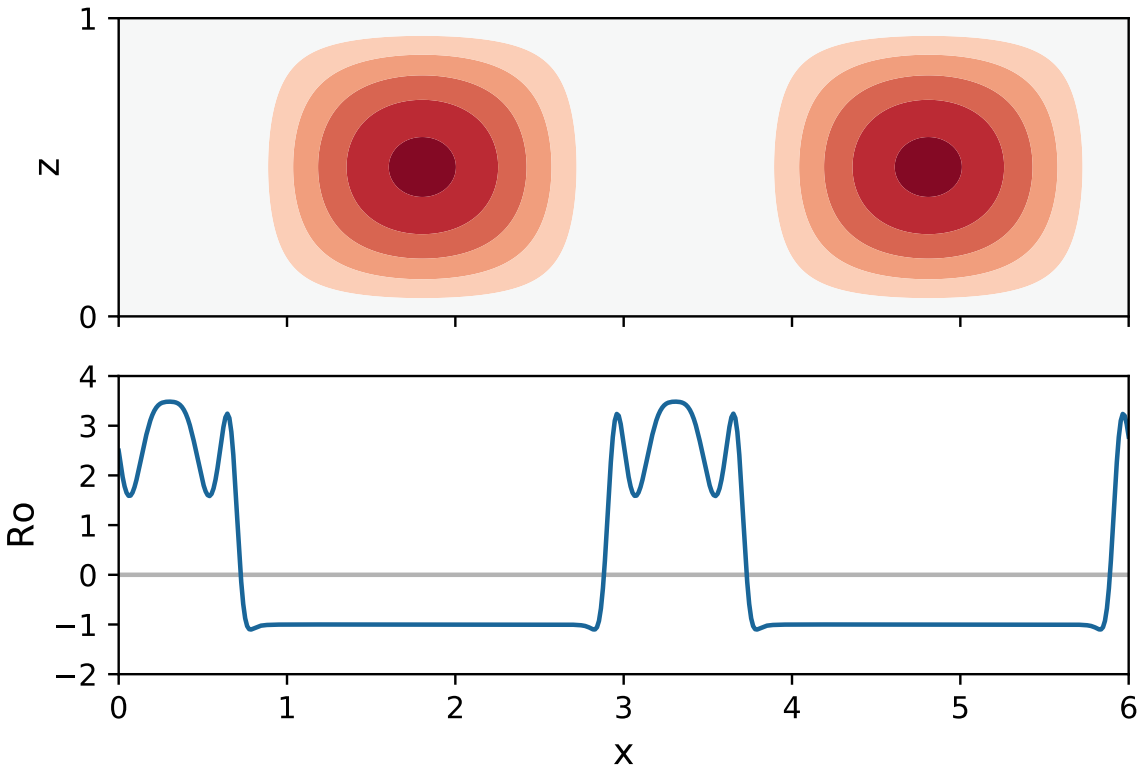


Figure 3.12: Contour plot of the streamfunction and the Rossby number, Ro, for the '2x 1sl' convecton at $\mathrm{Pr} = 0.05$, $\mathrm{Ra} = 1.1 \times 10^4$ and $\mathrm{Ta} = 2 \times 10^5$.

At other Prandtl numbers, we locate stable solutions that include multiple isolated convectons which co-exist in the same computational domain (e.g. the '2x 1sl' solution displayed in Figure 3.12), as well as time-dependent localised states. When convectons co-exist, they appear to act almost independently, with both localised regions associated with $Ro = -1$ and thus a local reduction in the effective rotation where convection occurs. Similarly, outside of the co-existing convectons we observe an increase in the effective rotation which suppresses convection entirely.

In time-dependent solutions we observe oscillations in the Nusselt number. An example of a '1ol' convecton at $\mathrm{Pr} = 0.05$, $\mathrm{Ra} = 2 \times 10^4$ and $\mathrm{Ta} = 5 \times 10^6$ is shown in Figure 3.13. Although we label such solutions as oscillatory, it is important to note that the localised regions do not change sign during oscillations, in contrast to oscillatory convectons explored in magnetoconvection (Buckley & Bushby, 2013). We define oscillatory localised states as those where time-outputted quantities, such as the Nusselt number, are oscillating. Instead, weak convection onsets in the region outside of the localised state, which oscillates and spans the full computational domain, shown in Figures 3.13(b)-(d). In practice, these convectons act like steady convectons with the addition of oscillatory fluctuations which periodically form and decay. This is not necessarily surprising as such solutions are subcritical respective to the stationary onset of convection, Ra_c, but su-

percritical with respect to the oscillatory onset of convection, Ra_0. In this example, the maximum Nusselt number occurs when the convecton exists almost alone. As oscillatory convection onsets in the background, it causes a reduction in the Nusselt number and slightly distorts the convecton. However this does not occur in all cases. It is clear also from the Rossby number across the horizontal domain that the convecton is still characterised by $Ro = -1$, but in the remainder of the region, the increase in Ro associated with suppressed convection becomes less pronounced. Perhaps it is unsurprising that at larger Ta, the oscillating background convection becomes strong enough to destroy the '1ol' convecton, leading to the 8-roll pattern state which is no longer localised. In other time-dependent cases, the planform of the background convection varies. For example, at $\mathrm{Pr} = 0.05$, $\mathrm{Ra} = 7 \times 10^3$, and $\mathrm{Ta} = 2 \times 10^5$, we observe an oscillatory '1ol' solution where a second, weaker single roll convecton oscillates in and out, changing sign as it oscillates in the more traditional sense. As with the previous example, when we increase the Rayleigh number, this oscillating convecton eventually becomes strong enough to fully form, no longer oscillates, and we locate the steady '2x 1sl' case.

Parametric Dependence

In previous work, Beaume *et al.* (2013) present rotational convectons at Prandtl numbers of $\mathrm{Pr} = 0.1$ and $\mathrm{Pr} = 0.6$, Taylor numbers which are $\mathcal{O}(10) \leq \mathrm{Ta} \leq \mathcal{O}(10^4)$ and Rayleigh numbers ranging from $\mathcal{O}(10^2) \leq \mathrm{Ra} \leq \mathcal{O}(10^3)$, exploring subcriticality and moderate supercriticality. In this work, we perform a wider parametric survey locating convectons at other Prandtl, Taylor and Rayleigh numbers. Specifically, we have explored lower Prandtl numbers, more relevant to the liquid metals found in planetary cores, and higher Taylor numbers, more relevant to the rapid rotation observed in planetary systems. Furthermore, we have studied localised states at higher Rayleigh numbers, which despite being supercritical still pose some relevance to the Earth since it is likely in the supercritical regime. Expanding on previous work, we now explore Prandtl numbers in the range 0.025-0.5, Taylor numbers as high as $\mathcal{O}(10^7)$ and Rayleigh numbers as high as $\mathcal{O}(10^4)$. Meanwhile in the Earth, these parameters are estimated to be $0.05 \lesssim \mathrm{Pr} \lesssim 0.2$, $\mathrm{Ta} \sim \mathcal{O}(10^{30})$, and $\mathrm{Ra} \sim \mathcal{O}(10^{22})$ which is highly supercritical (Olson, 2015).

Whilst we have explored wide parameter regimes, discovering many different forms of localised convection, the sensitivity of such solutions to changes in the parameters makes it difficult to draw clear conclusions on their parametric dependence. For example, we have not been able to locate a single state which exists at every Prandtl number studied. However, we can comment on general trends in the existence and appearance of convectons as we vary the three key dimensionless parameters.

Noticeably, in Figure 3.10 it is clear that we have only been able to locate subcritical convectons (for $\mathrm{Ra} < \mathrm{Ra}_0$) at $\mathrm{Pr} = 0.1$, when branch-tracking from our initial AUTO

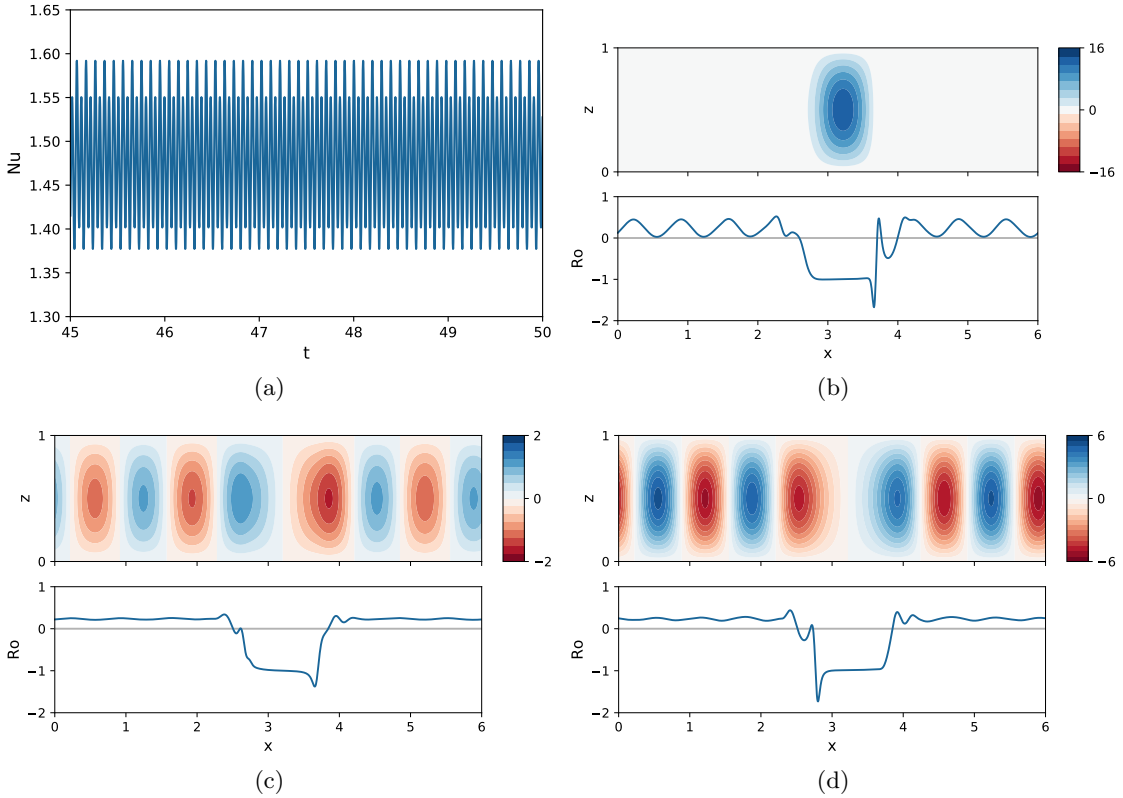


Figure 3.13: (a): Time series of the Nusselt number, Nu, for the '1ol' convecton at Pr = 0.05, Ra = 2×10^4 and Ta = 5×10^6. (b)-(d): The streamfunction and Rossby number taken from snapshots at (b): $Nu = Nu_{max}$, when the convecton is most localised, (c): $Nu = \overline{Nu}$, the midpoint of an oscillation and (d) $Nu = Nu_{min}$. In (c)-(d) the convecton's streamfunction is subtracted from the overall streamfunction to show the oscillatory nature of the background convection. At all times throughout oscillation, the convecton is much stronger than the oscillatory convection outside of the localised region.

solution. At Pr = 0.1 in Figure 3.10(c), as we increase the Rayleigh and Taylor numbers, the width of the subcritical branch at which we are able to locate convectons decreases. The initial '2sl' solution obtained from AUTO at Ta = 1000 can be maintained as low as Ra $\approx 0.56\text{Ra}_c \approx 0.63\text{Ra}_0$. In contrast, at Ta = 2.2×10^4, the '1sl' solution can only be tracked subcritically as far as Ra $\approx 0.97\text{Ra}_c \approx 1.1\text{Ra}_0$, with no subcritical convectons located at all for Ta $> 10^5$. In Beaume *et al.*, at Pr = 0.6, subcritical convectons are only located at moderate Taylor numbers, of order $\mathcal{O}(10^2)$-$\mathcal{O}(10^3)$, because at moderate Tayor numbers, Ra_0 and Ra_c are closer together. We are then no longer able to locate subcritical convections when Ta $> 6.4 \times 10^3$. Comparably, for Pr > 0.1 (Figures 3.10(a)-(b)) we are also unable to obtain subcritical convectons at much higher Taylor numbers because as the Taylor number increases, the distance in Ra between Ra_0 and Ra_c widens.

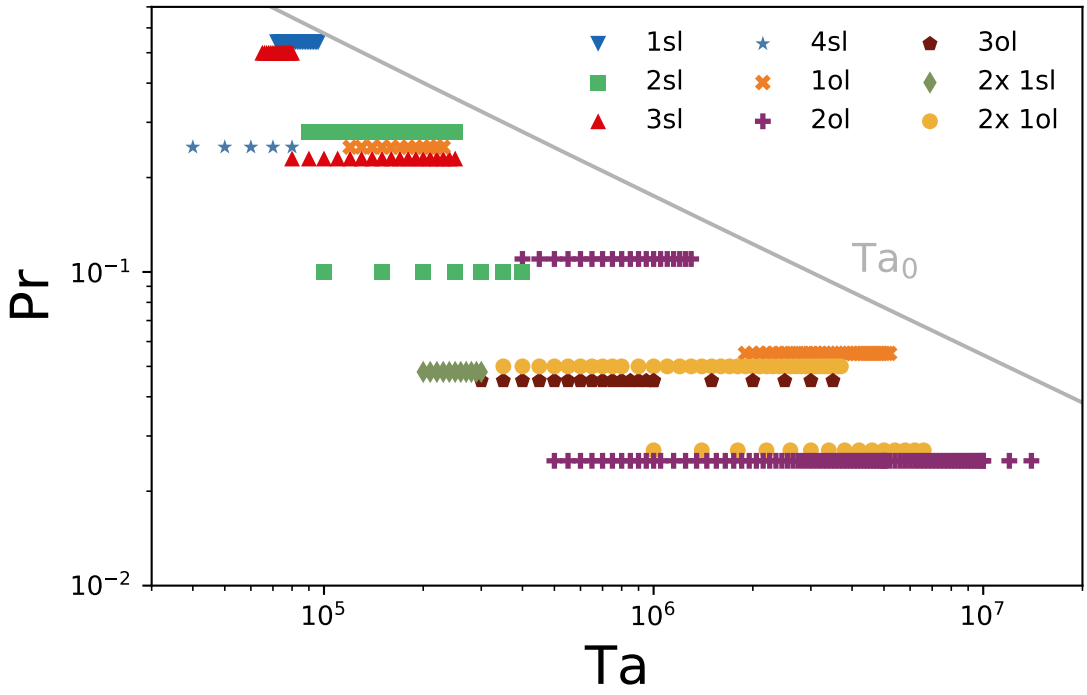
At lower Prandtl numbers and higher Rayleigh numbers, we observe solutions which exhibit multiple isolated convectons, e.g. the '2x 1ol' and '2x 1sl' states in Figures 3.10(d)-

(e). These states seem to occur at more extreme parameters (i.e. at higher Ra or Ta), presumably due to insufficiently strong shear to eliminate convection everywhere except for in one localised region. Insufficiently strong shear tends to lead to cases of this kind, or cases which we refer to as oscillatory.

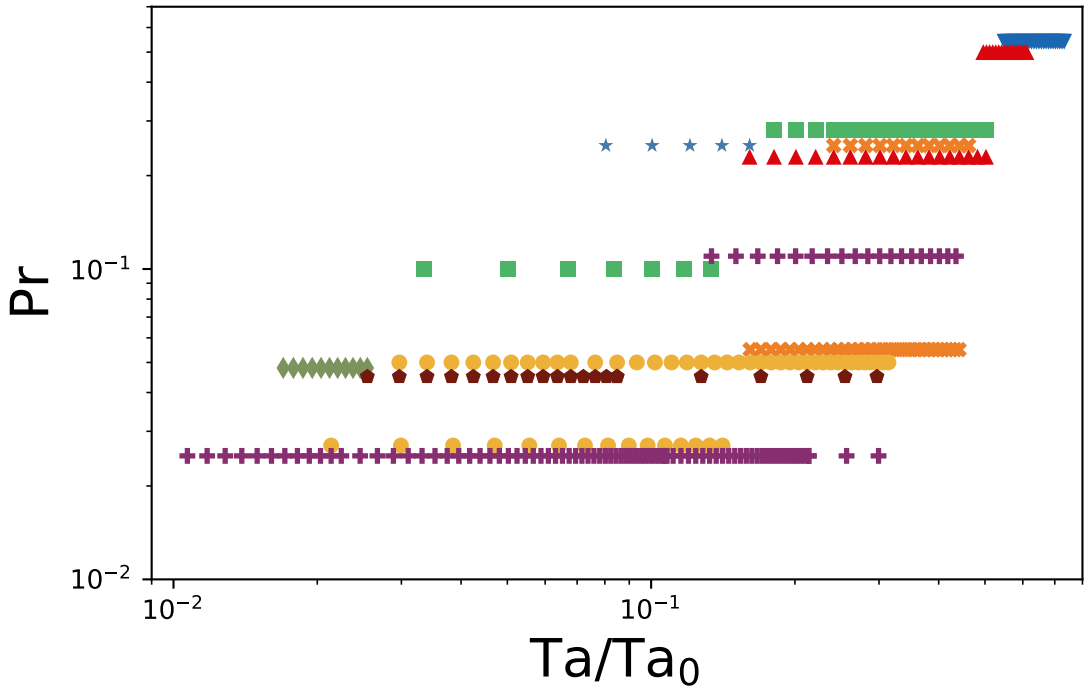
At $\mathrm{Ra} = 2 \times 10^4$, we investigate the criticality of our convectons as a function of the Prandtl number, shown in Figure 3.14. Since Ra is fixed, we calculate a corresponding critical Taylor number, for the onset of overstable convection, Ta_0, where $\mathrm{Ra} = \mathrm{Ra}_0(\mathrm{Pr}, \mathrm{Ta}_0)$. Subcritical solutions therefore possess $\mathrm{Ta} > \mathrm{Ta}_0$. Branch tracking in the Taylor number can then be scaled with respect to Ta_0 in order to compare the criticality across different Prandtl numbers. We observe that at lower Prandtl numbers, localised states are located at higher Taylor numbers. However, with the associated increase in critical Taylor number, these low Pr and high Ta convectons exist more supercritically, leaving them further from convective onset.

At fixed Pr and Ta, as we increase the Rayleigh number we observe an increase in the convective heat transport, via the Nusselt number, and the convecton length, L_{conv}, shown in Figure 3.15. At higher Rayleigh numbers, becoming more supercritical, and with more convective rolls in the streamfunction, convectons are able to transport heat more efficiently. Furthermore, the lack of discontinuity in Nu when changing from a steady state to an oscillatory state implies that oscillatory states do not necessarily transfer heat more efficiently. The horizontal length of a convecton (normalised with respect to the size of the computational domain and number of convective rolls) increases with Ra and is also larger in convectons that possess more rolls in the streamfunction. For comparison, within the convecton we previously showed that $\widetilde{\mathrm{Ta}} = 0$. The width of a single convective roll based on the critical wavelength for the linear onset of convection in the absence of rotation, gives $L_c/\Gamma = \sqrt{2}/\Gamma \approx 0.236$. The dependence of the convecton length on Ra does appear to be more complicated when we change from a steady branch to an oscillatory branch, likely due to the oscillatory background convection distorting the original convecton. Additionally, our method of measuring the convecton length is more difficult to assess within oscillatory cases due to the distortion of the edges of the convecton by the oscillatory convection. To some extent, the computational domain limits the number of convective rolls attainable in our convectons. For example, if a '1sl' state has a convecton length of $L_{conv} \approx 0.3$ then we are unlikely to fit a 4 roll convecton into the computational domain without a decrease in the convecton length.

Similarly, if we keep the Prandtl number and Rayleigh number fixed, we can investigate the effects of increasing Ta on the Nusselt number and convecton length, shown in Figure 3.16. The critical wavelength for the linear onset of convection scales like $\mathrm{Ta}^{-1/6}$, here we observe a more rapid decay in the convecton length with Ta. As we increase Ta, we gradually reduce the number of rolls in our convectons and also decrease in Nu and

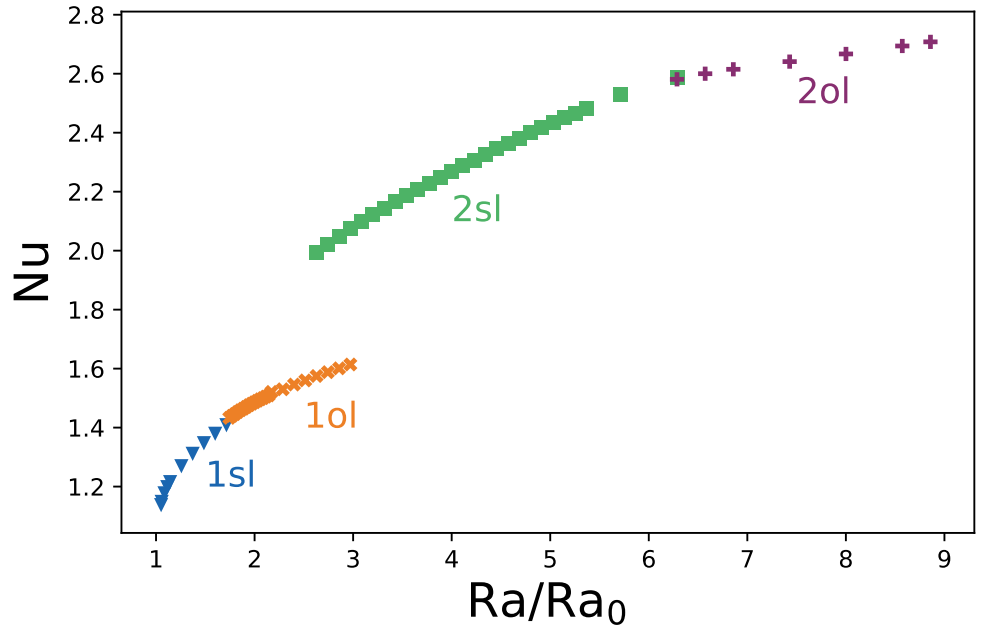


(a)

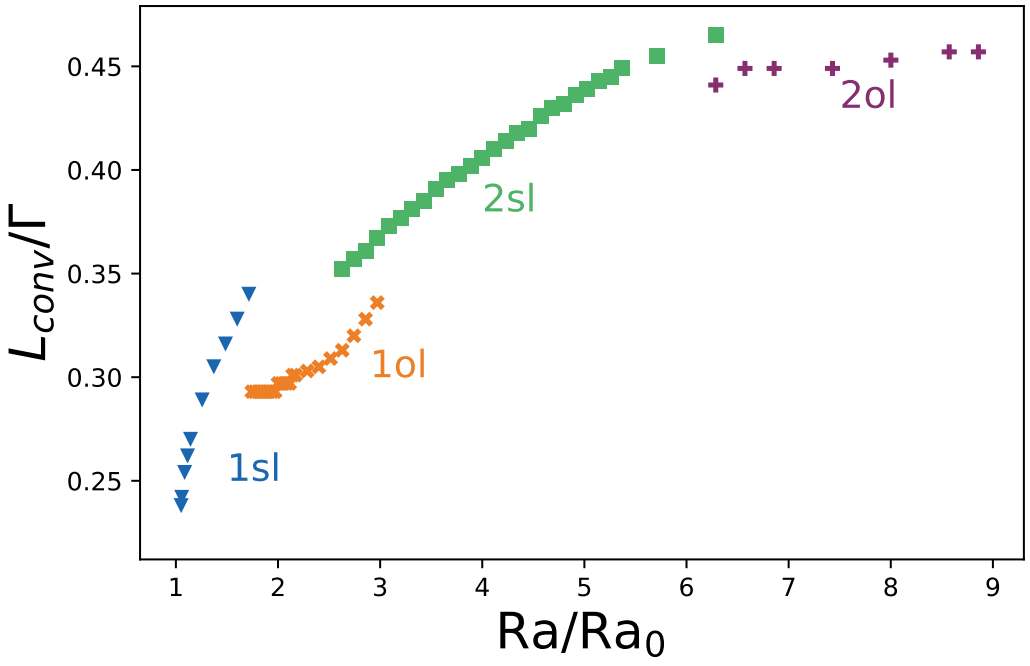


(b)

Figure 3.14: Pr versus (a) the Taylor number, Ta, and (b) the Taylor number scaled with respect to the critical Taylor number for the onset of overstable convection, $\mathrm{Ta}/\mathrm{Ta}_0$, for localised states only. The Rayleigh number is fixed at $\mathrm{Ra} = 2 \times 10^4$. Ta_0 is the critical Taylor number for the onset of overstable convection, i.e. where $\mathrm{Ra} = \mathrm{Ra}_0(\mathrm{Pr}, \mathrm{Ta}_0)$. Subcritical states therefore have $\mathrm{Ta} > \mathrm{Ta}_0$ or $\mathrm{Ta}/\mathrm{Ta}_0 > 1$. Colours of solution branches are consistent with convectons presented in Figure 3.10.

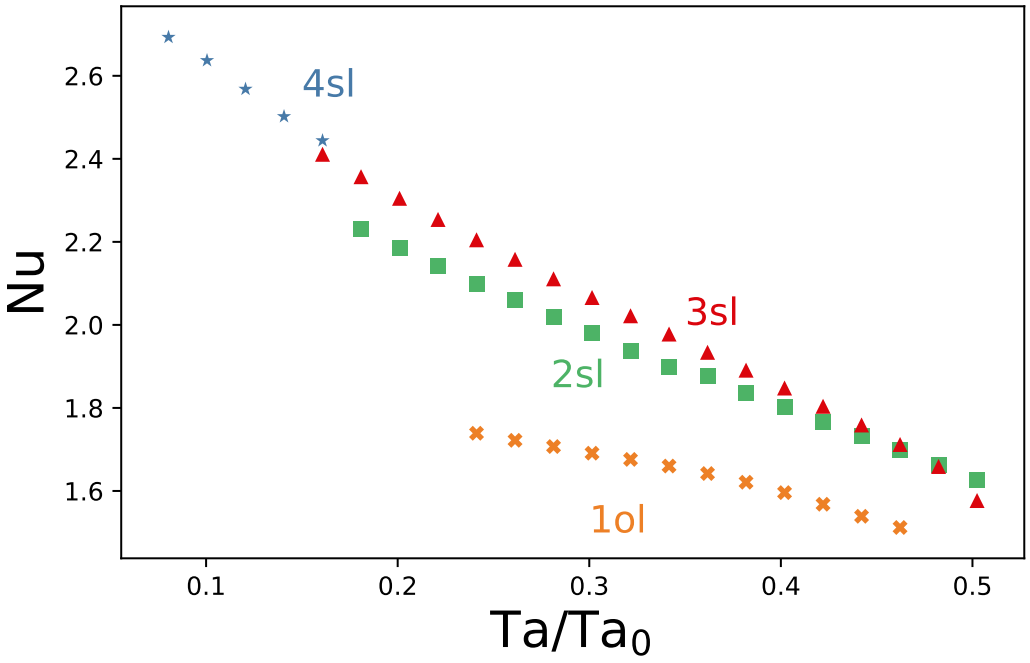


(a)

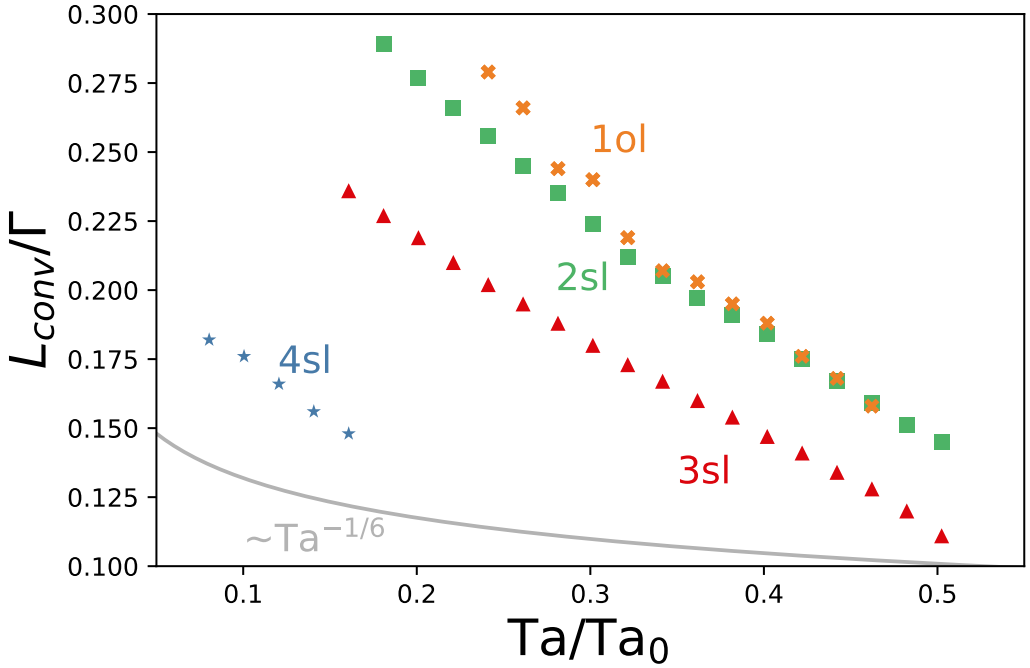


(b)

Figure 3.15: Bifurcation structure of (a) the Nusselt number, Nu, and (b) the convecton width, L_{conv}, in proportion to the size of the computational domain, Γ, versus $\mathrm{Ra}/\mathrm{Ra}_0$ at $\mathrm{Pr} = 0.025$, $\mathrm{Ta} = 2 \times 10^5$. In cases where Nu oscillates, the Nusselt number is time-averaged, whilst L_{conv} is calculated by time-averaging multiple snapshots of the coefficients before calculating the convecton length. $\mathrm{Ra}_0 = 1749.8$ is the onset for overstable convection at this Pr and Ta.



(a)



(b)

Figure 3.16: Bifurcation structure of (a) the Nusselt number, Nu, and (b) the convecton width, L_{conv}, in proportion to the size of the computational domain, Γ, versus $\mathrm{Ta}/\mathrm{Ta}_0$ at $\mathrm{Pr} = 0.25$, $\mathrm{Ra} = 2 \times 10^4$. In cases where Nu oscillates, the Nusselt number is time-averaged, whilst L_{conv} is calculated by time-averaging multiple snapshots of the coefficients before calculating the convecton length. $Ta_0 \approx 4.98 \times 10^5$ is the onset for overstable convection at this Pr and Ra.

L_{conv}. This is equivalent to the behaviour observed with decreasing Ra. Basically, as we become more supercritical (either by increasing Ra at fixed Ta, or by decreasing Ta at fixed Ra), the Nusselt number and convecton length increases. Conversely, as we approach onset, convectons get thinner and become less efficient at transporting heat.

Varying The Aspect Ratio

At lower Prandtl numbers (Pr = 0.05, Pr = 0.025) and higher Rayleigh numbers (Ra > 10^4), we previously discussed solutions consisting of multiple isolated convectons, which co-exist in the same computational domain. Furthermore, it was mentioned that the computational domain restricts the size of convectons and how many convective rolls they possess, depending on L_{conv}. Since the geometry of our problem involves a periodic box in the horizontal direction, we can artificially vary the size of the computational domain. States consisting of multiple isolated convectons then act in the same way as if we had only a single convecton. For example, the '2x 1sl' localised states acts similarly to the simplified '1sl' case. The only difference is that, at such parameters, the system chooses to fit two convectons into the computational domain of size $\Gamma = 6$. To produce states that possess only a single convecton at identical parameters, we can therefore artificially adapt the computational domain to one which is only large enough to fit a single convecton within it. For example, taking the '2x 1sl' state presented in Figure 3.12 with a domain size of $\Gamma = 6$, we can artificially cut the solution and box in half to $\Gamma = 3$ and we successfully obtain a '1sl' convecton at the same parameters, which involves a single stable convecton, shown in Figure 3.17. Similarly, creating a second copy of the '2x 1sl' state and doubling the size of the computational domain to $\Gamma = 12$ results in a '4x 1sl' state, consisting of four co-existing single roll convectons. In short, this is because at these parameters, the computational domain is large enough to fit multiple convectons within it. Whilst we struggle to achieve the '1sl' and '1ol' convectons at low Pr and high Ra with a computational domain of size $\Gamma = 6$, the '2x 1sl' and '2x 1ol' can be treated equivalently. Furthermore, we are able to track the '1sl' and '1ol' convectons at such low Prandtl numbers and high Rayleigh numbers in the $\Gamma = 3$ domain, finding little difference in the criticality to branch tracking in a larger domain. It is worth noting that at Pr = 0.05, Ra = 2×10^5, with $\Gamma = 6$ we obtain both '2x 1ol' and '1ol' convectons which differ in convecton length.

Beginning from the '1sl' state, artificially achieved at $\Gamma = 3$, we can gradually increase the size of the computational domain back towards $\Gamma = 6$. This does involve stretching the previous solution each time the domain size is increased, but to begin with we retain the steady single roll convecton up until $\Gamma = 4$. At $\Gamma > 4$, the convecton nucleates an additional convective roll either side, becoming a localised 3 roll steady state, labelled '3sl'. At $\Gamma = 5$, the '3sl' convecton began to generate oscillatory background convection giving a '3ol' state, which remained at $\Gamma = 6$. The 3 roll convectons presented in Fig-

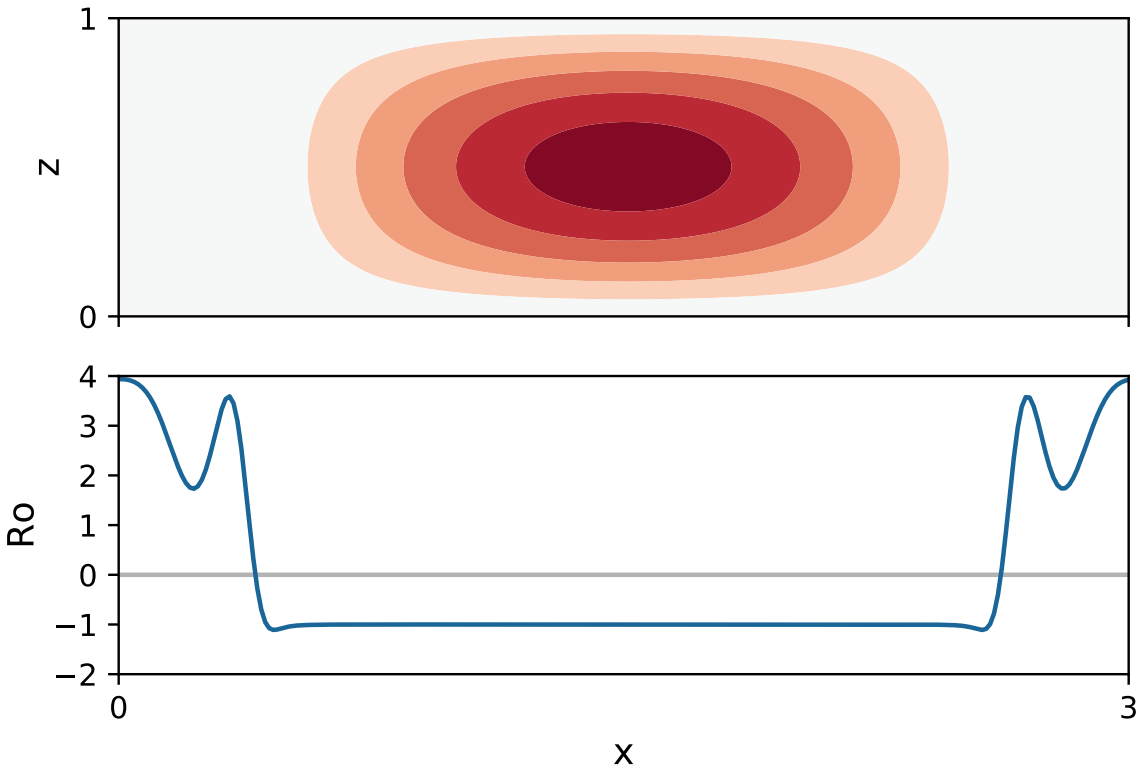


Figure 3.17: Contour plot of the streamfunction and the Rossby number, Ro, for the '1sl' convecton in a reduced computational domain of size $\Gamma = 3$ at $\mathrm{Pr} = 0.05$, $\mathrm{Ra} = 1.1 \times 10^4$ and $\mathrm{Ta} = 2 \times 10^5$. This convecton was located by artificially halving the solution presented in Figure 3.12.

ure 3.10(d) had not previously been discovered and tracked at $\mathrm{Pr} = 0.05$ before varying the computational domain size. This tactic therefore enabled us to locate convectons that we had not previously discovered.

3.5 Conclusions

We have studied two-dimensional rotating convection in a planar geometry, successfully obtaining localised states, known as convectons. Localised states have previously been studied in both two-dimensional and three-dimensional magnetoconvection (e.g. Blanchflower, 1999; Blanchflower & Weiss, 2002; Buckley & Bushby, 2013), however previous work on convectons in a rotating system, without a magnetic field, was only able to locate them at moderate rotation and could not establish their stability (Beaume *et al.*, 2013).

Here we conclude that convectons in rotating planar convection are stable and exist at more extreme parameters than previously studied. We present convectons at lower Prandtl numbers ($0.025 \leq \mathrm{Pr} \leq 0.5$), higher Taylor numbers ($\mathcal{O}(10) \leq \mathrm{Ta} \leq \mathcal{O}(10^7)$), and higher Rayleigh numbers ($\mathcal{O}(10^2) \leq \mathrm{Ra} \leq \mathcal{O}(10^4)$) than previously discovered. However, we only obtain subcritical convectons at moderate Taylor numbers, close to those in Beaume *et al.*.

At moderate Taylor numbers, Ra_c and Ra_0 are closer together making it easier to obtain subcritical convectons that are subcritical to both onsets. The only subcritical convectons, relative to both convective onsets, that we obtain are at $\mathrm{Pr} = 0.1$ and $\mathcal{O}(10^2) \leq \mathrm{Ta} \leq \mathcal{O}(10^3)$, with Rayleigh numbers up to 37% below the critical Rayleigh number for the onset of overstable convection. At all Prandtl numbers we obtain convectons that are subcritical relative to the stationary onset of convection, however it was only at $\mathrm{Pr} = 0.1$ and moderate Ta where they were also subcritical relative to the oscillatory onset of convection. Further work may explore the regime where Ra_c and Ra_0 are close together at other Pr, however we were primarily interested in localised states at higher Taylor numbers, relevant to planetary cores. We also expect that it would result in states which are much the same as those in Beaume *et al.*. Furthermore, at lower Pr, convectons are located more supercritically, making subcritical convectons less likely at lower Prandtl numbers, more relevant to planetary cores.

In magnetoconvection, convectons are associated with magnetic flux expulsion, leading to locally reduced magnetic field in the region where the convecton exists. Since the magnetic flux is a conserved quantity, the field must build up elsewhere, leading to an amplified magnetic field outside of the convecton which suppresses convection entirely. The importance of a conserved quantity on localised states is discussed in Matthews & Cox (2000). In rotating convection, the angular momentum acts as the relevant conserved quantity, since in our system the integral of the zonal velocity is conserved due to using horizontal stress-free boundaries (Cox & Matthews, 2001). Whilst the systems for magnetoconvection and rotating convection display many similar behaviours, they are not identical systems. Clearly the Lorentz force and Coriolis force influence the system in different ways, with the magnetic flux and zonal velocity the important quantities in the formation of convectons. Beaume *et al.* observed that convectons existed within a self-generated shear layer, where rotation is locally reduced by up to 70%. The positive shear then builds up elsewhere leading to the suppression of convection outside of the convecton. Whilst Beaume *et al.* explore this through the depth-averaged zonal velocity, we calculate a local Rossby number as a function of the horizontal position, which shows the 'effective' rotation across the computational domain. In all cases, convectons are associated with a local Rossby number of $Ro = -1$, whilst the remainder of the domain typically possesses $Ro > 0$. This indicates that a region of negative shear mitigates the effect of rotation on convection, allowing a localised region to occur. Meanwhile, positive shear amplifies the effect of rotation elsewhere, suppressing convection. This local Rossby number can be used to calculate an effective Taylor number, $\widetilde{\mathrm{Ta}} = \mathrm{Ta}(1 + Ro)^2$, showing that within the convecton, the effective rotation is truly zero. Convectons therefore exist in a localised region where they are unaffected by rotation due to negative shear, whilst the angular momentum builds up in the remainder of the region due to positive shear, suppressing

convection.

In magnetoconvection, time-dependent convectons have also been studied (Buckley & Bushby, 2013). However, Beaume *et al.*'s system was not able to study such states. Buckley & Bushby discovered oscillatory convectons where the localised region changed sign as it oscillated over time. Unfortunately, we were unsuccessful in locating a rotational equivalent in our system. However, we were able to study time-dependent convectons of a different nature. We have also referred to these as oscillatory convectons throughout this chapter, but in practice the localised regions act similarly to steady convectons. The oscillatory nature comes from the regions where convection was previously fully suppressed by the angular momentum. Instead of observing a steady convecton, we see oscillatory background convection which changes sign as it oscillates. Essentially, since these states are subcritical relative to stationary onset, but supercritical relative to oscillatory onset, they acts as a superposition of a subcritical stationary convecton and supercritical oscillatory convection. The background convection is typically weaker than the convecton, but is able to distort and affect the convecton as it oscillates. As in steady convectons, the localised region is still identified as possessing a local Rossby number of $Ro = -1$ and so is still effectively irrotational. However, the edges of the convecton are affected by the oscillatory background convection surrounding it. Considering that rotation appears to play an equivalent role to the magnetic field in the generation of convectons, we speculate that oscillatory convectons may exist in this system which change sign as they oscillate.

We also observe convectons consisting of multiple isolated convective regions in the same computational domain. Clearly the size of the computational domain affects how many convective rolls a convecton can possess, depending on the convecton length, but in some cases the system chooses to fit two thinner convectons within the domain rather than a single convecton. Since our system consists of a horizontally periodic box, such states act almost identically to the single convecton states previously discussed. However, artificially varying the computational domain size did allow us to study states we previously had not, such as single roll convectons at lower Pr and higher Ta.

The major limitation of this work is that we are restricted to only two spatial dimensions and two-dimensional convective rolls are likely to be unstable to three-dimensional perturbations. Following on from studies of two-dimensional convectons in magnetoconvection, Blanchflower & Weiss (2002) produce stable, time-dependent, three-dimensional convectons in a vertically truncated model. Such three-dimensional convectons typically appear as either cylinders or cigar shapes. Whilst stable convectons appear commonly in 2D magnetoconvection, only time-dependent cases were located in 3D at relatively low Rayleigh number. Convectons proved more difficult to locate in 3D since the expulsion of magnetic flux by the convecton is less able to separate the domain into a region with locally reduced field (where the convecton exists) and a region with almost uniform field

(where convection is suppressed) since field lines can merely move around the convecton. In our system, the localisation occurs as a consequence of zonal jets directed along the axis of the convective rolls, producing shearing behaviour that locally reduces the effects of rotation. However, in 3D rotating convection where the rotational and gravitational axes are aligned, no breaking of horizontal symmetry occurs. We therefore do not expect to observe the formation of uni-directional flows. System-size flows do occur in the form of large-scale vortices (LSVs) at large Taylor numbers and moderately supercritical Rayleigh numbers (e.g. Julien *et al.*, 2012; Guervilly *et al.*, 2014; Favier *et al.*, 2014; Guervilly *et al.*, 2017). So far, LSVs have only been studied for Prandtl numbers of unity or greater and have been shown to exhibit hysteretic behaviours (Favier *et al.*, 2019). However, it remains to be answered whether these LSVs can occur at low Prandtl numbers, potentially allowing subcritical localised convection to exist in three-dimensions.

Chapter 4

Subcritical Dynamos in Rapidly Rotating Plane Layer Convection

This chapter contains a modified version of the work published in PRF as Cooper *et al.* (2020). The key difference is that in the publication we also discuss preliminary results at low Ekman number which are now deferred until Chapter 5 and discussed in more detail. Some further analysis is included in this chapter, in particular surrounding Figure 4.5(c) and Figure 4.6.

4.1 Introduction

Understanding the physical mechanisms that generate magnetic fields in electrically-conducting fluids is one of the fundamental challenges in magnetohydrodynamics. In most astrophysical bodies, magnetic fields are thought to be generated by a hydromagnetic dynamo, which converts the kinetic energy of fluid motions into magnetic energy, leading to the amplification of the magnetic field. In the case of the geodynamo for example, convectively-driven motions in the liquid core are responsible for the generation of the Earth's magnetic field. Whilst numerical simulations have successfully replicated many of the features of the geodynamo (e.g. Glatzmaier & Roberts, 1995; Christensen *et al.*, 2010; Christensen & Wicht, 2015), it is currently not possible to carry out simulations at Earth-like parameter values. One particularly problematic parameter for numerical simulations is the Ekman number, Ek, which estimates the strength of the viscous forces with respect to the strength of the Coriolis force. With considerable computational effort, modern spherical geodynamo calculations can reach Ekman numbers as small as $\mathrm{Ek} = 10^{-7}$ (Schaeffer *et al.*, 2017; Aubert, 2019), but this is still approximately 8 orders of magnitude larger than the estimated Ekman number for the Earth's liquid core, so all such simulations overestimate the relative importance of viscous forces compared to the Coriolis force. Whilst

it may be possible to use scaling laws (e.g. Christensen & Aubert, 2006) to bridge the gap in parameter space between numerical dynamos and planetary dynamos, this remains controversial (Stelzer & Jackson, 2013; King & Buffett, 2013; Oruba & Dormy, 2014), thus further exploration of the low Ekman number regime is necessary. One productive approach to this problem is to consider the more idealised case of convectively-driven dynamos in simpler geometries, for example a plane layer. Although there are still limitations on how small the Ekman number can be made, these simpler problems are more amenable to a systematic study of the computationally accessible regions of parameter space. Other simplified geometries include studying convection and dynamo action within a cylinder (e.g. Nore *et al.*, 2015) or in an annular model, for example with a series of cylindrical columns (e.g. Calkins *et al.*, 2013).

Many previous studies have focused upon layers of electrically-conducting fluid in uniformly rotating Cartesian domains, in which convection is driven by heating the layer from below. If the layer is rotating about the vertical axis (with the angular velocity vector anti-parallel to the constant gravitational acceleration) then it is well known that rotation tends to inhibit convection; furthermore, near convective onset, the horizontal lengthscale of the convective motions decreases with increasing rotation rate, leading to tall, narrow convective cells Chandrasekhar (1953). For a rapidly-rotating domain, Childress & Soward (Childress & Soward, 1972; Soward, 1974) were the first to demonstrate that these near-onset convective motions are capable of sustaining a dynamo. One of the key results of their study was the identification of several possible force balances in the governing equations, depending upon the strength of the generated magnetic field. These balances suggest the existence of multiple dynamo branches. If the induced magnetic field is weak (Soward, 1974), it plays a negligible dynamical role and the dominant force balance is geostrophic. In the (so-called) "intermediate" and "strong" field limits (e.g. Fautrelle & Childress, 1982), the Lorentz force plays an increasingly important role in the dynamics of the dynamo, significantly perturbing the driving flow.

Different aspects of the Childress-Soward dynamo have been explored by many authors (e.g. St. Pierre, 1993; Jones & Roberts, 2000; Rotvig & Jones, 2002; Stellmach & Hansen, 2004; Favier & Proctor, 2013; Calkins *et al.*, 2015). Arguably the most relevant study to that of the present work is that of Stellmach & Hansen (2004), who carried out a range of convective dynamo simulations at low Ek (down to $\mathrm{Ek} = 5 \times 10^{-7}$). The level of convective driving in such systems is often quantified in terms of the Rayleigh number, Ra, which is a dimensionless measure of buoyancy effects relative to diffusion. Stellmach & Hansen focused primarily upon a weakly supercritical regime in which the Rayleigh number was only 15-20% above its critical value at the non-magnetic convective onset under the influence of rotation (denoted Ra_c). They found efficient dynamos, characterised by an initial phase of exponential growth in the magnetic energy, followed by a brief period

of super-exponential growth as the magnetic field becomes strong enough to influence the flow (also accompanied by a similar growth in the kinetic energy). The dynamo then saturates, reaching a statistically steady state in which the magnetic energy typically exceeds the kinetic energy of the system. We can gain some insight into the mechanisms responsible for this phase of super-exponential growth by considering related magnetoconvection studies (Chandrasekhar, 1961; Eltayeb, 1972). Like rotation, imposed magnetic fields tend to have a stabilising effect upon convection in electrically-conducting fluids, raising the corresponding critical Rayleigh number for the onset of convection. However, when magnetic fields are applied across rapidly-rotating domains, the Lorentz force can relax some of the rotational constraints, thus facilitating convection rather than impeding it (of course, this depends crucially upon the field strength and direction; the Lorentz force and the Coriolis force must be of comparable magnitudes at a certain lengthscale). In these dynamo calculations, phases of super-exponential growth are indicative of a similar effect, with the dynamo-generated magnetic field becoming locally strong enough to break some of the rotational constraints. The field that is produced significantly perturbs the flow, allowing the dynamo to reach a balanced state in which the magnetic field plays an important dynamical role in the nonlinear dynamo. Low Ekman number dynamos that are able to sustain sufficiently strong magnetic fields that play an important dynamical role are relevant for astrophysical systems such as the geodynamo (Gillet *et al.*, 2010), but remain largely unexplored due to the difficulty in performing numerical simulations in this regime. The case described in Stellmach & Hansen is an important example of such a dynamo, which we explore further in the next two chapters.

One of the most interesting findings of Stellmach & Hansen (see also the related study of St. Pierre (1993)) was the fact that it is possible to follow dynamo solution branches into the subcritical regime (below convective onset), which is characterised by a Rayleigh number that is less than Ra_c. This branch tracking is achieved by taking a supercritical dynamo solution as an initial condition and then gradually lowering the Rayleigh number. The existence of this subcritical behaviour is a direct consequence of the field having changed the flow geometry. If the magnetic field were to be removed, the system would gradually relax back to a hydrostatic state; to put this another way, these subcritical solutions exhibit bistability with the trivial conducting state. Examples of subcritical dynamo action have also been found in rotating spherical shells Morin & Dormy (2009); Sreenivasan & Jones (2011); Dormy (2016), where nonlinear dynamo solutions can be found below the critical Rayleigh number for the onset of dynamo action, but not below the critical Rayleigh number for the onset of convection. It is worth emphasising that the existence of subcritical dynamos is more than simply a mathematical curiosity: it has been suggested that the comparatively rapid cessation of the Martian dynamo could have been a direct consequence of the Martian dynamo reaching the end of a subcritical

dynamo branch Kuang *et al.* (2008); Hori & Wicht (2013). If the Rayleigh number were to gradually decrease, for example by gradual cooling within the core, then the dynamo could be sustained below onset. However, once it reached the end of the subcritical dynamo branch it would then rapidly decay towards the trivial conducting state.

There has not yet been a systematic study of the parametric dependence of subcritical convectively-driven dynamos in rapidly rotating Cartesian domains. Whilst individual examples of such subcritical dynamos have been presented (St. Pierre, 1993; Stellmach & Hansen, 2004), it is not clear what the optimal parameter regime is for the existence of these solutions. The primary aim of this work is to address this issue. In the next section, we begin by presenting the governing equations and defining the output quantities used for the analysis of the data. Section 4.3 presents the results of our study, beginning with an analysis of near-onset supercritical dynamo action before decreasing the Rayleigh number below the linear onset of convection to explore subcritical dynamos. Finally, we summarise our key findings in Section 4.4.

4.2 Model

4.2.1 Governing Equations and Boundary Conditions

We study dynamo action driven by rotating Boussinesq convection in a three-dimensional planar model. The computational domain has depth d in the vertical direction and width λd in each of the horizontal directions. The gravitational acceleration is $\boldsymbol{g} = -g\hat{\mathbf{z}}$, where $\hat{\mathbf{z}}$ is the unit vector in the z-direction. The layer rotates about the vertical axis at constant rotation rate Ω. A vertical temperature difference ΔT is imposed across the layer such that the fluid is uniformly heated from below. The fluid has constant kinematic viscosity ν, thermal diffusivity κ, magnetic diffusivity η, density ρ, thermal expansion coefficient α and magnetic permeability μ_0. The system of governing equations is solved in dimensionless form. We scale lengths with d, times with d^2/κ (the thermal diffusion timescale), velocities with κ/d, temperature with ΔT and magnetic field with $(\mu_0\rho_0)^{1/2}\kappa/d$. The non-dimensional governing equations are

$$\frac{\partial \boldsymbol{u}}{\partial t} + \boldsymbol{u}\cdot\nabla\boldsymbol{u} + \frac{\mathrm{Pr}}{\mathrm{Ek}}\hat{\mathbf{z}}\times\boldsymbol{u} = -\nabla P + \mathrm{Pr}\nabla^2\boldsymbol{u} + \mathrm{PrRa}\theta\hat{\mathbf{z}} + \boldsymbol{J}\times\boldsymbol{B}, \tag{4.1}$$

$$\nabla\cdot\boldsymbol{u} = 0, \tag{4.2}$$

$$\frac{\partial \theta}{\partial t} + \boldsymbol{u}\cdot\nabla\theta = w + \nabla^2\theta, \tag{4.3}$$

$$\frac{\partial \boldsymbol{B}}{\partial t} + \boldsymbol{u}\cdot\nabla\boldsymbol{B} - \boldsymbol{B}\cdot\nabla\boldsymbol{u} = \frac{\mathrm{Pr}}{\mathrm{Pm}}\nabla^2\boldsymbol{B}, \tag{4.4}$$

$$\nabla\cdot\boldsymbol{B} = 0, \tag{4.5}$$

where $\boldsymbol{u}$ is the velocity, p is the pressure, $\boldsymbol{B}$ is the magnetic field, θ is the temperature fluctuation from the linear background profile, and $\boldsymbol{J} = \nabla \times \boldsymbol{B}$ is the dimensionless current density. The dimensionless parameters that appear in the governing equations are the Prandtl number Pr, magnetic Prandtl number Pm, Ekman number Ek, and Rayleigh number Ra, which are defined as

$$\mathrm{Pr} = \frac{\nu}{\kappa}, \quad \mathrm{Pm} = \frac{\nu}{\eta}, \quad \mathrm{Ek} = \frac{\nu}{2\Omega d^2}, \quad \mathrm{Ra} = \frac{\alpha g \Delta T d^3}{\kappa \nu}. \tag{4.6}$$

In order to avoid the numerical challenges of solving viscous boundary layers in the low Ekman number regime we choose the lower and upper boundaries to be stress-free. Furthermore this allows us to compare our results directly with those of previous studies such as Stellmach & Hansen (2004). The lower and upper boundaries are also impermeable and perfect thermal and electrical conductors, i.e.

$$\theta = u_z = \frac{\partial u_x}{\partial z} = \frac{\partial u_y}{\partial z} = B_z = \frac{\partial B_x}{\partial z} = \frac{\partial B_y}{\partial z} = 0 \quad \text{at} \quad z = \{0, 1\}, \tag{4.7}$$

with periodic boundaries in the x and y directions. Supercritical simulations are initiated by a weak small-scale temperature pertubation to the trivial conducting state in the presence of a weak imposed small-scale horizontal magnetic field with zero net flux. In subcritical simulations, we initialise the system using supercritical solutions, before gradually decreasing the Rayleigh number below the critical value for the onset of convection.

The governing equations are solved using the pseudospectral code described in Cattaneo *et al.* (2003), where more details about the numerical scheme can be found.

4.2.2 Definition of the Output Quantities

The magnetic Reynolds number, Rm, gives an estimate of the ratio of magnetic induction to magnetic diffusion. Rm is based on the layer depth and the root mean square (r.m.s) velocity amplitude. In terms of our dimensionless variables,

$$\mathrm{Rm} = \frac{\mathrm{Pm}}{\mathrm{Pr}} U_*, \tag{4.8}$$

where $U_* = \sqrt{\langle \boldsymbol{u}^2 \rangle_V}$. Throughout this chapter we denote volume averages as $\langle (...) \rangle_V$ where V is the volume of the computational domain, and horizontal averages over x and y as $\overline{(...)}$. The ratio of magnetic to kinetic energy is

$$M = \frac{B_*^2}{U_*^2}, \tag{4.9}$$

with $B_* = \sqrt{\langle \boldsymbol{B}^2 \rangle_V}$.

As previously noted, one of the key balances in this system is the comparison between Coriolis effects and the Lorentz force in order to determine the influence of the magnetic field on the dynamics of the system. In particular we are interested in the ability of the magnetic field to loosen some of the rotational constraints which inhibit convection. Motivated by these considerations, we therefore use the Elsasser number, Λ, which measures the ratio of the Lorentz force to Coriolis forces, as the primary measure of the magnetic field strength. In these dimensionless units,

$$\Lambda = \frac{\mathrm{PmEk}}{\mathrm{Pr}^2} B_*^2. \tag{4.10}$$

Given that these dynamos produce a non-negligible mean magnetic field (in a horizontally-averaged sense), it is also of interest to consider an alternative definition of the Elsasser number that is based upon this mean field,

$$\overline{\Lambda} = \frac{\mathrm{PmEk}}{\mathrm{Pr}^2} \overline{B}_*^2, \tag{4.11}$$

where $\overline{B}_* = \sqrt{\langle \overline{\boldsymbol{B}}^2 \rangle_V}$ is the r.m.s. amplitude of the horizontally-averaged magnetic field. These definitions of the Elsasser number are based on the standard formulation for this quantity, which assumes (in dimensional terms) that d is a possible appropriate lengthscale for the dynamo and that η/d is an appropriate velocity scale (equivalently this assumes that the appropriate timescale is ohmic, based on the layer depth). Another important lengthscale for the magnetic field is the magnetic dissipation lengthscale, ℓ_b, defined by

$$\ell_b^2 = \frac{\langle \boldsymbol{B}^2 \rangle_V}{\langle |\nabla \times \boldsymbol{B}|^2 \rangle_V}. \tag{4.12}$$

Having introduced appropriate lengthscales for the magnetic field, it is natural to do the same for the flow. Recalling that the convective cells near onset are long and thin, the vertical scale is roughly unity in these units. Our estimate for the typical flow lengthscale in the horizontal direction is based on the vertical velocity,

$$\ell_u = \frac{\sum\limits_{k_x,\, k_y,\, k_z} \left(\hat{u}_z(k_x, k_y, k_z)\right)^2}{\sum\limits_{k_x,\, k_y,\, k_z} \sqrt{k_x^2 + k_y^2}\, \left(\hat{u}_z(k_x, k_y, k_z)\right)^2}, \tag{4.13}$$

where $\hat{u}_z$ denotes the three-dimensional Fourier transform of the vertical velocity, whilst k_x, k_y and k_z are the wavenumbers in the x, y and z directions respectively (Guervilly *et al.*, 2014). A similar estimate can be made for the vertical flow lengthscale, replacing $\sqrt{k_x^2 + k_y^2}$ with k_z.

The efficiency of convective heat transport produced by the flow is quantified via the

ratio of total heat flux to conductive heat flux in the absence of motions, known as the Nusselt number,

$$\mathrm{Nu} = 1 + \langle |\nabla\theta|^2 \rangle_V. \tag{4.14}$$

Arguably the most natural timescale to use for dynamo calculations is the magnetic diffusion (ohmic) timescale, t_η, based on the depth of the domain. In dimensional terms, $t_\eta = d^2/\eta$, which is a factor of Pm/Pr longer than our characteristic timescale (based on the thermal diffusion time). This estimate for the relevant dynamo timescale is likely to be an overestimate, as it is based on the molecular magnetic diffusivity as opposed to the turbulent magnetic diffusivity. Following Cattaneo *et al.* (1991), we define an alternative characteristic timescale, t_e, which is an estimate for the decay time of the large-scale field due to turbulent diffusion. In dimensional terms,

$$t_e = \left(\frac{d}{\ell_u}\right)^2 \frac{\langle \boldsymbol{B}^2 \rangle_V}{\eta \langle |\nabla \times \boldsymbol{B}|^2 \rangle_V}. \tag{4.15}$$

In dimensionless form, $t_e = (\mathrm{Pm}/\mathrm{Pr})(\ell_b^2/\ell_u^2)$. Cattaneo *et al.* (1991) argue that a dynamo exists only if the field survives for times much longer than t_e; all of the successful dynamo calculations that are reported in this chapter satisfy this condition.

Finally, in dynamos driven by spherical rotating convection, Sreenivasan & Jones (2011) show that dipolar magnetic fields lead to an increase in helicity due to feedback on the flow. This enhancement in the helicity then leads to subcritical behaviour in their simulations. In this Cartesian domain, the kinetic helicity at each depth is given by

$$\mathcal{H}(z) = \overline{\boldsymbol{u} \cdot \nabla \times \boldsymbol{u}}. \tag{4.16}$$

The relative kinetic helicity normalises the helicity relative to the flow intensity. At each depth this is then given by

$$\mathcal{H}_{rel} = \frac{\overline{\boldsymbol{u} \cdot \nabla \times \boldsymbol{u}}}{\left(\overline{\boldsymbol{u}^2}\right)^{1/2} \left(\overline{(\nabla \times \boldsymbol{u})^2}\right)^{1/2}}, \tag{4.17}$$

where $|\mathcal{H}_{rel}| \leq 1$. Maximally helical flows produce a relative kinetic helicity of $\mathcal{H}_{rel} = \pm 1$.

4.3 Results

Table 4.1 summarises the input and output quantities of the numerical simulations reported in this chapter. The Ekman number is varied in the range $\mathrm{Ek} \in [5 \times 10^{-7}, 3.16 \times 10^{-4}]$ and the magnetic Prandtl number is in the range $\mathrm{Pm} \in [1, 5]$. In rotating convection studies, the Taylor number $\mathrm{Ta} = 1/\mathrm{Ek}^2$ is often used as an alternative to the Ekman

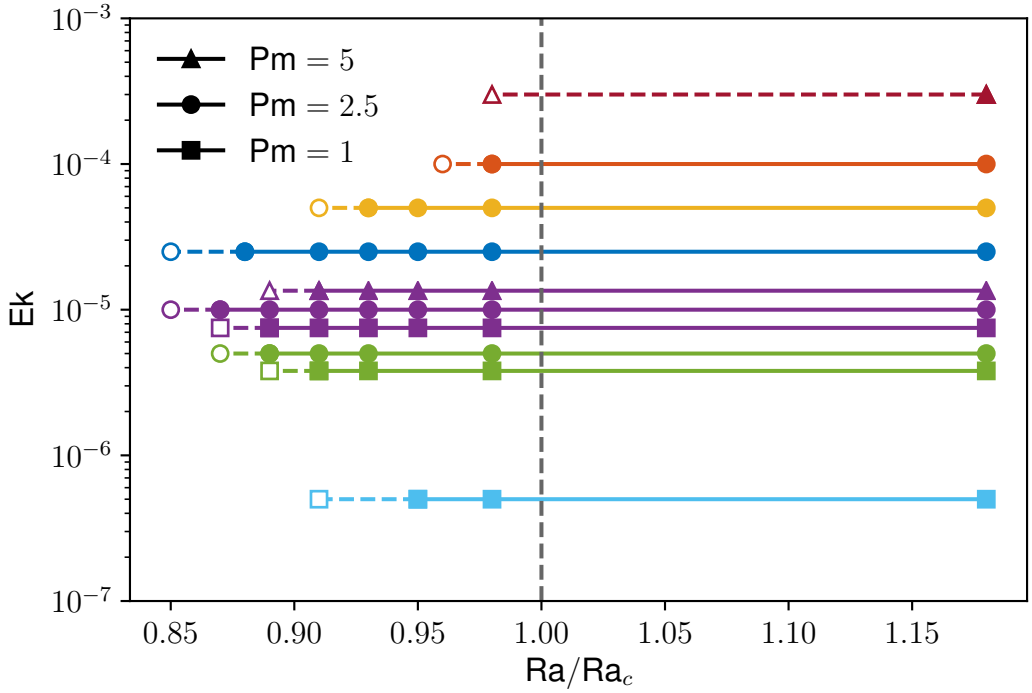


Figure 4.1: Location of the simulations in the parameter space Ek-Ra/Ra$_c$. Filled symbols represent cases where a dynamo is sustained and the open symbols represent cases where the dynamo fails. The marker colour denotes Ek and the marker shape Pm. For Ek $= 10^{-5}$ and Ek $= 5 \times 10^{-6}$, points with different Pm have been shifted vertically for visibility. It should be noted that an infinite time series would be required to conclusively state the existence of a subcritical dynamo. The majority of the cases presented here persist for long integrations (for a period of time much greater than t_e), however cases at Ek $= 5 \times 10^{-7}$ were only run for a comparatively short time (see Table 4.1).

number; our upper limit of Ek $= 3.16 \times 10^{-4}$ corresponds to Ta $= 1 \times 10^7$. We focus on dynamos generated near the onset of convection and the Rayleigh number is varied between 0.85Ra$_c$ and 1.18Ra$_c$, where Ra$_c$ is the critical Rayleigh number at the linear onset of rotating convection calculated from the analytical study of Chandrasekhar (1961). The fluid Prandtl number is fixed to be Pr $= 1$ in all cases.

Figure 4.1 shows the location of the dynamo simulations in the parameter space Ek-Ra/Ra$_c$, where simulations with different magnetic Prandtl numbers are indicated by different marker shapes. The behaviour of the dynamo changes drastically at the lowest Ekman number that we calculated (Ek $= 5 \times 10^{-7}$), so the regimes with moderate Ekman numbers where Ek $\geq 5 \times 10^{-6}$ (§4.3.1 and 4.3.2) and with small Ekman numbers where Ek $= 5 \times 10^{-7}$ (Chapter 5) are presented separately. To benchmark some of our results, we have reproduced the dynamo results of Stellmach & Hansen (2004) (hereafter SH04). The benchmarked cases are indicated by an asterisk in Table 4.1. Values of Rm and Λ are in agreement with the results of SH04 within 5%.

Case	Ek	Ra	$\mathrm{Ra}/\mathrm{Ra}_c$	Pm	λ	$N_x \times N_y \times N_z$	t_r	t_r/t_e	Rm	ℓ_b	ℓ_u	Λ	$\overline{\Lambda}$	M
A1	3.16×10^{-4}	4.8934×10^5	1.18	5	2	128^3	17.28	198.0	123 ± 11	0.044	0.33	0.30 ± 0.13	0.030	0.31
A2	3.16×10^{-4}	4.0640×10^5	0.98	5	2	128^3	1.30	–	–	–	–	–	–	–
B1*	1×10^{-4}	2.2345×10^6	1.18	2.5	1	128^3	9.84	133.2	108 ± 18	0.041	0.24	0.30 ± 0.14	0.061	0.63
B2	1×10^{-4}	1.8619×10^6	0.98	2.5	1	128^3	6.56	72.4	71 ± 15	0.048	0.25	0.26 ± 0.13	0.079	1.25
B3	1×10^{-4}	1.8201×10^6	0.96	2.5	1	128^3	1.34	–	–	–	–	–	–	–
C1*	5×10^{-5}	5.6050×10^6	1.18	2.5	1	128^3	4.51	58.4	141 ± 24	0.035	0.20	0.36 ± 0.11	0.068	0.93
C2	5×10^{-5}	4.6628×10^6	0.98	2.5	1	128^3	4.92	52.5	91 ± 18	0.041	0.21	0.30 ± 0.10	0.080	1.80
C3	5×10^{-5}	4.5201×10^6	0.95	2.5	1	128^3	4.10	41.4	84 ± 19	0.042	0.21	0.27 ± 0.10	0.077	1.95
C4	5×10^{-5}	4.4250×10^6	0.93	2.5	1	128^3	4.92	47.6	81 ± 17	0.043	0.21	0.27 ± 0.09	0.078	2.09
C5	5×10^{-5}	4.3298×10^6	0.91	2.5	1	128^3	3.28	–	–	–	–	–	–	–
D1*	2.5×10^{-5}	1.4081×10^7	1.18	2.5	1	128^3	1.64	19.7	170 ± 35	0.030	0.16	0.39 ± 0.11	0.068	1.39
D2	2.5×10^{-5}	1.1715×10^7	0.98	2.5	1	128^3	3.28	31.9	110 ± 23	0.036	0.17	0.30 ± 0.09	0.074	2.51
D3	2.5×10^{-5}	1.1357×10^7	0.95	2.5	1	128^3	4.10	37.2	101 ± 23	0.037	0.17	0.27 ± 0.10	0.071	2.71
D4	2.5×10^{-5}	1.1118×10^7	0.93	2.5	1	128^3	3.28	28.9	96 ± 23	0.037	0.18	0.27 ± 0.09	0.072	2.95
D5	2.5×10^{-5}	1.0640×10^7	0.91	2.5	1	128^3	2.73	25.0	86 ± 21	0.039	0.18	0.23 ± 0.09	0.070	3.25
D6	2.5×10^{-5}	1.0520×10^7	0.88	2.5	1	128^3	3.55	28.7	81 ± 22	0.039	0.17	0.21 ± 0.10	0.059	3.23
D7	2.5×10^{-5}	1.0161×10^7	0.85	2.5	1	128^3	1.04	–	–	–	–	–	–	–
E1	1×10^{-5}	4.7712×10^7	1.18	5	1	128^3	0.98	7.0	340 ± 87	0.020	0.12	0.41 ± 0.11	0.042	1.93
E2	1×10^{-5}	3.9660×10^7	0.98	5	1	128^3	1.15	4.9	166 ± 74	0.027	0.13	0.25 ± 0.14	0.048	5.46
E3	1×10^{-5}	3.8447×10^7	0.95	5	1	128^3	1.15	4.8	143 ± 50	0.028	0.13	0.22 ± 0.11	0.049	5.84
E4	1×10^{-5}	3.7672×10^7	0.93	5	1	128^3	1.15	5.1	145 ± 44	0.027	0.13	0.23 ± 0.09	0.049	5.82
E5	1×10^{-5}	3.6810×10^7	0.91	5	1	128^3	7.22	28.9	129 ± 46	0.029	0.13	0.21 ± 0.10	0.045	6.68
E6	1×10^{-5}	3.6019×10^7	0.89	5	1	128^3	1.31	–	–	–	–	–	–	–
F1*	1×10^{-5}	4.7712×10^7	1.18	2.5	1	128^3	1.80	16.4	196 ± 42	0.025	0.12	0.31 ± 0.07	0.057	2.11
F2	1×10^{-5}	3.9660×10^7	0.98	2.5	1	128^3	1.05	8.3	129 ± 29	0.030	0.13	0.24 ± 0.07	0.060	3.76
F3	1×10^{-5}	3.8447×10^7	0.95	2.5	1	128^3	2.59	20.2	125 ± 30	0.030	0.13	0.22 ± 0.08	0.055	3.72
F4	1×10^{-5}	3.7672×10^7	0.93	2.5	1	128^3	2.07	15.6	116 ± 26	0.031	0.13	0.21 ± 0.07	0.055	4.05
F5	1×10^{-5}	3.6810×10^7	0.91	2.5	1	128^3	2.13	15.7	111 ± 28	0.031	0.13	0.20 ± 0.07	0.049	4.16
F6	1×10^{-5}	3.6019×10^7	0.89	2.5	1	128^3	3.17	21.6	103 ± 23	0.031	0.13	0.19 ± 0.06	0.051	4.44
F7	1×10^{-5}	3.5209×10^7	0.87	2.5	1	128^3	3.28	21.9	97 ± 26	0.032	0.13	0.18 ± 0.08	0.044	4.80
F8	1×10^{-5}	3.4400×10^7	0.85	2.5	1	128^3	0.82	–	–	–	–	–	–	–
G1	1×10^{-5}	4.7712×10^7	1.18	1	1	128^3	1.64	26.1	108 ± 16	0.033	0.13	0.22 ± 0.04	0.068	1.90
G2	1×10^{-5}	3.9660×10^7	0.98	1	1	128^3	1.31	18.5	81 ± 13	0.036	0.14	0.16 ± 0.04	0.059	2.46
G3	1×10^{-5}	3.8447×10^7	0.95	1	1	128^3	1.48	20.4	76 ± 12	0.037	0.14	0.15 ± 0.04	0.058	2.63
G4	1×10^{-5}	3.7672×10^7	0.93	1	1	128^3	1.31	17.1	70 ± 15	0.037	0.13	0.13 ± 0.05	0.053	2.65
G5	1×10^{-5}	3.6810×10^7	0.91	1	1	128^3	1.48	19.6	68 ± 11	0.037	0.14	0.12 ± 0.03	0.053	2.66
G6	1×10^{-5}	3.6019×10^7	0.89	1	1	128^3	2.62	33.6	65 ± 12	0.038	0.13	0.11 ± 0.04	0.051	2.70
G7	1×10^{-5}	3.5209×10^7	0.87	1	1	128^3	0.16	–	–	–	–	–	–	–
H1*	5×10^{-6}	1.2000×10^8	1.18	2.5	1	128^3	1.16	8.8	217 ± 55	0.022	0.10	0.25 ± 0.07	0.049	2.89
H2	5×10^{-6}	1.0000×10^8	0.98	2.5	1	128^3	1.56	10.7	150 ± 37	0.026	0.11	0.20 ± 0.06	0.048	4.70
H3	5×10^{-6}	9.5000×10^7	0.93	2.5	1	128^3	2.25	17.2	132 ± 34	0.027	0.11	0.18 ± 0.07	0.047	5.43
H4	5×10^{-6}	9.3000×10^7	0.91	2.5	1	128^3	1.21	8.2	120 ± 24	0.028	0.11	0.17 ± 0.05	0.046	5.93
H5	5×10^{-6}	9.0673×10^7	0.89	2.5	1	128^3	3.28	20.3	121 ± 24	0.027	0.11	0.16 ± 0.05	0.046	5.70
H6	5×10^{-6}	8.8636×10^7	0.87	2.5	1	128^3	3.36	–	–	–	–	–	–	–
I1*	5×10^{-6}	1.2000×10^8	1.18	1	1	128^3	1.72	25.9	131 ± 20	0.028	0.11	0.20 ± 0.04	0.057	2.41
I2*	5×10^{-6}	1.0000×10^8	0.98	1	1	128^3	1.64	21.1	99 ± 16	0.031	0.11	0.15 ± 0.04	0.051	3.08
I3	5×10^{-6}	9.5000×10^7	0.93	1	1	128^3	2.18	27.9	90 ± 18	0.031	0.11	0.13 ± 0.05	0.050	3.25
I4	5×10^{-6}	9.3000×10^7	0.91	1	1	128^3	1.64	20.2	88 ± 18	0.032	0.11	0.13 ± 0.05	0.048	3.34
I5*	5×10^{-6}	9.0673×10^7	0.89	1	1	128^3	2.28	–	–	–	–	–	–	–

Table 4.1: Summary of the input and output quantities in the numerical simulations. N_x, N_y and N_z are the numerical resolution in x, y and z. t_r is the total run time in units of a thermal diffusion timescale, $t_\kappa = d^2/\kappa$. t_e is a characteristic timescale for the decay of the large-scale field due to turbulent diffusion from Cattaneo *et al.* (1991). In all cases the Prandtl number is kept constant at $\mathrm{Pr} = 1$. Dashes in the output quantities indicate that the simulation decayed to the trivial conducting state, and thus output values became trivial also. The asterisk next to the case number denotes the simulations performed in Stellmach & Hansen (2004) for comparison. The output quantities (defined in §4.2.2) are time averaged during the saturated phase.

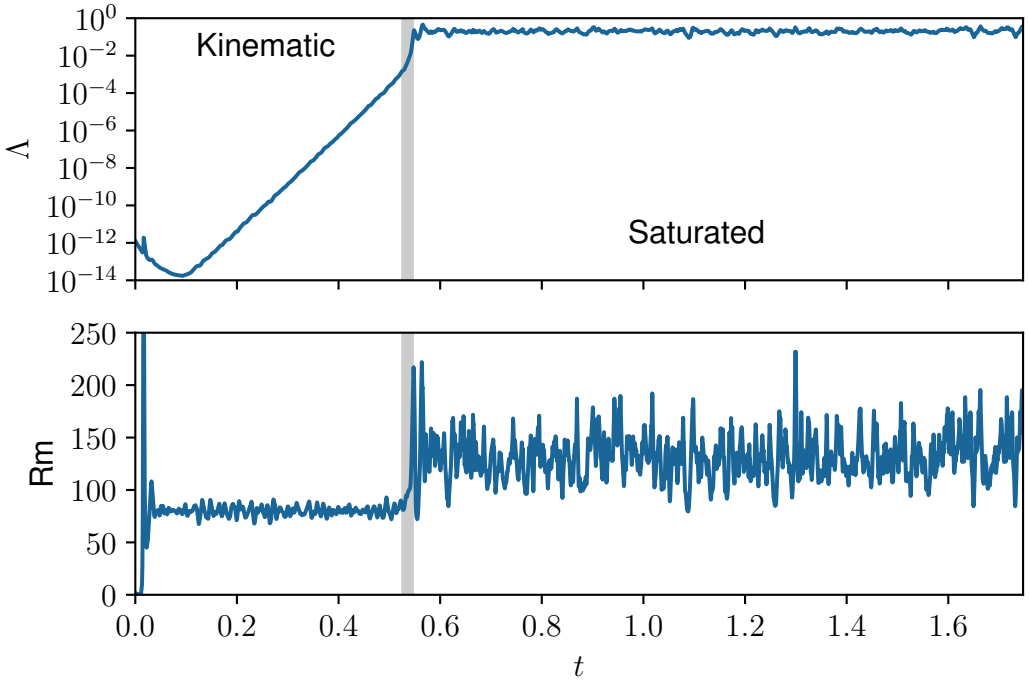


Figure 4.2: Time series of the Elsasser number Λ and magnetic Reynolds number Rm for Case I1 at Pm = 1, Ek = 5×10^{-6}, and Ra/Ra$_c$ = 1.18. The grey area indicates the super-exponential growth phase.

4.3.1 Supercritical Dynamos at Moderate Ekman Numbers

We first examine dynamo action in the supercritical range, that is for Ra > Ra$_c$. The main characteristics of the flow and magnetic field in this system were previously described in SH04. Here we briefly recall some of these characteristics and identify the important ingredients for the subcritical behaviour (at Ra < Ra$_c$) that we will explore in the next section. Additionally, we present the generation mechanism of the coherent horizontally-averaged field, which we call the mean field. In this section, we focus primarily on a representative simulation at Ek = 5×10^{-6}, Pm = 1, Ra = 1.2×10^8 = 1.18Ra$_c$ and $\lambda = 1$ (Case I1 in Table 4.1), which is typical of these supercritical dynamo calculations.

Modification of the Convection by the Magnetic Field

For Case I1, the time evolution of the Elsasser number Λ and magnetic Reynolds number Rm are shown in Figure 4.2. During the kinematic phase, where the magnetic energy grows exponentially and the Lorentz force does not significantly affect the flow, Rm takes an average value of 80. Around $t = 0.5$ in dimensionless units, the magnetic energy undergoes a short super-exponential growth phase. This phase occurs when the magnetic field reaches a sufficiently strong amplitude to alter the flow, leading to an amplification of the magnetic Reynolds number (and equivalently the kinetic energy), which is accompanied

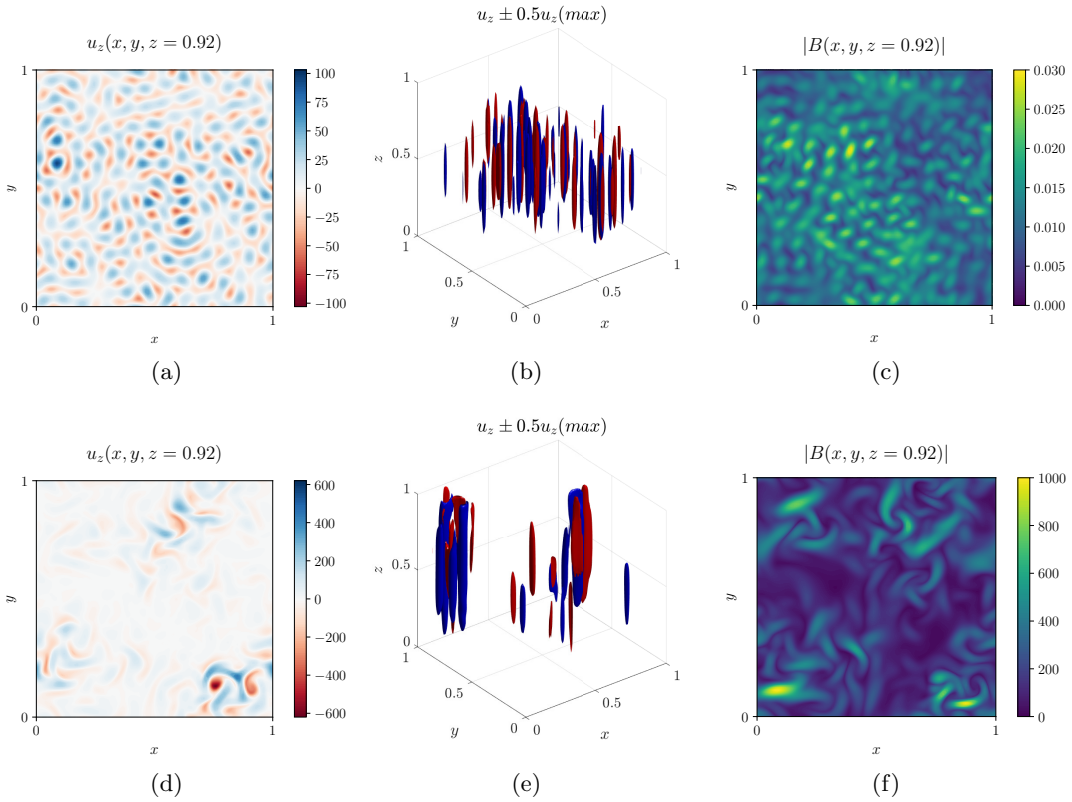


Figure 4.3: Snapshots in the (a-c) kinematic phase and (d-f) saturated phase of (a, d) u_z in a horizontal slice, (b, e) 3D isosurfaces of u_z and (c, f) the absolute value of the magnetic field, $|\boldsymbol{B}|$, in a horizontal slice for Case I1 at Pm $= 1$, Ek $= 5 \times 10^{-6}$, and Ra/Ra$_c = 1.18$. The horizontal slices are taken at $z = 0.92$. The isosurfaces correspond to $\pm 50\%$ of the maximum at that time.

by an increasing growth rate of the magnetic energy due to the favourable effect on the dynamo action. Saturation then occurs and the magnetic field amplitude reaches an average value corresponding to $\Lambda \approx 0.2$. During the saturated phase, the magnetic Reynolds number exhibits greater fluctuations than in the kinematic phase and its average value is approximately 130, which shows that the flow is significantly altered by the magnetic field. The ratio of magnetic to kinetic energies, M, is approximately $2-3$ in the saturated phase. Values of $M > 1$ and $\Lambda < 1$ are typical of our saturated dynamos. For comparison, small-scale dynamos in rotating planar convection are typically characterised by a moderate reduction in Rm as the dynamo saturates and $M \sim \mathcal{O}(0.1)$ (Favier & Bushby, 2011). Some recent studies (e.g. Soderlund *et al.*, 2012; Dormy, 2016) have adopted an alternative definition of the Elsasser number that is based on the typical velocity scale, U_*, and the magnetic dissipation scale, ℓ_b. In all cases, the modified Elsasser number, $\Lambda' = (\mathrm{Ek}/\mathrm{Pr}^2)B_*^2/U_*\ell_b$, is small, of the order of 10^{-2}.

Changes in the flow between the kinematic and saturated phases can be observed in Figure 4.3, which shows horizontal slices and 3D isosurfaces of the vertical velocity. In the

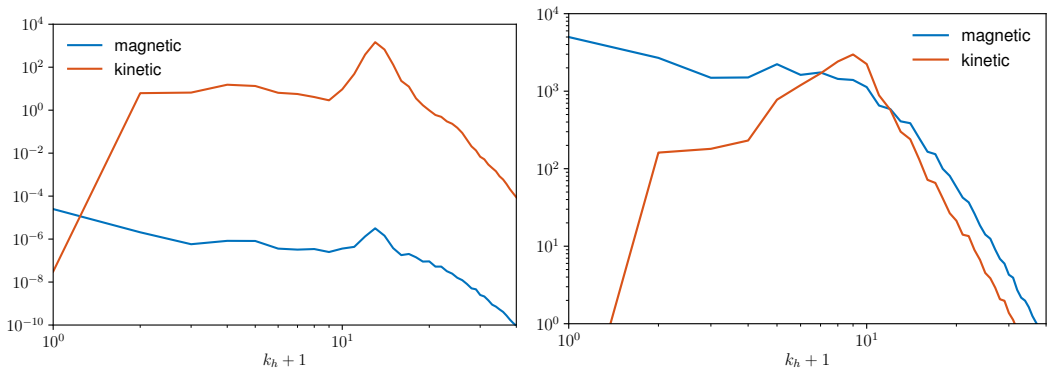
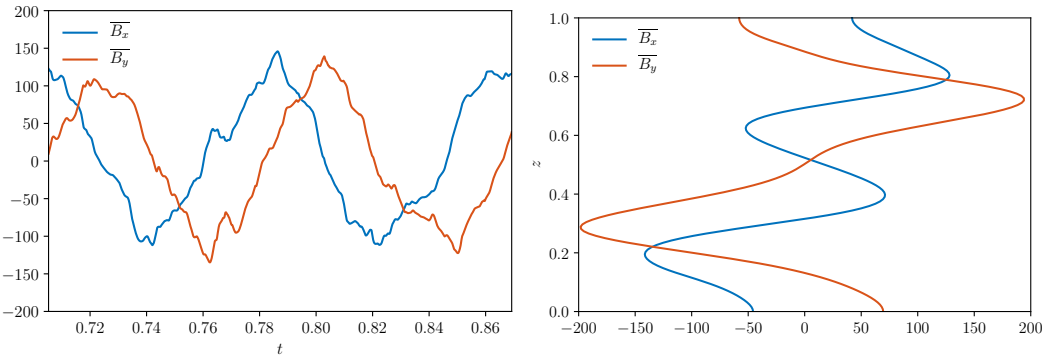


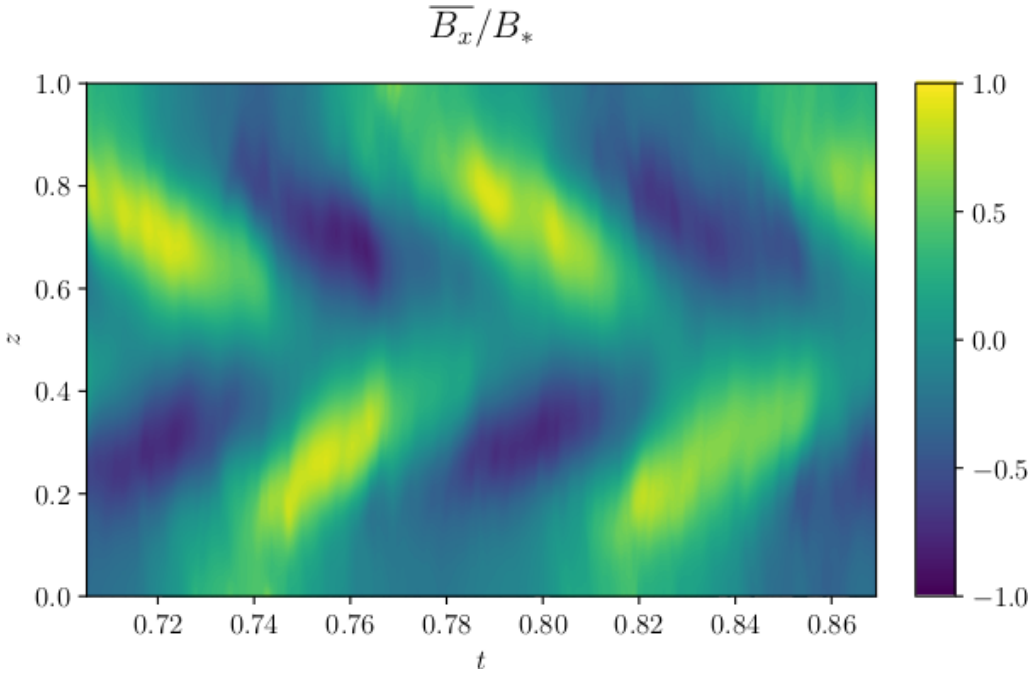
Figure 4.4: Power spectra (calculated from representative snapshots) of the magnetic energy and kinetic energy as a function of the horizontal wavenumber, $k_h = (k_x^2 + k_y^2)^{1/2}$, during (a) the kinematic and (b) the saturated phases for Case I1 at Pm = 1, Ek = 5×10^{-6}, and Ra/Ra$_c$ = 1.18. In order to include the contribution from the mean magnetic field (for which $k_h = 0$) on the logarithmic scale, the horizontal wavenumbers are shifted to $k_h + 1$.

kinematic phase, the convection takes the form of tall and narrow columns that fill the space homogeneously. In the saturated phase, the convection becomes localised in a small number of large amplitude patches. The flow is still columnar but the columns appear fatter. This is confirmed by calculations of the horizontal flow lengthscale, which increases from a mean value of 0.08 to 0.11. In the kinematic phase, the vertical flow lengthscale is approximately box-sized (i.e. close to unity) but decreases by approximately 20% in the saturated phase, suggesting a weakening of the rotational constraints. This indicates that the convective columns become less depth-invariant as the dynamo saturates. The increase in the column width and the amplitude of the vertical velocity leads to an improved efficiency of the convective heat transport with an increase in the Nusselt number of 40%.

In order to observe the change in lengthscales as the dynamo saturates, Figure 4.4 shows the power spectra of the kinetic and magnetic energies in the two phases as a function of the horizontal wavenumber, $k_h = (k_x^2 + k_y^2)^{1/2}$. The spectra are calculated at each depth and then averaged in z. They are calculated from data snapshots, but upon visual comparison with other snapshots are a good representation of each phase. The peak in the kinetic energy spectrum shifts from a horizontal wavenumber $k_h \approx 11$ to $k_h \approx 9$, consistent with the change in the flow lengthscale. The peak is less pronounced in the saturated phase as a broad range of wavenumbers have significant energy. The magnetic field in the kinematic phase is dominated by the mean field (corresponding to $k_h = 0$). A secondary peak is also visible around the convection scale. In the saturated phase, the mean field is still dominant and contributes to approximately a quarter of the magnetic energy. The magnetic spectrum of the saturated phase is fairly flat from $k_h = 1$ down to the convective scale. Figure 4.3(f) shows that the fluctuating magnetic field (i.e. the field



(a) (b)



(c)

Figure 4.5: (a) Time series of the x and y components of the mean magnetic field at $z = 0.85$, (b) snapshots of their vertical profile at $t \approx 0.76$, and (c) time series of the x-component of the mean field as a function of depth, scaled by the field r.m.s value. All figures are during the saturated phase for Case I1 at $\mathrm{Pm} = 1$, $\mathrm{Ek} = 5 \times 10^{-6}$, and $\mathrm{Ra}/\mathrm{Ra}_c = 1.18$.

corresponding to $k_h \geq 1$) is mainly concentrated in the regions of localised convection.

The Mean Magnetic Field

Focusing again upon Case I1, Figure 4.5 shows the temporal evolution of the two horizontal components of the mean magnetic field alongside a snapshot of their vertical profiles in the saturated phase. In both the kinematic and the saturated phases, the mean field oscillates in time, generating the spiral staircase structure seen in SH04. Throughout its

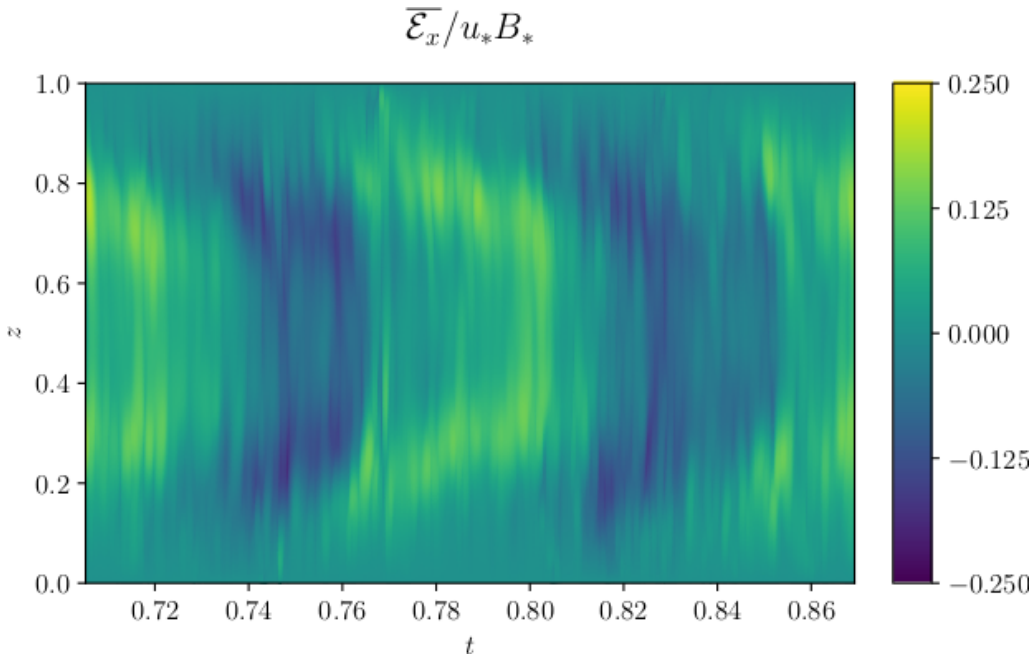


Figure 4.6: Time series of the x-component of the mean e.m.f as a function of depth, scaled by the r.m.s values, during the saturated phase of Case I1 at Pm = 1, Ek = 5×10^{-6}, and Ra/Ra$_c$ = 1.18.

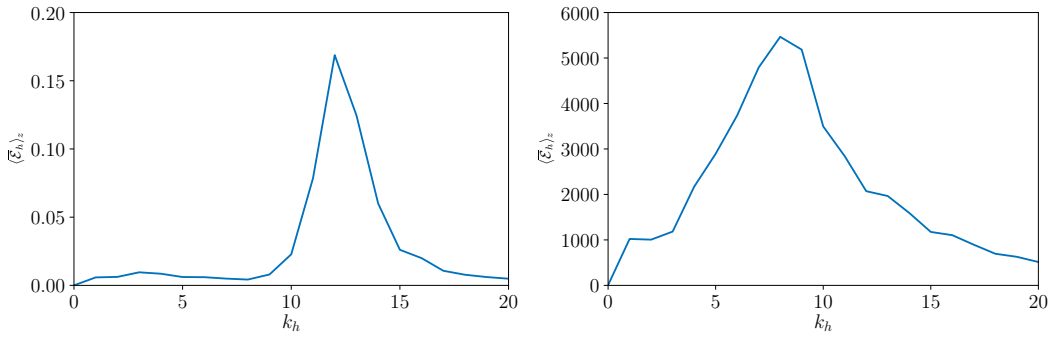
temporal evolution, the mean field remains approximately antisymmetric about the midplane ($z = 0.5$) with a well-defined phase lag between the two horizontal components. The time period of oscillation is influenced by the parameters chosen. The magnetic Prandtl number has little effect on the time period of the mean field but higher Pm results in larger fluctuations, as indicated by standard deviations in the output quantities in Table 4.1, whereas at lower Ek the time period of oscillation decreases with increasing rotation rate. The depth-profiles of each component of the mean horizontal field display a 'butterfly' pattern in their time series, shown in Figure 4.5(c). Figure 4.6 shows a time series of the x-component of the mean electromotive force (e.m.f.), $\overline{\boldsymbol{\mathcal{E}}} = \overline{\boldsymbol{u} \times \boldsymbol{B}}$, as a function of depth. Correlations between the field and flow result in a mean e.m.f. that is symmetric across the midplane, oscillating over time as positive and negative mean e.m.f. are produced.

In the plane layer dynamo model of Childress & Soward (1972), the dynamo operates as a two-scale mechanism, where the two scales involved are the box-size and the small horizontal scale that is associated with the near-onset convective flows. A small-scale magnetic field is produced by the distortion of a box-size (mean) field by the small-scale flow; the mean field is then produced by the mean e.m.f. generated by the coherent interaction of small-scale field and flow. This dynamo process is thought to operate efficiently only close to the dynamo onset, where the Rayleigh number is small enough so that the convective motions are sufficiently laminar to cooperate in the production of the mean e.m.f. (Courvoisier *et al.*, 2009; Tilgner, 2012; Guervilly *et al.*, 2015).

We want to establish whether the dynamo in these simulations operates along the same principle as the two-scale dynamo in the saturated phase. We anticipate that the picture might be more complicated in our simulations because: (i) although the kinetic energy spectra has a fairly well defined convective scale $k_h \approx 8$ (Figure 4.4(b)), the intermediate scales (i.e. the scales between the box size and the convective scale) have significant energy; (ii) the magnetic energy spectrum tends to be flat at the intermediate scales, without a clear peak at the convective scale. Following Bushby *et al.* (2018), we study the contributions to the mean e.m.f., which is responsible for the generation of the mean field, $\overline{\boldsymbol{\mathcal{E}}} = \overline{\boldsymbol{u} \times \boldsymbol{B}}$. To investigate the contributions of different scales of motion to this mean e.m.f., we can filter the velocity field in Fourier space into contributions from each mode. Note that any flow filtering is done post-processing from representative data snapshots, so the dynamo calculation is not affected by the filtering process. We study the respective contributions from individual horizontal wavenumbers to the mean horizontal e.m.f., $\overline{\mathcal{E}}_h$. Essentially, we filter the velocity field into contributions from each wavenumber, then calculate each component of the mean e.m.f. followed by calculating $\overline{\mathcal{E}}_h = (\overline{\mathcal{E}}_x^2 + \overline{\mathcal{E}}_y^2)^{1/2}$ as a function of depth, from these filtered flows, before depth-averaging this quantity. This depth-averaged value is then plotted in Figure 4.7 and can be thought of as 'which horizontal wavenumbers in the velocity contribute the most to the horizontal mean field'. In the kinematic phase, we observe a dominant contribution to the mean e.m.f. produced by $k_h \sim 12$ with little contribution from lower or higher wavenumbers, indicating a two-scale mechanism. These 'active' wavenumbers (i.e. those producing the largest spectral contributions) shift to lower values in the saturated phase and approximately corresponds to the dominant convective scale. A wider range of active wavenumbers exist in the saturated phase. Figure 4.8 shows the unfiltered and filtered versions of the x-component of the mean e.m.f., $\overline{\mathcal{E}_x}$, where we consider the depth-dependence of the mean e.m.f. produced by low, active and high wavenumbers. In the kinematic phase, the mean e.m.f. is almost entirely produced by contributions from the convective scales at $10 \leq k_h \leq 14$ with little contribution from lower or higher wavenumber. In the saturated phase, the mean e.m.f is mostly produced by motions at wavenumbers $6 \leq k_h \leq 11$, although the contribution from lower wavenumbers is more sizeable in this phase. These results suggest that the production of the coherent mean e.m.f. is dominated by motions at the convective scale, especially in the kinematic phase. Therefore the dynamo does indeed operate as a two-scale process.

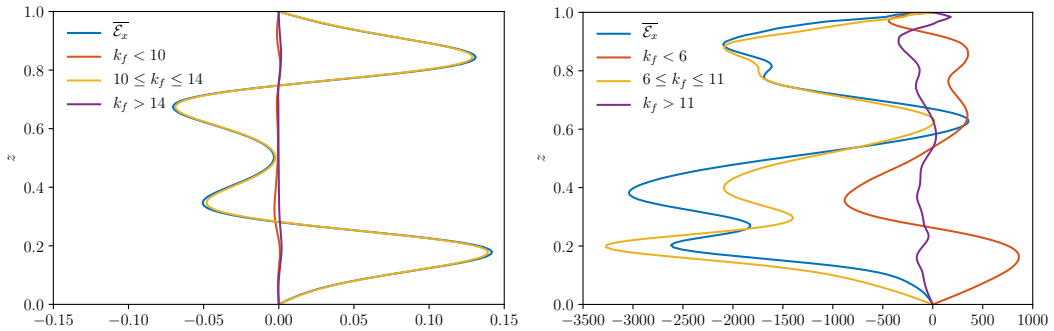
Variation in the Dominant Force Balances

The dominant force balances involved in dynamo action at low Ek are a source of wide speculation due to numerical restrictions on simulations (e.g. Cattaneo & Hughes, 2017; Schwaiger *et al.*, 2019). Here we compare the strength of the different terms in the vorticity



(a) (b)

Figure 4.7: Spectral contributions to the depth-averaged horizontal mean e.m.f., $\langle\overline{\mathcal{E}}_h\rangle_z = \langle(\overline{\mathcal{E}}_x^2 + \overline{\mathcal{E}}_y^2)^{1/2}\rangle_z$, taken from representative snapshots in (a) the kinematic phase and (b) the saturated phase of Case I1 at Pm = 1, Ek = 5×10^{-6}, and Ra/Ra$_c$ = 1.18. Here $\langle ...\rangle_z$ denotes averaging in z.



(a) (b)

Figure 4.8: Vertical profile of the unfiltered and filtered versions of $\overline{\mathcal{E}_x}$ in (a) the kinematic phase and (b) the saturated phase (snapshot) for Case I1 at Pm = 1, Ek = 5×10^{-6}, and Ra/Ra$_c$ = 1.18, where contributions from $k_h = k_f$ are kept and other wavenumbers are filtered out.

equation at different horizontal lengthscales in order to understand how the field modifies the flow and the relevant force balances, including any variations in these balances across different scales. Using the vorticity equation is a convenient way to eliminate the pressure terms which form a geostrophic balance with part of the Coriolis force. In dimensionless form, the vorticity equation is

$$\frac{\partial \boldsymbol{\omega}}{\partial t} + (\boldsymbol{u}\cdot\nabla)\boldsymbol{\omega} - (\boldsymbol{\omega}\cdot\nabla)\boldsymbol{u} - \frac{\mathrm{Pr}}{\mathrm{Ek}}\frac{\partial \boldsymbol{u}}{\partial z} = \mathrm{Pr}\nabla^2\boldsymbol{\omega} + \mathrm{PrRa}\nabla\times(\theta\hat{\mathbf{z}}) + \nabla\times(\boldsymbol{J}\times\boldsymbol{B}). \quad (4.18)$$

The spectral distribution of each term in either the x- or z-components of the vorticity equation, as a function of the horizontal wavenumber, is given in Figure 4.9. Here we show representative snapshots of the x-component of the vorticity, however analysis in the y-direction yields similar results. Each term is calculated from a snapshot of the velocity,

magnetic field and temperature, which is then transformed into Fourier space at each depth, before being squared and then averaged along z. In order to determine the effects of the mean and fluctuating parts of the magnetic field separately, the term corresponding to the curl of the Lorentz force is separated into the contributions from the fluctuating field only (i.e. the modes $k_h \geq 1$, which we denote by a prime) $\mathcal{L}' = \nabla \times (\boldsymbol{J}' \times \boldsymbol{B}')$, and the contributions involving the mean field $\overline{\mathcal{L}} = \nabla \times (\overline{\boldsymbol{J}} \times \overline{\boldsymbol{B}} + \overline{\boldsymbol{J}} \times \boldsymbol{B}' + \boldsymbol{J}' \times \overline{\boldsymbol{B}})$ where $\boldsymbol{B}'$ and $\overline{\boldsymbol{B}}$ are directly outputted by the code. The remaining terms are the nonlinear inertial terms $\mathcal{I} = (\boldsymbol{u} \cdot \nabla)\boldsymbol{\omega} - (\boldsymbol{\omega} \cdot \nabla)\boldsymbol{u}$, the contribution from the Coriolis force $\mathcal{C} = (\mathrm{Pr}/\mathrm{Ek})\partial_z \boldsymbol{u}$, the viscous term $\mathcal{V} = \mathrm{Pr}\nabla^2\boldsymbol{\omega}$, and the term due to buoyancy $\mathcal{B} = \mathrm{PrRa}\nabla \times (\theta \boldsymbol{e}_z)$.

In the kinematic phase, the main balance for the horizontal vorticity is between the buoyancy term and the Coriolis term at the convective scale, with a smaller contribution from the viscous term. A similar balance is also observed at larger scales. The inertial terms are significantly smaller, but not completely negligible even though Ra is only just above Ra_c. There is no buoyancy source for the vertical vorticity, so the Coriolis term is balanced by the viscous term at the convective scale. This picture is similar to the force balance expected at the linear onset of non-magnetic rotating convection (Chandrasekhar, 1961). After comparing the force balances of multiple snapshots during the temporal evolution, this particular snapshot is a good representation of the dynamics during this phase. In the saturated phase, the main balance for the horizontal vorticity is still between the buoyancy and Coriolis terms. In the vertical vorticity equation, the Coriolis term is now mostly balanced by the Lorentz term involving the interactions of the fluctuating field. This balance occurs at a larger wavenumber, where the viscous term is smaller. This picture differs somewhat from the force balances expected in linear rotating magnetoconvection (Chandrasekhar, 1961; Eltayeb, 1972), where it is the linear Lorentz forces (i.e. the interaction between the mean and fluctuating fields) that balances the pressure gradient and the Coriolis force. Nevertheless, the presence of a coherent mean field is crucial for the flow changes that we observe because the values of the magnetic Reynolds numbers obtained in these near-onset dynamos are not large enough to produce small-scale dynamo action (Tilgner, 2012; Guervilly *et al.*, 2017). The generation of the fluctuating field therefore relies on the presence of the mean field. The mean field does not need to be particularly strong in terms of an Elsasser number: values of $\overline{\Lambda} \approx 0.05$ are sufficient. The threshold value of $\overline{\Lambda}$ for which flow changes are significant will be explored in §4.3.2.

4.3.2 Subcritical Dynamos at Moderate Ekman Numbers

Subcritical behaviour that is able to produce a dynamo, where convection and dynamo action are sustained for $\mathrm{Ra} < \mathrm{Ra}_c$, is made possible in this system due to the significant changes in the flow that are induced by the presence of a non-negligible magnetic field.

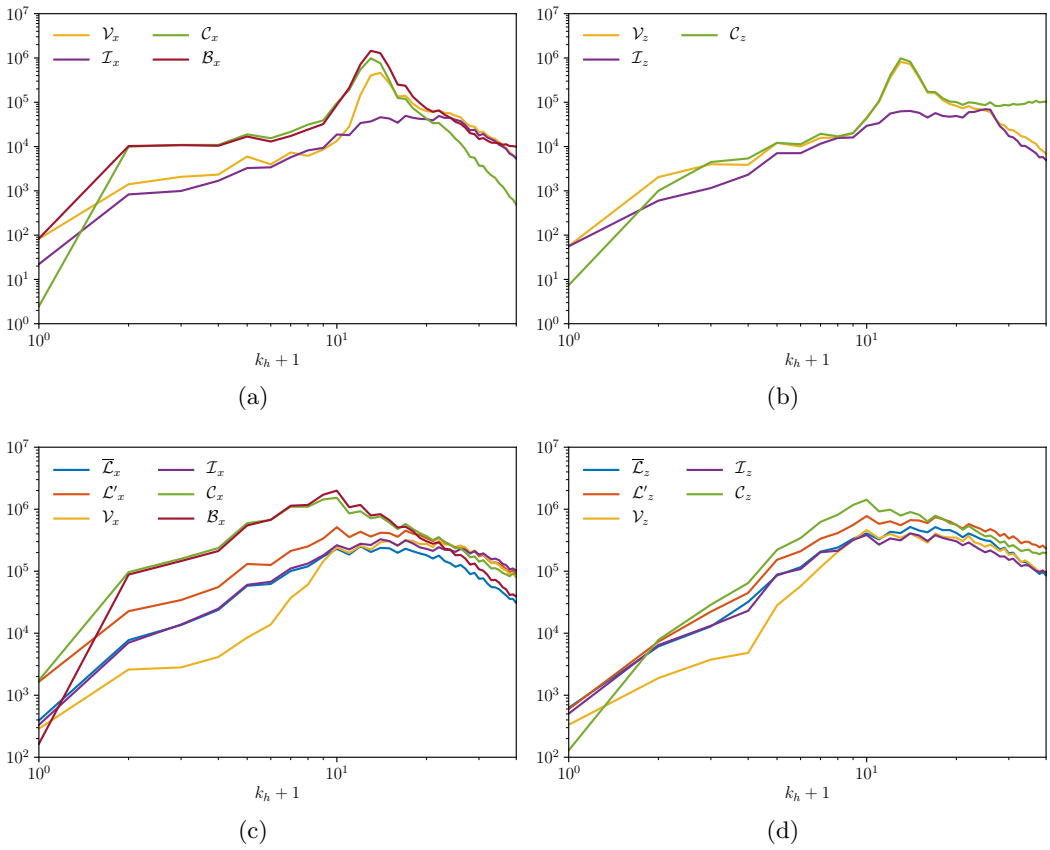
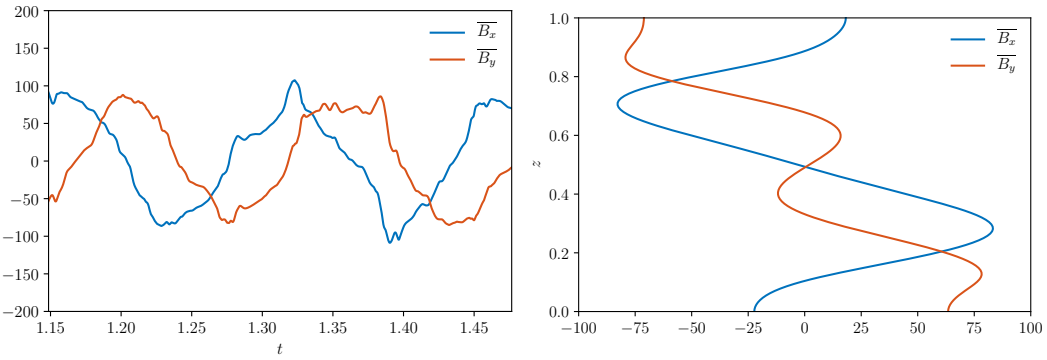


Figure 4.9: Spectral distributions of the terms generating the (left) horizontal and (right) vertical vorticity as a function of the horizontal wavenumber for representative snapshots of Case I1 at $\mathrm{Pm} = 1$, $\mathrm{Ek} = 5 \times 10^{-6}$, and $\mathrm{Ra}/\mathrm{Ra}_c = 1.18$, in the (a-b) kinematic and (c-d) saturated phases. The nonlinear inertial terms are denoted by $\mathcal{I} = (\boldsymbol{u} \cdot \nabla)\boldsymbol{\omega} - (\boldsymbol{\omega} \cdot \nabla)\boldsymbol{u}$, the Coriolis term by $\mathcal{C} = (\mathrm{Pr}/\mathrm{Ek})\partial_z \boldsymbol{u}$, the viscous term by $\mathcal{V} = \mathrm{Pr}\nabla^2\boldsymbol{\omega}$, the buoyancy term by $\mathcal{B} = \mathrm{PrRa}\nabla \times (\theta \boldsymbol{e}_z)$, the Lorentz force term involving the mean field by $\overline{\mathcal{L}}$, and the Lorentz force term involving the fluctuating field only by $\mathcal{L}'$.

Indeed, SH04 have already obtained a probable subcritical dynamo for a slightly subcritical Rayleigh number, $\mathrm{Ra}/\mathrm{Ra}_c = 0.98$ for $\mathrm{Ek} = 5 \times 10^{-6}$ and $\mathrm{Pm} = 1$ (Case I2). However, as they pointed out, an infinitely long simulation would be needed to categorically prove the persistence of the subcritical behaviour in direct numerical simulations. For practical reasons, these simulations cannot be performed for more than a few magnetic diffusion timescales, but persistent magnetic field generation for the duration of a long calculation is strongly indicative of a subcritical dynamo. The running time t_r is given in Table 4.1. As times are scaled with d^2/κ, $t_r\mathrm{Pr}/\mathrm{Pm}$ gives the running time in units of the ohmic decay time, $t_\eta = d^2/\eta$. The subcritical cases are run for somewhere between t_η and $2t_\eta$; in terms of t_e, which is the equivalent timescale that is based on the turbulent magnetic diffusivity (which is probably the most relevant timescale for these dynamos), the most



(a) (b)

Figure 4.10: (a) Time series of the x and y components of the mean magnetic field at $z = 0.85$, and (b) snapshot of its vertical profile in the Case G5 at $\mathrm{Ra}/\mathrm{Ra}_c = 0.91$ with $\mathrm{Pm} = 1$ and $\mathrm{Ek} = 1\times10^{-5}$.

subcritical cases are run for longer than $20t_e$. In this section, all analysis is performed across all simulations and we observe similar behaviour, however we predominantly focus on representative cases.

We reproduced the subcritical dynamo simulation of SH04 over a running time of $1.64t_\eta$ or $21t_e$. The simulation was initialised by a snapshot from $\mathrm{Ra} = 1.18\mathrm{Ra}_c$ (Case I1). Pushing the Rayleigh number towards smaller values, SH04 found that the dynamo did not survive for $\mathrm{Ra}/\mathrm{Ra}_c = 0.89$ (a result that we also recover, Case I5). This suggests that the subcriticality remains confined to a small range of Ra near Ra_c.

Similarly to the supercritical case, in all subcritical simulations the horizontally-averaged mean field oscillates over time as shown in Figure 4.10(a). However, in the subcritical regime the time period of oscillation tends to be slightly larger in comparison to the supercritical time period. The mean field is therefore oscillating more slowly below the onset of convection. Figure 4.10(b) shows that the mid-plane antisymmetry, phase lag and spiral staircase structure observed in the supercritical case and SH04 remain. The dominant force balances observed are also similar to those in the supercritical saturated phase. At least in qualitative terms, these subcritical dynamos are very similar to their supercritical counterparts in terms of their behaviour.

We explore the parameter space where the subcritical behaviour occurs to study the dependence on the Ekman number, which is varied between 3.16×10^{-4} and 5×10^{-6} for these simulations. For a given series of simulations at fixed Ek and Pm, the subcritical behaviour is studied by branch tracking, where the initial condition at a given Ra is taken from a data snapshot at a slightly larger Ra. Figure 4.11 shows the time series of Rm and Λ for two representative cases: Case H5, where the dynamo is sustained for the whole duration of the simulation (which lasts $1.31t_\eta$ or $3.275t_\kappa$), and Case H6, where the magnetic field eventually decays. The collapse in this case occurs suddenly, after the

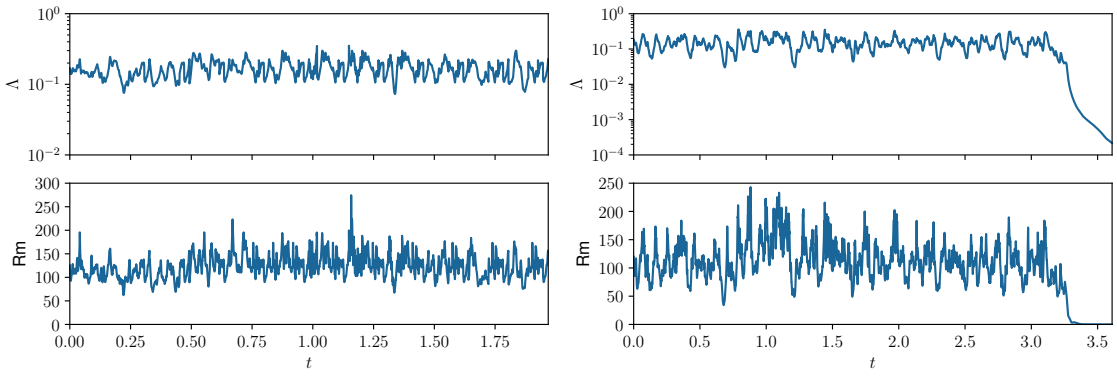


Figure 4.11: Time series of the Elsasser number, Λ, and magnetic Reynolds number, Rm, for (a) Case H5 ($\mathrm{Ra} = 0.89\mathrm{Ra}_c$) and (b) H6 ($\mathrm{Ra} = 0.87\mathrm{Ra}_c$), both at $\mathrm{Pm} = 2.5$ and $\mathrm{Ek} = 5 \times 10^{-6}$. Note that only a section of the full time series is shown in (a) for visual clarity.

magnetic field was sustained for approximately $1.34t_\eta$ (or $3.35t_\kappa$). This collapse is likely due to a strong fluctuation that caused the system to transition to the non-dynamo (and non-convective) state. Pinpointing precisely the end point of the subcritical branch (i.e. the lowest $\mathrm{Ra}/\mathrm{Ra}_c$ where a dynamo occurs) would require multiple numerical realisations at the same parameters to examine the transition statistics (e.g. van Kan *et al.*, 2019). This technique would have a considerable computational cost for the resolutions required here. Consequently, we are only able to determine the approximate end point of each branch, with a possible dependence of their location on the running times of the simulations and on the aspect ratio of the computational domain. Indeed, the system might be more sensitive to fluctuations, and hence prone to a dynamo collapse, when the scale separation between the box size and horizontal convective scale is small. In order to test the impact of smaller aspect ratio, we reproduced Cases I1-I5 at $\mathrm{Ek} = 5 \times 10^{-6}$ and $\mathrm{Pm} = 1$, reducing the computational domain to $\lambda = 0.5$ and again to $\lambda = 0.25$ with the horizontal resolution accordingly rescaled to 64^2 and 32^2 respectively and with similar run time. At $\lambda = 0.5$ the dynamo behaved similarly, with global output quantities approximately unchanged on average but experiencing larger fluctuations. Subcritical dynamo action was sustained as far as $0.93\mathrm{Ra}_c$. At $\lambda = 0.25$ fluctuations in the global output quantities were severe. For example, fluctuations in the Elsasser number and magnetic Reynolds number led to values in the range $O(10^{-2}) \lesssim \Lambda \lesssim O(10)$ and $O(1) \lesssim \mathrm{Rm} \lesssim O(10^3)$ respectively. This resulted in the dynamo decaying at $0.98\mathrm{Ra}_c$. For this set of parameters, reducing the aspect ratio has therefore decreased the depth of the subcritical branch. This is likely due to the decreased aspect ratio inhibiting the two-scale mechanism.

Figure 4.1 shows the location of the failed and sustained dynamo simulations for each series. The range of Ra where subcritical dynamos are maintained deepens when Ek

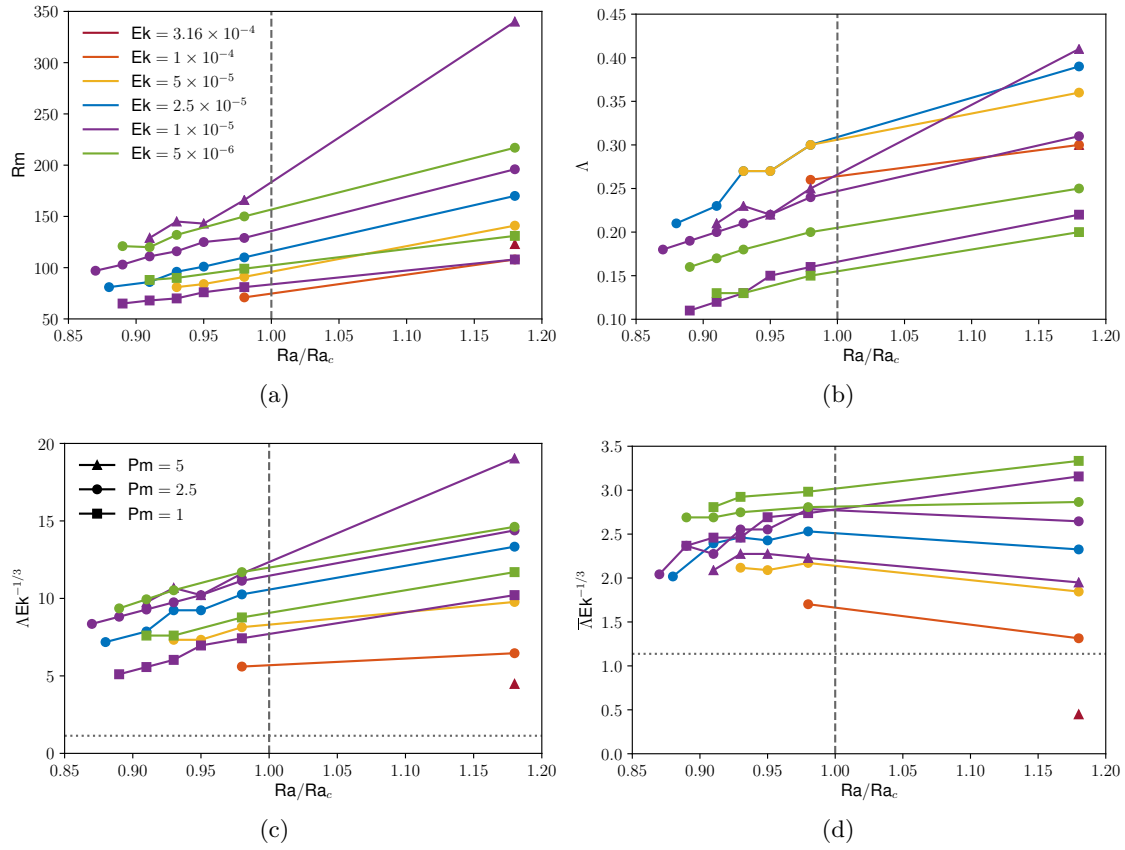


Figure 4.12: The dependence of some of the global output quantities as a function of $\mathrm{Ra}/\mathrm{Ra}_c$: (a) Rm, (b) Λ, (c) $\Lambda\mathrm{Ek}^{-1/3}$ and (d) $\overline{\Lambda}\mathrm{Ek}^{-1/3}$. The horizontal dotted line in (c)-(d) represents the switch-over value $\Lambda_{sw}\mathrm{Ek}^{-1/3} = 1.14$. As in Figure 4.1, each colour corresponds to a different value of Ek, as indicated in (a), whilst the different symbols correspond to different choices of Pm, as indicated in (c).

decreases in the moderate Ekman number regime. The effect of increasing Pm is not monotonic at this Ekman number: the subcritical range deepens when Pm increases from 1 to 2.5, but shrinks when Pm is increased further (the generally stronger fluctuations at higher Pm are more likely to cause the solution to drop off the dynamo branch). To understand the dependence of the subcritical range on Ek and Pm, we consider the necessary conditions for the existence of subcritical dynamos, suggesting an optimum parameter region at which subcritical dynamos exist. At least two conditions must be met: (i) a dynamo producing a coherent mean field must be operating, and (ii) the mean magnetic field must be of sufficiently large amplitude to alter the convective flows. The first condition is quantified by the existence of a threshold magnetic Reynolds number, Rm_t, and the second condition by a threshold Elsasser number, Λ_t. A dynamo can only survive in the subcritical range if $\mathrm{Rm} > \mathrm{Rm}_t$ and $\Lambda > \Lambda_t$. Violating one of these conditions would lead to a dynamo collapse and can possibly mark the location of the end point of the

subcritical branch. In practice, determining whether the transition $\mathrm{Rm} \approx \mathrm{Rm}_t$ or $\Lambda \approx \Lambda_t$ corresponds to the end points might prove difficult if the threshold values depend on Ek and Pm and because of the approximate location of the end points from the numerical results. Furthermore, variation in the efficiency of the two-scale dynamo mechanism due to the box-size introduces an additional parameter which may affect the transition. Determining a precise threshold at which dynamo action can no longer be sustained is clearly difficult as we cannot accurately determine whether a fluctuation is sufficiently strong enough to cause the dynamo to decay, especially considering that fluctuations are local events which may not accurately be captured by a globally averaged quantity such as Λ or Rm.

With these caveats in mind, we plot Rm as a function of $\mathrm{Ra}/\mathrm{Ra}_c$ in Figure 4.12(a). The end points of each series are located around $\mathrm{Rm} \approx 70-100$, although some dispersion exists due to the large temporal fluctuations of Rm. Overall, our simulations are in broad agreement with the idea that the dynamo collapse occurs when $\mathrm{Rm} \approx \mathrm{Rm}_t$. For a given Pm at fixed $\mathrm{Ra}/\mathrm{Ra}_c$, Rm increases when Ek decreases, which is consistent with the deepening of the subcritical range in this case. For fixed Ek and $\mathrm{Ra}/\mathrm{Ra}_c$, increasing Pm leads to a increase of the mean value of Rm, which is favourable for the subcriticality up to a point, but it also leads to an increase of the temporal fluctuations of Rm (see the standard deviation values in Table 4.1 for the series E, F and G for instance), which is detrimental for subcritical dynamo action because of the higher chances of pushing the system towards the non-dynamo state. These two competing effects lead to an optimal value of Pm, which here is around $\mathrm{Pm} \approx 2.5$. However, it should be noted that we have only explored a limited range in Pm which should be explored further in future work.

Figure 4.12(b) shows Λ as a function of $\mathrm{Ra}/\mathrm{Ra}_c$. For $\mathrm{Ek} < 10^{-4}$, Λ decreases with Ek for a fixed $\mathrm{Ra}/\mathrm{Ra}_c$ and Pm. The subcritical branch terminates when $\Lambda < 0.27$ for $\mathrm{Ek} = 5 \times 10^{-5}$ and when $\Lambda < 0.17$ for $\mathrm{Ek} = 5 \times 10^{-6}$ at $\mathrm{Pm} = 2.5$, so the dependence of the threshold value of Λ is weakly dependent on Ek. Eltayeb (1972) studied linear magnetoconvection in the presence of rotation (with the rotation axis aligned with the direction of gravity) and an imposed uniform horizontal magnetic field. Similarly to the case with imposed uniform vertical field (Chandrasekhar, 1961), three dynamically distinct regimes exist at a given Ekman number depending on the value of the Elsasser number that controls the strength of the imposed field, Λ_0: a rotation-dominated regime for $\Lambda_0 < \mathcal{O}(\mathrm{Ek}^{1/3})$, a magnetically-dominated regime for $\Lambda_0 > \mathcal{O}(1)$, and an intermediate regime, where Coriolis and Lorentz forces are of equal importance. The critical Rayleigh number in the intermediate regime is always smaller than in the rotation-dominated regime for low Ek, so the presence of an imposed horizontal field favours convection in this regime. The switch-over value of Λ_0 that marks the transition from the rotation-dominated regime and the intermediate regime occurs for $\Lambda_{sw} = 1.14\mathrm{Ek}^{1/3}$ for the same boundary conditions as the ones considered here (Equation (4.7)). Although the mean field generated in our fully

nonlinear dynamo simulations is not uniform, Λ_{sw} could be regarded as a lower bound for the threshold value Λ_t required for the existence of magnetically-modified convection and subcritical dynamos. Figure 4.12(c) shows $\Lambda \mathrm{Ek}^{-1/3}$ as a function of $\mathrm{Ra}/\mathrm{Ra}_c$ in our simulations. The subcritical branches terminate for $\Lambda \mathrm{Ek}^{-1/3} \approx 8 - 10$ when $\mathrm{Ek} < 10^{-4}$ and are always located above the theoretical switch-over value $\Lambda_{sw}\mathrm{Ek}^{-1/3} = 1.14$. This is consistent with Λ_{sw} being a lower bound for Λ_t. Since it is mainly the mean magnetic field that alters the convection, considering $\overline{\Lambda}\mathrm{Ek}^{-1/3}$, where $\overline{\Lambda}$ is based on the mean field amplitude only, might be more suitable. The evolution of $\overline{\Lambda}\mathrm{Ek}^{-1/3}$ as a function of $\mathrm{Ra}/\mathrm{Ra}_c$ plotted in Figure 4.12(d) shows that $\overline{\Lambda}\mathrm{Ek}^{-1/3}$ takes values around $2 - 4$ in the subcritical range and is, again, always above the theoretical switch-over value. The only Ekman number for which we did not observe a subcritical behaviour ($\mathrm{Ek} = 3.16 \times 10^{-4}$) has a supercritical dynamo which produces values of $\overline{\Lambda}\mathrm{Ek}^{-1/3}$ below the theoretical switch-over value. Perhaps at other values of Pm the dynamo could cross this switch-over value at this Ekman number.

If the magnetoconvection set-up of Eltayeb (1972) is a suitable simplified model to explain the results of our nonlinear simulations near the onset of convection, then a third condition exists for the depth of the subcritical range at fixed Ek: Ra must be greater than the theoretical critical Rayleigh number for convective onset at a given Λ, denoted by $\mathrm{Ra}_c(\Lambda)$. $\mathrm{Ra}_c(\Lambda)$ is the smallest possible Ra where subcritical dynamos might occur. Figure 4.13 shows $\mathrm{Ra}_c(\Lambda_0)$ normalised by $\mathrm{Ra}_c(\Lambda_0 = 0)$ as a function of $\Lambda_0 \mathrm{Ek}^{-1/3}$ in the rotation-dominated regime ($\Lambda_0 < \Lambda_{sw}$) and in the intermediate regime ($\Lambda_0 > \Lambda_{sw}$) based on the results of Eltayeb (1972) in the same configuration as described earlier. The minimum values of $\overline{\Lambda}\mathrm{Ek}^{-1/3}$ obtained in our subcritical dynamos are around $2 - 4$, which corresponds to values of $\mathrm{Ra}_c(\Lambda_0)/\mathrm{Ra}_c(\Lambda_0 = 0)$ around $0.3 - 0.6$. The subcritical range found in our simulations, which is always above $\mathrm{Ra} = 0.85\mathrm{Ra}_c(\Lambda_0 = 0)$, is consistent with these theoretical lower values. The quantity $\overline{\Lambda}\mathrm{Ek}^{-1/3}$ tends to increase when Ek decreases (for a fixed Pm), although this dependence is relatively small. This suggests that the possible subcritical range might extend slowly below $0.3 - 0.6\mathrm{Ra}_c(\Lambda_0 = 0)$ for dynamos at lower Ek and $\mathrm{Pm} = \mathcal{O}(1)$.

To conclude this section, we study the role of the kinetic helicity in our subcritical dynamos. In a study of dynamos driven by spherical rotating convection, Sreenivasan & Jones (2011) found that dipolar magnetic fields feedback on the flow such that they enhance the kinetic helicity. As kinetic helicity is often thought to be an important ingredient for large-scale dynamo action (e.g. Moffatt, 1978), its enhancement might lead to the subcritical behaviour observed in the simulations of Sreenivasan & Jones. To test whether a similar idea applies in our planar dynamos, we have compared the vertical profiles of the horizontally-averaged kinetic helicity $\mathcal{H}$ in the kinematic and saturated phases of all supercritical cases (nots shown). The comparison of the two phases is not entirely straight-

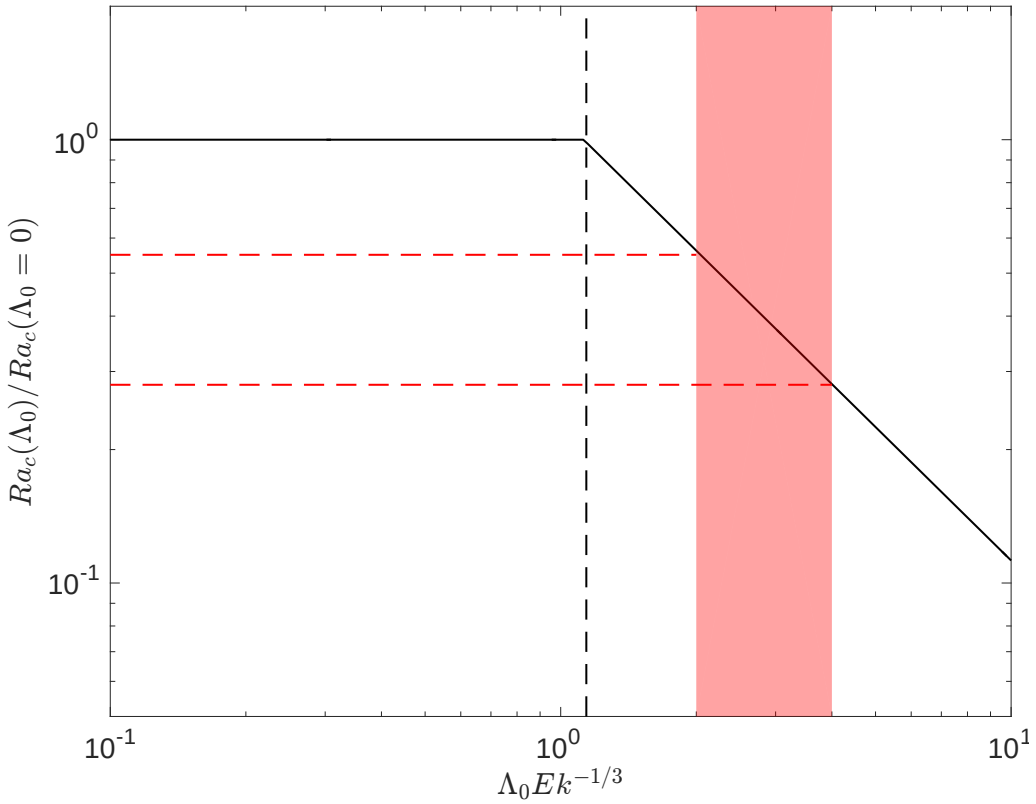


Figure 4.13: Critical Rayleigh number at the linear onset of rotating magnetoconvection (from Eltayeb, 1972) normalised by the critical Rayleigh number in the non-magnetic case as a function of $\Lambda_0 \mathrm{Ek}^{-1/3}$, where Λ_0 is the Elsasser number based on the imposed field strength, in the case where the rotation axis is aligned with gravity and the imposed field is uniform and horizontal. The boundary conditions are the same as in equation (4.7). The vertical dashed line corresponds to the switch-over value $\Lambda_{sw} \mathrm{Ek}^{-1/3} = 1.14$. The red area corresponds to the approximate values of $\overline{\Lambda} \mathrm{Ek}^{-1/3}$ in our subcritical simulations.

forward because the flow is more vigorous in the saturated phase, so we have also compared the profiles of the relative kinetic helicity $\mathcal{H}_{rel}$. The profiles are approximately sinusoidal (antisymmetric about the mid-plane), which is typical of planar rotating convection at low Ra (e.g. Cattaneo & Hughes, 2006). The maxima of $\mathcal{H}$ increase by approximately 20% in the saturated phase, but the maxima of $\mathcal{H}_{rel}$ decrease by approximately 30%. The increase of $\mathcal{H}$ that we observe here is very small compared with the increase measured by Sreenivasan & Jones in the presence of a dipolar magnetic field, suggesting that the enhancement of the helicity by the action of the magnetic field is probably not responsible for subcritical behaviour in our system.

4.4 Conclusions

We have studied dynamo action driven by rotating convection in a planar geometry, exploring a subcritical region of parameter space (below the non-magnetic convective onset) where dynamically-significant magnetic fields can be sustained for multiple magnetic diffusion times. These are therefore likely examples of subcritical dynamo action. In previous studies modelling this system, subcritical dynamo action was observed for either a fraction of a magnetic diffusion time (St. Pierre, 1993) or at a single Ekman number (Stellmach & Hansen, 2004). Here we have investigated the subcritical range for various Ekman numbers (smaller than 3.16×10^{-4}) and magnetic Prandtl numbers (greater than, or equal to, unity) to determine the conditions required for this behaviour. It is worth noting that in our dynamo simulations, where the sustained magnetic field has a marked effect on the convective flow, the magnetic energy is always larger than the kinetic energy in the saturated phase, while the Elsasser number (obtained either from the standard definition based on the box-size ohmic timescale or from the modified definition based on the dynamical timescale, §4.2.2) is always smaller than 1. The magnetic field visibly affects the convection when the standard Elsasser number based on the mean magnetic field, $\overline{\Lambda}$, becomes order $\mathrm{Ek}^{1/3}$, in agreement with results from linear magnetoconvection analysis (Chandrasekhar, 1961; Eltayeb, 1972).

At moderate Ekman numbers, the flow in the saturated phase of the dynamo clearly differs from the flow in the kinematic phase: it still takes the form of columnar cells aligned with the rotation axis, but with a larger horizontal lengthscale and a localised pattern. In this regime, Lorentz and Coriolis forces are of equal importance. We found that this magnetically-modified convection generates a coherent mean magnetic field according to a dynamo process similar to the two-scale mechanism of Childress & Soward (1972), which operates in the kinematic phase from the small-scale convection. This dynamo mechanism thus requires a sufficient scale separation between the box size and the convective roll size. The solutions first obtained in the supercritical regime near the onset are then tracked into the subcritical regime by gradually decreasing the Rayleigh number. Some of the subcritical branches extend down to $\mathrm{Ra} = 0.87\mathrm{Ra}_c$, with the dynamo and convection collapsing for smaller Ra. We identified two necessary conditions for subcritical dynamos: (i) the magnetic Reynolds number must be larger than approximately $70 - 100$ to produce a coherent mean magnetic field; (ii) $\overline{\Lambda}$ must be of order $\mathrm{Ek}^{1/3}$, so that the Lorentz and Coriolis forces are of equal importance at the convective scale. For a given ratio $\mathrm{Ra}/\mathrm{Ra}_c$, these two conditions are more easily met at lower Ek and larger Pm, so small Ek and large Pm favour subcriticality. However, larger values of Pm, and hence Rm, are also associated with larger fluctuations in the velocity, which can push the system away from the dynamo branch and towards the trivial state. We therefore find optimal values of Ek and Pm for

the subcritical range, which are approximately Ek = 10^{-5} and Pm = 2.5. However, it should be noted that we have only investigated a limited range in Pm which could be expanded upon in future work.

Chapter 5

Intermittent Dynamo Action at Low Ekman Numbers

In the previous chapter we explored dynamo action driven by rotating plane layer convection focussing on dynamo action below the critical Rayleigh number for the onset of convection in the absence of a magnetic field. At the Ekman numbers we considered in the previous chapter ($\mathrm{Ek} \geq 5 \times 10^{-6}$) we observed large-scale dynamos, where the magnetic field was dominated by a horizontal mean field, which we were able to extend into the subcritical regime. However, at smaller Ekman numbers ($\mathrm{Ek} = 5 \times 10^{-7}$) the behaviour of the nonlinear dynamo shows stark differences in the dynamics from cases at moderate Ekman number. In this chapter we will further explore these differences at low Ekman number. Preliminary results concerning only Cases J1-J4 in Table 5.1 were published alongside the previous chapter in Cooper *et al.* (2020).

5.1 Introduction

In Stellmach & Hansen (2004) (referred to as SH04), the Childress-Soward dynamo was explored as low as $\mathrm{Ek} = 5 \times 10^{-7}$. In the previous chapter, we successfully reproduce their results and further study subcritical dynamo action. In the supercritical scenario, at moderate Ekman numbers we observe the generation of a large-scale dynamo, influenced by a horizontal mean magnetic field. We then decrease the Rayleigh number below the onset of convection where we are able to sustain subcritical dynamos exhibiting similar behaviour.

At the lowest Ekman number studied in their work, SH04 observe different behaviour in the temporal evolution of the dynamo at $\mathrm{Ek} = 5 \times 10^{-7}$. A time series of the Elsasser number with snapshots of the flow is shown in Figure 5.1. At a reduced box size from their previous simulations, SH04 observe intermittent behaviour in the dynamo, fluctuating

between periods of stronger and weaker magnetic field. When the field is strong, large-scale convection is able to occur which transports heat more effectively than smaller-scale convection. However, the resulting flow is then unable to sustain the strong field and is broken down. As large-scale flow structures decay, the associated magnetic field also slowly decays. Whilst the field decays, instabilities generate small-scale convection. The regular structure of the small-scale convection thus leads to a re-amplification of the magnetic field, by a two-scale mechanism, which eventually leads to larger-scale convection again and so on, giving intermittent behaviour. At low Ekman numbers, convection responds sensitively to relatively minor changes in the strength of the applied magnetic field. Furthermore, from kinematic dynamo theory, minor changes in the flow structures can lead to relatively major changes in the efficiency of dynamo action. SH04 suggest that these effects likely result in a fluctuating dynamo which is highly time-dependent, where the dynamo fluctuates between bistable states.

A similar process is proposed based on magnetoconvection studies in spherical geometries by Zhang & Gubbins (2000*a*,*b*). According to Zhang & Gubbins, palaeomagnetic data suggests that the geomagnetic field might experience intermittent behaviour, fluctuating between a strong field state and weak field state, where the strength of the field drops by a factor of 5-10.

It is plausible that stable large-scale dynamos (which could display subcritical behaviour) exist at lower Ekman numbers than presented in the previous chapter near the convective onset for magnetic Prandtl numbers smaller than unity. For example, the geodynamo is estimated to exhibit large-scale dynamo action at Pm $\sim \mathcal{O}\left(10^{-6}\right)$ and Ek $\sim \mathcal{O}\left(10^{-15}\right)$ (Olson, 2015). We therefore consider the influence of Pm on large-scale dynamo action at lower Ekman numbers in this chapter.

5.2 Results

At low Ekman number, the behaviour of the supercritical dynamo in the saturated phase changes from that presented in Chapter 4. Table 5.1 summarises results from numerical simulations performed at Ek $= 5 \times 10^{-7}$ in a reduced computational domain of size $\lambda = 0.25$. For this low Ekman number, the computational domain is restricted to small aspect ratios to ensure that the convective motions can be sufficiently resolved without using substantially more grid points for the simulations. For $\lambda = 0.25$, there are approximately seven convective cells across the domain in the purely hydrodynamical case near the convective onset, so the scale separation between the box and convective scale is modest, but still probably sufficient to study large-scale dynamo action (Hughes & Cattaneo, 2008). In addition, a smaller aspect ratio restricts the maximum scales to which the convection can grow. It is possible that subcritical dynamos in smaller domains will be more prone to

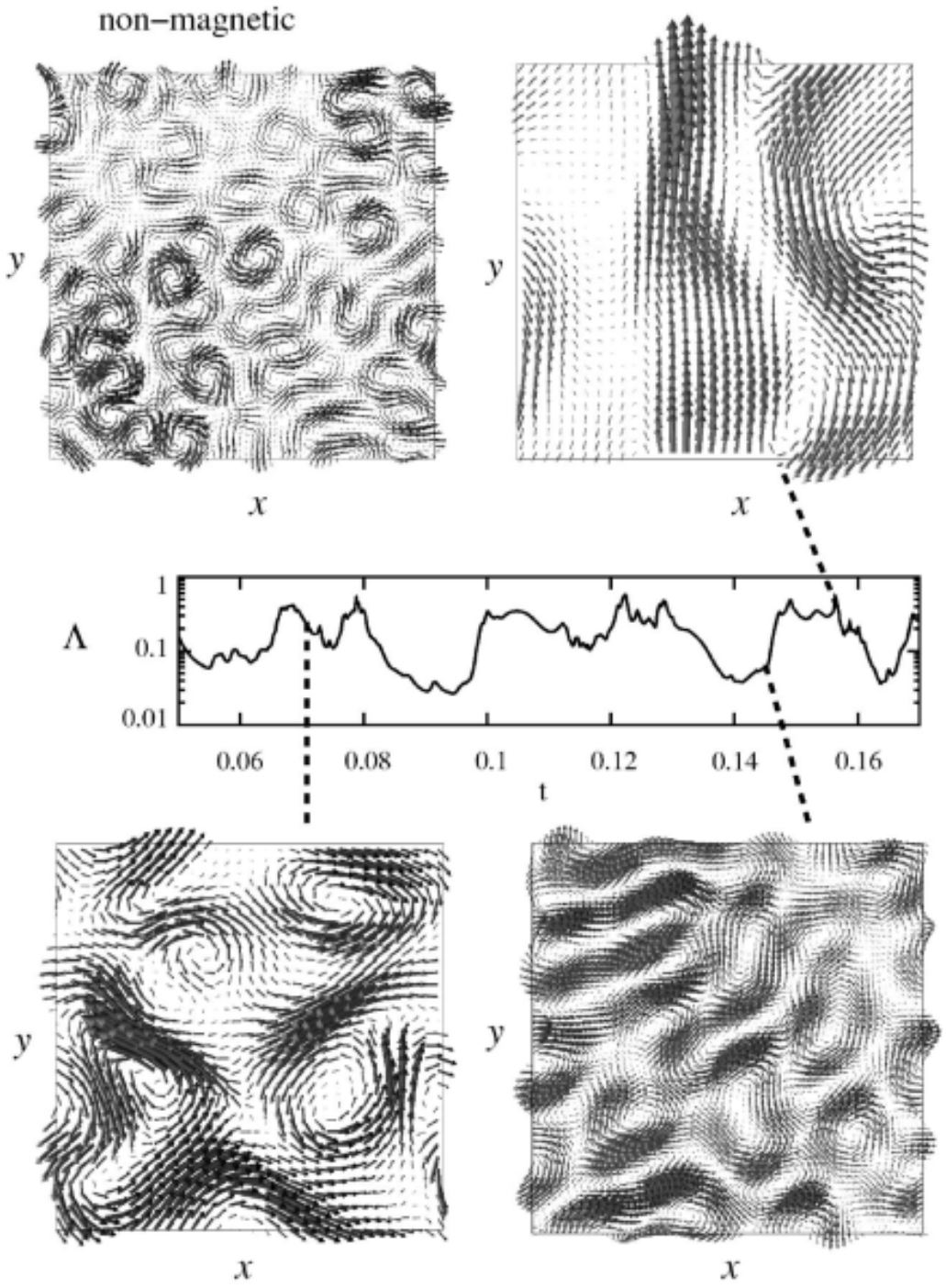


Figure 5.1: An intermittent dynamo simulation at $\mathrm{Pr} = 1$, $\mathrm{Pm} = 1$, $\mathrm{Ek} = 5 \times 10^{-7}$ and $\mathrm{Ra}/\mathrm{Ra}_c = 1.09$ in a computational domain of size $\lambda = 0.25$ showing a time series of the Elsasser number, Λ, and snapshots of the flow. Figure taken from Stellmach & Hansen (2004).

Case	Ek	Ra	$\mathrm{Ra}/\mathrm{Ra}_c$	Pm	λ	$N_x \times N_y \times N_z$	t_r	t_r/t_e	Rm	Λ	$\overline{\Lambda}$	M
J1	5×10^{-7}	2.5866×10^9	1.18	1	0.25	$64^2 \times 256$	0.14	0.85	$(17, 619)$	$(0.0026, 0.573)$	$(0.002, 0.141)$	$(0.38, 25.7)$
J2	5×10^{-7}	2.0824×10^9	0.98	1	0.25	$64^2 \times 256$	0.12	0.74	$(53, 891)$	$(0.040, 4.13)$	$(0.029, 0.100)$	$(2.48, 158.0)$
J3	5×10^{-7}	2.0385×10^9	0.95	1	0.25	$64^2 \times 256$	0.11	1.62	$(13, 757)$	$(0.010, 1.432)$	$(0.010, 0.154)$	$(1.88, 170.1)$
J4	5×10^{-7}	1.9947×10^9	0.91	1	0.25	$64^2 \times 256$	0.02	–	–	–	–	–
K1	5×10^{-7}	2.5866×10^9	1.18	2.5	0.25	$64^2 \times 256$	0.36	0.98	$(24, 2188)$	$(0.0093, 1.87)$	$(0.007, 0.175)$	$(0.64, 115)$
K2*	5×10^{-7}	2.5866×10^9	1.18	2.5	0.25	$128^2 \times 256$	0.034	0.16	–	–	–	–
K3*	5×10^{-7}	2.5866×10^9	1.18	2.5	0.25	$192^2 \times 256$	0.032	0.11	–	–	–	–
L1	5×10^{-7}	2.5866×10^9	1.18	0.5	0.25	$64^2 \times 256$	0.30	4.32	$(58, 659)$	$(0.051, 1.014)$	$(0.026, 0.270)$	$(0.65, 38.9)$

Table 5.1: Summary of the input and output quantities in the numerical simulations. N_x, N_y and N_z are the numerical resolution in x, y and z. t_r is the total run time in units of a thermal diffusion timescale, $t_\kappa = d^2/\kappa$. t_e is a characteristic timescale for the decay of the large-scale field due to turbulent diffusion from Cattaneo *et al.* (1991). In all cases the Prandtl number is kept constant at $\mathrm{Pr} = 1$. Dashes in the output quantities indicate that the simulation either never reached saturation or decayed to the trivial conducting state. The output quantities (defined in §4.2.2) quoted are the (minimum, maximum) values attained during low and high phases of intermittency respectively. The asterisk next to the case number denotes that the simulation performed has not yet saturated or is still in the exponential growth phase. Cases K2 and K3 were run to check the growth rates and spatial resolutions, in comparison to Case K1.

disruption by fluctuations. However, this reduction in domain size is a pragmatic choice that allows the lower Ek regime to be explored.

Intermittent Behaviour and Subcriticality

In Cases J1-J4 we remain at $\mathrm{Pm} = 1$ and study Rayleigh numbers ranging from $0.91\mathrm{Ra}_c$-$1.18\mathrm{Ra}_c$. Figure 5.2(a) shows the time series of Λ and Rm in Case J1 ($\lambda = 0.25$) for $\mathrm{Ra}/\mathrm{Ra}_c = 1.18$ and $\mathrm{Pm} = 1$, which exhibits different behaviour upon saturation to cases at the more moderate Ekman numbers explored in §4. We observe an intermittent behaviour: once the magnetic field reaches a sufficiently large amplitude, corresponding to $\Lambda \approx 10^{-0.5}$, the kinetic energy decays under the influence of the magnetic field, which (in turn) leads to a decay of the magnetic energy. Once Λ is sufficiently small, of the order of $10^{-2.5}$, the kinetic energy starts to increase again as the convection recovers. This is followed by a subsequent growth of the magnetic energy, and the cycle continues. SH04 demonstrated a similar intermittent behaviour for a slightly less supercritical case ($\mathrm{Ra}/\mathrm{Ra}_c = 1.09$) for the same aspect ratio. This intermittency is due to drastic changes in the flow during the phases of larger ($\Lambda \approx 10^{-0.5}$) and weaker ($\Lambda \approx 10^{-2.5}$) field strength. In § 4.3.2, we calculated a switch-over value for the Elsasser number where the system transitions from a rotationally-dominated regime to an intermediate regime with the Coriolis and Lorentz forces of equal importance (Eltayeb, 1972). The switch-over value of the Elsasser number is $\Lambda_{sw} = 1.14\mathrm{Ek}^{1/3} = 0.09$ at this Ekman number. In Case J1, both the traditional Elsasser number and mean-field Elsasser number drop below this switch-over value, entering the rotationally-dominated regime during the lowest intermittent phase. We therefore suspect that in this regime we will struggle to sustain a subcritical dynamo due to the Lorentz

force being unable to balance the Coriolis force at the convective scale, meaning that the flow becomes more rotationally constrained. Horizontal slices of the vertical velocity at different times are shown in Figure 5.3. At times corresponding to high values of Λ, the flow takes the form of a (near) box-sized mode suggesting that our results could be affected by the box-size. This large-scale mode is associated with an enhanced vertical velocity and temperature perturbation, and is thus efficient at transporting heat across the layer (corresponding to an increase in the Nusselt number of 180% compared with the purely hydrodynamical state). The emergence of this large-scale convective mode is a much more dramatic indication of the dynamical importance of the Lorentz forces than the fat localised convection columns observed in Figure 4.3 during the saturated phase of the dynamos at more moderate Ek (§4.3.1). At all times in the saturated phase, the mean e.m.f. is almost entirely produced by the box-sized mode at $k_h = 4$. As a reminder, this is the minimum non-trivial wavenumber in a computational domain of size $\lambda = 0.25$. The collapse of the magnetic energy following the emergence of the large-scale mode indicates that this type of flow is inefficient at driving the dynamo necessary to maintain a sufficiently strong magnetic field. It is possible that in a larger computational domain, a box-sized mode may not be produced that inhibits the dynamo. This may mean that in a larger box we observe behaviour more similar to that of Chapter 4. During the decaying phase, the flow becomes somewhat two-dimensional in Figure 5.3(c), displaying reduced x-dependence in u_z. At other times, similar behaviour is observed with reduced y-dependence also. The kinetic energy spectra in Figure 5.3 show that the small-scale convection is suppressed when the field is strong. Since these scales of motion are important contributors to the mean e.m.f. via the two-scale mechanism, this inhibits the dynamo. As the magnetically-driven large-scale mode decays with the magnetic field, the small-scale convection re-emerges, which allows the dynamo to recover.

Whilst the Elsasser number for given $\mathrm{Ra}/\mathrm{Ra}_c$ and Pm decreases with Ek in our (more moderately rotating) dynamo calculations (Figure 4.12(b)), the important parameter for the transition to magnetically-modified convection is $\overline{\Lambda}\mathrm{Ek}^{-1/3}$, which increases when Ek decreases (Figure 4.12(c)). For $\mathrm{Ek} = 5 \times 10^{-7}$, $\overline{\Lambda}\mathrm{Ek}^{-1/3} \approx 10$ at the peak of the magnetic energy, so the system enters more deeply into the intermediate regime described earlier than the cases at moderate Ek, which remain on its margins with $\overline{\Lambda}\mathrm{Ek}^{-1/3} \approx 2 - 4$ (Figure 4.13). The intermittent behaviour is therefore due to the ability of the small-scale convection to sustain magnetic fields of relatively stronger amplitude at low Ekman numbers, and then the apparent inability of the subsequent magnetically-driven large-scale convection mode to sustain the dynamo.

Figure 5.2(b) shows the time series of Λ and Rm in Case J2 ($\lambda = 0.25$) for $\mathrm{Ra}/\mathrm{Ra}_c = 0.98$. This is in the weakly subcritical regime, and has only been evolved for a short period of time. However, it exhibits similar intermittent behaviour to its supercritical

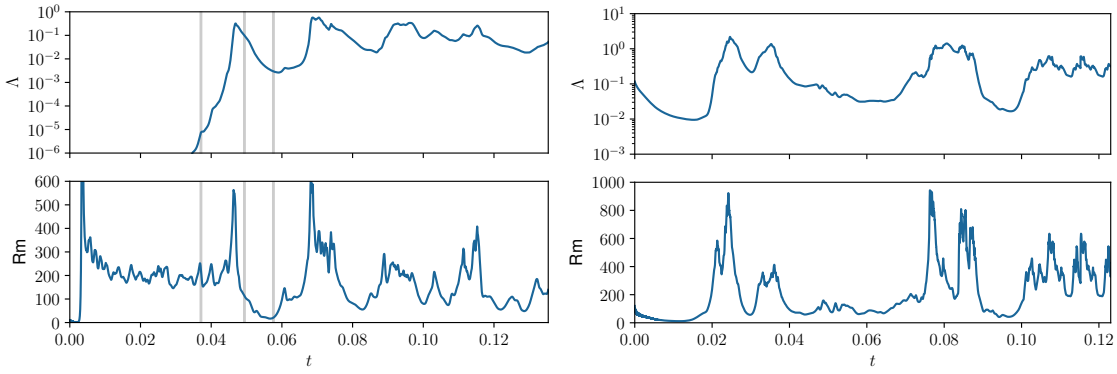


Figure 5.2: Time series of the Elsasser number Λ and magnetic Reynolds number Rm for Case J1 ($\mathrm{Ra}/\mathrm{Ra}_c = 1.18$) and Case J2 ($\mathrm{Ra}/\mathrm{Ra}_c = 0.98$) in Table 5.1. The grey lines indicate the locations of the snapshots presented in Figure 5.3.

counterpart. These preliminary results (albeit at low aspect ratio) suggest that it should still be possible to find convincing candidates for subcritical dynamo action in this low Ek regime, despite intermittent behaviour.

Higher Magnetic Prandtl Number

Intermittent behaviour is also observed at $\mathrm{Pm} = 2.5$ (Case K1), for the same Ekman number ($\mathrm{Ek} = 5 \times 10^{-7}$), Rayleigh number ($\mathrm{Ra} = 1.18\mathrm{Ra}_c$) and spatial resolution ($64^2 \times 256$) as in Case J1. The time evolution of the Elsasser number and magnetic Reynolds number are shown in Figure 5.4(a).

At higher Pm, the run time is quicker and we are able to perform simulations approximately as long as one decay time for the large-scale magnetic field. Additionally, higher Pm results in higher Rm, meaning that the dynamo is more efficient. Higher Rm can however prove more challenging to remain well-resolved during numerical simulations. Over this period, we observe multiple intermittent phases of varying extremity. Specifically, we focus on a long period of reduced Elsasser number from $t \approx 0.13$ to $t \approx 0.23$ (lasting approximately $0.1t_\kappa$), with extreme intermittency appearing to be more common at higher Pm. Other shorter phases of intermittency are observed which appear similar to the phases described for Case J1 previously, however this intermittent phase is particularly long-lasting, with the Elsasser number dropping from $\Lambda \approx 0.75$ to $\Lambda \approx 0.1$. This is accompanied by a drastic decrease in the magnetic Reynolds number down to $\mathrm{Rm} \sim \mathcal{O}(10)$. As previously discussed, the switch-over value of the Elsasser number for this Ekman number is $\Lambda_{sw} = 1.14\mathrm{Ek}^{1/3} = 0.09$. This is almost exactly the minimum Λ and $\overline{\Lambda}$ achieved during this extreme period of intermittency, suggesting that during periods of intermittency we again approach the rotationally dominant regime, before the convection eventually grows

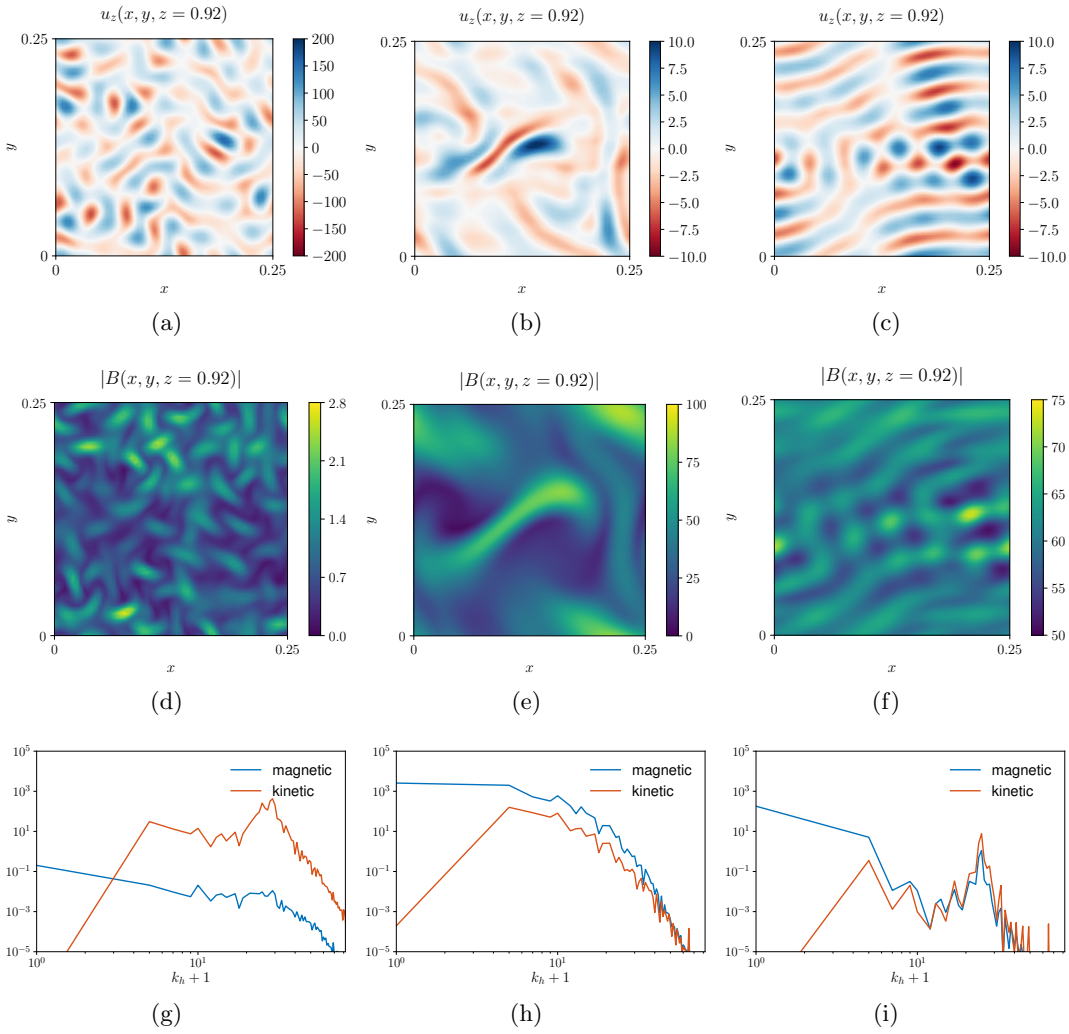


Figure 5.3: Snapshots of the horizontal distribution of the vertical velocity (a-c) and absolute value of the magnetic field (d-f) at $z = 0.92$ for Case J1 in (a,d) the kinematic phase, (b,e) near the peak of Λ and (c,f) during the decaying phase. The bottom row shows the corresponding power spectra for the magnetic energy (blue) and the kinetic energy (red), as a function of the horizontal wavenumber, $k_h = \left(k_x^2 + k_y^2\right)^{1/2}$, for (g) the kinematic phase, (h) near the peak in Λ and (i) during the decaying phase. The locations of each of these snapshots are represented by grey lines in Figure 5.2(a). In a computational domain of size $\lambda = 0.25$, the largest non-trivial scale is at $k_h = 4$.

again. When the convection begins to grow again, it does so rapidly in Λ and Rm, reaching similar levels to before their decrease. The appearance of the flow during weak and strong field phases of intermittency are shown in Figure 5.5, displaying a more extreme version of the behaviour observed in Figure 5.3. At peak Λ, large-scale convection is observed in the flow in Figure 5.5(g-l), along with a strong, large-scale magnetic field dominated by its mean component. However, the flow becomes unable to continue to sustain the

large-scale field. The field then breaks down the large-scale convection, accompanied by a decrease in the field itself. Similarly to Case J1 at Pm = 1, the flow decays as low as Rm $\sim \mathcal{O}(10)$ and the flow becomes more horizontally aligned along the x-direction than before, shown in Figure 5.5(a-f). Power spectra of the magnetic and kinetic energies are shown in Figure 5.6. In both phases of intermittency we observe peaks in the kinetic energy at $k_h \approx 4$, the largest-scale non-trivial wavenumber associated with the (near) box-sized mode. Eventually, smaller-scale convection begins to onset, visible in u_y (see 5.5(b)). The appearance of this small-scale convection takes the form of regular columnar convection in u_y, similar to that observed in the kinematic phase (where the Lorentz force is unable to alter the flow), and this begins to break the alignment along the x-direction. As the convection grows, the magnetic field regenerates with Λ reaching similar levels to before the decayed phase. In less extreme cases of intermittency than presented in Figures 5.3 and 5.5, we still observe large-scale structures which become unsustainable and are broken down before small-scale convection onsets, however these typically do not display the level of invariance along a particular axis during low phases of intermittency as the snapshots presented. It appears as though we observe a dynamo which oscillates between two bistable dynamo states. Sometimes the dynamo reaches a weak field state where the Elsasser number is approximately constant, and at other times it enters a more time-dependent strong field state, fluctuating between the two.

We often also observe strong larger-scale vortices at periods of enhanced Λ such as those shown in Figure 5.7. Intermittent dynamos have been observed in the large-scale vortex (LSV) dynamo at low Ekman numbers (Guervilly *et al.*, 2017). LSVs occur in rapidly rotating Rayleigh-Bènard convection at supercritical Rayleigh numbers. They are characterised by a system-sized vortex which spans the full computational domain in the z-direction. However, in our case these larger-scale structures typically exist across half of the computational domain and are associated with strong horizontal flows. When we study the time series of the contribution to the kinetic energy from each component of the velocity field, u_z is strongest during the kinematic phase. Once the system saturates onto our intermittent dynamo branch, the horizontal components of the flow dominate.

Similarly to the velocity field, once the field has broken down the large-scale convection, resulting in a decay of the field itself, we also observe a strongly aligned magnetic field, still dominated by its horizontal mean component, shown in Figure 5.8. During this particular low phase of intermittency, it is again almost x-invariant, like the flow. However, weak small-scale convection leads to some weak variation in the field, especially in B_y. Furthermore, the structure of the mean horizontal magnetic field is less complex in z than during phases of weaker field (Figure 5.9). The x-component of the mean field is approximately anti-symmetric across the midplane, whilst the y-component is almost symmetric. In contrast, during periods of increased field this is no longer the case, the

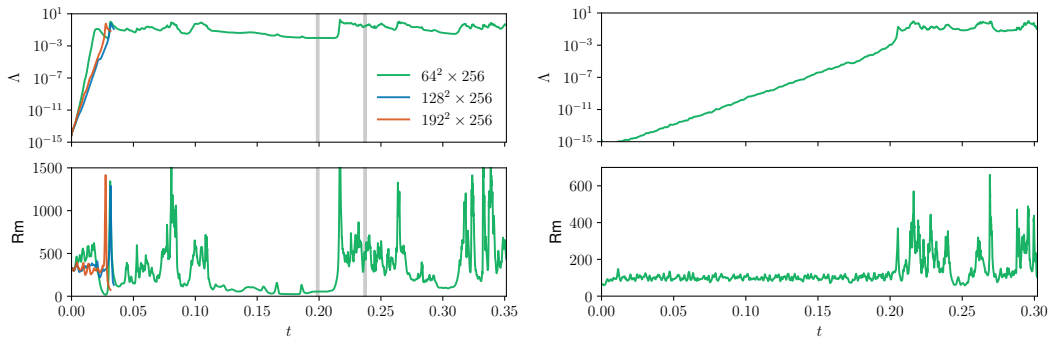


Figure 5.4: Time series of the Elsasser number Λ and magnetic Reynolds number Rm for (a) Cases K1-K3 at Pm = 2.5, and (b) Case L1 at Pm = 0.5. Both cases are at Ek = 5×10^{-7}, $\mathrm{Ra}/\mathrm{Ra}_c = 1.18$, and in a computational domain of size $\lambda = 0.25$.

field acts on large scales and displays no symmetry across the midplane in $\overline{B_x}$ but some anti-symmetry in $\overline{B_y}$.

A time series of both components of the horizontal mean magnetic field are shown in Figure 5.9(c). During phases of higher magnetic field, the mean-field components somewhat oscillate in time, similarly to our dynamos in §4, but exhibiting greater time-dependence. However, during low phases in the magnetic field, both components decay with the overall field and become approximately constant whilst the convection regenerates. This is often observed in weak field dynamos in spherical geometries (e.g. Dormy, 2016). It is noticeable that $\overline{B_y}$ decays more slowly than $\overline{B_x}$, potentially due to its higher anti-symmetry before the decaying phase. Furthermore, during higher phases we also observe some symmetry in the depth-dependence across the midplane which becomes less clear due to the colourscale but still exists during phases of decayed field, shown in Figure 5.10. A time series of the horizontal components of the mean e.m.f. are shown in Figure 5.11. During phases of larger-scale convection and stronger magnetic field, both components of the mean e.m.f are mostly positive across the majority of the vertical domain producing a mean e.m.f but exhibiting little/no symmetry across the midplane. During phases of weak magnetic field the horizontal mean e.m.fs are both very weak indicating that there is little/no production of the mean field during low phases.

Lower Magnetic Prandtl Number

For the same Ekman number, Rayleigh number and spatial resolution as in Cases J1 and K1, we also study intermittency at Pm = 0.5 (Case L1). As aforementioned, at lower Pm we aim to produce a weaker Elsasser number, such that the magnetically-driven box-sized mode is no longer produced, potentially avoiding intermittent behaviour. However lower Pm does lead to lower Rm and hence the dynamo is less efficient. The time evolution of

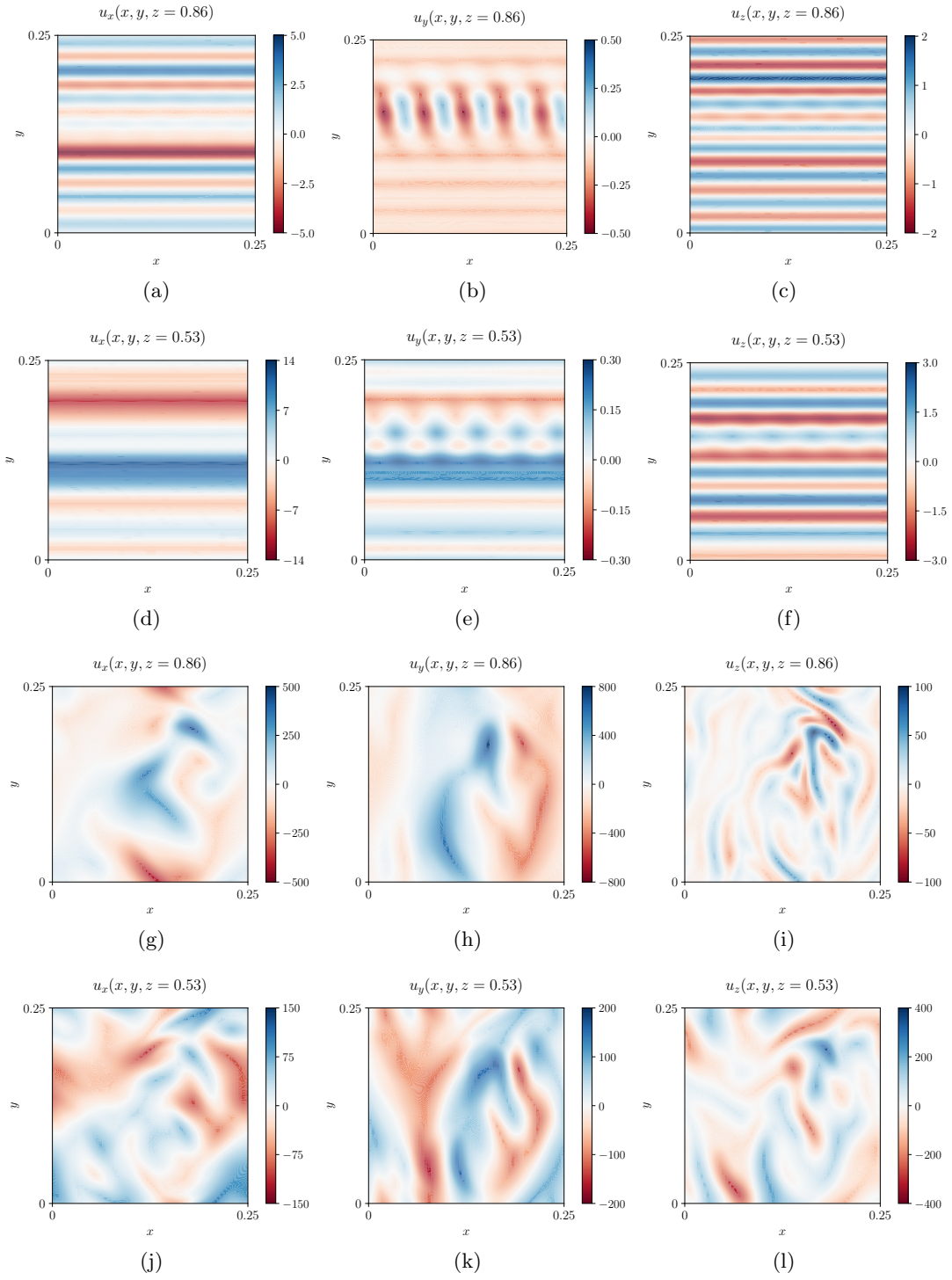


Figure 5.5: Snapshots from Case K1 at $\mathrm{Ek} = 5 \times 10^{-7}$, $\mathrm{Ra}/\mathrm{Ra}_c = 1.18$ and $\mathrm{Pm} = 2.5$ with resolution $64^2 \times 257$, showing (left) u_x, (middle) u_y, and (right) u_z, all in slices at either $z = 0.86$ or $z = 0.53$. Snapshots are taken at (a-f) $t = 0.1989$, where Λ is in a weak field phase, and (g-l) $t = 0.2372$, where Λ is in a stronger field phase. The locations of each of these snapshots are represented by grey lines in Figure 5.4.

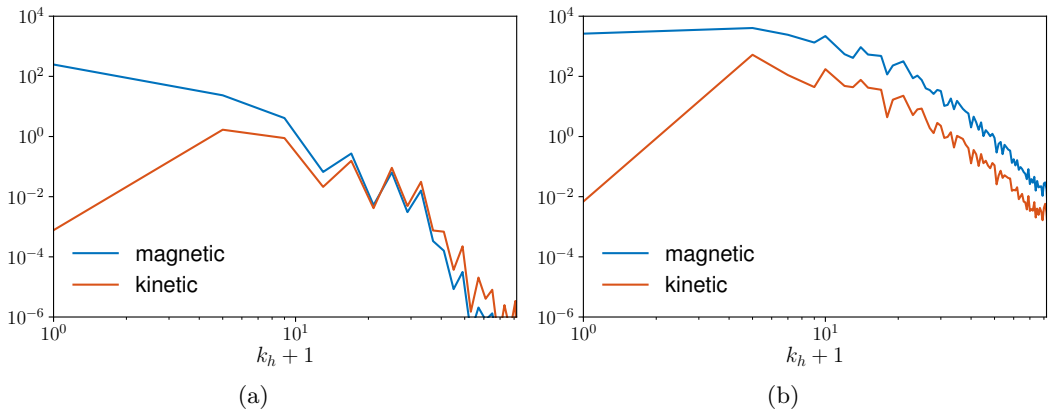


Figure 5.6: Power spectra (calculated from representative snapshots) of the magnetic energy and kinetic energy as a function of the horizontal wavenumber, $k_h = (k_x^2 + k_y^2)^{1/2}$, at (a) $t = 0.1989$, where Λ is at the bottom of an intermittent phase, and (b) $t = 0.2372$, where Λ is in a stronger phase of intermittency in Case K1. In order to include the contribution from the mean magnetic field (for which $k_h = 0$) on the logarithmic scale, the horizontal wavenumbers are shifted to $k_h + 1$.

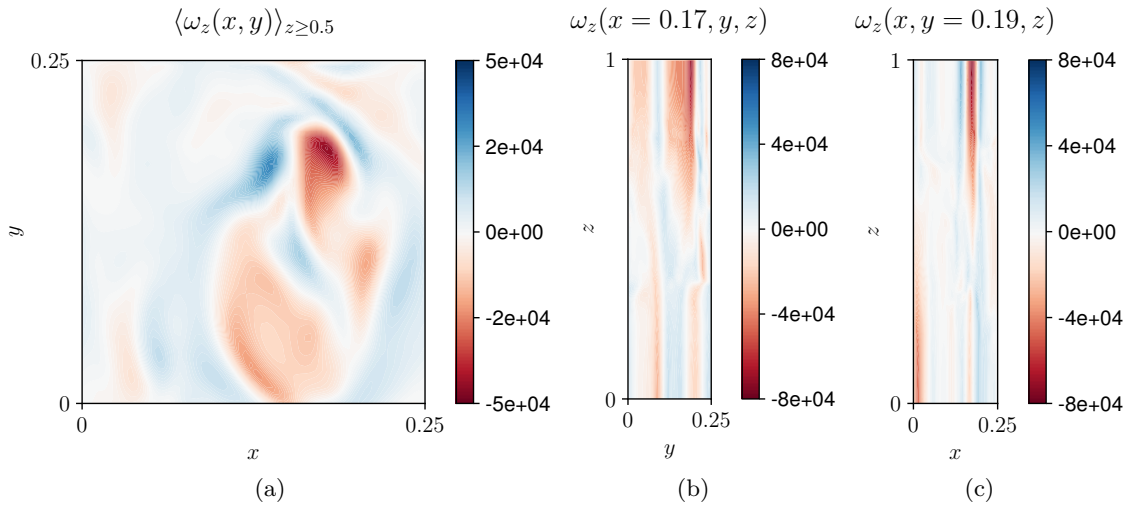


Figure 5.7: Snapshots from Case K1 at $t = 0.2372$, where Λ is in a stronger phase of intermittency, showing the z-component of the vorticity, ω_z, when (a) averaged over the upper half of the domain, (b) in a slice at $x = 0.17$, and (c) in a slice at $y = 0.19$.

the Elsasser number and magnetic Reynolds number are shown in Figure 5.4(b).

At lower Pm the growth rate of the magnetic field in the kinematic phases is much slower, taking approximately $0.2t_\kappa$ to reach the super-exponential growth phase before saturating. We see little Pm-dependence in the maximum or minimum values of Λ or Rm attained during intermittent phases. However, phases of low magnetic field do appear to be shorter-lived than at higher magnetic Prandtl numbers in units of t_κ. However, in units of t_η (the magnetic diffusion timescale), they are approximately the same. At Pm = 0.5

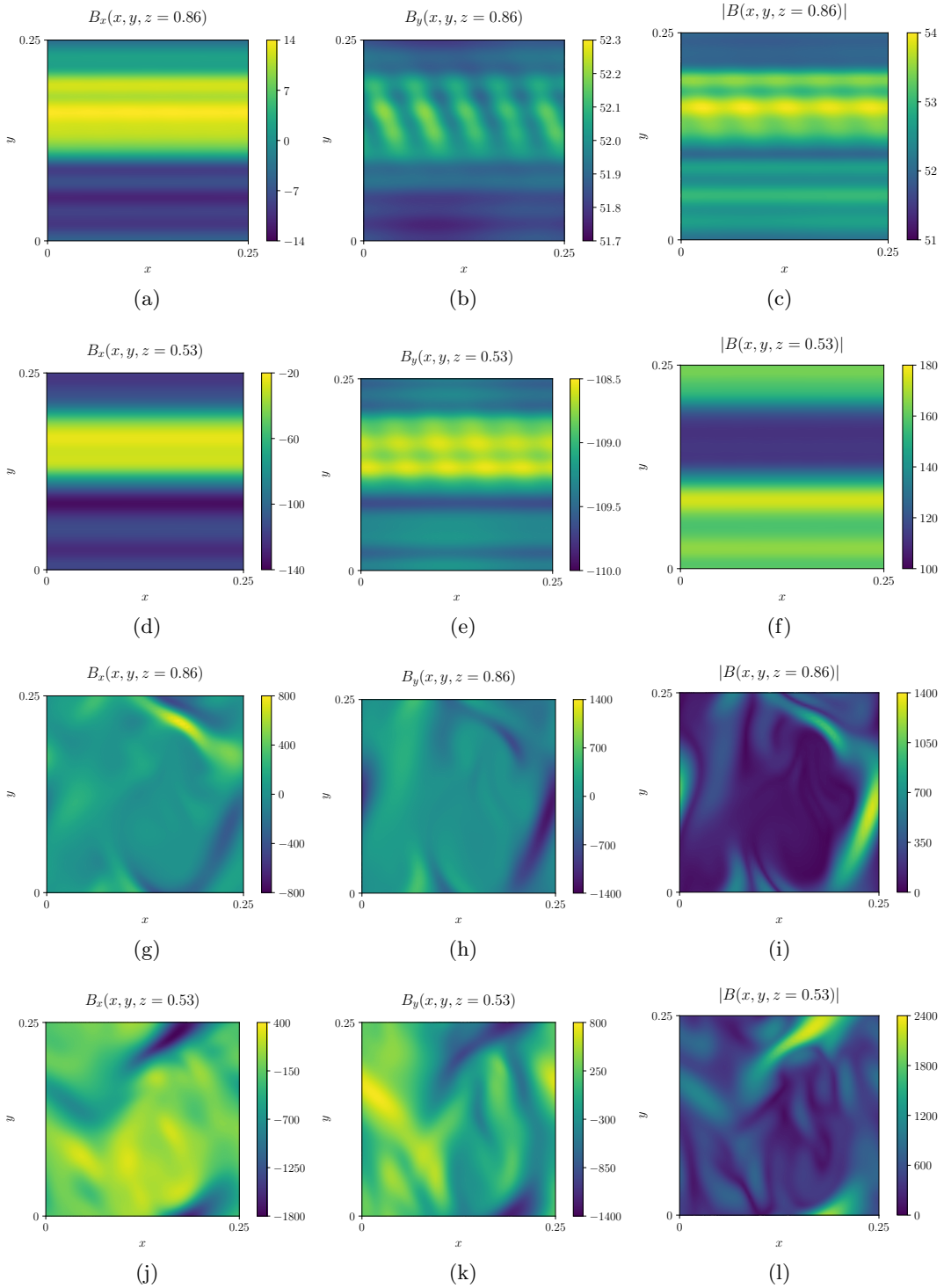


Figure 5.8: Snapshots from Case K1 at $\mathrm{Ek} = 5\times10^{-7}$, $\mathrm{Ra}/\mathrm{Ra}_c = 1.18$ and $\mathrm{Pm} = 2.5$ with resolution $64^2 \times 257$, showing (left) B_x, (middle) B_y, and (right) the absolute value of the magnetic field, $|\boldsymbol{B}|$, all in slices at either $z = 0.86$ or $z = 0.53$. Snapshots are taken at (a-f) $t = 0.1989$, where Λ is at the bottom of an intermittent phase, and (g-l) $t = 0.2372$, where Λ is in a stronger phase of intermittency. The locations of each of these snapshots are represented by grey lines in Figure 5.4.

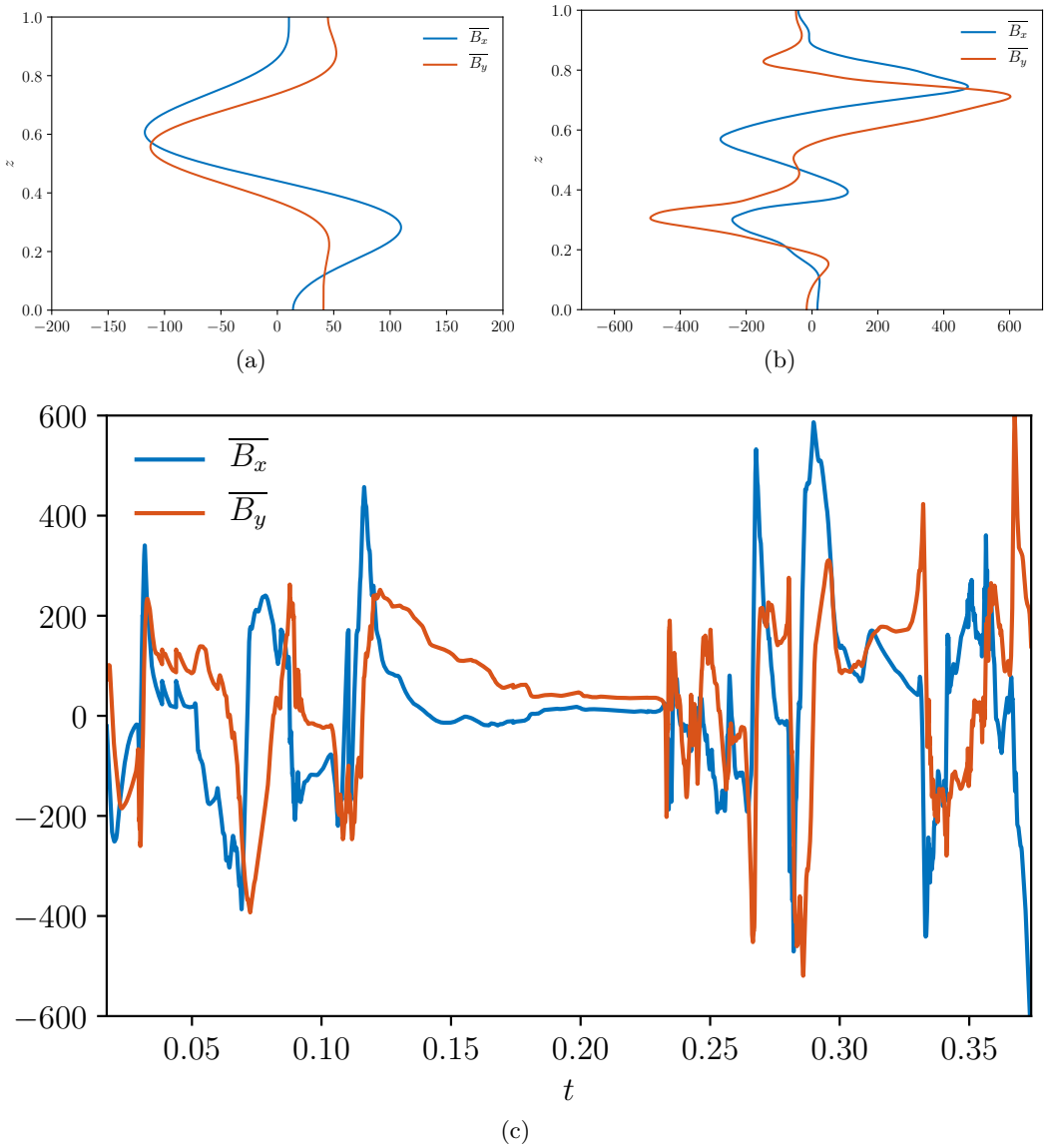
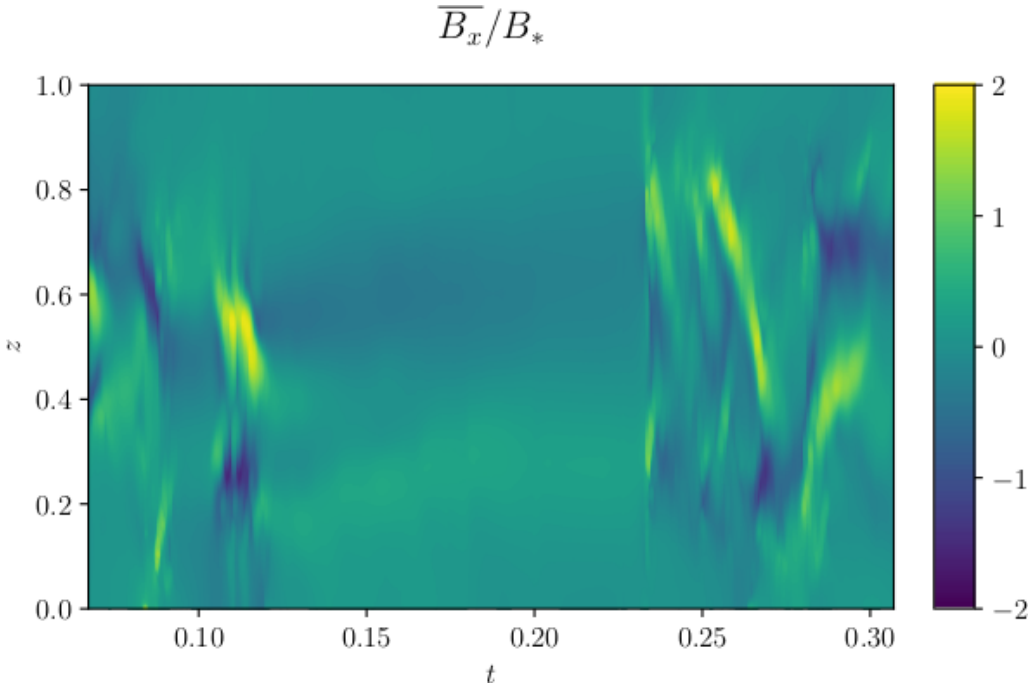
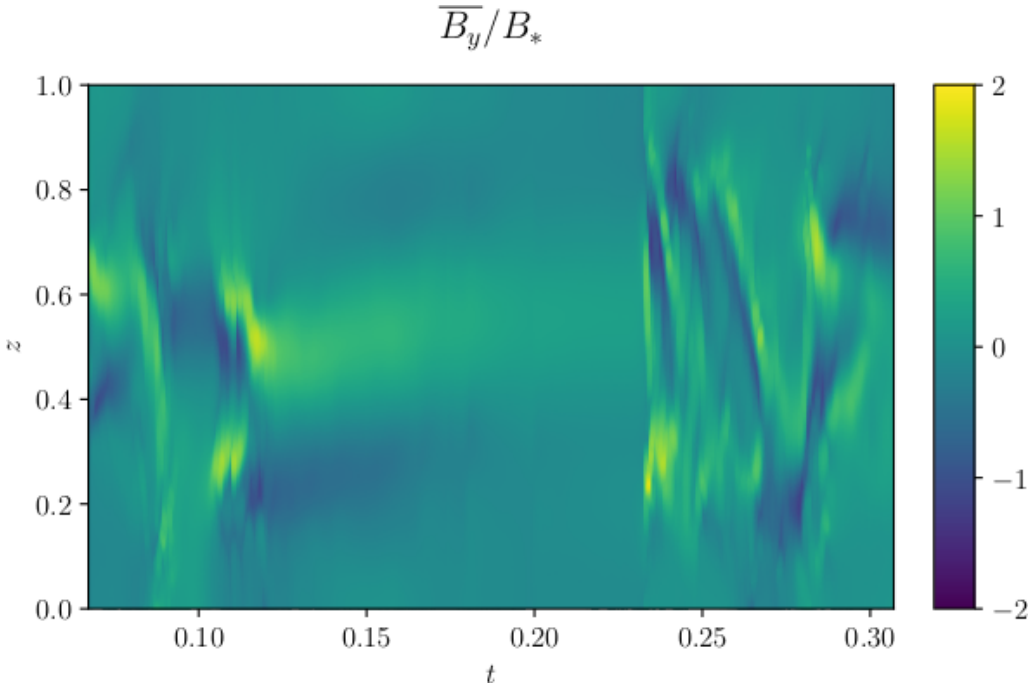


Figure 5.9: Snapshots from Case K1 at Ek $= 5 \times 10^{-7}$, Ra/Ra$_c$ $= 1.18$ and Pm $= 2.5$ with resolution $64^2 \times 257$, showing the z-profile of the horizontal mean magnetic field at (a) $t = 0.1989$, where Λ is at the bottom of an intermittent phase, and (b) $t = 0.2372$, where Λ is in a stronger phase of intermittency. The locations of each of these snapshots are represented by grey lines in Figure 5.4. (c) A time series of the x and y components of the mean magnetic field at $z = 0.43$.

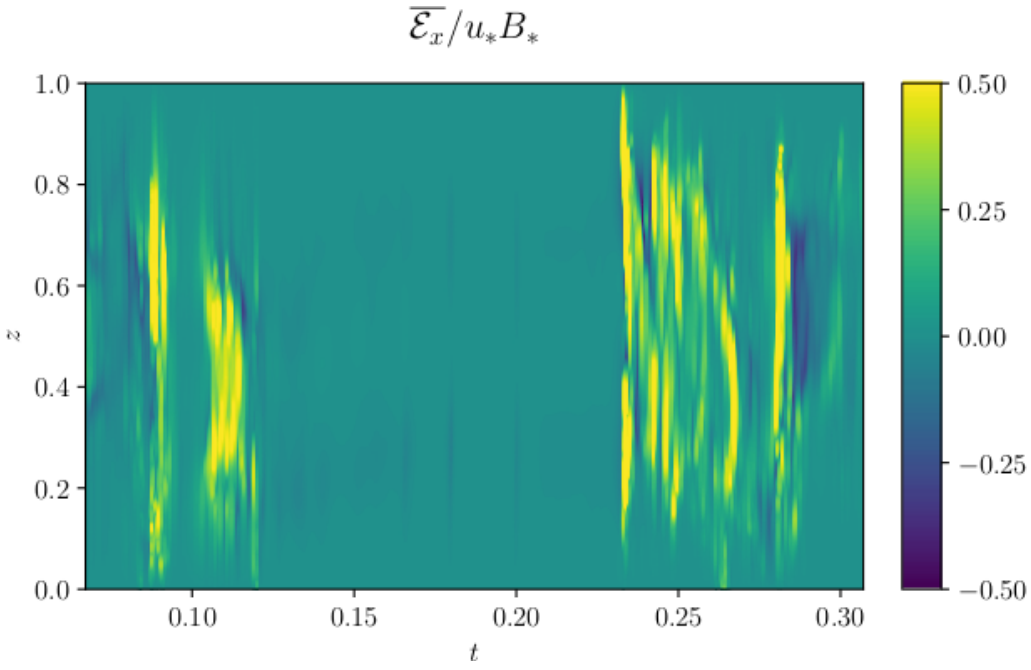


(a)

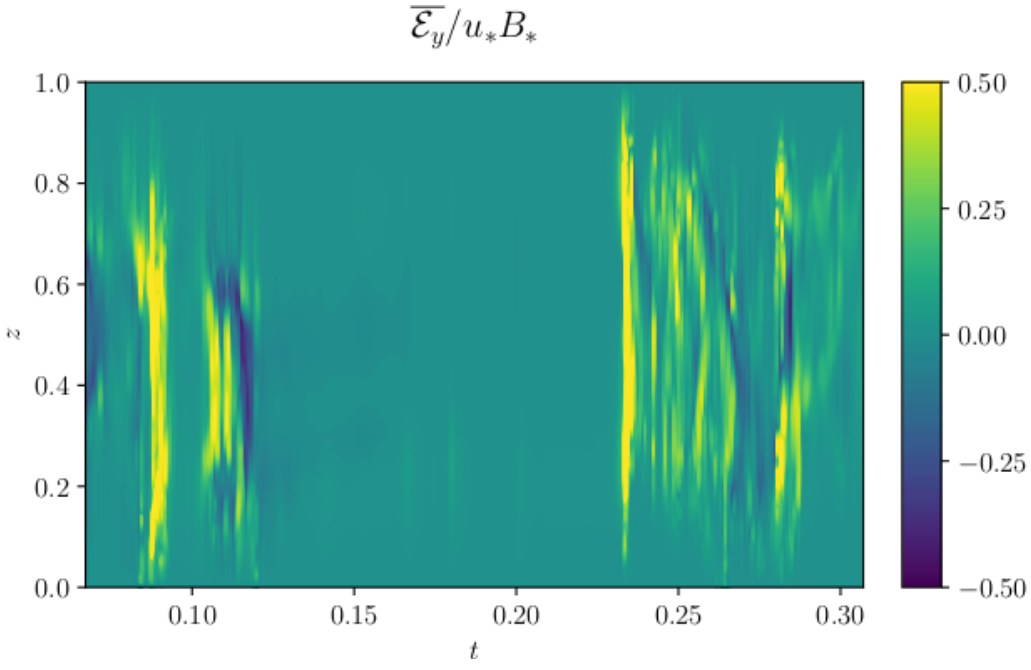


(b)

Figure 5.10: Time series for Case K1 of (a) the x-component, and (b) the y-component of the mean horizontal magnetic field as a function of depth, scaled with respect to the r.m.s of the field.



(a)



(b)

Figure 5.11: Time series for Case K1 showing (a) the x-component and (b) the y-component of the mean e.m.f as a function of depth and scaled with respect to r.m.s values.

the longest phase of reduced magnetic field lasts $\approx 0.02t_\kappa = 0.04t_\eta$, whilst at Pm = 2.5 we studied a phase lasting $\approx 0.1t_\kappa = 0.04t_\eta$.

It is important to note that we have only investigated $0.5 \leq \mathrm{Pm} \leq 2.5$ so have not studied many orders of magnitude in Pm and may have introduced some parameter bias. However, if we use the growth rates during the kinematic phases at Pm = 0.5 and Pm = 1 to estimate the minimum Pm for the dynamo to onset (by basic linear regression) we find that $\mathrm{Pm} \gtrapprox 0.39$ so we cannot study magnetic Prandtl numbers much lower than we have already if we want to study dynamo action.

In the flow and field, we observe similar behaviour to that discussed in the previous section, however the alignment of the flow and field along a particular axis during weak field phases of intermittency appears to be less common and less strongly aligned at lower Pm, likely due to the weaker field being less able to influence the flow.

Increasing the Numerical Resolution

To determine the effects of varying the spatial resolution, we perform additional simulations at Pm = 2.5, keeping the Ekman number, Rayleigh number and domain size the same as previous simulations within this chapter. The larger magnetic Prandtl number case was chosen in order to speed up the run time (since the code uses an adaptive timestep), enabling us to compare the growth rates across different spatial resolutions and their behaviour upon saturation. Furthermore, comparing the values in Table 5.1 we observe that this high Pm case reaches higher magnetic Reynolds numbers than our other cases and so leads to more efficient dynamo action, but is also more prone to being under-resolved. In Cases K1-K3 of Table 5.1, we perform simulations with horizontal resolutions consisting of 64, 128 and 192 points, whilst the vertical resolution remains constant at 256 points.

For Cases K1-K3, the time evolution of the Elsasser number Λ and magnetic Reynolds number Rm are shown in Figure 5.4(a). We observe slight discrepancies in the growth rate of the magnetic field during the kinematic phase between Case K1 (at $64^2 \times 256$ resolution) and its higher resolution counterparts, though these were estimated by a simple linear regression. The growth rates at resolutions of $128^2 \times 256$ (Case K2) and $192^2 \times 256$ appear to be slightly slower (at $\ln \Lambda \sim 975t$ and $\ln \Lambda \sim 1028t$ respectively) than in Case K1 (with growth rate $\ln \Lambda \sim 1709t$) but appear to be consistent with each other. Cases K1 to K3 have all saturated at approximately the same Elsasser number indicating that despite the resolution being marginal in Case K1, it is likely still sufficient. Although the growth rate of Case K1 did not identically match that of Cases K2-K3, the energy power spectra presented in Figure 5.6 appear well-resolved, covering just under two orders of magnitude between the box-sized convective mode and the highest wavenumbers before dealiasing.

Unfortunately, we have been unable to confidently explore intermittent behaviour in

Cases K2 and K3 post-saturation. After reaching peak Λ, the flow and field both decay suggesting we may be entering into a period of weak field similar to that observed in Case K1 before observing intermittency. Alternatively, the solution could be heading towards a completely different state. Snapshots of the flow and the field become extremely two-dimensional, becoming x-invariant, as previously discussed in the lower-resolved case. However, over further temporal evolution these cases never exited the weak field phase and the flow and field exhibited no variance at all in the x-direction. For this reason we have cut our time series short and not presented any data post-saturation, focussing only on the growth phases which appeared reasonable. Furthermore, some output files exhibited discontinuities, notably time series exported as .txt files such as a time series of the energy by mode. Due to time constraints, we could not investigate this in more detail, however, this does not appear to be an issue with our other low Ekman number simulations at lower resolutions and was not an issue during the growth phases of Cases K2 and K3. Since other time series outputted by the code do not exhibit discontinuities we suspect that our issues could be related to the outputting procedures of particular files. The numerical code used also has an adaptive timestep which depends on the spatial resolution and Ekman number, amongst other parameters. The size of this timestep becomes extremely small at extreme parameters (of order $\sim 10^{-10}$), so this outputting error could be related to such a small timestep.

5.3 Conclusions

Following on from Chapter 4, we have further explored dynamo action driven by rotating planar convection at lower Ekman numbers ($\mathrm{Ek} = 5\times10^{-7}$) and multiple magnetic Prandtl numbers $\mathrm{Pm} = \{0.5, 1, 2.5\}$, observing different behaviour from simulations performed at moderate Ekman numbers. At small Ekman numbers, we obtain an intermittent dynamo in the saturated phase due to the emergence of a (near) box-size convection mode. This large-scale mode is produced in the regime where Lorentz and Coriolis forces are of equal importance when $\overline{\Lambda} \gg \mathcal{O}(\mathrm{Ek}^{1/3})$, a situation that arises for all magnetic Prandtl numbers studied and $\mathrm{Ek} = 5 \times 10^{-7}$ in our simulations. The large-scale mode is unable to sustain the large-scale dynamo, unlike the magnetically-modified convection at larger Ek, and so this leads to cycles of growth and decay of the magnetic field. This appears to be the same as the intermittent dynamo presented in Stellmach & Hansen (2004). Speculatively, if the computational domain was increased then we may not observe the production of a box-sized mode, and may therefore obtain dynamos similar to those presented in Chapter 4, which could be explored in future work. Surprisingly, despite this intermittent behaviour it appears that we are able to sustain dynamo action below the onset of convection, albeit only just below Ra_c. In the subcritical cases we still observe intermittent behaviour

although it should be noted that these cases have not been run for long (approximately 10% of a thermal diffusion time), and are at relatively low spatial resolutions, so further study of this regime is needed. Before we can accurately study subcritical behaviour at low Ekman numbers in our intermittent dynamos, we need to further understand the intermittent mechanism, performing simulations at higher numerical resolutions.

In the previous chapter we showed that Rm needs to be sufficiently large to produce a coherent mean magnetic field in order to sustain a subcritical dynamo. However larger Rm also means larger fluctuations in the velocity. With subcritical dynamos being so sensitive to perturbations, larger fluctuations may push the system away from the dynamo branch, causing it to decay to the trivial conducting state. In this chapter we observed intermittent behaviour due to the production of a magnetically-driven large-scale mode. We studied lower magnetic Prandtl number, aiming to produce an Elsasser number that was sufficiently small (of order $\mathrm{Ek}^{1/3}$) to avoid the production of such a magnetically-driven mode, hence preventing intermittent behaviour. However, even at $\mathrm{Pm} = 0.5$, this box-sized mode was still produced and intermittent behaviour was observed. We found that varying the magnetic Prandtl number showed little evidence of affecting the presence of intermittent behaviour and since our lowest Pm case is fairly close to the minimum Pm for the dynamo to onset, we cannot study values much lower. The only noticeable difference of varying Pm is how long-lasting low phases of intermittency are observed more frequently at higher Pm. However this may depend on the selection of timescale, since on the magnetic diffusion timescale the low phases last for approximately the same length of time. At $\mathrm{Pm} = 2.5$ we observe a long-lasting phase of reduced field for $\approx 0.1t_\kappa$ or $\approx 0.04t_\eta$, at $\mathrm{Pm} = 1$ the longest-lasting low phase takes $\approx 0.03t_\kappa$ or $\approx 0.03t_\eta$ before the flow and field regenerate, and at $\mathrm{Pm} = 0.5$ low phases of intermittency last at most $\approx 0.02t_\kappa$ or $\approx 0.04t_\eta$. Longer runs should be performed to clarify whether this remains true overall. Further study of subcritical behaviour at low Ekman numbers is required despite this intermittency, although we expect that intermittent behaviour would inhibit subcriticality.

Few examples of numerical dynamo simulations producing coherent large-scale magnetic fields exist in rapidly-rotating planar convection, except for the dynamos operating near the convective onset. Another example of an intermittent dynamo in this system is the large-scale-vortex dynamo that occurs for moderately supercritical values of the Rayleigh number, typically $\mathrm{Ra} > 3\mathrm{Ra}_c$ (Guervilly *et al.*, 2017). This dynamo relies on the presence of the large-scale vortices that form spontaneously in non-magnetic rotating convection when the small-scale convective flow is both sufficiently turbulent (hence the condition that $\mathrm{Ra} > 3\mathrm{Ra}_c$) and anisotropic due to the rapid rotation (Julien *et al.*, 2012; Guervilly *et al.*, 2014; Favier *et al.*, 2014). The large-scale vortices play a crucial part in the dynamo mechanism, but tend to be disrupted when the magnetic field reaches a

critical strength, leading to an intermittent behaviour. The key difference between the near-onset intermittent dynamo described here and the large-scale-vortex dynamo is that the large-scale mode of the near-onset dynamo is magnetically driven and is unable to maintain dynamo action, while the large-scale vortices at larger Ra are hydrodynamically driven and play an active role in the magnetic field generation. A stable (i.e. not intermittent) large-scale dynamo also exists for similar parameters as the large-scale-vortex dynamo (Masada & Sano, 2014; Bushby *et al.*, 2018). This dynamo also requires the presence of the large-scale vortices during the kinematic phase, but the dynamo then persists without the regeneration of the large-scale vortices. However, it only works when vertical field boundary conditions are used (Bushby *et al.*, 2018) or when convectively stable layers are included above or below the convective layer (Käpylä *et al.*, 2013), which permit the magnetic flux to escape from the convective domain. Dynamo simulations using perfectly conducting magnetic boundary conditions outside of the parameter windows where near-onset dynamos and large-scale-vortex dynamos operate produce only small-scale magnetic fields with no coherent large-scale fields (e.g. Cattaneo & Hughes, 2006; Tilgner, 2012; Favier & Bushby, 2013).

Chapter 6

Conclusions

In this section we outline the key conclusions of this thesis and discuss how they affect our knowledge of rapidly rotating convection and convectively driven dynamos.

It is clear that convection is an important mechanism in the fluid mechanics of geophysical and astrophysical systems, especially regarding the generation of a self-sustaining fluid dynamo, such as the geodynamo. With many planets and stars exhibiting rapid global rotation and large-scale magnetic fields, it is unsurprising that the Coriolis and Lorentz forces play an important role in the dynamics. However, despite decades of research replicating many of the observed features of the geodynamo, we still do not fully understand how these forces interact with convective fluid motions and each other at parameters relevant to planetary cores.

In this thesis, we have mostly focussed on subcritical behaviour, motivated by the cessation of the Martian dynamo and the ability of the Coriolis and Lorentz forces to allow convection and dynamo action to be sustained below the critical values predicted by linear theory.

In Chapter 3 we explored the qualitative effects of rapid rotation on the form and efficiency of two-dimensional plane layer convection, producing localised states known as convectons. Following on from this we studied subcritical dynamo action in Chapter 4, where convectively-driven dynamos were sustained at Rayleigh numbers below the linear onset of convection. At more rapid rotation (lower Ekman numbers), intermittent behaviour was observed, which was discussed in Chapter 5. Summaries of our findings will be presented in the following sections.

6.1 Rapidly Rotating Convection

At low Prandtl numbers relevant to the liquid metals found in planetary cores, inertial forces are strong and zonal flows exhibit large amplitudes which can lead to localisation.

Localised convection has been observed numerically in rapidly rotating convection, where convective nests of locally enhanced convection exist due to such strong zonal flows, promoted by shearing from differential rotation and Reynolds stresses. However, the effects of rotation on localised convection have been less studied than localised magnetoconvection, for example.

In Chapter 3, we studied two-dimensional Boussinesq convection in a rotating plane layer. We solved the governing equations considering two different truncated models: firstly we implemented a bifurcation and continuation software called AUTO-07p on a model where we truncated our variables in both directions; we then further explored the parameter regime using a higher resolution pseudospectral code, where the full horizontal structure was allowed, but the vertical direction was truncated onto a minimal number of Fourier modes.

Localised states, known as convectons have previously been observed at moderate rotation, however their stability and existence at more realistic parameters to planetary cores had not yet been fully addressed. For example, previous work studied Prandtl numbers larger than $\mathrm{Pr} = 0.1$ and Taylor numbers less than $\mathcal{O}\left(10^4\right)$, whilst estimates of Earth's outer core conditions give $\mathrm{Pr} = 0.05 - 2$ and $\mathrm{Ta} \sim \mathcal{O}\left(10^{30}\right)$. Rotational convectons are shown to exist within a self-generated shear layer with locally reduced angular momentum. In this thesis, we show that these convectons are stable and actually exist in localised regions where the angular momentum is fully reduced to zero, leaving regions which are 'effectively' free from the effects of rotation.

We presented convectons at lower Prandtl numbers (as low as $\mathrm{Pr} = 0.025$), higher Taylor numbers (as high as $\mathrm{Ta} \sim \mathcal{O}\left(10^7\right)$) and higher Rayleigh numbers (up to $\mathrm{Ra} = 2 \times 10^4$) than previously discovered, more relevant to the conditions in planetary cores. Whilst we reproduce subcritical convectons at moderate rotation, as in previous work, we were unable to observe convectons below convective onset at rapid rotation, indicating that such states may not exist subcritically under more realistic planetary conditions.

For the first time we were also able to present time-dependent rotational convectons. Such states existed as strong localised regions, acting similarly to their steady counterparts, surrounded by weaker oscillatory convection which was somewhat able to affect and distort the localised region. This suggests that we were in fact observing the superposition of a subcritical steady convecton and supercritical oscillatory convection at onset. Furthermore, we also located cases where multiple convectons co-existed within our computational domain. In magnetoconvection, oscillatory convectons were observed which oscillated by changing sign and were less efficient at transferring heat. Whilst we were unable to discover similar states in rotating convection, such states could potentially still exist in our system and may be of interest for future work. One possible route to oscillatory convectons may be to gradually increase the Taylor number along an oscillatory

branch until it becomes unstable, hoping that eventually the solution will settle onto a localised oscillatory branch when a sufficiently strong shear layer is formed surrounding a convecton. However this may be time consuming and we briefly attempted it without success. In our work, AUTO proved unable to track oscillatory solutions due to them possessing complex eigenvalues, although it was still able to detect the Hopf bifurcations at which they appear. This information may prove useful in determining where in the parameter space such states could exist.

Further study may also consider removing the vertical truncation which we implemented in our system. Our truncation involved projecting onto a minimal number of Fourier modes in z which retained nonlinearity. Truncating onto a higher number of modes or allowing the full structure entirely introduces further nonlinearity to the system which could disrupt our convectons. The vertical structure of convection is relatively simple close to onset, however many of our convectons are obtained at more moderately supercritical Rayleigh numbers. In Chapter 4, we studied dynamo action in a 3D Cartesian domain. During the kinematic phase (when the Lorentz force was unable to affect the flow), the flow mimics that of 3D rotating convection. We observed relatively simple columnar structures, similar to the structures close to onset which take the form of $\sin(\pi z)$ or $\cos(\pi z)$, implying that our convectons may still exist even if full z-dependence is allowed in our system. Minor variations in the exact regions of parameter space where convectons are located may be observed, but overall we suspect that these states will still exist.

The major limitation of our system is that two-dimensional convective rolls are likely to be unstable to three-dimensional perturbations, leaving it unclear as to whether convectons like those presented will exist in three-dimensions. Stable, time-dependent convectons have been obtained in three-dimensional magnetoconvection which appeared as either cylinders or cigar shapes. However, these did prove more difficult to locate. In our system, convectons were produced as a result of zonal jets along the axis of the convective rolls producing shearing that locally reduced the angular momentum. However, in 3D rotating convection we suspect that such zonal flows would be difficult to maintain due to a lack of horizontal symmetry breaking when the rotational and gravitational axes are aligned. In magnetoconvection, three-dimensional localised states were obtained by using artificial initial conditions and evolving them in time. For example, in one case a cigar shape was artificially created and evolved, which resulted in a partially-isolated time-dependent state. Increasing the strength of the field eventually then led to a three-dimensional convecton. A similar procedure could be attempted in 3D rotating convection: impose a similar artificial state, evolve it in time, then increase the Taylor number. This could be investigated in future work using the same code as in Chapter 4 since the code can be run purely hydrodynamically. However, clearly rotating convection and magnetoconvection

are not identical systems so there is no guarantee this would work.

6.2 Subcritical Dynamos

In Chapter 4 we studied convectively driven dynamo action in a rotating plane layer. It is currently not possible to study dynamo action at realistic parameter regimes however many of the key observed features can be replicated in numerical simulations, providing useful insight. In particular, we wish to study lower Ekman numbers, possible in simplified geometries. Hence we studied a Cartesian system.

In our work, we further investigated the mechanisms involved in the generation of a large-scale magnetic field by convective fluid motions at moderate Ekman numbers. We observed clear differences in the flow between the kinematic and saturated phases of the dynamo, with a transition from columnar cells aligned with the rotation axis, to larger horizontal lengthscales and localised patterns. In this regime, the Lorentz and ageostrophic part of the Coriolis force are of equal importance and magnetically-modified convection generates a coherent mean magnetic field according to a dynamo process. Vital to the generation of the mean magnetic field is a two-scale mechanism, where the coherent mean e.m.f. is generated mostly by motions at the convective lengthscale, especially in the kinematic phase. This dynamo mechanism thus requires a sufficient scale separation between the box size and the convective roll size.

Motivated by the cessation of the Martian dynamo, we go on to study subcritical dynamos at Rayleigh numbers below those predicted by linear theory for the onset of convection. Individual cases of subcritical dynamos have been presented in previous studies for either a fraction of a magnetic diffusion time or at a single Ekman number in planar geometries. Meanwhile, spherical dynamo simulations have produced subcritical dynamos below the critical Rayleigh number for dynamo action, but not below the linear onset of convection. However, we are able to produce subcritical dynamos where dynamically-significant magnetic fields can be sustained for multiple magnetic diffusion times and at various Ekman numbers. We have investigated the subcritical range for various Ekman numbers (smaller than 3.16×10^{-4}) and magnetic Prandtl numbers (greater than, or equal to, unity) to determine the conditions required for this behaviour. Some of the subcritical branches extend down to $\mathrm{Ra} = 0.87\mathrm{Ra}_c$, with the dynamo and convection collapsing for smaller Ra. We identified two necessary conditions for subcritical dynamos: (i) the magnetic Reynolds number must be large enough to produce a coherent mean magnetic field ($\mathrm{Rm} \gtrsim 70 - 100$); (ii) the magnetic field must be strong enough $\left(\overline{\Lambda} \sim \mathcal{O}\left(\mathrm{Ek}^{1/3}\right)\right)$ such that the Lorentz and Coriolis forces are of equal importance at the convective scale. For a given ratio $\mathrm{Ra}/\mathrm{Ra}_c$, these two conditions are more easily met at lower Ek and larger Pm, so small Ek and large Pm seem to favour subcriticality. However, larger values of

Pm, and hence Rm, are also associated with larger fluctuations in the velocity, which can push this sensitive balance away from the dynamo branch, causing the dynamo to decay towards the trivial state. We therefore find optimal values of Ek and Pm for the subcritical range, which are approximately $\mathrm{Ek} = 10^{-5}$ and $\mathrm{Pm} = 2.5$, though it should be noted that we have only explored a limited range in parameters, especially in Pm.

In the Earth's outer core we expect $\mathrm{Ek} \sim \mathcal{O}\left(10^{-15}\right)$ and $\mathrm{Pm} \sim \mathcal{O}\left(10^{-6}\right)$ which are both many orders of magnitude lower than the optimal values we present. Observations estimate that the magnetic Reynolds number in the Earth is $\mathrm{Rm} \sim 200$, which is enough to produce a coherent mean magnetic field. Additionally, the magnetic field strength is estimated as ranging from $\Lambda \sim 10$ (for the traditional Elsasser number) to $\Lambda \sim 10^{-2}$ (for the dynamic Elsasser number). Either way, at $\mathrm{Ek} = 10^{-15}$ then Λ should be at least $\mathcal{O}\left(\mathrm{Ek}^{1/3}\right) = 10^{-5}$ at the convective scale in order to be in the regime where Lorentz and Coriolis forces are of equal importance. Therefore, the Earth in theory could sustain a subcritical dynamo if it became subcritical whilst maintaining its current field strength. However, the Ekman number is far lower than the moderate values we study, which could lead to intermittent behaviour, discussed in the following section. Whilst the Earth is presently at supercritical Rayleigh number, the Rayleigh number could gradually decrease due to cooling in the core. This gradual cooling could also reduce the effectiveness of the flow in generating a magnetic field by dynamo action, resulting in a lower Elsasser number and approaching the switch-over value presented. The correct force balance for the Earth's outer core is often disputed, however many studies expect a QG-MAC balance at large scales. This is similar to what we observe in our moderate Ek dynamos. In the vorticity equation (which assumes geostrophic balance at leading order by taking the curl of the momentum equation which eliminates the pressure terms due to a balance with the geostrophic part of the Coriolis force), the next order force balance is primarily between the Lorentz force produced by the fluctuating field, the buoyancy and the ageostrophic portion of the Coriolis force. However, even in simpler geometries the relevant force balances and lengthscales are disputed.

It is known that Mars previously possessed a self-generated magnetic field produced by a dynamo, similar to the geodynamo. However, the Martian dynamo suddenly became extinct around 4.1 billion years ago. This cessation likely occurred rapidly, over less than 20 million years, and subcritical behaviour was suggested as a possible cause. In Chapter 4 we were able to sustain long-lasting subcritical dynamos which proved sensitive to fluctuations, resulting in a rapid decay of the magnetic field towards the conducting state once a sufficiently large fluctuation is encountered. If Mars had been in a similar state and experienced a large fluctuation in the field, it may have behaved similarly. Again, our subcritical dynamos are only sustained at moderate Ekman numbers ($\mathrm{Ek} \geq 5 \times 10^{-6}$) and Mars' Ekman number is $\sim \mathcal{O}\left(10^{-14}\right)$ (Kuang *et al.*, 2008), much lower than the parameters

we studied. Its magnetic field strength at the surface was measured by Acuña *et al.* (1999) to be of order 1500nT, whilst in the Earth's core the field strength is approximately 2mT (Olson, 2015). The Elsasser number within the Martian core is probably therefore at least $\mathcal{O}(1)$ (Stevenson, 2001) meaning that both the Lorentz and Coriolis forces may have been important, similarly to our subcritical dynamos.

Furthermore, in order to study more extreme parameter regimes relevant to planetary cores we have performed numerical simulations in a rotating plane layer. Clearly, further work should consider subcritical dynamo action in spherical geometries, despite the fact that previous studies have been unable to study systems far below the dynamo onset, never mind convective onset. Additionally, the interior structure of Mars remains relatively unknown, especially whether it possesses an inner core and whether it is solid. It would be interesting to consider whether the presence of a solid inner core affects subcritical dynamo action if it could be sustained in spherical geometries.

6.3 Intermittent Dynamos at Rapid Rotation

At lower Ekman numbers ($\mathrm{Ek} = 5\times10^{-7}$), different behaviour is observed. At small Ekman numbers, we obtain an intermittent dynamo in the saturated phase due to the emergence of a (near) box-size convection mode. This large-scale mode is produced in the regime where Lorentz and Coriolis forces are of equal importance at the convective scale when $\overline{\Lambda} \gg \mathcal{O}(\mathrm{Ek}^{1/3})$, a situation that arises for $\mathrm{Ek} = 5\times10^{-7}$ in our simulations. The large-scale mode is unable to sustain the large-scale dynamo, unlike the magnetically-modified convection at larger Ek, and so this leads to cycles of growth and decay of the magnetic field. It is possible that at larger aspect ratios this box-sized mode may not be produced and we may observe dynamos similar to those in Chapter 4, hence this should be investigated in future work. Surprisingly, despite this intermittent behaviour it appears that we are able to sustain dynamo action below the onset of convection, albeit only just below Ra_c. In the subcritical cases, we still observe intermittent behaviour although it should be noted that these cases have not been run for long (approximately 10% of a thermal diffusion time), so further study of this regime is needed. We hypothesise that the intermittency may hamper the presence of subcritical dynamos, since in the subcritical regime the dynamo is often very sensitive to perturbations which can destabilise the dynamo and cause it to decay towards the trivial state. With such drastic reductions in the magnetic Reynolds number and Elsasser number during decayed phases of intermittency, we expect that these could quite easily result in the overall decay of the dynamo.

Few examples of numerical dynamo simulations producing coherent large-scale magnetic fields exist in rapidly-rotating planar convection, except for the dynamos operating near the convective onset. Another example of an intermittent dynamo in this system is

the large-scale-vortex (LSV) dynamo. LSV dynamos occurs at moderately supercritical Rayleigh numbers and rely on the presence of large-scale vortices. These form spontaneously in non-magnetic rotating convection when the small-scale convective flow is both sufficiently turbulent (hence existing at higher Rayleigh numbers) and anisotropic due to the rapid rotation. LSVs play a crucial part in the dynamo mechanism, but are often disrupted when the magnetic field becomes sufficiently strong, leading to an intermittent behaviour. However, our near-onset intermittent dynamo is due to a large-scale mode driven by the magnetic field, whereas LSVs at larger Rayleigh numbers are purely hydrodynamic in origin and play an active role in the generation of the magnetic field. In rapidly rotating convection, LSVs have been shown to exhibit hysteretic behaviours at $\mathrm{Pr} = 1$ and supercritical Rayleigh number. However, it remains to be answered whether these LSVs can occur at lower Prandtl numbers and whether subcritical dynamos could be produced by the LSV dynamo.

We attempted to avoid the production of the magnetically-driven large-scale convective mode by studying lower magnetic Prandtl numbers, however this proved unsuccessful. Even at low Pm we still observed the formation of a box-sized convective mode and intermittent behaviour. If subcritical behaviour at lower Ekman number is to be further explored, a route must be found such that the Elsasser number remains sufficiently small (of order $\mathrm{Ek}^{1/3}$) to avoid the emergence of the magnetically-driven large-scale convective mode. Additionally, restricting our simulations to small aspect ratios may also have affected the system, since the large-scale mode was the maximum non-trivial mode allowed in our system. In a larger computational domain the convection may reach even larger scales, leading to convective flows struggling even further to sustain the large-scale magnetic field. Furthermore, in a larger computational domain the mean field may be weaker since structures are less likely to correlate across the domain, producing a less strong mean electromotive force. These effects may lead to even more extreme intermittency.

6.4 Final Remarks

In this thesis we have explored the effects of both rotation and magnetic field on convective flows and their ability to sustain a hydromagnetic dynamo. Throughout our work, we have studied rotating convection and convectively-driven dynamos in a planar geometry (as opposed to spherical geometries which are more realistic), motivated by the quest to explore more realistic parameter regimes than ever before. However, we still remain some way from realistic parameters.

In the case of rotating convectons, the key question now is whether such states are able to be produced in rapidly rotating three-dimensional convection. For our convectively-driven dynamos, a route towards large-scale dynamos at lower Ekman numbers must be

found which avoids intermittent behaviour. Furthermore, our intermittent dynamos could be a source of further work, studying them at higher numerical resolutions and for larger aspect ratios, whilst investigating their subcriticality further.

We have also briefly discussed large-scale vortices (LSVs). The LSV dynamo exhibits intermittency, similar to our intermittent dynamos. However, LSVs have only really been studied at Prandtl numbers of unity and supercritical Rayleigh numbers. Whether LSVs can exist at lower Prandtl numbers and their relevance to subcritical behaviour remains to be investigated.

Appendix A

Derivations in Fully Truncated Model

A.1 Nonlinear Terms in AUTO-07p

In Chapter 3 we solved the governing equations of 2D rotating planar Boussinesq convection. In Section 3.2.1 we implemented a restricted symmetries approach and fully truncated the streamfunction ψ, temperature perturbation T and axial velocity v as follows:

$$\psi = \left\{ \sum_{k=1}^{N} A_k \sin\left(\frac{2\pi k}{\Gamma} x\right) \right\} \sin(\pi z), \tag{A.1}$$

$$T = \left\{ \sum_{k=0}^{N} B_k \cos\left(\frac{2\pi k}{\Gamma} x\right) \right\} \sin(\pi z) + \left\{ \sum_{k=0}^{N} C_k \cos\left(\frac{2\pi k}{\Gamma} x\right) \right\} \sin(2\pi z), \tag{A.2}$$

$$v = \sum_{k=1}^{N} D_k \sin\left(\frac{2\pi k}{\Gamma} x\right) + \left\{ \sum_{k=1}^{N} E_k \sin\left(\frac{2\pi k}{\Gamma} x\right) \right\} \cos(\pi z), \tag{A.3}$$

where N is the number of modes in the expansion. This led to a set of equations governing each of our truncation coefficients, $\{A_k, ..., E_k\}$ shown in Equations 3.14-3.18. Many of these governing equations have nonlinear terms, which require a summation over pairs of wavenumbers to determine how each nonlinear term contributes at wavenumber k. The nonlinear terms involve contributions from $A'C$, AC', $A'B$, AB', $A'E$, AE' and AD' where a prime denotes the x-derivative.

A.1.1 Cosine-Cosine Nonlinearities

The nonlinear $A'C$ term involves a double summation over cosine-cosine terms,

$$A'C = \left\{ \sum_{m=1}^{N} \left(\frac{2\pi m}{\Gamma} \right) A_m \cos\left(\frac{2\pi m}{\Gamma} x \right) \right\} \left\{ \sum_{n=0}^{N} C_n \cos\left(\frac{2\pi n}{\Gamma} x \right) \right\}. \tag{A.4}$$

Using the fact that $\cos(ax)\cos(bx) = (1/2)\left\{\cos\left([a-b]\,x\right) + \cos\left([a+b]\,x\right)\right\}$ this can be rewritten as

$$A'C = \sum_{m=1}^{N} \sum_{n=0}^{N} \frac{\pi m}{\Gamma} A_m C_n \left\{ \cos\left(\frac{2\pi(m-n)}{\Gamma} x \right) + \cos\left(\frac{2\pi(m+n)}{\Gamma} x \right) \right\}. \tag{A.5}$$

The contributions to the k-th wavenumber can then be determined from $m+n=k$ or $m-n=\pm k$. For example,

$$\left[A'C\right]_k = \begin{cases} +\frac{\pi m}{\Gamma} A_m C_n & m-n=\pm k \quad \text{or} \quad m+n=k, \quad \text{for} \quad k>0, \\ +\frac{\pi m}{\Gamma} A_m C_n & m-n=0, \quad \text{for} \quad k=0. \end{cases} \tag{A.6}$$

A similar result holds for the nonlinear $A'B$ term which is also a sum over pairs of cosine coefficients.

A.1.2 Sine-Sine Nonlinearities

The nonlinear AC' term involves a double summation over sine-sine terms,

$$AC' = \left\{ \sum_{m=1}^{N} A_m \sin\left(\frac{2\pi m}{\Gamma} x \right) \right\} \left\{ \sum_{n=0}^{N} \left(\frac{-2\pi n}{\Gamma} \right) C_n \sin\left(\frac{2\pi n}{\Gamma} x \right) \right\}. \tag{A.7}$$

Using the fact that $\sin(ax)\sin(bx) = (1/2)\left\{\cos\left([a-b]\,x\right) - \cos\left([a+b]\,x\right)\right\}$ this can be rewritten as

$$AC' = \sum_{m=1}^{N} \sum_{n=0}^{N} \frac{-\pi n}{\Gamma} A_m C_n \left\{ \cos\left(\frac{2\pi(m-n)}{\Gamma} x \right) - \cos\left(\frac{2\pi(m+n)}{\Gamma} x \right) \right\}. \tag{A.8}$$

The contributions to the k-th wavenumber can then be determined from when $m+n=k$ or $m-n=\pm k$. For example,

$$\left[AC'\right]_k = \begin{cases} -\frac{\pi n}{\Gamma} A_m C_n & m-n=\pm k, \quad \text{for} \quad k>0, \\ +\frac{\pi n}{\Gamma} A_m C_n & m+n=k, \quad \text{for} \quad k>0, \\ -\frac{\pi n}{\Gamma} A_m C_n & m-n=0, \quad \text{for} \quad k=0. \end{cases} \tag{A.9}$$

A similar result holds for the nonlinear AB' term which is also a sum over pairs of sine coefficients.

A.1.3 Sine-Cosine Nonlinearities

The nonlinear AE' term involves a double summation over sine-cosine terms,

$$AE' = \left\{ \sum_{m=1}^{N} A_m \sin\left(\frac{2\pi m}{\Gamma} x\right) \right\} \left\{ \sum_{n=1}^{N} \left(\frac{2\pi n}{\Gamma}\right) C_n \cos\left(\frac{2\pi n}{\Gamma} x\right) \right\}. \tag{A.10}$$

Using the fact that $\sin(ax)\cos(bx) = (1/2)\left\{\sin\left([a-b]\,x\right) + \sin\left([a+b]\,x\right)\right\}$ this can be rewritten as

$$AE' = \sum_{m=1}^{N} \sum_{n=1}^{N} \frac{\pi n}{\Gamma} A_m E_n \left\{ \sin\left(\frac{2\pi(m-n)}{\Gamma} x\right) + \sin\left(\frac{2\pi(m+n)}{\Gamma} x\right) \right\}. \tag{A.11}$$

The contributions to the k-th wavenumber can then be determined from when $m+n=k$ or $m-n=\pm k$. For example,

$$\left[AE'\right]_k = \begin{cases} +\frac{\pi n}{\Gamma} A_m E_n & m-n=k, \quad \text{for} \quad k>0, \\ -\frac{\pi n}{\Gamma} A_m E_n & m-n=-k, \quad \text{for} \quad k>0, \\ +\frac{\pi n}{\Gamma} A_m E_n & m+n=k, \quad \text{for} \quad k>0, \\ +\frac{\pi n}{\Gamma} A_m E_n & m-n=0, \quad \text{for} \quad k=0. \end{cases} \tag{A.12}$$

A similar result holds for the nonlinear $A'E$ and $A'D$ terms which are also sums over sine-cosine coefficients.

A.2 AUTO-07p Output Quantities

In Beaume *et al.* (2013), the average poloidal kinetic energy is defined as

$$\mathcal{E} = \frac{1}{2\Gamma} \int_D |\nabla\psi|^2 dxdz, \tag{A.13}$$

which is basically the volume average over the 2D computational domain D of $|\nabla\psi|^2$. In our fully truncated model,

$$|\nabla\psi|^2 = \left[\sum_{k=1}^{N} \frac{2\pi k}{\Gamma} A_k \cos\left(\frac{2\pi k}{\Gamma} x\right) \right]^2 \sin^2(\pi z) + \left[\sum_{k=1}^{N} A_k \sin\left(\frac{2\pi k}{\Gamma} x\right) \right]^2 \pi^2 \cos^2(\pi z). \tag{A.14}$$

which we now integrate over the computational domain from $0 \leq x \leq \Gamma$ and $0 \leq z \leq 1$. Thus the kinetic energy is then

$$\mathcal{E} = \frac{1}{2\Gamma}\int_{x=0}^{\Gamma}\int_{z=0}^{1}\left\{\left[\sum_{k=1}^{N}\frac{2\pi k}{\Gamma}A_k\cos\left(\frac{2\pi k}{\Gamma}x\right)\right]^2\sin^2(\pi z) + \left[\sum_{k=1}^{N}A_k\sin\left(\frac{2\pi k}{\Gamma}x\right)\right]^2\pi^2\cos^2(\pi z)\right\}dxdz. \quad \text{(A.15)}$$

We first integrate in z noting that $\int_{z=0}^{1}\sin^2(\pi z)dz = \int_{z=0}^{1}\cos^2(\pi z)dz = 1/2$ giving

$$\mathcal{E} = \left(\frac{1}{2\Gamma}\right)\frac{1}{2}\int_{x=0}^{\Gamma}\left\{\left[\sum_{k=1}^{N}\frac{2\pi k}{\Gamma}A_k\cos\left(\frac{2\pi k}{\Gamma}x\right)\right]^2 + \pi^2\left[\sum_{k=1}^{N}A_k\sin\left(\frac{2\pi k}{\Gamma}x\right)\right]^2\right\}dx. \quad \text{(A.16)}$$

We can expand the square of each summation using the relation $\left(\sum_i a_i\right)^2 = \sum_i a_i^2 + 2\sum_{i<j}a_i a_j$ which gives

$$\mathcal{E} = \left(\frac{1}{2\Gamma}\right)\frac{1}{2}\int_{x=0}^{\Gamma}\left\{\sum_{k=1}^{N}\frac{4\pi^2k^2}{\Gamma^2}A_k^2\cos^2\left(\frac{2\pi k}{\Gamma}x\right) + \sum_{k=1}^{N}\pi^2A_k^2\sin^2\left(\frac{2\pi k}{\Gamma}x\right) + 2\sum_{i<j}\left(\frac{4\pi^2ij}{\Gamma^2}\right)A_iA_j\cos\left(\frac{2\pi i}{\Gamma}x\right)\cos\left(\frac{2\pi j}{\Gamma}x\right) + 2\pi^2\sum_{i<j}A_iA_j\sin\left(\frac{2\pi i}{\Gamma}x\right)\sin\left(\frac{2\pi j}{\Gamma}x\right)\right\}dx. \quad \text{(A.17)}$$

Now we use $\cos(ax)\cos(bx) = (1/2)\left\{\cos\left([a-b]\,x\right) + \cos\left([a+b]\,x\right)\right\}$ and $\sin(ax)\sin(bx) = (1/2)\left\{\cos\left([a-b]\,x\right) - \cos\left([a+b]\,x\right)\right\}$ to rewrite as

$$\mathcal{E} = \left(\frac{1}{2\Gamma}\right)\frac{1}{2}\int_{x=0}^{\Gamma}\left\{\sum_{k=1}^{N}\frac{4\pi^2k^2}{\Gamma^2}A_k^2\cos^2\left(\frac{2\pi k}{\Gamma}x\right) + \sum_{k=1}^{N}\pi^2A_k^2\sin^2\left(\frac{2\pi k}{\Gamma}x\right) + \sum_{i<j}\left[\frac{4\pi^2ij}{\Gamma^2}+\pi^2\right]A_iA_j\cos\left(\frac{2\pi(i-j)}{\Gamma}x\right) + \sum_{i<j}\left[\frac{4\pi^2ij}{\Gamma^2}+\pi^2\right]A_iA_j\cos\left(\frac{2\pi(i+j)}{\Gamma}x\right)\right\}dx, \quad \text{(A.18)}$$

which we can now integrate in x. We note that $\int_{x=0}^{\Gamma}\sin^2(2\pi kx/\Gamma)dx = \int_{x=0}^{\Gamma}\cos^2(2\pi kx/\Gamma)dx = \Gamma/2$ and that $\int_{x=0}^{\Gamma}\cos(2\pi(i\pm j)x/\Gamma)dx = 0$ for all pairs of positive

integers i, j. This gives

$$\mathcal{E} = \frac{1}{8}\sum_{k=1}^{N}\left\{\left(\frac{2\pi k}{\Gamma}\right)^2 + \pi^2\right\} A_k^2, \tag{A.19}$$

in terms of our unscaled AUTO coefficients.

In our scaled variables we simply replace A_k with $(2p)^{1/2}\,(\Gamma/\pi)\,\widetilde{A}_k$ giving

$$\mathcal{E} = \frac{1}{8}\,(2p)\,\frac{\Gamma^2}{\pi^2}\sum_{k=1}^{N}\left\{\left(\frac{2\pi k}{\Gamma}\right)^2 + \pi^2\right\} \widetilde{A}_k^2, \tag{A.20}$$

where $p = (2\pi/\Gamma)^2 + \pi^2$.

Bibliography

Acuña, M. H., Connerney, J. E. P., Ness, N. F., Lin, R. P., Mitchell, D., Carlson, C. W., McFadden, J., Anderson, K. A., Rème, H., Mazelle, C., Vignes, D., Wasilewski, P. & Cloutier, P. 1999 Global distribution of crustal magnetization discovered by the mars global surveyor mag/er experiment. *Science* **284**, 790–793.

Acuña, M. H. & Ness, N. F. 1976 The main magnetic field of jupiter. *Journal of Geophysical Research* **81** (16), 2917–2922.

Alfvén, H. 1942 Existence of electromagnetic-hydrodynamic waves. *Nature* **150**, 405–406.

Anderson, B. J., Acuña, M. H., Korth, H., Slavin, J. A., Uno, H., Johnson, C. L., Purucker, M. E., Solomon, S. C., Raines, J. M., Zurbuchen, T. H., Gloeckler, G. & McNutt Jr, R. L. 2010 The magnetic field of mercury. *Space science reviews* **152** (1-4), 307–339.

Arnold, B. 1904 *The letter of Petrus Peregrinus on the magnet AD 1269*. New York: McGraw Publishing.

Aubert, J. 2013 Flow throughout the earth's core inverted from geomagnetic observations and numerical dynamo models. *Geophysical Journal International* **192** (2), 537–556.

Aubert, J. 2019 Approaching Earth's core conditions in high-resolution geodynamo simulations. *Geophysical Journal International* **219** (Sup 1), S137–S151.

Aubert, J. 2020 Recent geomagnetic variations and the force balance in earth's core. *Geophysical Journal International* **221** (1), 378–393.

Aubert, J., Gastine, T. & Fournier, A. 2017 Spherical convective dynamos in the rapidly rotating asymptotic regime. *Journal of Fluid Mechanics* **813**, 558–593.

Aurnou, J. M. & King, E. M. 2017 The cross-over to magnetostrophic convection in planetary dynamo systems. *Proceedings of the Royal Society A: Mathematical, Physical and Engineering Sciences* **473** (2199), 20160731.

Beaume, C., Bergeon, A., Kao, H.-C. & Knobloch, E. 2013 Convectons in a rotating fluid layer. *J. Fluid Mech.* **717**, 417–448.

Bernoff, A. 1994 Finite amplitude convection between stress-free boundaries; ginzburg-landau equations and modulation theory. *European Journal of Applied Mathematics* **5**, 267–282.

Birch, F. 1952 Elasticity and constitution of the Earth's interior. *Journal of Geophysical Research* **57**, 227–286.

Birch, F. 1964 Density and composition of mantle and core. *Journal of Geophysical Research* **69**, 4377–4388.

Blanchflower, S. 1999 Magnetohydrodynamic convectons. *Physics Letters A* **261** (1-2), 74–81.

Blanchflower, S. & Weiss, N. 2002 Three-dimensional magnetohydrodynamic convectons. *Physics Letters A* **294** (5-6), 297–303.

Braginsky, S. I. 1964 Self excitation of a magnetic field during the motion of a highly conducting fluid. *Soviet Phys. JETP* **20**, 726–735.

Brown, B. P., Browning, M. K., Brun, A. S., Miesch, M. S., Nelson, N. J. & Toomre, J. 2007 Strong dynamo action in rapidly rotating suns. *Unresolved problems in stellar physics* **948** (1), 271–278.

Brown, B. P., Browning, M. K., Brun, A. S., Miesch, M. S. & Toomre, J. 2008 Rapidly rotating suns and active nests of convection. *The Astrophysical Journal* **689** (2), 1354–1372.

Buckley, M. C. & Bushby, P. J. 2013 Localized oscillatory states in magnetoconvection. *Physical Review E* **87** (2), 023019.

Bullard, E. & Gellman, H. 1954 Homogeneous Dynamos and Terrestrial Magnetism. *Phil. Trans. R. Soc. Lond. A* **247**, 213–278.

Burke, J. & Knobloch, E. 2006 Localized states in the generalized swift-hohenberg equation. *Physical Review E* **73** (5), 056211.

Bushby, P. J., Käpylä, P. J., Masada, Y., Brandenburg, A., Favier, B., Guervilly, C. & Käpylä, M. J. 2018 Large-scale dynamos in rapidly rotating plane layer convection. *Astron. & Astrophys.* **612**, A97.

Busse, F. H. 1970 Thermal instabilities in rapidly rotating systems. *J. Fluid Mech.* **44**, 441–460.

Calkins, M. A. 2018 Quasi-geostrophic dynamo theory. *Physics of the Earth and Planetary Interiors* **276**, 182–189.

Calkins, M. A., Julien, K. & Marti, P. 2013 Three-dimensional quasi-geostrophic convection in the rotating cylindrical annulus with steeply sloping endwalls. *Journal of Fluid Mechanics* **732**, 214–244.

Calkins, M. A., Julien, K., Tobias, S. M. & Aurnou, J. M. 2015 A multiscale dynamo model driven by quasi-geostrophic convection. *J. Fluid Mech.* **780**, 143–166.

Campbell, W. H. 2003 *Introduction to geomagnetic fields*. Cambridge University Press.

Cattaneo, F., Emonet, T. & Weiss, N. O. 2003 On the interaction between convection and magnetic fields. *Astrophys. J.* **588**, 1183.

Cattaneo, F. & Hughes, D. W. 2006 Dynamo action in a rotating convective layer. *J. Fluid Mech.* **553**, 401–418.

Cattaneo, F. & Hughes, D. W. 2017 Dynamo action in rapidly rotating Rayleigh–Bénard convection at infinite Prandtl number. *J. Fluid Mech.* **825**, 385–411.

Cattaneo, F., Hughes, D. W. & Weiss, N. O. 1991 What is a stellar dynamo? *Mon. Not. R. Astron. Soc.* **253** (3), 479–484.

Cavallucci, T., Murata, Y., Takamura, M., Hibino, H., Heun, S. & Tozzini, V. 2018 Unraveling localized states in quasi free standing monolayer graphene by means of density functional theory. *Carbon* **130**, 466–474.

Chandrasekhar, S. 1953 The instability of a layer of fluid heated below and subject to Coriolis forces. *Proc. R. Soc. Lond. A* **217**, 306–327.

Chandrasekhar, S. 1961 *Hydrodynamic and Hydromagnetic Stability*. Oxford: Clarendon.

Childress, S. & Soward, A. M. 1972 Convection-driven hydromagnetic dynamo. *Phys. Rev. Lett.* **29**, 837–839.

Christensen, U. R. 2019 Planetary magnetic fields and dynamos.

Christensen, U. R. & Aubert, J. 2006 Scaling properties of convection-driven dynamos in rotating spherical shells and application to planetary magnetic fields. *Geophy. J. Int.* **166**, 97–114.

Christensen, U. R., Aubert, J. & Hulot, G. 2010 Conditions for Earth-like geodynamo models. *Earth Planet. Sci. Lett.* **296** (3-4), 487–496.

Christensen, U. R. & Wicht, J. 2015 Numerical dynamo simulations. In *Treatise on Geophysics (Second Edition)* (ed. G. Schubert), , vol. 8, pp. 245 – 277. Amsterdam: Elsevier.

Cisowski, S. M., Collinson, D. W., Runcorn, S. K., Stephenson, A. & Fuller, M. 1983 A review of lunar paleointensity data and implications for the origin of lunar magnetism. *Journal of Geophysical Research: Solid Earth* **88** (S02), A691–A704.

Connerney, J. E. P., Acuña, M. H. & Ness, N. F. 1991 The magnetic field of Neptune. *J. Geophys. Res.* **96**, 19023–19042.

Connerney, J. E. P., Acuna, M. H. & Ness, N. F. 1987 The magnetic field of uranus. *J. Geophys. Res.* **92**, 15329–15336.

Cooper, R. G., Bushby, P. J. & Guervilly, C. 2020 Subcritical dynamos in rapidly rotating planar convection. *Phys. Rev. Fluids* **5** (11), 113702.

Courvoisier, A., Hughes, D. W. & Tobias, S. M. 2009 Mean induction and diffusion: the influence of spatial coherence. *J. Fluid Mech.* **627**, 403–421.

Cowling, T. G. 1934 The magnetic field of sunspots. *MNRAS* **94**, 39–48.

Cox, S. M. & Matthews, P. C. 2001 New instabilities in two-dimensional rotating convection and magnetoconvection. *Physica D: Nonlinear Phenomena* **149** (3), 210–229.

Deissler, R. J. & Brand, H. R. 1994 Periodic, quasiperiodic, and chaotic localized solutions of the quintic complex ginzburg-landau equation. *Physical Review Letters* **72** (4), 478–482.

Dietrich, W. & Wicht, J. 2013 A hemispherical dynamo model: Implications for the Martian crustal magnetization. *Physics of the Earth and Planetary Interiors* **217**, 10–21.

Doedel, E. J., Champneys, A. R., Dercole, F., Fairgrieve, T. F., Kuznetsov, Y. A., Oldeman, B., Paffenroth, R. C., Sandstede, B., Wang, X. J. & Zhang, C. H. 2007 AUTO-07P: Continuation and bifurcation software for ordinary differential equations .

Dormy, E. 2016 Strong-field spherical dynamos. *J. Fluid Mech.* **789**, 500–513.

Dormy, E., Oruba, L. & Petitdemange, L. 2018 Three branches of dynamo action. *Fluid Dynamics Research* **50** (1), 011415.

Elsasser, W. M. 1939 On the origin of the earth's magnetic field. *Physical Review* **55** (5), 489–498.

Eltayeb, I. A. 1972 Hydromagnetic convection in a rapidly rotating fluid layer. *Proc. R. Soc. Lond. A* **326** (1565), 229–254.

Fautrelle, Y. & Childress, S. 1982 Convective dynamos with intermediate and strong fields. *Geophys. Astrophys. Fluid Dyn.* **22** (3-4), 235–279.

Favier, B. & Bushby, P. J. 2011 Small-scale dynamo action in rotating compressible convection. *J. Fluid Mech.* **690**, 262–287.

Favier, B. & Bushby, P. J. 2013 On the problem of large-scale magnetic field generation in rotating compressible convection. *J. Fluid Mech.* **723**, 529–555.

Favier, B., Guervilly, C. & Knobloch, E. 2019 Subcritical turbulent condensate in rapidly rotating rayleigh–Bénard convection. *Journal of Fluid Mechanics* **864**, R1.

Favier, B. & Proctor, M. R. E. 2013 Kinematic dynamo action in square and hexagonal patterns. *Phys. Rev. E* **88** (5), 053011.

Favier, B., Silvers, L. J. & Proctor, M. R. E. 2014 Inverse cascade and symmetry breaking in rapidly-rotating Boussinesq convection. *Phys. Fluids* **26** (9), 096605.

Fearn, D. R. 1979*a* Thermal and magnetic instabilities in a rapidly rotating fluid sphere. *Geophysical & Astrophysical Fluid Dynamics* **14** (1), 103–126.

Fearn, D. R. 1979*b* Thermally driven hydromagnetic convection in a rapidly rotating sphere. *Proceedings of the Royal Society of London. A. Mathematical and Physical Sciences* **369** (1737), 227–242.

Gilbert, W. 1600 De Magnete .

Gillet, N., Jault, D., Canet, E. & Fournier, A. 2010 Fast torsional waves and strong magnetic field within the Earth's core. *Nature* **465**, 74–77.

Gillet, N., Schaeffer, N. & Jault, D. 2011 Rationale and geophysical evidence for quasi-geostrophic rapid dynamics within the Earth's outer core. *Phys. Earth Planet. Inter.* **187**, 380–390.

Glatzmaier, G. & Roberts, P. H. 1995 A three-dimensional self-consistent computer simulation of a geomagnetic field reversal. *Nature* **377**, 203–209.

Grote, E. & Busse, F. H. 2000 Hemispherical dynamos generated by convection in rotating spherical shells. *Phys. Rev. E* **62**, 4457–4460.

Grote, E. & Busse, F. H. 2001 Dynamics of convection and dynamos in rotating spherical fluid shells. *Fluid Dyn. Res.* **28**, 349–368.

Guervilly, C., Hughes, D. W. & Jones, C. A. 2014 Large-scale vortices in rapidly rotating Rayleigh-Bénard convection. *J. Fluid Mech.* **758**, 407–435.

Guervilly, C., Hughes, D. W. & Jones, C. A. 2015 Generation of magnetic fields by large-scale vortices in rotating convection. *Phys. Rev. E* **91** (4), 041001.

Guervilly, C., Hughes, D. W. & Jones, C. A. 2017 Large-scale-vortex dynamos in planar rotating convection. *J. Fluid Mech.* **815**, 333–360.

Gutenberg, B. 1912 Uber Erdbebenwellen. *Gottingen Nachr* **VIIA**, 125–176.

Halley, E. 1683 A theory of the variation of the magnetical compass. *Philosophical Transactions* **13**, 208–221.

Halley, E. 1692 An account of the cause of the change of the variation of the magnetical needle, with an hypothesis of the structure of the internal parts of the Earth. *Philosophical Transactions* **16**, 563–578.

Hori, K. & Wicht, J. 2013 Subcritical dynamos in the early Mars' core: Implications for cessation of the past Martian dynamo. *Physics of the Earth and Planetary Interiors* **219**, 21–33.

Hughes, D. W. 2018 Mean field electrodynamics: triumphs and tribulations. *Journal of Plasma Physics* **84** (4), 735840407.

Hughes, D. W. & Cattaneo, F. 2008 The alpha-effect in rotating convection: size matters. *J. Fluid Mech.* **594**, 445–461.

Jackson, A. & Finlay, C. 2015 Geomagnetic secular variation and its applications to the core. In *Treatise on Geophysics*, Second edition edn. (ed. G. Schubert), pp. 137–184. Oxford: Elsevier.

Jeffreys, H. 1926 The rigidity of the Earth's central core. *Monthly Notices of the Royal Astronomical Society, Geophysical Supplement* **1**, 371–383.

Jones, C. A. 2011 Planetary magnetic fields and fluid dynamos. *Annual Review of Fluid Mechanics* **43** (1), 583–614.

Jones, C. A. 2015 Thermal and compositional convection in the outer core. In *Treatise on Geophysics*, Second edition edn. (ed. G. Schubert), pp. 115–159. Oxford: Elsevier.

Jones, C. A. & Roberts, P. H. 2000 Convection-driven dynamos in a rotating plane layer. *J. Fluid Mech.* **404** (1), 311–343.

Julien, K., Rubio, A. M., Grooms, I. & Knobloch, E. 2012 Statistical and physical balances in low Rossby number Rayleigh–Bénard convection. *Geophys. Astrophys. Fluid Dyn.* **106**, 392–428.

van Kan, A., Nemoto, T. & Alexakis, A. 2019 Rare transitions to thin-layer turbulent condensates. *arXiv preprint arXiv:1903.05578* .

Käpylä, P. J., Mantere, M. J. & Brandenburg, A. 2013 Oscillatory large-scale dynamos from cartesian convection simulations. *Geophys. Astrophys. Fluid Dyn.* **107** (1-2), 244–257.

King, E. M. & Buffett, B. A. 2013 Flow speeds and length scales in geodynamo models: The role of viscosity. *Earth Planet. Sci. Lett.* **371**, 156–162.

Kivelson, M. G., Khurana, K. K., Russell, C. T., Walker, R. J., Warnecke, J., Coroniti, F. V., Polanskey, C., Southwood, D. J. & Schubert, G. 1996 Discovery of ganymede's magnetic field by the galileo spacecraft. *Nature* **384**, 537–541.

Knobloch, E., Weiss, N. O. & Da Costa, L. N. 1981 Oscillatory and steady convection in a magnetic field. *J. Fluid Mech.* **113**, 153–186.

Kono, M. & Tanaka, H. 1995 Intensity of the geomagnetic field in geological time: A statistical study. In *The Earth's Central Part: Its Structure and Dynamics* (ed. T. Yukutake), pp. 75–94. Tokyo, Japan: Terra Scientific Publishing Co.

Kuang, W., Jiang, W. & Wang, T. 2008 Sudden termination of martian dynamo?: Implications from subcritical dynamo simulations. *Geophysical Research Letters* **35**, 1–5.

Landeau, M. & Aubert, J. 2011 Equatorially asymmetric convection inducing a hemispherical magnetic field in rotating spheres and implications for the past martian dynamo. *Physics of the Earth and planetary interiors* **185** (3-4), 61–73.

Larmor, J. 1919 How could a rotating body such as the Sun become a magnet? *Rep. Brit. Adv. Sci.* pp. 159–160.

Lee, P. A. 1993 Localized states in a d-wave superconductor. *Physical review letters* **71** (12), 1887–1890.

Lillis, R. J., Frey, H. V. & Manga, M. 2008 Rapid decrease in martian crustal magnetization in the noachian era: Implications for the dynamo and climate of early mars. *Geophysical Research Letters* **35**, L14203.

Malkus, W. V. R. 1994 Energy sources for planetary dynamos. In *Lectures on Solar and Planetary Dynamos* (ed. M. R. E. Proctor & A. D. GIlbert), , vol. 2, pp. 161–179. Cambridge: Cambridge University Press.

Masada, Y. & Sano, T. 2014 Mean-field modeling of an α^2 dynamo coupled with direct numerical simulations of rigidly rotating convection. *Astrophys. J. Lett.* **794** (1), L6.

Matthews, P. C. & Cox, S. M. 2000 Pattern formation with a conservation law. *Nonlinearity* **13** (4), 1293–1320.

Moffatt, H. K. 1978 *Magnetic field generation in electrically conducting fluids*. Cambridge: University Press.

Morin, V. & Dormy, E. 2009 The dynamo bifurcation in rotating spherical shells. *International Journal of Modern Physics B* **23**, 5467–5482.

Needham, J. 1976 Science and civilisation in china. vol. 4: Physics and physical technology. part iii: Civil engineering and nautics. *Orientalische Literaturzeitung* **71** (1), 89–93.

Ness, N. F., Acuña, M. H., Lepping, R. P., Connerney, J. E., Behannon, K. W., Burlaga, L. F. & Neubauer, F. M. 1981 Magnetic field studies by voyager 1: Preliminary results at saturn. *Science* **212** (4491), 211–217.

Niemela, J. J., Ahlers, G. & Cannell, D. S. 1990 Localized traveling-wave states in binary-fluid convection. *Physical review letters* **64** (12), 1365–1368.

Nore, C., Quiroz, D. C., Guermond, J. L., Léorat, J. & Luddens, F. 2015 Numerical dynamo action in cylindrical containers. *The European Physical Journal Applied Physics* **70** (3), 31101.

Oldham, R. D. 1906 The constitution of the Earth, as revealed by earthquakes. *Nature* **92**, 684–685.

Olson, P. 2015 Core dynamics: An introduction and overview. In *Treatise on Geophysics*, Second edition edn. (ed. G. Schubert), pp. 1–25. Oxford: Elsevier.

Oruba, L. & Dormy, E. 2014 Predictive scaling laws for spherical rotating dynamos. *Geophys. J. Int.* **198** (2), 828–847.

Pais, M. A. & Jault, D. 2008 Quasi-geostrophic flows responsible for the secular variation of the Earth's magnetic field. *Geophy. J. Int.* **173**, 421–443.

Parker, E. N. 1955 Hydromagnetic dynamo models. *The Astrophysical Journal* **122**, 293–314.

Proudman, J. 1916 On the motion of solids in liquids possessing vorticity. *Proceedings of the Royal Society of London A* **92**, 408–424.

Roberts, P. H. 1978 Magneto-convection in a rapidly rotating fluid. In *Fluids in Geophysics* (ed. P. H. Roberts & A. M. Soward), pp. 421–435. Cambridge: Academic Press.

Roberts, P. H. 2015 Theory of the geodynamo. In *Treatise on Geophysics*, Second edition edn. (ed. G. Schubert), pp. 57–90. Oxford: Elsevier.

Roberts, P. H. & Soward, A. M. 1992 Dynamo theory. *Annual review of fluid mechanics* **24** (1), 459–512.

Rotvig, J. & Jones, C. A. 2002 Rotating convection-driven dynamos at low Ekman number. *Phys. Rev. E* **66** (5), 056308.

Russell, C. T. 1980 Planetary magnetism. *Reviews of Geophysics* **18** (1), 77–106.

Sakaguchi, H. & Brand, H. R. 1997 Stable localized squares in pattern-forming nonequilibrium systems. *Europhysics Letters* **38** (5), 341–346.

Schaeffer, N., Jault, D., Nataf, H.-C. & Fournier, A. 2017 Turbulent geodynamo simulations: a leap towards Earth's core. *Geophys. J. Int.* **211**, 1–29.

Schekochihin, A. A., Cowley, S. C., Taylor, S. F., Maron, J. L. & McWilliams, J. 2004 Simulations of the small-scale turbulent dynamo. *The Astrophysical Journal* **612** (1), 276–307.

Schwaiger, T., Gastine, T. & Aubert, J. 2019 Force balance in numerical geodynamo simulations: a systematic study. *Geophys. J. Int* **219**, S101–S114.

Schwaiger, T., Gastine, T. & Aubert, J. 2021 Relating force balances and flow length scales in geodynamo simulations. *Geophys. J. Int* **224** (3), 1890–1904.

Siemens, W. 1867 Über die uwandlung von arbeitskraft in electrischen strom ohneanwendlung permanenter magnete. *Annalen der Physik* **206**, 332–335.

Sobotka, M., Brandt, P. N. & Simon, G. W. 1997 Fine structure in sunspots. I. Sizes and lifetimes of umbral dots. *Astronomy and Astrophysics* **328**, 682–688.

Sobotka, M. & Puschmann, K. G. 2009 Morphology and evolution of umbral dots and their substructures. *Astronomy & Astrophysics* **504** (2), 575–581.

Soderlund, K. M., King, E. M. & Aurnou, J. M. 2012 The influence of magnetic fields in planetary dynamo models. *Earth Planet. Sci. Lett.* **333**, 9–20.

Solomatov, V. S. 2012 Localized subcritical convective cells in temperature-dependent viscosity fluids. *Physics of the Earth and Planetary Interiors* **200**, 63–71.

Soward, A. M. 1972 A kinematic theory of large magnetic reynolds number dynamos. *Proceedings of the Royal Society of London A* **275**, 611–651.

Soward, A. M. 1974 A convection-driven dynamo: I. the weak field case. *Phil. Trans. Royal Soc. London A* **275** (1256), 611–646.

Soward, A. M. 1979 Convection driven dynamos. *Physics of the Earth and Planetary Interiors* **20** (2-4), 134–151.

Spiegel, E. A. & Veronis, G. 1960 On the boussinesq approximation for a compressible fluid. *The Astrophysical Journal* **131**, 442–447.

Sreenivasan, B. & Jones, C. A. 2011 Helicity generation and subcritical behaviour in rapidly rotating dynamos. *J. Fluid Mech.* **688**, 5.

St. Pierre, M. 1993 The Strong Field Branch of the Childress-Soward Dynamo. *Solar and Planetary Dynamos* pp. 295–302.

Stanley, S., Elkins-Tanton, L., Zuber, M. T. & Parmentier, E. M. 2008 Mars' paleomagnetic field as the result of a single-hemisphere dynamo. *Science* **321** (5897), 1822–1825.

Stellmach, S. & Hansen, U. 2004 Cartesian convection driven dynamos at low Ekman number. *Phys. Rev. E* **70**, 056312.

Stelzer, Z. & Jackson, A. 2013 Extracting scaling laws from numerical dynamo models. *Geophys. J. Int.* **193** (3), 1265–1276.

Stevenson, D. 2001 Mars' core and magnetism. *Nature* **412** (6843), 214–219.

Strom, R. G., Croft, S. K. & Barlow, N. G. 1992 The martian impact cratering record. *Mars* pp. 383–423.

Tarduno, J. A., Cottrell, R. D., Watkeys, M. K., Hofmann, A., Doubrovine, P. V., Mamajek, E. E., Liu, D., Sibeck, D. G., Neukirch, L. P. & Usui, Y. 2010 Geodynamo, solar wind, and magnetopause 3.4 to 3.45 billion years ago. *Science* **327** (5970), 1238–1240.

Taylor, G. I. 1916 Motion of solids in fluids when the flow is not irrotational. *Proceedings of the Royal Society of London A* **93**, 99–113.

Tilgner, A. 2007 Kinematic dynamos with precession driven flow in a sphere. *Geophysical and Astrophysical Fluid Dynamics* **101** (1), 1–9.

Tilgner, A. 2012 Transitions in rapidly rotating convection driven dynamos. *Phys. Rev. Lett.* **109** (24), 248501.

Tobias, S. 2021 The turbulent dynamo. *Journal of Fluid Mechanics* **912**, P1.

Veronis, G. 1966 Motions at subcritical values of the rayleigh number in a rotating fluid. *Journal of Fluid Mechanics* **24** (3), 545–554.

Wadee, M. A. & Gardner, L. 2012 Cellular buckling from mode interaction in i-beams under uniform bending. *Proceedings of the Royal Society A: Mathematical, Physical and Engineering Sciences* **468** (2137), 245–268.

Weiss, N. O. 1966 The expulsion of magnetic flux by eddies. *Proceedings of the Royal Society of London. Series A. Mathematical and Physical Sciences* **293** (1434), 310–328.

Weiss, N. O. & Proctor, M. R. E. 2014 *Basic MHD*, p. 9–37. Cambridge University Press.

Wicht, J., Gastine, T., Duarte, L. D. & Dietrich, W. 2019 Dynamo action of the zonal winds in jupiter. *Astronomy & Astrophysics* **629** (A125), 1–11.

Wicht, J. & Sanchez, S. 2019 Advances in geodynamo modelling. *Geophysical & Astrophysical Fluid Dynamics* **113** (1-2), 2–50.

Wiechert, E. 1897 Uber die Massenvertheilung im Innern der Erde. *Gottingen Nachr* pp. 221–243.

de Wijs, G. A., Kresse, G., Vočadlo, L., Dobson, D., Alfe, D., Gillan, M. & Price, G. 1998 The viscosity of liquid iron at the physical conditions of the earth's core. *Nature* **392** (6678), 805–807.

Yadav, R. K., Gastine, T., Christensen, U. R., Wolk, S. J. & Poppenhaeger, K. 2016 Approaching a realistic force balance in geodynamo simulations. *Proceedings of the National Academy of Sciences* **133** (43), 12065–12070.

Yoder, C. F., Konopliv, A. S., Yuan, D. N., Standish, E. M. & Folkner, W. M. 2003 Fluid core size of mars from detection of the solar tide. *Science* **300** (5617), 299–303.

Zhang, K. & Gubbins, D. 2000*a* Is the geodynamo process intrinsically unstable? *Geophysical Journal International* **140** (1), F1–F4.

Zhang, K. & Gubbins, D. 2000*b* Scale disparities and magnetohydrodynamics in the earth's core. *Philosophical Transactions of the Royal Society of London. Series A: Mathematical, Physical and Engineering Sciences* **358** (1768), 899–920.

Zollner, F. 1871 Uber den Ursprung des Erdmagnetismus und die magnetischen Beziehungen der Weltkorper. *Gesellschaft der Wissenschaften, Mathematisch-Physikalische, Leipzig* **23**, 479–575.